UAB
Universitat Autònoma de Barcelona

Modeling Liver–Skeletal Muscle Crosstalk in Metabolic Dysfunction–Associated Steatotic Liver Disease Using Bioengineered Human Tissues: Toward a Multi–Organ–on–Chip Platform

Armando Cortés Reséndiz

ADVERTIMENT. L'accés als continguts d'aquesta tesi queda condicionat a l'acceptació de les condicions d'ús establertes per la següent llicència Creative Commons: https://creativecommons.org/licenses/?lang=ca

ADVERTENCIA. El acceso a los contenidos de esta tesis queda condicionado a la aceptación de las condiciones de uso establecidas por la siguiente licencia Creative Commons: https://creativecommons.org/licenses/?lang=es

WARNING. The access to the contents of this doctoral thesis it is limited to the acceptance of the use conditions set by the following Creative Commons license: https://creativecommons.org/licenses/?lang=en

Universitat Autònoma de Barcelona

PhD program in Biotechnology

Doctoral Thesis

Modeling Liver–Skeletal Muscle Crosstalk in Metabolic Dysfunction-Associated Steatotic Liver Disease Using Bioengineered Human Tissues: Toward a Multi-Organ-on-Chip Platform

Presented by

Armando Cortés Reséndiz

Director Dr. Javier Ramón Azcón

Tutor Dr. Arben Merkoçi Hyka

Universitat Autònoma de Barcelona

Institute for Bioengineering of Catalonia

Armando Cortés Reséndiz, 2026

The research presented in this thesis was carried out in the Biosensors for Bioengineering group at the Institute for Bioengineering of Catalonia (IBEC), Barcelona, Spain. This work was funded by the former Mexican National Council of Science and Technology (CONACyT), now the Secretariat of Science, Humanities, Technology and Innovation of Mexico (SECIHTI) and Project PID2022-136833OB-C22 funded by MCIN/AEI/10.13039/501100011033.

Acknowledgements

Quiero comenzar agradeciendo a todas las personas que me acompañaron y estuvieron involucradas en este camino conmigo. Cada uno dejó enseñanzas en mí a su manera. He aprendido tanto de ustedes que después de esta experiencia soy una persona muy diferente.

Al Dr. Javier Ramón Azcón, mi director de tesis, quiero agradecer la confianza que tuvo en mí desde el inicio y la apertura para recibirme en su laboratorio. El valor de la independencia en la investigación es algo muy valioso que aprendí de él y se ve reflejado en el gran equipo que ha construido con el paso de los años. Aunque mi paso por su laboratorio ha sido solamente una pequeña parte de su carrera, estoy seguro de que vienen cosas muy emocionantes y muchos éxitos más para el B4b.

Which brings me to thank all my amazing colleagues at the B4b group. Besides being all diverse, deeply passionate and incredibly interesting people, in every single one of you I saw a very open scientific calling. Thank you for being up for answering questions, discussing ideas, making suggestions, sharing experience, expertise, and for never keeping your valuable ideas to yourselves. During my time in the lab, I knew so many people I cannot even count, and I am happy you all left such a good impression on me in the personal and professional field. I am looking forward to the most thrilling updates from your scientific career. Special thanks to my fellow PhDs, because we know we did our best and I am proud of us.

A la autoridad máxima en el laboratorio, Natalia, que gobierna sobre todos, muchas gracias por tu amistad y por acompañarme en los últimos meses de jornadas interminables. Todo fue más llevadero con tu apoyo moral. Además, gracias por siempre subirte a los planes y conectar tanto conmigo desde la música y todos nuestros hobbies.

Majo, tengo muchísimo que agradecerte. Estos cuatro años han sido los más duros, pero gracias por siempre confiar en mí, por estar aquí para mí, por el tiempo de calidad, por escucharme, por acompañarme y por tener la fuerza cuando yo no la tenía. Creo que ni tú te imaginas lo mucho que he aprendido de ti, pero algo que sabemos muy bien los dos es que hacemos un súper equipo. Tu futuro profesional te traerá cosas aún mejores y no puedo esperar para ver qué será porque te lo mereces de verdad.

Familia, esta tesis es de ustedes también. Papá, Abuelita, Ricardo, Ale, tío César, aunque nunca hemos estado tanto tiempo separados, pienso mucho en ustedes todos los días y son mi orgullo. A diferencia de mí, ustedes jamás dudaron que yo llegaría hasta aquí. Gracias por darme toda esa confianza y la fuerza para continuar cuando todo parecía tan difícil, porque su trabajo duro y ejemplo son mi inspiración.

Mami, creo que nunca había dimensionado el valor de tu experiencia e historia profesional hasta que llegué aquí a comenzar mi propia carrera. Por eso, además de mamá y pilar en mi vida, te

admiro como científica y profesional. Gracias por los consejos profesionales y sobre la vida. Gracias porque suena el teléfono todos los días para saber cómo estoy. Nunca has dejado de apoyarme en este camino y eso es lo más valioso para mí. El futuro a veces da miedo, sé que tú estás tan emocionada como yo por lo que viene. Esta tesis es para ti también porque todo lo que he logrado se los debo a ustedes.

A Comisario, mi perrito y compañero, le agradezco su amor incondicional y por ayudarme a disfrutar las cosas simples de cada día. Los dos pasamos cosas muy difíciles en estos cuatro años, pero ha sido un ejemplo de ternura, fuerza, valentía y resiliencia para mí.

A mis amigos de toda la vida quiero agradecerles las visitas, las llamadas, las risas, las salidas. Hemos cambiado mucho y hemos visto tantas versiones de nosotros que me siento honrado de estar acompañado por ustedes hasta hoy. Sammy, Elo, Frida, Luis, Manuel, Óscar, Kay, Dianita… gracias por traer un pedacito de México.

A mis chilenos favoritos, Carla y Juanpi, los quiero mucho y también les dedico esta tesis. Nos iremos a celebrar la amistad entre México y Chile. A mis amigos que conocí aquí: Elia, Ainhoa, Ainoa, Mr. Jose Huget, Sheeza, Anas, gracias por sus consejos, compañía y empatía.

Abstract

Metabolic Dysfunction-Associated Steatotic Liver Disease (MASLD) is the most prevalent chronic liver disease worldwide and represents a major clinical and socioeconomic challenge. It is associated with obesity, insulin resistance, type 2 diabetes, and systemic metabolic dysfunction. Although the liver is the central pathological organ, MASLD is increasingly recognized as a multi-organ disorder in which disease progression and patient outcomes are strongly influenced by extrahepatic complications. Among these, skeletal muscle impairment is particularly relevant, as reduced muscle mass, altered muscle quality, and impaired contractile performance are frequently associated with worse prognosis, metabolic deterioration, and progression toward more severe disease stages. However, the biological mechanisms through which the diseased liver contributes to skeletal muscle impairment remain difficult to dissect in patients and animal models, where systemic complexity limits causal interpretation.

Current preclinical models do not adequately reproduce the human liver–skeletal muscle axis under controlled and physiologically relevant conditions. Conventional two-dimensional cell cultures allow scalable mechanistic studies but lack tissue-level architecture, extracellular matrix interactions, multicellular signaling, and functional readouts. Animal models capture systemic physiology but are limited by species-specific differences and reduced control over individual organ contributions. Consequently, there is a pressing need for modular, human-relevant *in vitro* platforms capable of modelling defined stages of MASLD progression and evaluating their downstream impact on skeletal muscle function.

This doctoral research addresses this need through the development of a modular *in vitro* strategy based on bioengineered human three-dimensional liver and skeletal muscle tissues. First, a three-dimensional liver model was established by encapsulating HepaRG hepatocyte-like cells and LX-2 hepatic stellate cells in collagen-based hydrogels. A lipotoxic stimulus based on non-esterified fatty acids was used to induce a steatotic phenotype, while the subsequent addition of lipopolysaccharide generated a more severe MASH-like inflammatory and fibrogenic environment. This model reproduced key features of MASLD progression, including lipid accumulation, hepatocellular dysfunction, cell injury, inflammatory cytokine production, hepatic stellate cell activation, and early extracellular matrix remodeling. Combined NEFAs and LPS exposure exacerbated lipid accumulation, reduced albumin expression, increased AST and caspase-3 release, enhanced IL-6 secretion, and induced fibrogenic markers such as COL1A1, supporting the generation of a disease-stage-specific hepatic phenotype.

Separately, differentiated human three-dimensional skeletal muscle tissues were generated from AB1079 myoblasts embedded in Matrigel–fibrin hydrogels and matured into aligned contractile tissues capable of responding to electrical pulse stimulation. To model liver-derived effects on muscle, skeletal muscle tissues were exposed to conditioned media (CM) generated by the liver constructs under control, steatotic, MASH-like, and inflammatory-only conditions. After optimizing CM dilution to preserve baseline muscle viability and function, disease-stage-specific liver-derived media were shown to impair skeletal

muscle performance. The CM from steatotic liver constructs reduced myotube diameter and cross-sectional area, while MASH-like CM induced the most severe reduction in contractile force, particularly under high-frequency stimulation. These functional alterations were accompanied by changes in myogenic regulatory factors, repression of canonical atrogenes, and increased lysosomal/autophagy-associated readouts, suggesting that liver-derived disease signals can alter skeletal muscle quality through mechanisms that extend beyond classical atrophy.

Finally, this thesis explored the engineering transition from static CM transfer toward dynamic liver–skeletal muscle communication in an organ-on-chip framework. A first-generation microfluidic device was designed and fabricated to connect a liver chamber, a passive serpentine diluting and mixing unit, and a downstream skeletal muscle chamber. Using Rhodamine B fluorescence as a liver-medium surrogate, the device was fluidically characterized under pressure-driven flow. The serpentine geometry enabled progressive mixing along the channel, and inlet pressure conditions were identified that reproduced the biologically required 1:50 liver-medium dilution before entry into the skeletal muscle chamber. Although live tissue integration was not completed within the scope of this thesis, the device established the fluidic foundation for future dynamic co-culture studies.

Overall, this thesis contributes to the development of human-relevant *in vitro* models for systemic metabolic disease by integrating three-dimensional liver modelling, functional skeletal muscle bioengineering, inter-organ interrogation, and organ-on-chip design. The work demonstrates that disease-stage-specific hepatic environments generated *in vitro* are sufficient to impair human skeletal muscle structure and function, supporting the relevance of liver-derived cues in MASLD-associated muscle dysfunction. By adopting a modular strategy, this platform bridges reductionist cell culture systems and complex animal models, while providing a flexible experimental framework that can be expanded toward dynamic multi-organ-on-chip models, biomarker discovery, therapeutic testing, and more precise investigation of liver–skeletal muscle crosstalk in MASLD and MASH.

Table of contents

Acknowledgements vii
Abstract x
Table of contents xiii
List of abbreviations xviii
List of figures xxv
Chapter 1 | General Introduction 1
1.1 Current Understanding of Metabolic Dysfunction-Associated Steatotic Liver Disease (MASLD) 1
1.1.1 Context and Relevance of MASLD 1
1.1.2 Epidemiology of MASLD 2
1.1.3 Pathogenesis of MASLD 5
1.1.3.7.1 Cellular Heterogeneity and Macrophage Recruitment 16
1.1.3.7.2 Signal Transduction: DAMPs and PAMPs 16
1.1.4 The Diagnostic Challenges in MASLD 19
1.1.5 A Multisystemic Disorder: Extrahepatic implications of MASLD 21
1.2 The Skeletal Muscle: Functions and Implications 22
1.2.1 Organization and Tissue Architecture 22
1.2.2 Molecular Basis of Force Generation 23
1.2.3 Fiber Types and Specialization 25
1.2.4 Excitation-Contraction Coupling and Electrical Stimulation 27
1.2.5 Energy Metabolism and Muscle Plasticity 28
1.2.6 Protein Turnover, Atrophy, and Autophagy-Lysosome Homeostasis 29
1.2.7 Myogenic Maturation 30
1.3 The Liver-Muscle Axis: Sarcopenia and Muscle Wasting 32
1.3.1 Mechanistic Links between MASLD and Skeletal Muscle 34
1.4 Rationale of this Work: Modular *In vitro* Study of Liver-Muscle Crosstalk 35
Chapter 2 | Hypothesis and Objectives 37
Chapter 3 | Materials and Methods 41
3.1 Cell sources and culture conditions 41
3.1.1 Immortalized hepatic cells (HepaRG™) 41
3.1.2 Hepatic stellate cells (LX-2) 41
3.1.3 Human myoblasts (AB1079) 42
3.2 Preparation of lipotoxic and inflammatory stimuli 42
3.2.1 Preparation of non-esterified fatty acids 42
3.2.2 High lipid regime for HepaRG in 2D 42

3.3 Preliminary 2D assays for lipid-challenge optimization 43
3.3.1 Cell culture staining 43
3.3.2 Metabolic activity/viability and lysosomal activity assays 43
3.4 Three-dimensional liver module 44
3.4.1 Fabrication of 3D liver constructs 44
3.4.2 Recapitulation of steatosis and steatohepatitis in 3D livers 44
3.4.3 AdipoRed™ staining and quantitative analysis 44
3.4.4 LIVE/DEAD staining and quantitative analysis 45
3.4.5 Picro Sirius Red Staining 45
3.4.6 Albumin, AST, PINP, and PIIINP measurements 45
3.4.7 Cytokine measurements 45
3.5 Three-dimensional skeletal muscle module 46
3.5.1 Fabrication of PDMS casting molds 46
3.5.2 Fabrication and maturation of 3D bioengineered skeletal muscle tissues 46
3.6 Static liver–muscle communication experiments 47
3.6.1 Treatment of skeletal muscle tissues with conditioned media from 3D livers 47
3.6.2 Functional assessment of 3D skeletal muscle tissues 47
3.6.3 Histological assessment of skeletal muscle tissues 48
3.7 Structural and molecular characterization 48
3.7.1 Cryosectioning 48
3.7.2 Standard immunofluorescence staining 49
3.7.3 Gene expression analysis by real-time qPCR 49
3.8 Organ-on-chip device fabrication and fluidic characterization 50
3.8.1 Organ-on-chip device design 50
3.8.2 Fabrication and assembly of the microfluidic device 50
3.8.3 Rhodamine B calibration for fluorescence-based dilution analysis 51
3.8.4 Pressure-driven flow setup 51
3.8.5 Mixing efficiency analysis 52
3.8.6 Dilution analysis 52
3.9 Statistical analysis 52
3.10 Reagents, probes, and gene expression assays 53
3.10.1 Antibodies and cellular probes 53
3.10.2 Gene expression assays 54
Chapter 4 | Bioengineered Liver Module 57
4.1 Chapter rationale and modeling framework 57
4.2 Aims and scope 57
4.3 Introduction: Preclinical Modelling Strategies for Metabolic Dysfunction-Associated Steatotic Liver Disease 58
4.3.1 Clinical Studies 58

4.3.2 Animal Models 59
4.3.3 *In vitro* Models 60
4.4 Results 64
4.4.1 Strategy for model induction 64
4.4.2 Fabrication of 3D Liver Constructs and Structural Stability 66
4.4.3 Phenotypic Preservation 68
4.4.4 Steatosis and The Synergistic Transition to MASH 69
4.4.5 Hepatocellular Dysfunction and Damage 73
4.4.6 Markers of apoptosis and MASLD progression 76
4.4.7 Pro-fibrotic Remodeling 78
4.5 Discussion 84
4.5.1 The balance between biological faithfulness, scalability and modularity of the 3D liver constructs 84
4.5.2 Cell types and 3D hydrogel architecture 84
4.5.3 Disease induction strategy 85
4.5.4 The synergy in steatosis and hepatocellular injury 86
4.5.5 Apoptosis 87
4.5.6 HSC activation as a driver of a MASH-like progression 87
4.5.7 Temporal resolution of cytokine and growth factor responses 88
4.5.8 Pro-fibrotic remodeling and ECM markers 89
4.5.9 Summary of the model performance 89
Chapter 5 | Bioengineered Skeletal Muscle Module 91
5.1 Chapter rationale and modeling framework 91
5.2 Aims and scope 91
5.3 Introduction: Models of Skeletal Muscle 92
5.3.1 Native complexity of liver–muscle crosstalk 92
5.3.2 Limitations of conventional models 92
5.3.3 In-vitro skeletal muscle models 93
5.3.4 Functional readouts in models of skeletal muscle 97
5.3.5 Improvement of conventional models by advanced *in vitro* skeletal muscles 98
5.3.6 Design remarks for the skeletal muscle module 99
5.4 Results 100
5.4.1 Fabrication of 3D skeletal muscle tissues 100
5.4.2 Exposure to MASLD-conditioned media 102
5.4.3 MASLD-conditioned media induce a severity-dependent decline in muscle contractility 105
5.4.4 Myotube size and morphology under MASLD-conditioned media 108
5.4.5 MASLD-derived factors repress canonical atrogenes and alter the myogenic program 110
5.4.6 MASLD-conditioned media enhance autophagy and lysosomal activity in skeletal muscles 114
5.5 Discussion 118

5.5.1 MASLD-derived factors reproduce severity-dependent functional impairment and dissociation between muscle mass and strength 119
5.5.2 Myotube structural changes contribute to, but do not fully explain, contractile deficits 119
5.5.3 Downregulation of canonical atrogenes suggests non-classical mechanisms of muscle wasting 120
5.5.4 Myogenic program remodeling under steatotic liver- and MASH-like conditions 121
5.5.5 Autophagy–lysosome remodeling as a central axis of MASLD-induced muscle dysfunction 122
5.5.6 Integration with liver module: a multi-layered liver–muscle axis 123
5.5.7 Limitations and future directions 123
5.5.8 Implications for MASLD-associated muscle wasting and translational opportunities 124
Chapter 6 | Organ-on-Chip Device for Liver-Skeletal Muscle Interrogation 126
6.1 Introduction 126
6.1.1 Contribution statement and collaborative framework 126
6.1.2 Positioning of the Organ-on-Chip device 127
6.1.3 Biological motivation behind the Organ-on-Chip device 127
6.1.4 From conditioned medium transfer to dynamic organ-on-chip 128
6.1.5 Organ-on-chip and microfluidic background 128
6.1.6 Biological modules for future integration 132
6.1.7 Translating dilution requirements into engineering constraints 132
6.2 Aims and scope 133
6.3 Results 134
6.3.1 Design rationale for a liver–skeletal muscle organ-on-chip platform 134
6.3.2 Fabrication and layering of the first-generation device 135
6.3.3 Integration constraints for microscopy-compatible multi-tissue culture 136
6.3.4 Fluorescence-based characterization of mixing along the serpentine channel 137
6.3.5 Pressure-dependent mixing efficiency in the serpentine region 139
6.3.6 Identification of pressure conditions compatible with the target 1:50 liver-medium dilution 141
6.4 Discussion 142
6.4.1 Design constraints and engineering goal of the fluidic characterization 142
6.4.2 Limitations of the microfluidic characterization towards biological translation 144
6.4.3 Future work 145
Chapter 7 | Conclusions 147
Chapter 8 | References 150
Appendix A. Signal translation into inflammatory and fibrogenic programs in MASLD. 175
Appendix B. Biomaterial requirements and fabrication strategies for *in vitro* skeletal muscle models 179

List of abbreviations

2D	Two-dimensional
3D	Three-dimensional
3Rs	Replacement, Reduction, and Refinement
ACA	6-Aminocaproic acid
ACC	Acetyl-CoA carboxylase
ACLY	ATP-citrate lyase
ANOVA	Analysis of variance
APRI	Aspartate aminotransferase-to-platelet ratio index
ASMI	Appendicular skeletal muscle mass index
AST	Aspartate aminotransferase
ATP	Adenosine triphosphate
AU	Airy unit
BAMBI	BMP and activin membrane-bound inhibitor
BMI	Body mass index
BP	Blood pressure
BSA	Bovine serum albumin
CAD	Computer-aided design
CCL2	C-C motif chemokine ligand 2
CCR2	C-C chemokine receptor type 2
CD36	Cluster of differentiation 36
ChREBP	Carbohydrate response element-binding protein
CLD	Chronic liver disease
CM	Conditioned media / conditioned medium
CMRF	Cardiometabolic risk factor
CoA	Coenzyme A
CPT1	Carnitine palmitoyl transferase 1

CRP	C-reactive protein
CSA	Cross-sectional area
CVD	Cardiovascular disease
CXCL8	C-X-C motif chemokine ligand 8
CYP3A4	Cytochrome P450 family 3 subfamily A member 4
CYP450	Cytochrome P450
DAG	Diacylglycerol
DALY	Disability-adjusted life year
DAMP	Damage-associated molecular pattern
DAPI	4,6-diamidino-2-phenylindole
dECM	Decellularized extracellular matrix
DHPR	Dihydropyridine receptor
DM	Differentiation medium
DMEM	Dulbecco's Modified Eagle Medium
DNA	Deoxyribonucleic acid
DNL	De novo lipogenesis
EC	Endothelial cell
ECM	Extracellular matrix
ELF	Enhanced Liver Fibrosis
EPS	Electrical pulse stimulation
ER	Endoplasmic reticulum
ERK	Extracellular signal-regulated kinase
ETC	Electron transport chain
EV	Extracellular vesicle
FA	Fatty acid
$FADH_2$	Reduced flavin adenine dinucleotide
FAP	Fibro-adipogenic progenitor
FAS	Fatty acid synthase
FATP	Fatty acid transport protein

FBS	Fetal bovine serum
FFA	Free fatty acid
FGF21	Fibroblast growth factor 21
FIB-4	Fibrosis-4 index
FoxO3	Forkhead box O3
GAPDH	Glyceraldehyde-3-phosphate dehydrogenase
GCKR	Glucokinase regulator
GLP-1	Glucagon-like peptide-1
GM	Growth medium
HCC	Hepatocellular carcinoma
HCD	High-cholesterol diet
HDL	High-density lipoprotein
HFD	High-fat diet
HFHF	High-fat–high-fructose
HGM	Hepatocyte growth medium
HMGB1	High mobility group box 1
HNF4A	Hepatocyte nuclear factor 4 alpha
HSC	Hepatic stellate cell
HSD17B13	Hydroxysteroid 17-beta dehydrogenase 13
IGF-1	Insulin-like growth factor 1
IL-18	Interleukin-18
IL-1β	Interleukin-1 beta
IL-6	Interleukin-6
IL-8	Interleukin-8
IR	Insulin resistance
IRF	Interferon regulatory factor
IRS	Insulin receptor substrate
ITS-X	Insulin-transferrin-selenium-ethanolamine
JAK	Janus kinase

JNK	c-Jun N-terminal kinase
KC	Kupffer cell
KO-SR	KnockOut Serum Replacement
LAP	Lithium phenyl-2,4,6-trimethylbenzoylphosphinate
LC3B	Microtubule-associated protein 1 light chain 3 beta
LD	Lipid droplet
LDL	Low-density lipoprotein
LEC	Liver endothelial cell
LPS	Lipopolysaccharide
LSEC	Liver sinusoidal endothelial cell
LTR99	LysoTracker Red DND-99
MAPK	Mitogen-activated protein kinase
MASH	Metabolic Dysfunction-Associated Steatohepatitis
MASL	Metabolic Dysfunction-Associated Steatotic Liver
MASLD	Metabolic Dysfunction-Associated Steatotic Liver Disease
MBOAT7	Membrane-bound O-acyltransferase domain-containing 7
MCD	Methionine–choline-deficient
MDA	Malondialdehyde
MEF2	Myocyte enhancer factor 2
MELD	Model for End-Stage Liver Disease
MetS	Metabolic syndrome
MFI	Median fluorescence intensity
MHC	Myosin heavy chain
miRNA	MicroRNA
MPS	Microphysiological system
MRE	Magnetic resonance elastography
MRF	Myogenic regulatory factor
mRNA	Messenger RNA
mtDNA	Mitochondrial DNA

MTS	3-(4,5-dimethylthiazol-2-yl)-5-(3-carboxymethoxyphenyl)-2-(4-sulfophenyl)-2H-tetrazolium
MuRF1	Muscle RING-finger protein 1
MyD88	Myeloid differentiation primary response 88
NADH	Reduced nicotinamide adenine dinucleotide
NAFLD	Non-Alcoholic Fatty Liver Disease
NASH	Non-Alcoholic Steatohepatitis
NEFA	Non-esterified fatty acid
NF-κB	Nuclear factor kappa B
NFS	NAFLD Fibrosis Score
NLRP3	NLR family pyrin domain containing 3
NMJ	Neuromuscular junction
NR	Neutral Red
Nrf2	Nuclear factor erythroid 2-related factor 2
OA	Oleic acid
OCT	Optimal cutting temperature compound
OoC	Organ-on-chip
PA	Palmitic acid
PAMP	Pathogen-associated molecular pattern
PAX3	Paired box 3
PAX7	Paired box 7
PCR	Polymerase chain reaction
PDGF	Platelet-derived growth factor
PDGFRβ	Platelet-derived growth factor receptor beta
PDMS	Polydimethylsiloxane
PEDOT	Poly(3,4-ethylenedioxythiophene)
PEG	Polyethylene glycol
PFOTS	Trichloro(1H,1H,2H,2H-perfluorooctyl)-silane
PHH	Primary human hepatocyte

PI3K	Phosphoinositide 3-kinase
PIIINP	Procollagen type III N-terminal propeptide
PINP	Procollagen type I N-terminal propeptide
PMMA	Poly(methyl methacrylate)
PNPLA3	Patatin-like phospholipase domain-containing protein 3
PRR	Pattern-recognition receptor
PSG	Penicillin-streptomycin-glutamine
PSR	Picro Sirius Red
PUFA	Polyunsaturated fatty acid
RCF	Relative centrifugal force
RCT	Randomized controlled trial
RNA	Ribonucleic acid
ROS	Reactive oxygen species
RT-qPCR	Reverse transcription quantitative polymerase chain reaction
RyR1	Ryanodine receptor 1
SAA	Sarcomeric alpha-actinin
SEM	Standard error of the mean
SERCA	Sarco/endoplasmic reticulum Ca^{2+}-ATPase
SFA	Saturated fatty acid
SFM	Serum-free medium
SIRT1	Sirtuin 1
SkM DM	Skeletal muscle differentiation medium
SkM GM	Skeletal muscle growth medium
SL	Steatotic liver
SL-CM	Steatotic liver-conditioned media
SMAD	Small mothers against decapentaplegic
SREBP-1c	Sterol regulatory element-binding protein 1c
SRP	Signal recognition particle
STAT3	Signal transducer and activator of transcription 3

SU-8	SU-8 photoresist
T2D	Type 2 diabetes
TAG	Triacylglycerol
TAZ	Transcriptional coactivator with PDZ-binding motif
TCA	Tricarboxylic acid
TG	Triglyceride
TGF-β	Transforming growth factor beta
TLR	Toll-like receptor
TM6SF2	Transmembrane 6 superfamily member 2
TMAO	Trimethylamine N-oxide
TNF-α	Tumor necrosis factor alpha
UPR	Unfolded protein response
UV	Ultraviolet
VCTE	Vibration-controlled transient elastography
VEGF	Vascular endothelial growth factor
VEGFR	Vascular endothelial growth factor receptor
VLDL	Very-low-density lipoprotein
YAP	Yes-associated protein

List of figures

Figure 1.1. The "two-hit" hypothesis of NAFLD/NASH. *5*
Figure 1.2. Schematic representation of the Multiple Parallel Hits hypothesis of MASLD pathogenesis *6*
Figure 1.3. Overview of the MASLD progression. *8*
Figure 1.4. Hepatic de novo lipogenesis and lipid trafficking in MASLD and MASH. *10*
Figure 1.5. Potential drivers of hepatic lipid accumulation and its progression to lipotoxicity. *13*
Figure 1.6. Mitochondrial adaptation and dysfunction in MASLD–MASH. *14*
Figure 1.7. Phenotypes and functions of HSCs in healthy and diseased liver. *18*
Figure 1.8. Organization of the skeletal muscle *23*
Figure 1.9. Structure of the sarcomere in skeletal muscle. *24*
Figure 1.10. Sliding movement of sarcomeric proteins during skeletal muscle contraction. *25*
Figure 1.11. Fiber types stained with anti-myosin antibodies in a section of vastus lateralis muscle of a young adult. *26*
Figure 1.12. Basic structure of the NMJ and how acetylcholine binding to its receptors leads to muscle contraction and depolarization. *27*
Figure 1.13. Skeletal muscle as a metabolic organ and its interactions with the systemic metabolic milieu. *28*
Figure 1.14. Molecular regulation of protein balance in skeletal muscle in response to systemic glucose, amino acids, insulin/growth factors, and inflammatory signals. *30*
Figure 1.15. Transcription factors involved in skeletal muscle differentiation. *31*
Figure 1.16. Phenotypic changes in sarcopenia and its associated risk factors. *32*
Figure 1.17. Common features of MASLD and sarcopenia. *33*
Figure 4.1. Comparison of two-dimensional and three-dimensional in vitro strategies for MASLD modeling. *62*
Figure 4.2. Representative architecture of a commercial liver-on-chip platform. *63*
Figure 4.3. Experimental timeline for the characterization of steatosis in response to lipid load. *64*
Figure 4.4. Validation of lipid internalization by HepaRG cells in 2D culture. *65*
Figure 4.5. Histological validation of lipid internalization by HepaRG cells in 2D culture. *66*
Figure 4.6. Fabrication and disease-induction timeline of the 3D MASLD/MASH liver model. *67*
Figure 4.7. Macroscopic appearance of 3D liver constructs at different timepoints, evaluated by brightfield microscopy to assess hydrogel integrity. *68*
Figure 4.8. Assessment of phenotypic preservation in 3D liver constructs by confocal microscopy. *69*
Figure 4.9. First observations of steatosis in 3D liver constructs by brightfield microscopy *70*
Figure 4.10. Representative brightfield images of structures resembling apoptotic bodies. *71*
Figure 4.11. Assessment of steatosis in live 3D liver constructs. *72*
Figure 4.12. Quantitative assessment of steatosis in live 3D liver constructs. *73*
Figure 4.13. Evaluation of albumin expression and synthesis as a marker of hepatocyte identity. *74*
Figure 4.14. Hepatocellular damage and overall cell viability of 3D constructs. *75*
Figure 4.15. Representative confocal images of LIVE/DEAD™ staining at the final timepoint. *76*
Figure 4.16. Apoptotic effector caspase-3 in supernatants from 3D liver constructs. *77*
Figure 4.17. Inflammatory cytokines related to MASH progression in supernatants from 3D liver constructs. *78*
Figure 4.18. PDGF-BB isoform in supernatants from 3D liver constructs. *79*
Figure 4.19. Vimentin immunostaining at the final timepoint. *80*
Figure 4.20. Histological characterization of 3D liver construct cryosections with Picro Sirius Red staining. *81*

Figure 4.21. Relative mRNA expression of COL1A1 gene at the final timepoint. *82*
Figure 4.22. PIIINP and PINP in supernatants from 3D liver constructs at day 4 (after lipid hit) and 7 (after lipid hit and hepatic stellate cell stimulation). *83*
Figure 5.1. Engineered 2D skeletal muscle culture systems with topographical cues. *94*
Figure 5.2. Bioengineered myobundles as 3D in vitro skeletal muscle models. *95*
Figure 5.3. Fabrication and functional assessment workflow of 3D skeletal muscle-on-chip constructs. *96*
Figure 5.4. Representative contractile response of a 3D engineered skeletal muscle tissue under EPS. ... *98*
Figure 5.5. Schematic representation of 3D skeletal muscle fabrication, maturation, and experimental timeline. *100*
Figure 5.6. Skeletal muscle tissues imaged by brightfield microscopy at different timepoints. *101*
Figure 5.7. Inspection of 3D skeletal muscle whole mounts. *102*
Figure 5.8. Representative brightfield images of 3D tissues after exposure to CM from the liver model. *103*
Figure 5.9. Optimization of liver CM dilution for functional testing in 3D skeletal muscle tissues. *104*
Figure 5.10. Control comparison for CM exposure in 3D skeletal muscle tissues. *105*
Figure 5.11. Electrical stimulation and visualization of measured variables. *105*
Figure 5.12. Representative contractile profiles of skeletal muscle tissues after exposure to CM from the liver constructs. *106*
Figure 5.13. Functional evaluation at 2 Hz after exposure to CM from the liver constructs. *107*
Figure 5.14. Functional evaluation at 50 Hz after exposure to CM from the liver constructs. *108*
Figure 5.15. Histological examination of myotube morphology and size. *109*
Figure 5.16. Overlapped distribution of myotube size across experimental groups. *109*
Figure 5.17. Morphometric evaluation of skeletal muscle tissues after exposure to CM from the liver model. *110*
Figure 5.18. Relative expression of atrogenes in 3D skeletal muscle tissues after exposure to CM from the liver constructs. *111*
Figure 5.19. Relative expression of MRFs in 3D skeletal muscle tissues after exposure to CM from the liver constructs. *112*
Figure 5.20. Relative expression of MRFs in 3D skeletal muscle tissues after exposure to CM from the liver constructs. *113*
Figure 5.21. Relative expression of terminal differentiation marker MYH7 in 3D skeletal muscle tissues after exposure to CM from the liver constructs. *113*
Figure 5.22. Acidic compartments on tissue cryosections after exposure to CM from liver constructs. . *115*
Figure 5.23. Quantification of acidic compartments on tissue cryosections. *116*
Figure 5.24. LC3 puncta on tissue cryosections after exposure to CM from liver constructs. *117*
Figure 5.25. Quantification of LC3 puncta on tissue cryosections. *118*
Figure 6.1. General design of the liver–skeletal muscle organ-on-chip device. *135*
Figure 6.2. Layered structure, assembled prototype, and mixing-analysis regions of the liver–skeletal muscle organ-on-chip device. *136*
Figure 6.3. Rhodamine B calibration for fluorescence-based dilution and mixing analysis. *137*
Figure 6.4. Experimental setup for pressure-driven microfluidic dilution and mixing characterization. *138*
Figure 6.5. Fluorescence-based evaluation of progressive mixing along the serpentine channel. *139*
Figure 6.6. Mixing efficiency along the serpentine diluting/mixing unit at different liver inlet pressures. *140*
Figure 6.7. Fluorescence intensity profiles at the outlet of the serpentine diluting/mixing unit. *140*
Figure 6.8. Pressure-dependent dilution of Rhodamine B in unlabeled fluid before entry into the skeletal muscle chamber. *141*

Chapter 1 | General Introduction

1.1 Current Understanding of Metabolic Dysfunction-Associated Steatotic Liver Disease (MASLD)

1.1.1 Context and Relevance of MASLD

The global landscape of hepatology has experienced a deep transformation over the last quarter of a century. As the prevalence of viral hepatitis has declined due to effective vaccination and antiviral therapies, liver diseases related to metabolism have emerged as the dominant public health challenge of our modern era. Metabolic Dysfunction-Associated Steatotic Liver Disease (MASLD), formerly known as Non-Alcoholic Fatty Liver Disease (NAFLD), is now the most common chronic liver condition worldwide, affecting more than 30% of the global population [1,2]. This shift is not only epidemiological but reflects a fundamental change in the etiological paradigm of liver injury, moving from infectious drivers to systemic metabolic dysfunction rooted in the global increase in obesity, type 2 diabetes mellitus (T2D), and sedentary lifestyles [1].

The renaming of the disease from NAFLD to MASLD, achieved in a multi-society Delphi consensus in 2023, was a milestone in the field [3]. The previous nomenclature was defined by exclusion —diagnosis and classification based on what the disease is not, namely excessive alcohol consumption or viral infection. The issue with this former definition was that it failed to capture the positive diagnostic criteria that drive the disease's pathophysiology. Furthermore, the term "fatty" was generally perceived as stigmatizing towards patients. The new terminology, MASLD, is defined by the presence of hepatic steatosis in conjunction with at least one cardiometabolic risk factor (CMRF), such as adiposity, glucose intolerance, or dyslipidemia [2]. This affirmative definition explicitly links hepatic health to systemic metabolic homeostasis, acknowledging the liver is both a victim and driver of metabolic syndrome [4].

The clinical relevance of MASLD extends far beyond the liver. It is increasingly recognized as a key indicator of systemic health, with patient outcomes often dictated not by hepatic failure, but by cardiovascular events and extrahepatic malignancies [1]. However, MASLD is a disease continuum, and for a subset of patients, the disease progresses from simple steatosis (MASL) to Metabolic Dysfunction-Associated Steatohepatitis (MASH). MASH is characterized by a triad of steatosis, lobular inflammation, and hepatocellular ballooning, which collectively drive the activation of fibrogenic pathways [5]. This progression from simple lipid accumulation to inflammation, fibrosis, cirrhosis, and potentially hepatocellular carcinoma (HCC) is a central challenge of modern hepatology. MASH is rapidly becoming the leading indication for liver transplantation in western countries, surpassing hepatitis C and alcohol-associated liver disease [1].

Despite its prevalence and severity, the therapeutic landscape for MASLD remains largely uncertain and unclear. Of course, new non-invasive diagnostic tools and promising advances in drug development have pushed the field forward. Nevertheless, until the recent conditional approval of resmetirom on March 2024, a thyroid hormone receptor-β agonist, there were no FDA-approved pharmacotherapies for MASH [6–8]. This lack of treatment options is a direct consequence of the disease's complexity and the limitations of current preclinical models to provide relevant interrogation tools to investigate MASLD. The decade-long progression of MASLD in humans is difficult to replicate in animals, and the intricate intercellular crosstalk that drives fibrosis in MASH is often lost in simplified *in vitro* systems [9–11]. Consequently, future directions in the field focus on establishing physiologically relevant, scalable, and human centric models of MASLD. It is not just an important academic exercise but a critical necessity for drug discovery and personalized medicine.

1.1.2 Epidemiology of MASLD

1.1.2.1 Global Prevalence and Regional Disparities

The epidemiology of MASLD mirrors the trajectory of the obesity epidemic. Recent meta-analyses estimate the global prevalence of MASLD among adults to be 32% to 38% depending on geographical region, a figure that has risen by more than 50% since the 1990s [2]. This relentless increase is projected to continue, with forecasts suggesting that over half of the global population could be affected by 2040 if current metabolic trends persist [1].

As stated before, this burden is not distributed equally across the globe. The prevalence of MASLD exhibits significant geographic and ethnic heterogeneity.

Latin America

This region reports the highest prevalence rate globally, exceeding 44% [1]. This is attributed to a combination of rapid nutritional change towards high calorie processed foods and a high frequency of genetic risk variants, particularly the PNPLA3 I148M allele in Hispanic populations [12,13].

Middle East and North Africa (MENA)

This region is experiencing the fastest growth in prevalence, driven by skyrocketing rates of T2D and obesity. In some MENA cohorts, MASLD prevalence approaches 80% among patients with diabetes [1].

Asia

While overall prevalence has historically been lower than in the west, Asia is seeing an increase in "lean MASLD" phenotype. This manifestation occurring in individuals with a normal Body Mass Index (BMI) is

particularly common in Asian populations and challenges the outdated assumption that MASLD is solely a disease of the obese [14,15].

Western Europe and North America

These regions show high prevalence rates (25%-30%) but appear to be stabilizing in some regions, potentially due to improved public health awareness and the plateauing of obesity rates in certain subgroups [16].

1.1.2.2 Risk Factors and Comorbidities

The epidemiology of MASLD is tightly linked to its metabolic comorbidities. The presence of these conditions not only increases the likelihood of developing MASLD but also accelerates the progression to MASH and advanced fibrosis.

Table 1.1. Common risk factors strongly associated with MASLD.

Risk factor	Association with MASLD/MASH	Prevalence
Obesity (BMI ≥25 kg/m² or increased waist circumference)	Strongest predictor of steatosis. Visceral adiposity drives lipotoxicity via free fatty acid flux. [17]	70% - 75% of overweight and obese populations, severity-dependent. [18]
Type 2 Diabetes (T2D) (fasting glucose ≥5.6 mmol/L or diabetes diagnosis)	Shares a bidirectional relationship with MASLD, both increasing risk and prevalence of the other. [1]	68.8% of T2D population. [19]
Dyslipidemia (high triglycerides (TG) ≥1.70 mmol/L, low high-density lipoprotein (HDL) ≤1.0 mmol/L in males / ≤1.3 mmol/L in females)	High triglycerides reflect impaired hepatic lipoprotein export and adipose tissue insulin resistance. Low HDL reduces its anti-inflammatory and hepatoprotective properties, exacerbating MASH. High TG/HDL ratio is a predictor of MASLD and mortality. Hyperlipidemia fuels hepatic de novo lipogenesis. [20–22]	50% - 80% of the MASLD population. [5]

Hypertension (blood pressure ≥130/85 mmHg or antihypertensive therapy)	Hypertensive MASLD patients show 2.2-fold higher cardiac event risk and 1.35-fold higher hypertension incidence when F3-F4 fibrosis is present. [1]	50% - 80% of the MASLD population. [5]
Metabolic Syndrome (MetS) (≥3 of 5 criteria: central obesity, elevated glucose/diabetes, elevated TG, low HDL, elevated BP)	MASLD is known as the “hepatic manifestation of MetS. All five components interact synergistically to drive systemic inflammation, oxidative stress and hepatic lipotoxicity. [23,24]	MASLD in 73% of MetS patients; MetS in 42% of MASLD patients. [25,26]
Sarcopenia and Muscle Wasting (low skeletal muscle mass and/or strength, assessed by appendicular skeletal muscle mass index [ASMI] or dual-energy X-ray absorptiometry)	Sarcopenia is independently associated with fibrosis severity. [27]	43-60% in chronic MASLD; among MASLD patients, 43% exhibit sarcopenia. [28–30]

1.1.2.3 Economic and Healthcare Burden

The economic implications of the high MASLD prevalence are staggering. Economic impact arises both from medical costs and reductions in worker productivity [31]. In the United States alone, MASH cases are forecasted to increase from 11.6 million in 2020 to 19.53 million in 2039, with 18.7 million deaths overall. In the same period, healthcare costs associated with MASH are projected to increase from $3636 to $6968 per patient, and accumulated healthcare costs 2020-2039 are estimated at $1,662.35 billion dollars [32]. Even though hospital readmissions are decreasing slightly for chronic liver disease (CLD) patients in the United States, readmissions of MASLD patients are growing in frequency. MASLD patients are at higher risk of hospital readmission, and even higher with clinical comorbidities [33]. These numbers are driven by the management of advanced liver diseases and the associated systemic complications. As the baby boomer generation ages, the prevalence of MASH-related decompensated cirrhosis is expected to peak, straining liver transplantation procedures and healthcare budgets [31]. Furthermore, as MASLD is increasingly diagnosed in younger populations [2], it is reasonable to expect substantial rises in indirect costs—measured in lost productivity, disability-adjusted life years (DALYs), and reduced quality of life.

1.1.3 Pathogenesis of MASLD

Understanding the pathogenesis of MASLD is crucial for the development of effective models. It is in a thorough study of mechanisms that we can find powerful insights to simulate MASLD outside patients. Within the MASLD spectrum, the transitions from a healthy to a steatotic liver, and subsequently to a steatohepatitis and fibrotic state, involve a complex set of molecular events.

1.1.3.1 The "Two-Hit" Hypothesis

A previous description of the MASLD progression was termed as the "Two-Hit Hypothesis" by James and Day in 1998. Here, the authors proposed that while obesity and impaired lipid metabolism trigger fat deposition in the liver, an additional "hit" had to occur to induce inflammation and fibrosis [34], as the liver would otherwise remain largely non-inflammatory.

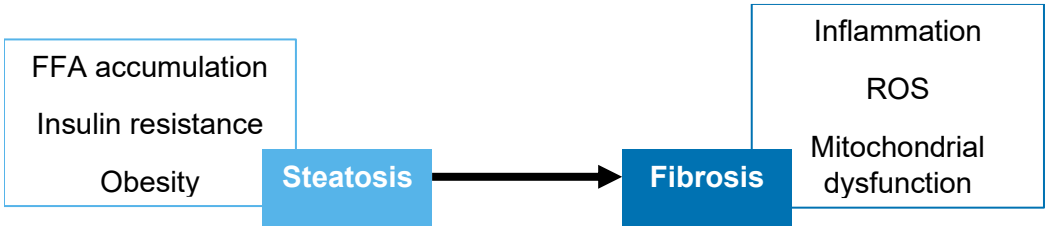


Figure 1.1. The "two-hit" hypothesis of NAFLD/NASH.
Schematic representation of the historical understanding of NAFLD/NASH pathogenesis. In this concept, obesity-driven insulin resistance first promotes hepatic triglyceride accumulation (simple steatosis) without substantial inflammation, which is then exacerbated by a second hit characterized by oxidative stress and inflammatory signaling that drives progression to steatohepatitis and fibrosis.

In this framework, obesity and insulin resistance are viewed as primary drivers of increased FFA flux to the liver, leading to a steatotic, relatively non-inflammatory state that is sensitized to further injury. The ensuing "second hit" comprises inflammatory mediators, ROS production, and mitochondrial dysfunction, which together promote progression from simple steatosis to steatohepatitis and fibrosis. Importantly, this model assumes that triglyceride accumulation is required for NASH development, whereas later work has shown that hepatocellular lipotoxicity can also result from impaired handling of other lipid types, including diacylglycerols, ceramides, and acylcarnitines.

1.1.3.2 The Multiple Parallel Hits Hypothesis

The pathogenesis of MASLD is incompletely understood to this day, as more complex and intricate phenomena are increasingly recognized. Despite the proposition of the two-hit nature of the disease was generally accepted for quite a long time, recent research shows that a more nuanced "Multiple Parallel Hits Hypothesis" better describes the pathogenesis of MASLD [35]. This new paradigm posits

that numerous insults act simultaneously to drive the disease. This updated concept reframes MASLD as a systems disease in which hepatic lipotoxicity, adipose tissue inflammation, gut dysbiosis, innate immune activation, and additional genetic/epigenetic factors act concurrently and actively interact. The liver is a central node for this interaction network, as it is responsible for the handling of multiple metabolites.

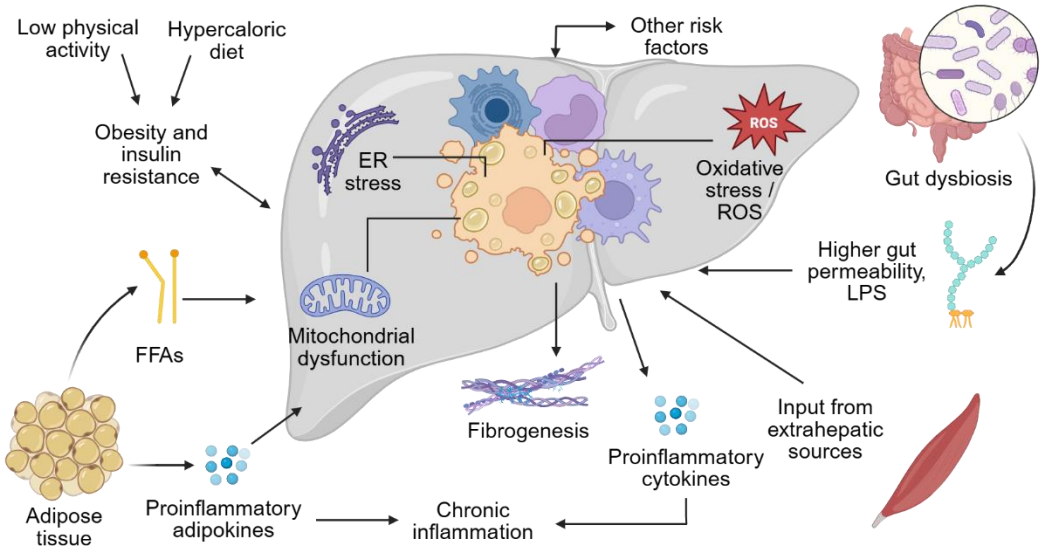


Figure 1.2. Schematic representation of the Multiple Parallel Hits hypothesis of MASLD pathogenesis
In this framework, obesity, lifestyle factors, adipose tissue inflammation, gut dysbiosis, skeletal muscle dysfunction, and genetic or epigenetic susceptibility interact concurrently to promote hepatic steatosis and lipotoxic stress, which, together with innate and adaptive immune activation, culminate in chronic inflammation, fibrogenesis, and progression to MASH and cirrhosis.

In Figure 1.2, the liver is depicted as a central metabolic hub that integrates numerous internal and external stimuli. Physical inactivity and a hypercaloric diet—hallmarks of modern lifestyles and common in individuals with MetS—drive obesity and insulin resistance, which in turn promote excess release of FFAs from dysfunctional adipose tissue and overload hepatic lipid-handling capacity. Within hepatocytes, ER stress and mitochondrial dysfunction contribute to the generation and downstream toxicity of lipotoxic lipid species. Genetic variants that affect lipid trafficking and storage further increase susceptibility to MASLD and to adverse extrahepatic manifestations of metabolic dysfunction. These processes are frequently accompanied by gut dysbiosis, characterized by increased intestinal permeability and translocation of bacterial products such as lipopolysaccharide (LPS) to the portal circulation, thereby amplifying inflammatory signaling in the liver. Additional environmental determinants, including food quality and broader lifestyle context, modulate this network of hits and collectively shape the risk and severity of MASLD [23,36–38].

1.1.3.3 Progressive Nature of MASLD

Currently, MASLD is understood as a disease spectrum with its stage-specific drivers and biological features. Steatosis marks the initial hallmark of MASLD at a histological level. It is defined as lipid accumulation exceeding 5% of hepatocytes. This process primarily results from increased free fatty acid (FFA) uptake from adipose tissue lipolysis (60%), enhanced hepatic de novo lipogenesis (26%), and reduced export of triglyceride-rich lipoproteins. Insulin resistance and hyperinsulinemia drive these metabolic alterations by stimulating lipogenic gene expression and suppressing fatty acid oxidation [39–41].

The progression to MASH is characterized by the emergence of lobular inflammation, hepatocellular ballooning—the rounding and size increase due to lipid overload—and perisinusoidal fibrosis. This transition involves activation of innate immune pathways, with non-parenchymal cell populations like hepatic stellate cells (HSCs), Kupffer cells and circulating macrophages playing central roles [42,43]. Mitochondrial dysfunction becomes increasingly prominent during MASH progression, with peridroplet mitochondria showing higher bioenergetic activity than cytoplasmic mitochondria in early disease stages [44]. Oxidative stress and lipid peroxidation damage mitochondrial respiratory chain enzymes, leading to ATP depletion and activation of pro-inflammatory signaling cascades.

Pro-inflammatory cascades along with other biochemical stimuli can induce a fibrogenic phenotype in the liver. Fibrosis represents one of the most significant predictors of long-term outcomes in MASLD patients [45–47]. The fibrotic process involves activation of hepatic stellate cells by inflammatory cytokines (TNF-α, IL-1β, IL-6) and transforming growth factor-β (TGF-β) signaling pathways [48–50]. Advanced fibrosis correlates strongly with adipose tissue inflammation, as demonstrated by transcriptomic studies showing increased inflammatory gene expression in visceral adipose tissue of patients with MASH compared to simple steatosis [51,52].

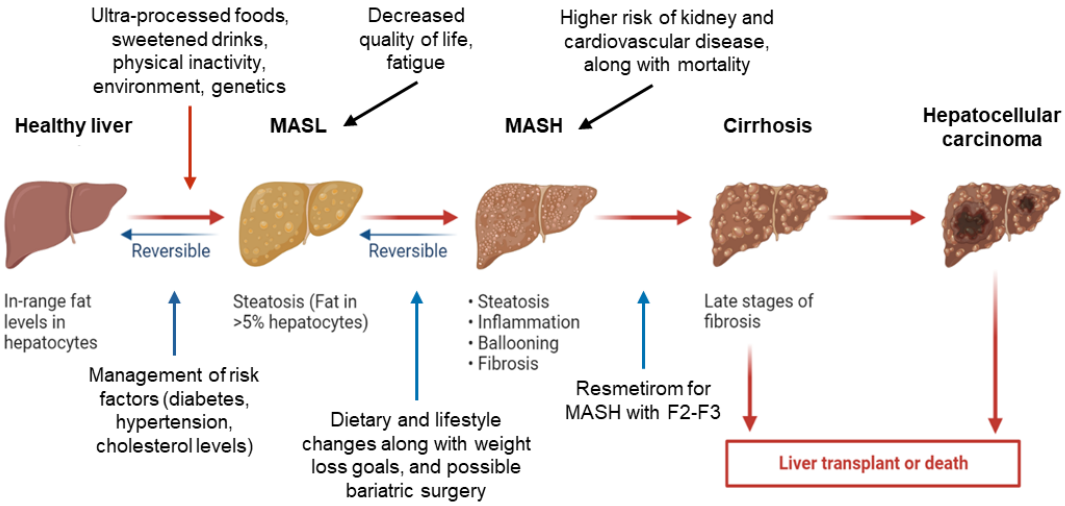


Figure 1.3. Overview of the MASLD progression.
Principal pathogenic drivers at each stage (red arrows), the corresponding opportunities for disease reversal and therapeutic intervention (blue arrows), and key stage-specific clinical and biological features are depicted. Adapted from Younossi *et al*., 2025 [1].

The systemic nature of MASLD progression is a great contributor to the complexity of its study. The progression of MASLD involves bidirectional communication between the liver, adipose tissue, and gastrointestinal tract [53]. Adipose tissue inflammation releases pro-inflammatory cytokines and adipokines that exacerbate hepatic inflammation and insulin resistance. Gut microbiota dysbiosis contributes to disease progression through increased intestinal permeability, bacterial translocation, and production of hepatotoxic metabolites such as trimethylamine N-oxide (TMAO) [54,55]. These systemic interactions support the conceptual framework of MASLD as a multi-organ metabolic disorder rather than an isolated hepatic condition.

In the following sections, the most important events and drivers of MASLD are described in detail.

1.1.3.4 Metabolic Overload and Steatosis

The initiating event in MASLD is the accumulation of intrahepatic triglycerides. This is defined as steatosis when it exceeds 5% of liver weight [3]. This abnormal accumulation arises from impaired balance of lipid acquisition and disposal. This neutral triglyceride accumulation coexists with a shift towards lipotoxic lipid species and organelle stress that predispose the patient to progress to MASH and develop fibrosis. The cellular stress caused by lipotoxicity can further exacerbate lipid accumulation [4,56]. The key players of steatosis are introduced below.

Insulin Resistance and Adipose Tissue Dysfunction

Insulin resistance (IR) occurs when insulin receptor signaling through receptor substrates (IRS-1/2), phosphoinositide 3-kinase (PI3K), and Akt is blunted by chronic nutrient excess, lipotoxic lipids, inflammatory cytokines, and endoplasmic reticulum (ER)/oxidative stress, which promote inhibitory phosphorylation and degradation of IRS proteins, uncoupling the receptor activation from metabolic responses [57–59]. This translates into impaired glucose uptake in muscle, failure to suppress hepatic gluconeogenesis, and the loss of insulin's antilipolytic action in adipose tissue [60]. In MASLD and particularly in MASH, systemic IR is almost universal and is tightly linked to visceral adiposity, along with other CMRFs. It is becoming clear that adipose tissue IR is an early event that amplifies hepatic lipid overload.

Dysfunctional adipose tissue is characterized by adipocyte hypertrophy and hypoxia, macrophage infiltration, low-grade inflammation—with increased release of TNF-α, IL-6 and chemokines, all of which promote the inhibitory IRS-1 serine phosphorylation and impaired PI3K-Akt signaling discussed earlier. As a result, insulin—that acts as a break on fat breakdown— fails to regulate lipases, allowing unchecked lipolysis. These non-esterified fatty acids (NEFAs) from adipose tissue flow into circulation, finally reaching the liver [61].

Circulating NEFAs, largely bound to albumin, are taken up by the liver via protein-mediated transport systems, such as fatty acid transport proteins (FATPs) —specifically FATP2 and FATP5 have been identified in the liver [4,39,62,63], rendering them available for esterification and storage as triglycerides in hepatocytes. Isotope tracer studies in human fatty liver disease have demonstrated that roughly 60% of intrahepatic triglycerides derive from circulating NEFAs released from adipose tissue, with additional contributions from dietary fat and de novo lipogenesis, underscoring the dominant role of adipose-derived lipid in driving hepatic steatosis [64]. The resulting intrahepatic accumulation of triglycerides and lipotoxic lipid species further impairs hepatic insulin signaling and promotes inflammatory and fibrogenic responses, establishing a vicious cycle between adipose tissue dysfunction, systemic insulin resistance, and progression from MASLD to MASH. Consistent with this pathophysiological axis, experimental models of hepatic steatosis commonly use NEFAs—alone or in mixtures that recapitulate circulating fatty acid profiles—to induce hepatocellular triglyceride accumulation and lipotoxic stress, and NEFAs overexposure remains the cornerstone for modelling pathogenic hepatic lipid build-up *in vitro* and *in vivo*.

De Novo Lipogenesis (DNL)

DNL is a key pathway for energy storage occurring in the liver. In this metabolic process, excess dietary carbohydrates are converted into new FAs and stored as triglycerides in lipid droplets. Hepatic DNL is now recognized as a driver of steatosis in MASLD and its progression to MASH. It does not act in isolation but is integrated with increased FA influx from adipose tissue, impaired mitochondrial oxidation and altered VLDL export, as summarized comprehensively by Carli *et al*. [61] in the following Figure 1.4.

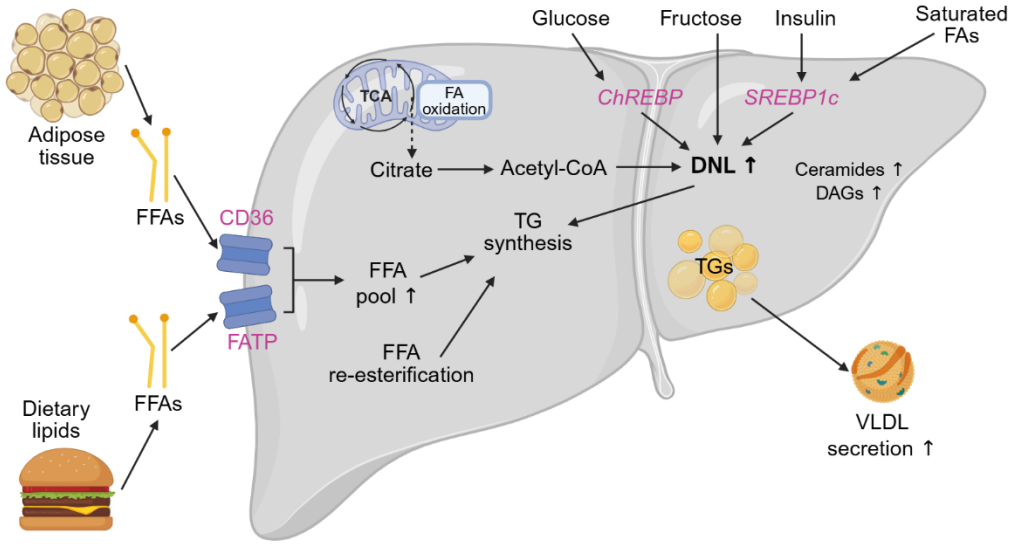


Figure 1.4. Hepatic de novo lipogenesis and lipid trafficking in MASLD and MASH.
Schematic representation of how nutrient excess and insulin resistance converge on hepatocytes to drive DNL and steatosis. In IR adipose tissue, uncontrolled lipolysis increases circulating FFAs and glycerol, which are taken up by the liver via fatty-acid transporters such as CD36 and FATP, expanding the intrahepatic FFA pool. Concurrently, dietary carbohydrates and hyperinsulinemia activate the lipogenic transcription factors ChREBP and SREBP-1c, respectively, enhancing DNL-derived palmitate synthesis. Newly formed fatty acids are re-esterified into triacylglycerols (TAGs) and stored in lipid droplets. Excess DNL also promotes the generation of lipotoxic species such as DAGs and ceramides, which further impair insulin signaling and contribute to hepatocellular injury and inflammation characteristic of MASH. To alleviate lipid overload, TAGs are packaged into large, TAG-rich very-low-density lipoprotein (VLDL) particles and secreted. Adapted from Carli *et al*. [61].

In healthy individuals, DNL contributes only around 5% of hepatic TGs of the intrahepatic triglyceride pool, as most hepatic FAs derive from diet and tissue lipolysis. However, under caloric excess and IR resistance, DNL flux increases disproportionately to about 26% of hepatic TGs, a hallmark metabolic change in early MASLD. Key cytoplasmic enzymes in this pathway include ATP-citrate lyase (ACLY), which generates acetyl-CoA from mitochondrial citrate, acetyl-CoA carboxylase (ACC), which converts acetyl-CoA into malonyl-CoA, and fatty acid synthase (FAS), which elongates malonyl-CoA to palmitate; all three are upregulated at the mRNA and protein level in MASLD livers and correlate with steatosis severity [65,66].

Hyperinsulinemia positively regulates the lipogenic transcription factor Sterol Regulatory Element-Binding Protein 1c (SREBP-1c) [67,68], which induces expression of ACC, FAS and other enzymes involved in fatty acid and TAG synthesis. In parallel, post-prandial hyperglycemia and increased flux of glucose and fructose into hepatocytes activate Carbohydrate Response Element-Binding Protein (ChREBP), which further stimulates expression of glycolytic and lipogenic genes, thereby reinforcing DNL. The Carli *et al*. figure captures this dual hormonal–nutrient control by showing dietary sugars and insulin converging on SREBP-1c and ChREBP, which together amplify the conversion of carbohydrate-derived acetyl-CoA into fatty acids and TGs.

At the same time, a tracer study showed that amino acids are not merely oxidized but represent a major carbon source for hepatic lipogenesis in overnutrition and obesity, supplying the tricarboxylic-acid cycle and, via reductive carboxylation, fueling DNL. Under conditions of excess energy, this routing of amino-acid carbon into DNL further increases palmitate and TAG synthesis even when carbohydrate intake is controlled, highlighting another driver of steatosis and highlighting the relevance of dietary control in MASLD [69].

Dietary Intake

The remaining lipid burden comes from dietary chylomicron remnants. These are large circulating lipid-rich lipoprotein particles that transport dietary fats to skeletal muscle and adipose tissue, after which their cholesterol- and triglyceride-enriched remnants are cleared by the liver, directly contributing to intrahepatic triglyceride accumulation and lipotoxic stress [70]. In the setting of chronic overnutrition, this continuous flux of remnant particles, together with increased uptake of non-esterified fatty acids from insulin-resistant adipose tissue and de novo lipogenesis from excess carbohydrates, drives the hepatic fat overload that characterizes MASLD.

The Western diet, commonly rich in saturated fats, cholesterol, and refined sugars but poor in fiber and omega-3 fatty acids, is a key driver of this lipid overload. High intakes of saturated and trans fatty acids favor steatosis by increasing chylomicron production, altering membrane lipid composition, and exacerbating systemic and hepatic insulin resistance, while combined high-fat and high-fructose feeding produces more severe steatosis and metabolic dysfunction than either nutrient excess alone. In contrast, dietary patterns enriched in mono- and omega-3 polyunsaturated fatty acids, such as the Mediterranean diet, are associated with lower hepatic fat content and improved metabolic profiles, underscoring that the quality of dietary fat is as important as its quantity in MASLD pathogenesis [71,72].

Though there is still debate on whether fructose is particularly steatogenic, it is taken up by hepatocytes independently of insulin and rapidly channels into triose phosphates and acetyl-CoA, thereby bypassing key glycolytic control points and strongly stimulating de novo lipogenesis, triglyceride synthesis, and VLDL overproduction [73,74]. Beyond providing substrate, chronic exposure to high-fructose or high-fat/high-fructose diets in experimental models downregulates protective sirtuin pathways such as SIRT1 and activates stress and inflammatory signaling, including NF-κB, thereby coupling lipogenesis to oxidative stress, hepatocellular injury, and inflammatory responses typical of MASH [75]. The recent observations of fructose implication in the onset of steatosis are prompting current recommendations to restrict their intake in MASLD [73].

Energy excess and its distribution also play a central role in the development of steatosis. Hypercaloric diets rich in refined carbohydrates, fructose, and ultra-processed foods promote weight gain and abdominal adiposity, increasing the flux of fatty acids from dysfunctional, insulin-resistant adipose tissue to the liver and amplifying adipokine imbalance and low-grade systemic inflammation [76,77]. In parallel, Western dietary habits alter the gut microbiota and impair intestinal barrier function, enhancing the portal

delivery of PAMPs such as LPS, which activate hepatic innate immune receptors and synergize with lipid overload to drive progression from simple steatosis to steatohepatitis and fibrosis [78,79]. This axis is reflected in the use of LPS *in vitro* to recapitulate MASH and fibrosis. Emerging data also point at common food additives in ultra-processed products as additional disruptors of intestinal homeostasis and the gut–liver axis, further linking modern dietary habits to MASLD [80].

Finally, diet acts through a set of factors that connect liver, adipose tissue, muscle, and gut. By shaping glycemic and insulinemic profiles, circulating lipid species, bile acid signaling, hormones, and microbiota-derived metabolites, Western diets modulate hepatocyte metabolism and the activation of Kupffer cells and HSCs, thereby influencing both steatosis and fibrogenesis. At the same time, insufficient protein intake and poor diet quality contribute to sarcopenia and sarcopenic obesity, reducing the skeletal muscle's capacity to dispose of glucose and lipids, worsening IR, and indirectly enhancing hepatic fat accumulation—an axis of special relevance when considering the bidirectional relationship between liver and skeletal muscle in MASLD and MASH. Therefore, high-fructose, high-fat Western-style diets are widely used in diet-induced models of steatotic liver disease, as they recapitulate the multi-hit dietary environment that initiates steatosis and promotes transition to MASH in humans [15,71,81].

1.1.3.5 Lipotoxicity

The liver employs the accumulation of TG as a very effective protective mechanism. This way, hepatocytes hold on to potentially toxic FAs in lipid droplets. However, when the huge FA influx and DNL overwhelm the hepatocyte's lipid handling capacity, several molecular mechanisms orchestrate lipotoxicity [82]. Lipotoxicity refers to the set of adverse effects of accumulated toxic lipids and overwhelmed lipid handling in hepatocytes. It comprises a variety of events, such as endoplasmic reticulum (ER) stress, oxidative stress, apoptosis, inflammation, and autophagy, making them hallmarks of MASLD progression (Figure 1.5) [83].

ER Stress

The ER ensures the folding and quality control of nascent proteins regardless of their subcellular destination. As the translation occurs in the cytoplasm, a topogenic signal sequence in the synthesized protein is recognized by the signal recognition particle (SRP) [84], which initiates its recruitment to the ER membrane along with the translational complex. Translation continues there or is further transported into the ER lumen, depending on the nature of the translated protein. If misfolding occurs, proteins remain in the ER lumen or enter ER-associated degradation, so preventing the secretion of anomalous proteins [85].

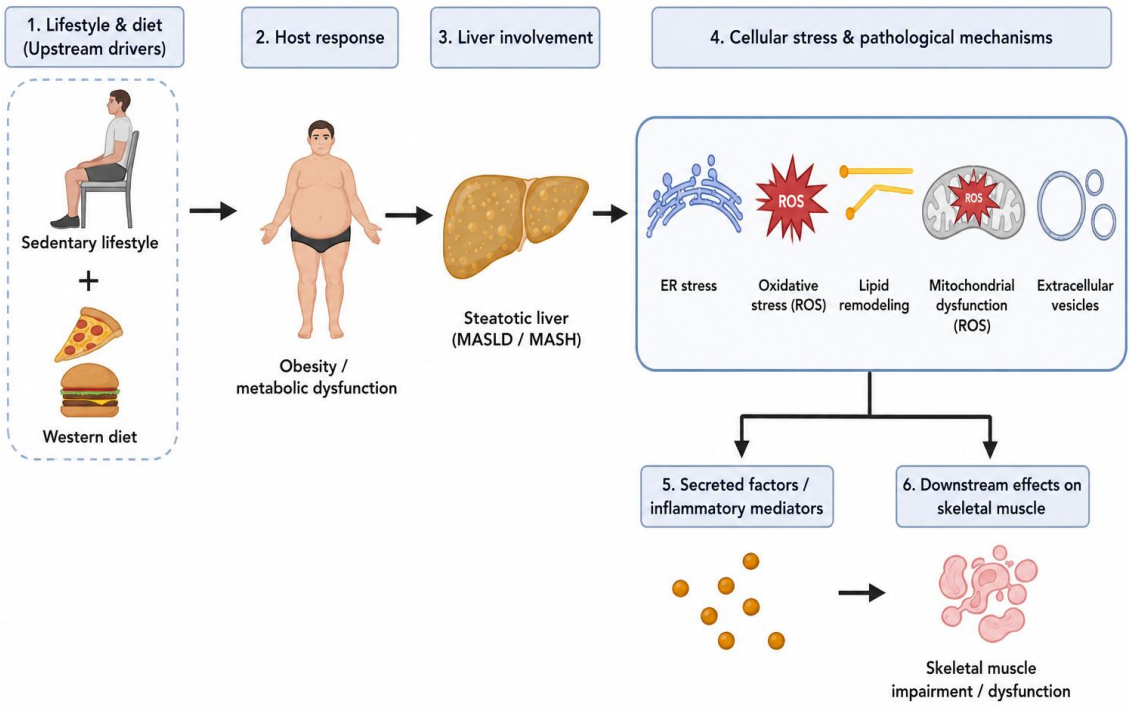


Figure 1.5. Potential drivers of hepatic lipid accumulation and its progression to lipotoxicity.
Genetic, lifestyle, and metabolic factors promote triglyceride and other lipid species deposition in hepatocytes, leading to lipotoxic stress. This lipotoxicity elicits oxidative stress–related signaling and intercellular communication via extracellular vesicles or diffusible mediators, ultimately triggering regulated cell death pathways and fostering the transition from simple steatosis to hepatic inflammation and fibrosis.

Tight quality control is placed by the ER to prevent accumulation of misfolded peptides. However, ER stress happens when cells fail to degrade unfolded/misfolded proteins, increase chaperone activity or inhibit translation of new proteins. These compensatory mechanisms are known as the Unfolded Protein Response (UPR), and are mediated by basally inactive specialized sensor enzymes, which activate in the presence of misfolded proteins.

Lipid biosynthesis is another crucial function of the ER [86]. Both smooth and rough ER membranes contain enzymes for lipid biosynthesis. In hepatocytes, smooth ER is especially abundant and synthesizes almost all lipid subclasses, including cholesterol, TG, lipid droplets, phospholipids and sphingolipids [82].

Some saturated fatty acids (SFA) such as palmitic acid (PA) can directly induce lipotoxicity, while monosaturated free FAs like oleic acid in low concentrations have protective effects against SFA toxicity. The overload of SFA may also disrupt the ER membrane's fluidity and protein folding capacity, activating the UPR [87]. Downstream effects of UPR activation include the inhibition of insulin signaling and apoptosis, a hallmark of MASLD [88–90].

1.1.3.6 Mitochondrial Dysfunction and Oxidative Stress

Mitochondria play a key role in MASLD pathogenesis. Initially, hepatocytes adapt to a high lipid load by upregulating lipid β-oxidation and the tricarboxylic acid (TCA) cycle to use excess fuel, leading to increased oxygen consumption and ATP production. This hypermetabolic state is a hallmark of early steatosis and can temporarily limit lipotoxicity by oxidizing surplus fatty acids [91]. As lipid overload persists, however, mitochondrial membrane composition and electron transport chain (ETC) complex organization become altered, and oxidative phosphorylation efficiency declines despite maintained or even increased respiratory flux, promoting electron leakage. With increasing lipid loads, the adaptive mitochondrial response collapses, and the sustained high flux of electrons through the ETC leads to electron leakage and the formation of superoxide anions and other reactive oxygen species (ROS). These species oxidize cardiolipin and other phospholipids, increase the permeability of mitochondrial membranes, and impair mitochondrial quality control mechanisms such as mitophagy, leading to the accumulation of dysfunctional mitochondria [38,92].

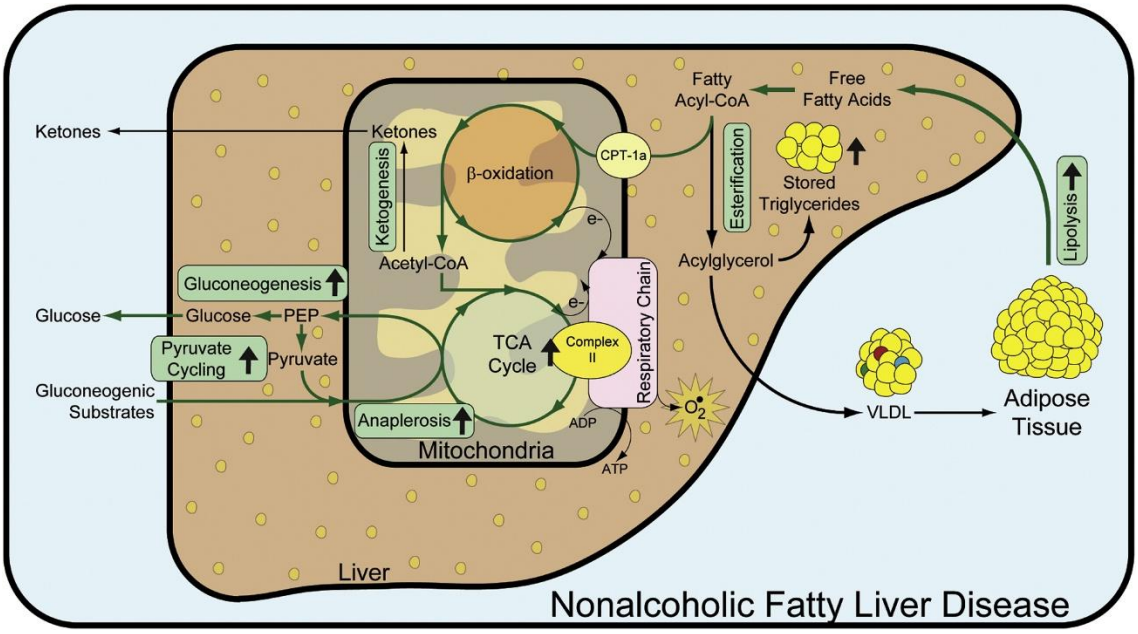


Figure 1.6. Mitochondrial adaptation and dysfunction in MASLD–MASH.
Elevated lipolysis in IR adipose tissue increases FFA flux to the liver, where they are taken up by hepatocytes and esterified into TGs or directed to mitochondrial β-oxidation. In early MASLD, increased FFA delivery enhances β-oxidation and TCA cycle activity, putting the mitochondrial respiratory chain in a hypermetabolic state that initially helps dispose of excess lipid. With persistent FFA oversupply, mitochondrial β-oxidation and TCA flux overload the ETC, causing electron leak and excessive ROS generation, which in turn promotes lipid peroxidation, mitochondrial DNA damage, and impaired mitophagy. These changes, together with ongoing hepatocyte and intrahepatic lipolysis, trigger NLRP3 inflammasome activation, inflammatory cytokine release, hepatocyte death, and stellate-cell-mediated fibrogenesis, driving progression from simple steatosis to steatohepatitis with fibrosis. Sunny N. *et al*. [92]

In a healthy state, FFAs released from adipose tissue during fasting are delivered to the liver, activated to acyl-CoAs, and transported into mitochondria via CPT1 to undergo β-oxidation, producing acetyl-CoA,

NADH, and $FADH_2$ for ATP generation. In MASLD, adipose insulin resistance increases basal lipolysis and circulating FFA flux, so that a larger fraction of hepatic lipid derives from adipose tissue and must be handled by mitochondrial β-oxidation.

Early in disease, hepatic β-oxidation is upregulated as an adaptive response and contributes to the hypermetabolic phenotype, increasing oxygen consumption and partly limiting triglyceride accumulation. However, when FFA supply chronically exceeds the oxidative capacity of the respiratory chain, components of the oxidative machinery—ETC complexes, β-oxidation enzymes and mtDNA—are damaged. This leads to β-oxidation becoming functionally uncoupled from efficient ATP production, leading to accumulation of incompletely oxidized intermediates, increased acylcarnitines, and enhanced ROS generation at mitochondrial complexes. This β-oxidation-driven oxidative stress promotes lipid peroxidation, mtDNA damage, and mitochondrial dysfunction, thereby linking excessive FFA flux and mitochondrial fat oxidation to hepatocellular injury and the transition from MASLD to inflammatory MASH [92,93].

Acetyl-CoA generated by β-oxidation enters the TCA cycle, where sequential enzymatic steps generate NADH and $FADH_2$ that fuel the mitochondrial respiratory chain to produce ATP. In MASLD, increased delivery of acetyl-CoA from β-oxidation, enhanced glycolysis and recharge intermediates for the TCA cycle (anaplerotic flux), amplify the cycle activity, which has been demonstrated by metabolic flux and metabolomics studies in obese individuals and experimental steatosis [92].

Increased TCA enhances reducing-equivalent supply to the electron transport chain, favoring a high proton motive force and promoting electron leak and ROS formation when respiratory capacity or complex integrity is compromised. Persistent ROS generation from an overfueled TCA–ETC axis impairs mitochondrial enzymes, alters respiratory complex organization, and further decreases oxidative phosphorylation efficiency, creating a vicious cycle of oxidative stress and energy failure. In this way, upregulation of the TCA cycle and respiratory chain in the setting of chronic FFA oversupply directly couples mitochondrial metabolism to oxidative damage, inflammatory signaling, and fibrogenic progression in MASLD–MASH [92,94,95].

ROS wreak intracellular havoc through multiple mechanisms. ROS attack polyunsaturated fatty acids (PUFAs) in cell membranes, generating toxic aldehydes like 4-hydroxynonenal (4-HNE) and malondialdehyde (MDA) [96], which bind with proteins and nucleic acids, disrupt membrane integrity, and amplify lipotoxic stress in hepatocytes. Mitochondrial DNA (mtDNA), located close to the ETC and relatively poorly protected by histones, is particularly susceptible to oxidative damage; accumulation of mtDNA mutations and deletions further impair ETC function, decreases ATP production, and feeds back to increase ROS generation [38]. In parallel, defective mitochondrial dynamics and quality control, imbalanced fission–fusion, and impaired mitophagy favor the persistence of damaged mitochondria and sensitize hepatocytes to apoptotic and necroptotic cell death, providing damage-associated molecular patterns that activate non-parenchymal cells and promote fibrogenesis.

Moreover, ROS are potent activators of the NLRP3 inflammasome, both in hepatocytes and liver-resident immune cells. Oxidative stress and lipid peroxidation products facilitate NLRP3 activation via pathways involving mitochondrial ROS, oxidized mitochondrial lipids such as cardiolipin, and ROS/TXNIP signaling, leading to the cleavage of pro-caspase-1 and the maturation of pro-inflammatory cytokines IL-1β and IL-18 [97,98]. These cytokines amplify hepatic inflammation, recruit and activate myeloid cells, and stimulate HSCs, thereby coupling mitochondrial ROS and inflammasome activation to the transition from simple steatosis to steatohepatitis [99].

1.1.3.7 The Inflammatory Cascade

Inflammation is the event that drives the progression from simple steatosis to MASH. This very complex response involves crosstalk between parenchymal and non-parenchymal cells in the liver, including hepatocytes, liver sinusoidal endothelial cells (LSECs), Kupffer cells (KCs), recruited monocyte-derived macrophages, and HSCs. Central to this response are the potent milieu of pro-inflammatory cytokines, chemokines, and pattern-recognition mechanisms that originate and amplify both inflammation and fibrogenesis.

1.1.3.7.1 Cellular Heterogeneity and Macrophage Recruitment

The liver harbors a population of resident macrophages known as Kupffer cells (KCs), not to be confused with macrophages recruited by a pro-inflammatory environment. Under homeostatic conditions, KCs maintain tissue integrity through the expression of immunoregulatory mediators; however, under chronic metabolic stress, the liver is progressively infiltrated by monocyte-derived macrophages, which significantly amplify the inflammatory environment through pattern recognition receptors (PRRs) and production of TNF-α, IL-1β, IL-6, and chemokines such as CCL2 and IL-8 (CXCL8) [100,101]. In parallel, HSCs also express several PRRs, including TLR2 and TLR4, directly responding to damage-associated molecular patterns (DAMPs) and pathogen-associated molecular patterns (PAMPs). HSCs can upregulate cytokines, chemokines, adhesion molecules and other ECM genes to enforce inflammation and cell recruitment, along with matrix deposition [102–105].

1.1.3.7.2 Signal Transduction: DAMPs and PAMPs

The activation of the innate immunity in MASLD is activated by DAMPs and PAMPs through a dual-signal mechanism involving both endogenous and exogenous ligands and converging in PRR-driven pathways such as NF-κB, MAPKs and the NLRP3 inflammasome [106,107].

Damage-Associated Molecular Patterns (DAMPs)

Lipotoxic injury to hepatocytes, mitochondrial dysfunction and cell death trigger the release or exposure of intracellular components, including apoptotic hepatocyte DNA, High Mobility Group Box 1 (HMGB1), free fatty acids (FFAs), mtDNA, ATP, S100 proteins, oxidized lipids and apoptotic bodies. These DAMPs are recognized by PRRs expressed on KCs, monocyte-derived macrophages and HSCs, notably TLR2, TLR4 and TLR9. Purinergic receptors such as the ionic channel P2X7, and cytosolic sensors that assemble the NLRP3 inflammasome are also involved in inflammation, cell proliferation and apoptosis of liver cell populations. Engagement of these receptors activates MyD88- and TRIF-dependent signaling, NF-κB and MAPKs, as well as NLRP3-caspase-1, promoting transcription of pro-inflammatory cytokines (TNF, IL-1β, IL-6, IL-18), chemokines like CCL2 and pro-fibrogenic mediators like TGF-β and PDGF. These signaling molecules together drive immune cell recruitment, HSC activation, and ECM deposition [104,108–113].

Pathogen-Associated Molecular Patterns (PAMPs)

In the context of obesity and Metabolic Syndrome (MetS), a compromised intestinal barrier —also known as "leaky gut"—and dysbiosis allow the translocation of LPS, bacterial CpG DNA, flagellin and other gut-derived PAMPs into portal circulation [114]. These microbial products are sensed by PRRs expressed on KCs, recruited macrophages, HSCs and other non-parenchymal cells, notably TLR4 for LPS, TLR2 for peptidoglycan, TLR5 for flagellin, and TLR9 for bacterial and mtDNA. The downstream effects of the receptor activation include NF-κB, IRF and MAPK signaling, which leads to production of pro-inflammatory cytokines and chemokines, ROS generation, and further NLRP3 inflammasome activation, thereby promoting monocyte recruitment, neutrophil influx, polarization of inflammatory macrophage subsets and sensitization of HSCs to TGF-β-driven fibrogenesis [115,116].

The downstream activation of NF-κB and JNK signaling pathways culminates in the robust secretion of pro-inflammatory cytokines, including TNF-α, IL-1β, IL-6, and IL-8 (CXCL8). This sustained inflammatory milieu creates a self-perpetuating cycle of hepatocyte death and stellate cell activation. If left unchecked, this chronic state drives the progression from simple steatosis toward advanced fibrosis, cirrhosis, and ultimately, hepatocellular carcinoma (HCC).

1.1.3.8 Hepatic Fibrosis: Hallmark of Progression

Chronic hepatic injury and persistent inflammatory signaling culminate in the excessive accumulation of collagen and extracellular matrix (ECM) components, a process defined as fibrosis. If unresolved, this progressive scarring compromises the liver's structural architecture and fundamental metabolic functions, facilitating the transition toward cirrhosis and significantly elevating the risk of hepatocellular carcinoma (HCC).

The Central Role of Hepatic Stellate Cells

HSCs are the primary cellular effectors of hepatic fibrogenesis. In the healthy liver, these cells reside in the space of Disse as quiescent, vitamin A-storing pericytes, comprising approximately 10% of the total resident liver population. However, in response to fibrogenic cytokines released by activated Kupffer cells and apoptotic hepatocytes, HSCs undergo a profound phenotypic trans-differentiation into myofibroblast-like cells. This activated state is characterized by increased proliferation, contractility, and the secretion of pro-inflammatory and chemotactic mediators, making them the principal source of pathological ECM deposition [117].

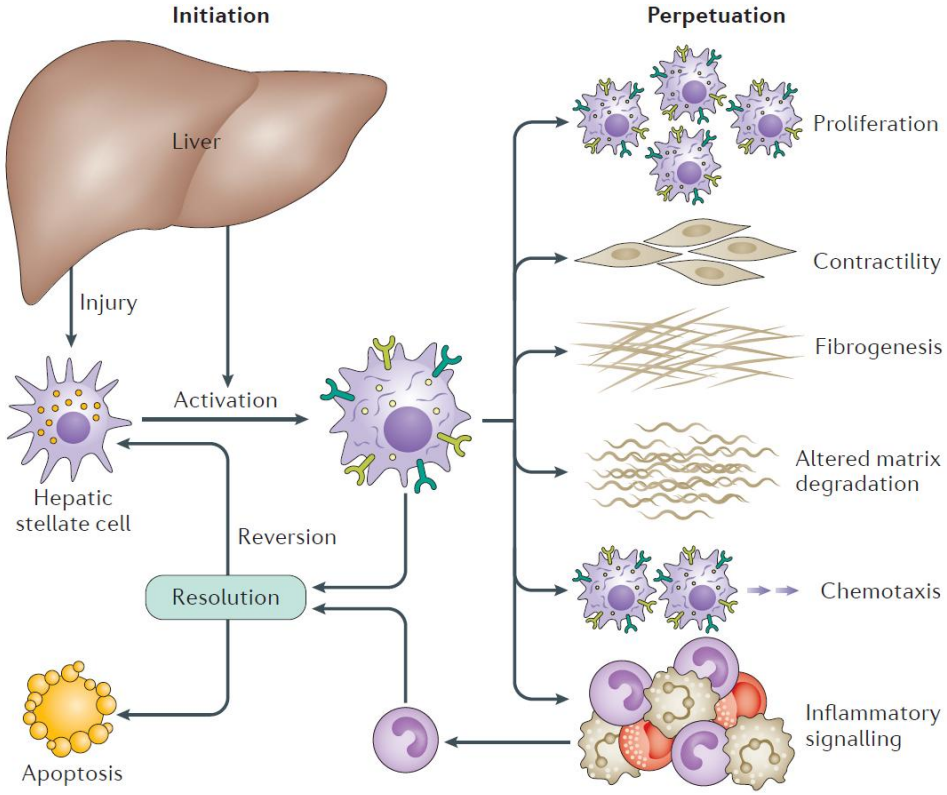


Figure 1.7. Phenotypes and functions of HSCs in healthy and diseased liver.
Injury drives transition from a quiescent to an activated state, in which HSCs display a variety of phenotypes, including proliferation, contractility, fibrogenesis, altered ECM degradation, chemotaxis, and inflammatory signaling. Tsuchida and Friedman, 2017. [117]

Cytokine Signaling and Mechanotransduction in Fibrosis

The activation and persistence of the myofibroblast phenotype are driven by a complex milieu of soluble factors.

Table 1.2. Factors perpetuating pro-fibrotic signaling during MASLD progression [117–119].

Signaling Category	Specific Mediator	Downstream Pathways	Effect on Fibrosis Progression
Fibrogenic	**TGFβ**	SMAD 2/3 phosphorylation	Direct transcriptional upregulation of Type I and III collagens, essential for myofibroblast transition.
Mitogenic	**PDGF**	PI3K/Akt and MAPK/ERK	Drives the proliferation and migration of activated HSCs to sites of hepatic injury.
Angiogenic	**VEGF**	VEGFR signaling	Promotes pathological angiogenesis, which provides structural support for expanding fibrotic tissue.
Mechanical	**Matrix Stiffness**	YAP/TAZ & Wnt/β-catenin	Triggers a self-perpetuating loop where the stiffened ECM maintains HSC activation independently of cytokines.
Inflammatory	**Chemokines**	CCR2 signaling	Recruit monocyte-derived macrophages, which provide additional TGFβ and PDGF for HSCs.

The complex molecular interplay and mechanosensitive features of the cell populations implicated in MASLD development pose a need to fine-tune the physical microenvironment of *in vitro* models to accurately interrogate disease dynamics.

1.1.4 The Diagnostic Challenges in MASLD

The study of MASLD is uniquely challenging due to its heterogeneity and chronicity. Unlike monogenic diseases, MASLD is a complex trait resulting from the interaction of polygenic risk scores and diverse environmental factors and exposures. Moreover, the field is transitioning from a biopsy-centered focus based on the former NAFLD exclusion criteria to a positive definition of MASLD, aligned with CMRFs. Non-invasive tools that can reliably distinguish disease- and fibrosis stages are being developed and still insufficient [120,121]. Clinically, most patients are asymptomatic and are identified incidentally through abnormal liver enzymes or imaging, which has poor sensitivity for early fibrosis and cannot differentiate MASH from mild steatosis. Biopsies are prone to bias, as they present inter-observer variability, while scoring steatosis, ballooning, inflammation, and fibrosis also rely on imaging-based data.

1.1.4.1 Phenotypic and Genotypic Heterogeneity

The onset and progression of MASLD are deeply heterogeneous. Patients with similar histological features, and even those classified within the same disease stage, may have reached that point through substantially different pathophysiological trajectories. In some individuals, disease development may be strongly influenced by genetic predisposition, including the common PNPLA3 I148M variant, or by altered hepatic metabolic processes such as impaired de novo lipogenesis (DNL). In others, MASLD may be driven predominantly by visceral adiposity, systemic insulin resistance, and broader cardiometabolic dysfunction [122,123]. This diversity is further illustrated by the so-called “lean MASLD” phenotype, in which individuals present with a normal BMI but still display visceral fat accumulation, metabolic dysfunction, and clinically relevant liver disease. This cohort challenges the traditional view of MASLD as a condition primarily associated with obesity and suggests the existence of distinct disease drivers that remain incompletely understood [124].

This phenotypic heterogeneity complicates both the study and clinical management of MASLD. Histology remains central for disease staging, but similar microscopic patterns may conceal divergent upstream mechanisms and different risks of progression. As a result, two patients with comparable steatosis, inflammation, or fibrosis may differ substantially in their metabolic background, genetic susceptibility, inflammatory profile, and likelihood of developing advanced liver disease or extrahepatic complications. Genetic variation contributes significantly to this variability. Common variants in genes such as *PNPLA3*, *TM6SF2*, *MBOAT7*, *GCKR*, and *HSD17B13* have been associated with differences in hepatic fat accumulation, inflammatory activity, fibrogenesis, and disease severity [125–127]. Consequently, individuals exposed to similar dietary, environmental, or metabolic risk factors may display markedly different histological outcomes and clinical trajectories.

These findings indicate that MASLD should be interpreted as a biologically heterogeneous continuum in which multiple combinations of genetic, metabolic, inflammatory, and environmental factors can converge on overlapping histological phenotypes. Therefore, traditional obesity-centric or histology-only interpretations risk oversimplifying the disease and may fail to capture the mechanistic diversity that underlies patient-to-patient variability in progression, prognosis, and therapeutic response.

1.1.4.2 Biomarkers in MASLD

There has been intense effort to develop non-invasive methods and novel biomarkers that can identify patients with steatohepatitis and significant fibrosis. Additionally, such methods should monitor disease dynamics over time. Simple serum-based indices such as Fibrosis-4 index (FIB-4), NAFLD Fibrosis Score (NFS), and Aspartate aminotransferase-to-platelet ratio index (APRI) are widely used as first tools to exclude advanced fibrosis in primary care settings because they are inexpensive and consist of routinely available laboratory parameters, although they show modest specificity and perform poorly in younger patients or those with borderline values [128].

More specialized tests exist at the expense of better access to medical care infrastructures, including the Enhanced Liver Fibrosis (ELF) score and composite panels on blood samples such as FibroTest, FibroMeter, Hepascore—the latter three measuring different biomarker sets to determine fibrotic grade and predicting cirrhosis—, and newer MASLD-specific panels. These improve the discrimination of significant and advanced fibrosis but are expensive and not universally available. Imaging biomarkers—vibration-controlled transient elastography (VCTE), shear-wave elastography, and magnetic resonance elastography (MRE)—have transformed non-invasive staging of fibrosis and steatosis while being used to counteract the underperformance of more simple tests. However, they still have gaps and are less accurate for intermediate fibrosis stages [129].

Histology samples from percutaneous liver biopsy remain the formal gold standard for diagnosing MASH and staging fibrosis, as they are required for regulatory approval of many pharmacological agents. However, biopsy is invasive, associated with bleeding and pain, difficult to repeat in longitudinal studies, and hampered by sampling error and inter-reader variability, prompting the search for non-invasive surrogate endpoints and composite outcome measures [130]. For all these reasons, current guideline-endorsed diagnostic pathways typically use a stepwise combination of non-invasive tests. Meta-analyses suggest that FIB-4 has the best performance among simple scores for detecting any fibrosis and cirrhosis, while more complex panels such as ELF or FibroMeter outperform simple scores for advanced fibrosis, particularly when combined with elastography [130].

Emerging biomarkers include metabolomic and lipidomic signatures, proteomic panels, circulating microRNAs, cell-free DNA, and disease mechanism–related multi-marker scores that show higher accuracy than legacy scores for staging fibrosis or detecting at-risk MASH in high-risk populations. Novel composite scores integrating metabolomics (like OWLiver/MASEF panels) with elastography and routine labs can achieve one-step non-invasive identification of MASH and significant fibrosis in patients with T2D and MASLD, but they require further external validation and standardization before widespread adoption [131,132].

1.1.5 A Multisystemic Disorder: Extrahepatic implications of MASLD

Although primarily a hepatic pathology, MASLD is increasingly recognized as the hepatic manifestation of a systemic metabolic collapse. The liver serves as a central hub, where metabolic dysfunction reverberates across the adipose tissue, skeletal muscle, and the cardiovascular system through complex endocrine and paracrine signaling.

1.1.5.1 Cardiovascular Disease and Systemic Inflammation

Cardiovascular disease (CVD) remains the leading cause of mortality among patients with MASLD [133]. The inflamed liver acts as a source of systemic pro-inflammatory cytokines and pro-atherogenic lipids.

This systemic overflow promotes vascular inflammation, endothelial dysfunction, and plaque instability, establishing MASLD as an independent risk factor for atherosclerosis [5,134,135].

1.1.5.2 Sarcopenia

A critical component of MASLD pathogenesis is the bidirectional crosstalk known as the muscle-liver axis. Sarcopenia—the loss of skeletal muscle mass and function—is highly prevalent in MASLD patients, even in non-cirrhotic stages. This relationship is synergistic: muscle loss exacerbates insulin resistance and hepatic lipid accumulation, while hepatic inflammation promotes muscle wasting, further accelerating fibrotic progression [136].

1.2 The Skeletal Muscle: Functions and Implications

Skeletal muscle is one of the largest and most dynamic organs in the human body, representing approximately 40% of total body mass and a major proportion of whole-body protein reserves. Although traditionally viewed as the organ responsible for voluntary movement, posture, and breathing, skeletal muscle also has essential metabolic and endocrine functions. It acts as a major reservoir of amino acids, contributes substantially to whole-body energy expenditure, and plays a central role in glucose and lipid handling. Because of this dual mechanical and metabolic role, skeletal muscle is highly sensitive to systemic disturbances, including inflammation, nutrient imbalance, insulin resistance, altered endocrine signaling, and metabolic stress associated with chronic diseases [137–139].

At its core, skeletal muscle is a highly organized tissue in which mechanical, electrical, metabolic, and biochemical processes are integrated. Force production depends on molecular interactions within sarcomeres, but a good muscle performance also requires appropriate fiber architecture, extracellular matrix organization, membrane excitability, calcium handling, mitochondrial ATP production, and efficient force transmission. This multiscale organization is important when studying muscle impairment, because weakness or reduced contractile output may arise not only from loss of muscle mass, but also from defects in muscle quality. This includes altered sarcomeric organization, impaired excitation–contraction coupling, disrupted protein balance, metabolic dysfunction, or inefficient transmission of force [140].

1.2.1 Organization and Tissue Architecture

Anatomically, skeletal muscles are composed of bundles of long, multinucleated muscle fibers organized into fascicles and embedded within a hierarchical connective tissue network. Individual myofibers are surrounded by the endomysium, fascicles by the perimysium, and the whole muscle by the epimysium. This ECM contains fibrillar collagens, laminins, proteoglycans, and other proteins providing structural support and providing mechanical connection between the contractile apparatus. As in other organs, the

skeletal muscle ECM also contributes to mechanotransduction, tissue stiffness, and repair after injury. Therefore, changes in ECM composition, fibrosis, tissue stiffness, or cell–matrix coupling can compromise functional output [141,142].

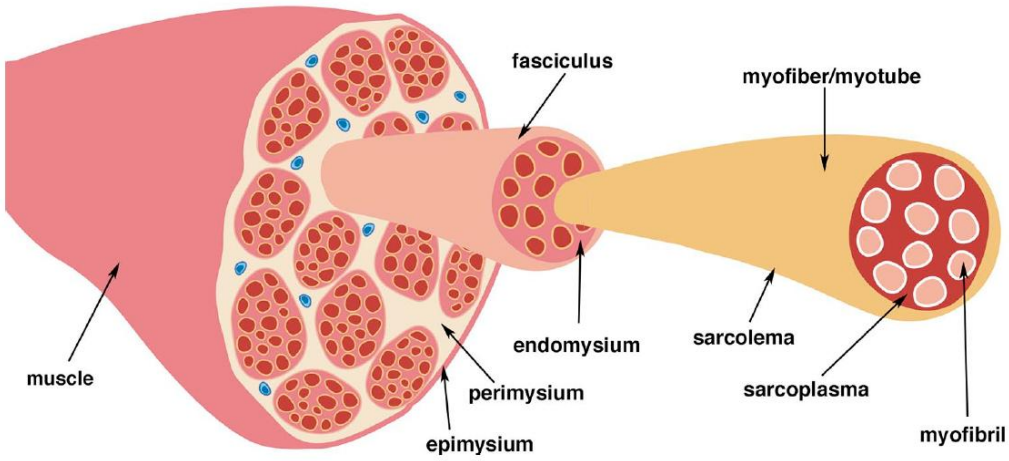


Figure 1.8. Organization of the skeletal muscle
Adapted from Fernández-Costa *et al*. [142]

Although engineered skeletal muscle tissues do not reproduce the complete anatomical hierarchy of native muscle, this native organization provides the biological rationale for designing *in vitro* platforms that promote myotube alignment, matrix-supported tension, and measurable contractile output. In this thesis, this principle is particularly relevant because the muscle model relies on three-dimensional hydrogel-based constructs anchored between flexible posts, allowing tissue compaction, alignment, and quantitative assessment of force generation.

1.2.2 Molecular Basis of Force Generation

The fundamental contractile unit of skeletal muscle is the sarcomere; a repeating structure composed primarily of thick myosin filaments and thin actin filaments organized into a highly ordered lattice. During contraction, myosin-II heads cyclically bind to actin, perform a power stroke, detach, and reattach in an ATP-dependent process known as cross-bridge cycling. This interaction produces sliding of actin and myosin filaments relative to one another, shortening the sarcomere and generating force. Calcium ions regulate this process through the troponin–tropomyosin complex: when cytosolic calcium rises, calcium binds to troponin C, tropomyosin shifts away from myosin-binding sites on actin, and cross-bridge cycling proceeds [138,139].

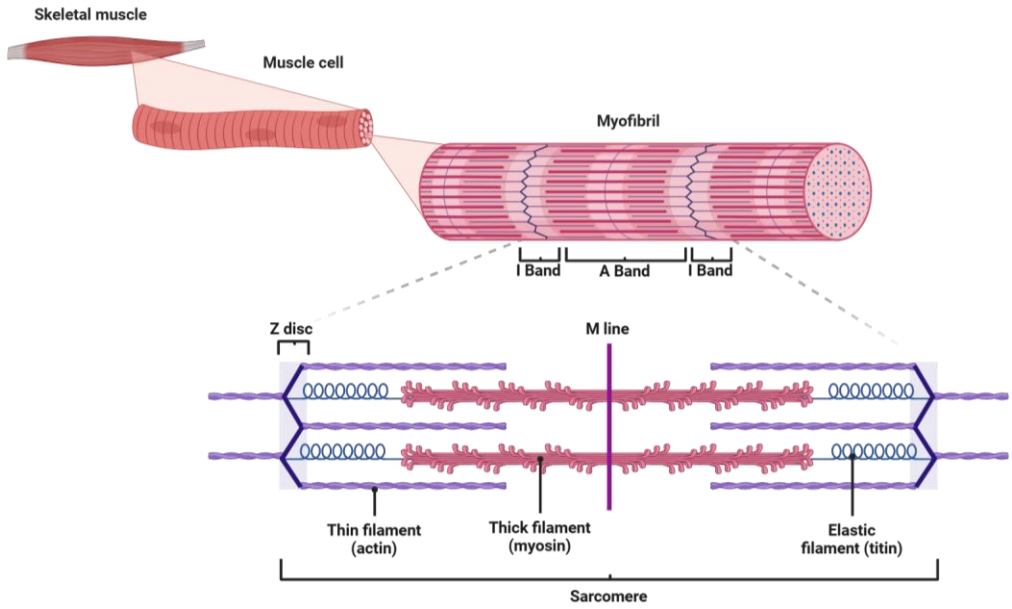


Figure 1.9. Structure of the sarcomere in skeletal muscle.
Created in BioRender. Fernández Costa, J. (2026) https://BioRender.com/6y7l62g

Sarcomere function also depends on structural proteins that preserve alignment and elasticity. Titin contributes to passive tension and centers myosin filaments within the sarcomere, while nebulin contributes to thin filament stability. These proteins help maintain the mechanical integrity of the contractile apparatus during repeated cycles of contraction and relaxation. Because sarcomeres are highly ordered structures, even subtle disturbances in their organization, protein composition, or energetic support can reduce force output. This is particularly important in disease models where functional impairment may occur without dramatic changes in myotube size [140].

At the subcellular level, sarcomeres are mechanically connected to the sarcolemma, nucleus, and extracellular matrix through cytoskeletal and membrane-associated complexes. Disruption of cytoskeletal organization or force transmission can therefore produce muscle weakness that is disproportionate to the apparent structural loss [140]. For this reason, contractile function becomes an essential readout in skeletal muscle models, as it captures tissue performance more directly than morphology alone.

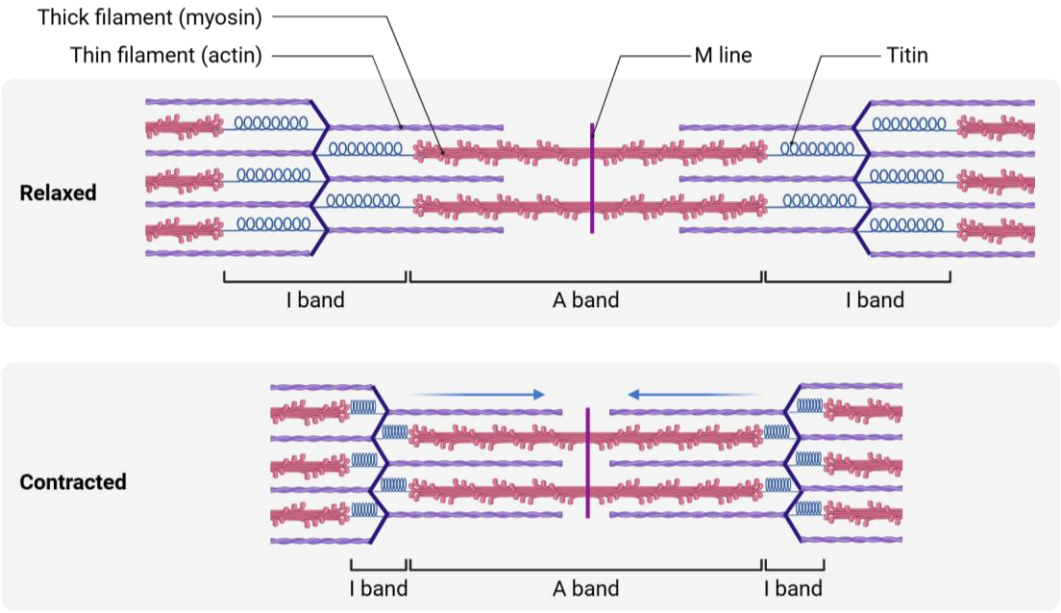


Figure 1.10. Sliding movement of sarcomeric proteins during skeletal muscle contraction.
Created in BioRender. (2026). https://BioRender.com/1op51cq

1.2.3 Fiber Types and Specialization

Human skeletal muscles contain heterogeneous fiber populations that differ in contractile speed, fatigue resistance, myosin heavy chain expression, mitochondrial content, and metabolic profile. Classical classifications distinguish type I slow-twitch oxidative fibers, which express β/slow myosin heavy chain and are adapted for sustained, fatigue-resistant activity, from type II fast-twitch fibers, which are generally specialized for more rapid and powerful contractions. Type II fibers can be further subdivided into more oxidative type IIa fibers and more glycolytic type IIx fibers. These categories are not rigid, and many human muscles contain hybrid fibers expressing more than one myosin heavy chain isoform [143,144].

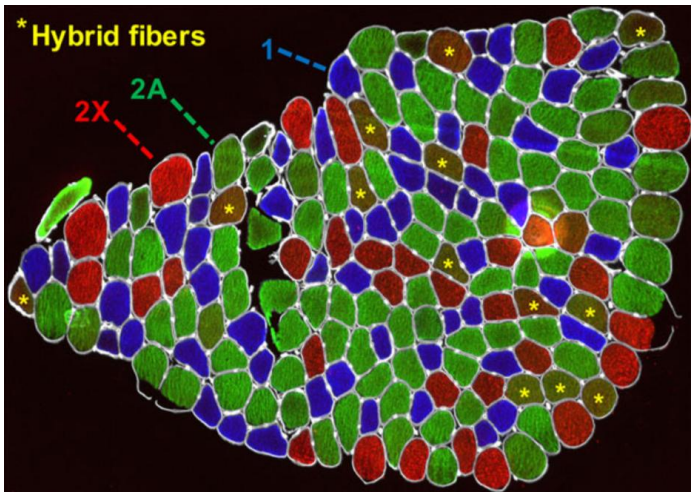


Figure 1.11. Fiber types stained with anti-myosin antibodies in a section of vastus lateralis muscle of a young adult.
Type 1, 2A, and 2X fibers are labeled. Fiber outlines are visualized by anti-laminin staining (white) [145].

Fiber-type composition is important because it influences both mechanical performance and metabolic function. Muscles enriched in oxidative fibers tend to display high mitochondrial density, greater capillarization, improved fatigue resistance, and enhanced lipid oxidation. In contrast, muscles enriched in fast glycolytic fibers generate higher peak power but fatigue more rapidly and rely more heavily on glycolysis and phosphocreatine for ATP supply. This specialization links muscle function to systemic metabolism, because skeletal muscle is a major site of insulin-stimulated glucose uptake and contributes substantially to lipid utilization, especially during sustained activity [141,144,146].

Skeletal muscle fibers are also highly plastic. Nutrient availability, inflammation, and metabolic stress among other factors can induce fiber phenotype shifts, mitochondrial capacity, and contractile protein expression. Endurance-type stimuli tend to promote oxidative remodeling and mitochondrial biogenesis, whereas resistance loading promotes hypertrophy and increased myofibrillar content. Conversely, unloading, denervation, chronic inflammation, and metabolic disease can induce atrophy, altered oxidative capacity, fiber-type shifts, and reduced contractile performance [141]. In the context of MASLD and MASH, this plasticity is highly relevant because liver-derived inflammatory and metabolic mediators may alter muscle phenotype and function even in the absence of direct injury.

In vitro skeletal muscle models do not fully reproduce the fiber-type diversity, vascularization, innervation, or loading history of native human muscle. However, they can preserve key features of myogenic differentiation, myotube alignment, sarcomeric organization, and contractile responsiveness. Markers such as *MYH7* can therefore provide useful information about differentiation-associated or contractile phenotype changes, particularly when interpreted alongside functional measurements.

1.2.4 Excitation-Contraction Coupling and Electrical Stimulation

Skeletal muscle contraction is triggered by membrane depolarization and coordinated calcium release. *In vivo*, this process begins at the neuromuscular junction (NMJ), where acetylcholine from motor neurons activates acetylcholine receptors (AChR) on the muscle fiber membrane. The resulting action potential propagates along the sarcolemma and into the transverse tubule system, where voltage-sensitive dihydropyridine receptors (DHPRs) interact with ryanodine receptor 1 (RyR1) channels in the sarcoplasmic reticulum. This interaction triggers calcium release into the cytosol, enabling calcium binding to troponin C and activation of actin–myosin cross-bridge cycling. Relaxation occurs when calcium is sequestered back into the sarcoplasmic reticulum by SERCA pumps [138].

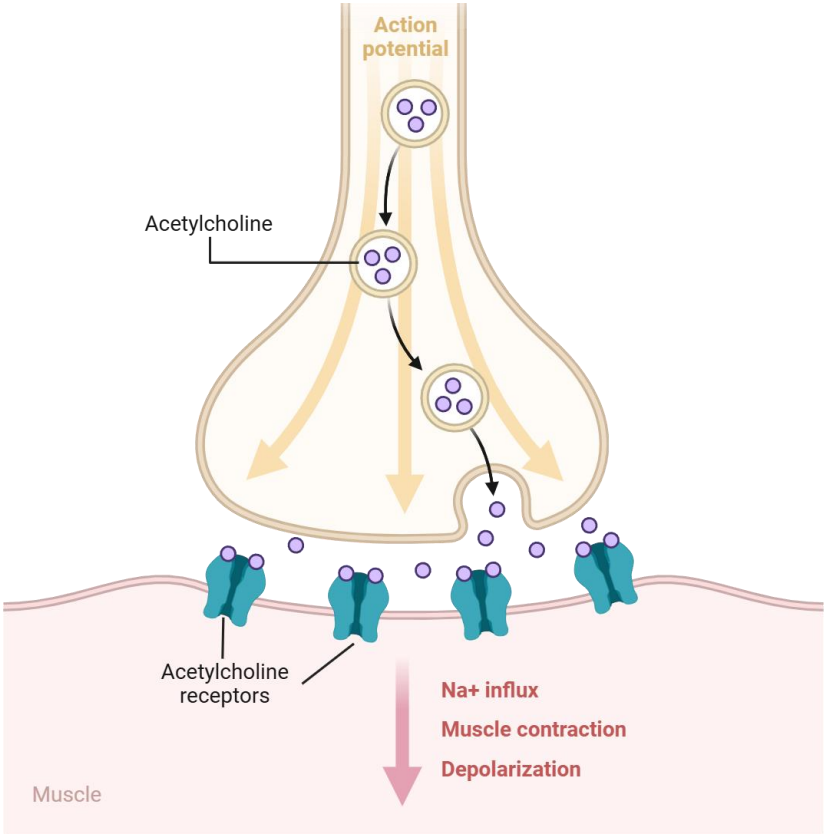


Figure 1.12. Basic structure of the NMJ and how acetylcholine binding to its receptors leads to muscle contraction and depolarization.
Created in BioRender. (2026). https://BioRender.com/yknuvfn

Defects in membrane excitability, calcium release, calcium reuptake, or contractile protein responsiveness can reduce force production without necessarily causing immediate loss of muscle mass. This is clinically relevant because several muscle diseases and systemic conditions are characterized by weakness or fatigability that cannot be fully explained by fiber atrophy alone. Altered calcium handling, mitochondrial dysfunction, oxidative stress, and inflammatory signaling can all

interfere with the efficiency of excitation–contraction coupling and thereby impair contractile performance [140].

1.2.5 Energy Metabolism and Muscle Plasticity

Skeletal muscle has high and variable energy demands. ATP is required for actin–myosin cross-bridge cycling, calcium reuptake by SERCA pumps, ion homeostasis, biosynthesis, and tissue maintenance. Depending on the intensity and duration of activity, ATP is supplied by a variety of pathways. The balance between these systems varies among fiber types and adapts in response to training, disuse, nutritional status, and disease [140].

Because of its large mass and metabolic flexibility, skeletal muscle is an important contributor to systemic glucose and lipid homeostasis. In response to insulin and contractile activity, skeletal muscle increases glucose uptake and glycogen synthesis. During fasting or prolonged activity, it can increase fatty acid oxidation and contribute to the regulation of circulating lipid levels. Skeletal muscle also releases myokines and metabolites that communicate with other organs, placing it within a broader inter-organ network that includes liver, adipose tissue, and pancreas, among the most relevant to this introduction [137,147].

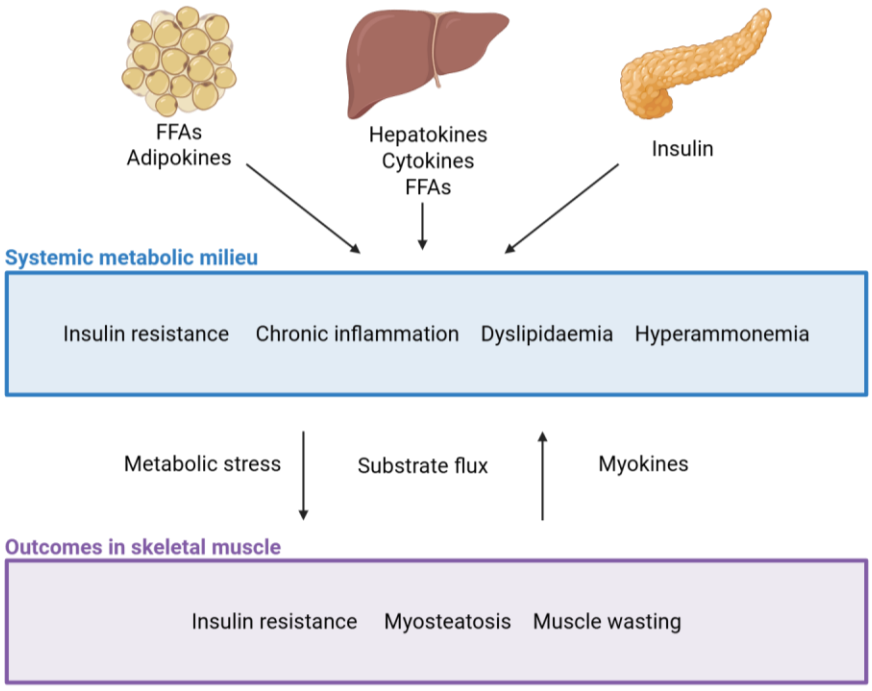


Figure 1.13. Skeletal muscle as a metabolic organ and its interactions with the systemic metabolic milieu.
Created in BioRender. (2026). https://BioRender.com/louw59g

Metabolic diseases can disrupt this balance. Insulin resistance, ectopic lipid accumulation, chronic low-grade inflammation, mitochondrial stress, and altered nutrient signaling can reduce muscle oxidative capacity, impair anabolic responses, and promote weakness or wasting [137]. In MASLD, these processes are particularly relevant because liver dysfunction is closely linked to systemic metabolic imbalance. The diseased liver may influence skeletal muscle through altered secretion of cytokines, hepatokines, lipids, metabolites, extracellular vesicles, or other soluble mediators [1,148]. Therefore, studying skeletal muscle impairment in MASLD requires models capable of assessing not only cell survival or morphology, but also functional performance and stress-associated molecular remodeling.

1.2.6 Protein Turnover, Atrophy, and Autophagy-Lysosome Homeostasis

Skeletal muscle size and quality are maintained through a dynamic balance between protein synthesis, protein degradation, organelle turnover, and repair mechanisms. Under healthy conditions, anabolic pathways such as IGF-1–PI3K–Akt–mTOR signaling promote protein synthesis and growth, whereas catabolic systems remove damaged or unnecessary proteins and organelles. These catabolic systems include the ubiquitin–proteasome pathway, the autophagy–lysosome system, calcium-dependent proteases, and caspase-related pathways. Rather than being detrimental, these mechanisms are essential for maintaining tissue quality; problems arise when degradation is excessive, insufficient, or activated improperly [137].

Muscle atrophy is commonly associated with activation of the ubiquitin–proteasome system. Two widely studied muscle-specific E3 ubiquitin ligases are atrogin-1, encoded by gene *FBXO32*, and MuRF1, encoded by gene *TRIM63*. These genes are frequently induced in experimental models of denervation, fasting, disuse, cachexia, and glucocorticoid exposure, where they contribute to degradation of myofibrillar and regulatory proteins. Their expression is often controlled by *Foxo* transcription factors, which respond to reduced Akt signaling, inflammation, oxidative stress, and nutrient deprivation. For this reason, *FBXO32* and *TRIM63* are commonly used as molecular markers of canonical muscle atrophy [149,150].

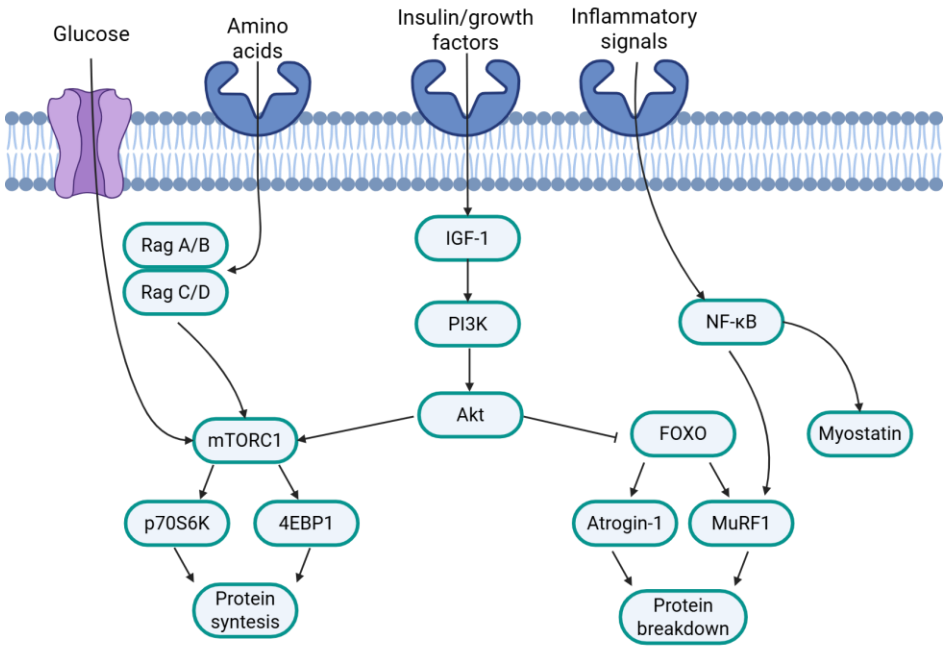


Figure 1.14. Molecular regulation of protein balance in skeletal muscle in response to systemic glucose, amino acids, insulin/growth factors, and inflammatory signals.
Adapted from [151]. Created in BioRender, (2026). https://BioRender.com/imiayhy

The autophagy–lysosome system is another essential regulator of skeletal muscle homeostasis. Autophagy contributes to the degradation of damaged proteins, protein aggregates, dysfunctional mitochondria, and other cellular components. During macroautophagy, cytoplasmic material is engulfed by autophagosomes, which subsequently fuse with lysosomes for degradation. LC3B lipidation and recruitment to autophagosomal membranes are commonly used to identify autophagosome accumulation, while acidotropic dyes label acidic lysosomal and autolysosomal compartments [149,152]. These markers provide useful information about autophagy–lysosomal remodeling, but they must be interpreted together with further markers that better resolve the specific alterations in these pathways in the context of disease. In this work, these markers are used to evaluate whether MASLD-derived conditioned media (CM) alter proteostasis features in mature skeletal muscle tissues.

1.2.7 Myogenic Maturation

Skeletal muscle formation and repair depend on tightly regulated myogenic programs. During development, myogenic progenitors are specified and progressively commit to the skeletal muscle lineage through the coordinated activity of transcription factors including *Pax3*, *Pax7*, *MYF5*, *MYOD1*, *MYOG*, and *MYF6*. *MYF5* and *MYOD1* are generally associated with myogenic commitment and lineage progression, while *MYOG* and *MYF6* participate in differentiation, fusion, and maturation of myotubes.

These transcription factors regulate the expression of structural, contractile, and fusion-related genes required to generate functional muscle fibers [153–155].

In adult skeletal muscle, growth and repair are supported by satellite cells, a resident stem cell population located between the sarcolemma and basal lamina. In homeostatic conditions, satellite cells remain largely quiescent and are characterized by expression of *Pax7*. Upon injury, stress, or disease-associated cues, they become activated, proliferate, and generate myogenic progenitors that differentiate and fuse with damaged fibers and can also form new myofibers. This regenerative response is regulated by transcriptional programs and external signals from the surrounding niche, including immune cells, fibro-adipogenic progenitors (FAP), endothelial cells, ECM components, growth factors, cytokines, and metabolic cues [156,157].

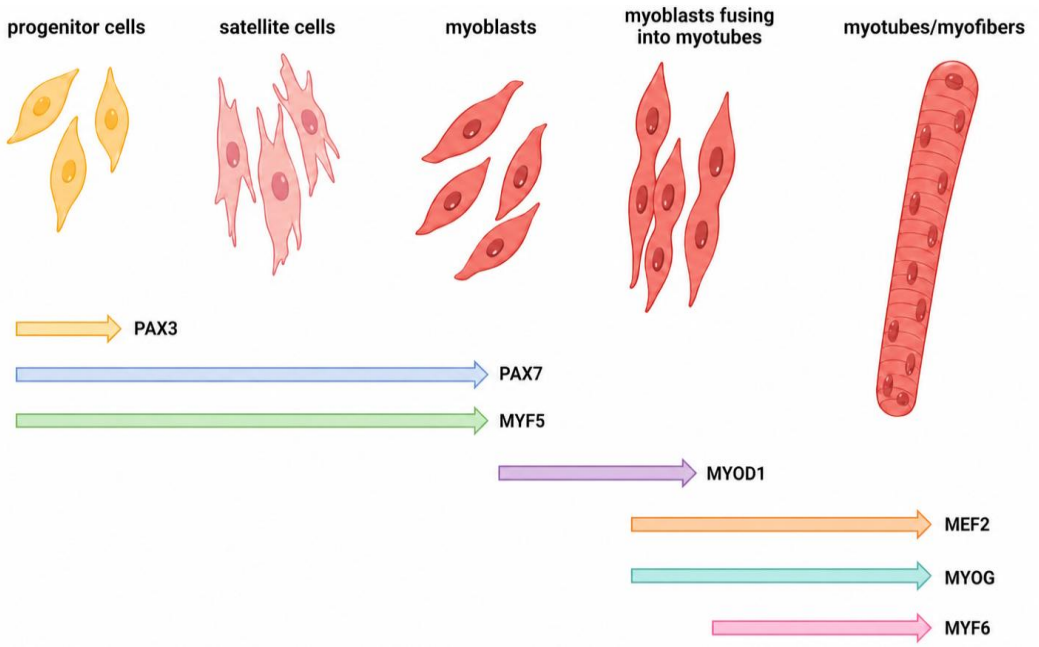


Figure 1.15. Transcription factors involved in skeletal muscle differentiation.
Schematic representation of the sequential activation of transcription factors that regulate skeletal muscle lineage commitment and terminal differentiation. PAX3/PAX7-positive progenitor cells give rise to PAX7-expressing satellite cells. Upon activation, satellite myogenic cells upregulate *MYF5*, initiating the myogenic program and promoting *MYOD1* expression as cells progress toward the myoblast stage. Terminal differentiation is associated with activation of *MYOG* and *MEF2*, together with the progressive downregulation of *MYF5* and, subsequently, *MYOD1*. *MYF6* expression is induced later during differentiation, after the initial *MYOG*-associated differentiation phase, contributing to myotube/myofiber maturation. Adapted from Fernández-Costa *et al.* [142]

Chronic inflammation, ageing, metabolic disease, fibrosis, and fatty infiltration can impair the regenerative environment. These conditions may reduce satellite cell function and alter myogenic transcriptional programs [140]. For this reason, myogenic regulatory factors are frequently studied in muscle disease and wasting contexts. However, interpretation depends strongly on the model and experimental design. The skeletal muscle constructs used here are exposed to liver-derived CM after a

period of *in vitro* differentiation, with the aim of assessing how an already formed human muscle tissue responds to a MASLD- or MASH-like hepatic secretome. Therefore, changes in myogenic regulatory factors are interpreted as alterations in the transcriptional state of mature muscle constructs, including differentiation-associated or stress-associated remodeling.

1.3 The Liver-Muscle Axis: Sarcopenia and Muscle Wasting

Sarcopenia is defined as a progressive and generalized skeletal muscle disorder characterized by loss of muscle strength and mass, with associated risk of physical disability, poor quality of life, and mortality [158–161]. Contemporary diagnostic frameworks emphasize low muscle strength as the primary criterion, with low muscle quality and impaired physical performance used to confirm severity [160]. Muscle wasting is a broader term that encompasses sarcopenia as well as disease-related muscle loss in conditions such as cancer, chronic heart failure, chronic obstructive pulmonary disease, and chronic liver disease. Myosteatosis, in contrast, refers to pathological fat infiltration within skeletal muscle—both intracellular lipids and intermuscular adipose tissue—that impairs contractile efficiency and is now recognized as an independent predictor of adverse outcomes in several chronic diseases, including NAFLD/MASLD [161–163].

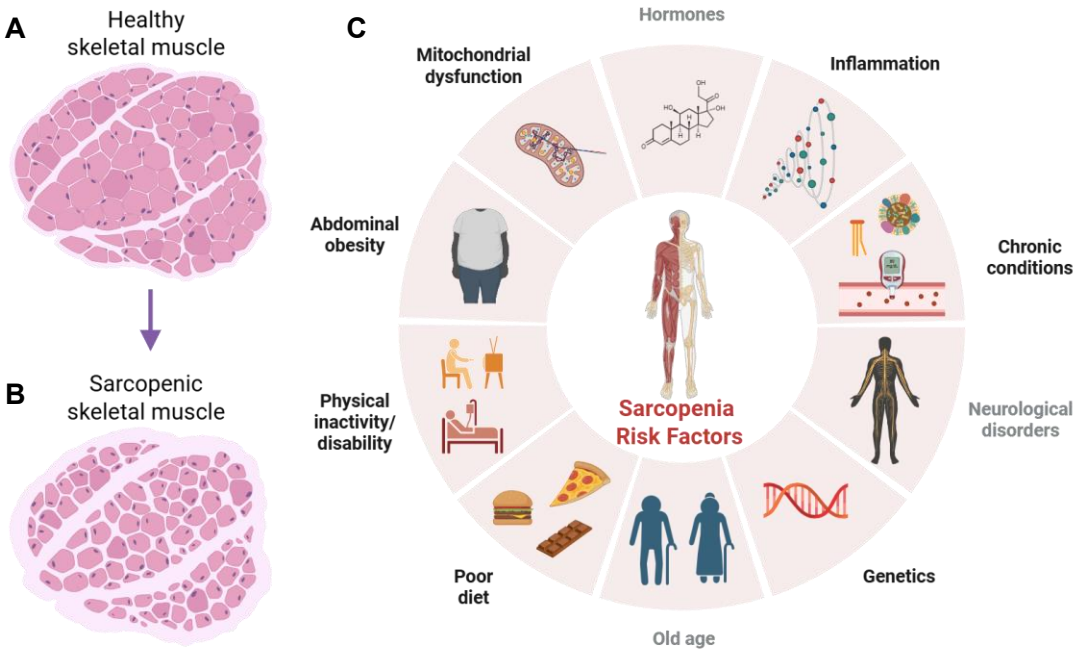


Figure 1.16. Phenotypic changes in sarcopenia and its associated risk factors.
A) Healthy amount of skeletal muscle mass. B) Decrease in muscle fiber size in sarcopenic skeletal muscle. C) Most relevant risk factors of sarcopenia are highlighted in bold. Initially thought a disease associated with aging alone, increasing evidence frames sarcopenia within systemic conditions frequently observed in MASLD, like abdominal obesity, poor diet, inflammation, and genetic predisposition. Created in BioRender, (2026) https://BioRender.com/6p0t6q8

In chronic liver disease, sarcopenia is highly prevalent and strongly associated with complications and post-transplant outcomes. Mechanistically, cirrhosis-associated sarcopenia reflects a convergence of reduced protein synthesis, increased proteolysis—including autophagy-mediated protein breakdown—, hyperammonemia-induced upregulation of myostatin, anabolic resistance to nutrition and exercise, and mitochondrial dysfunction, among other factors. While much of this work has focused on advanced cirrhosis, increasing attention is now directed towards muscle alterations earlier in the MASLD–MASH spectrum, where metabolic stress predominates and implications are greatly understudied [28,164,165].

Recent meta-analyses and large cohort studies confirm that sarcopenia and myosteatosis are common and clinically relevant in MASLD. A 2024 systematic review and meta-analysis including 29 studies and over 63,000 patients reported a pooled sarcopenia prevalence of 23.5% in MASLD, with sarcopenia associated with more than two-fold increased odds of MASLD and a 59% higher hazard of all-cause mortality [166]. Observational studies consistently show that sarcopenia and sarcopenic obesity are linked to more advanced fibrosis and worse prognosis in NAFLD/MASLD, even after adjusting for traditional metabolic risk factors. Importantly, myosteatosis appears to be particularly relevant: in a biopsy-proven NAFLD cohort, severe myosteatosis—but not reduced muscle mass—was significantly associated with early steatohepatitis, more severe lobular inflammation and ballooning, and accelerated fibrosis progression over a median 29-month follow-up [162]. Other studies using CT-based muscular quality indices similarly found that sarcopenia combined with myosteatosis confers the highest risk of NAFLD and adverse metabolic outcomes, especially in non-obese individuals [163].

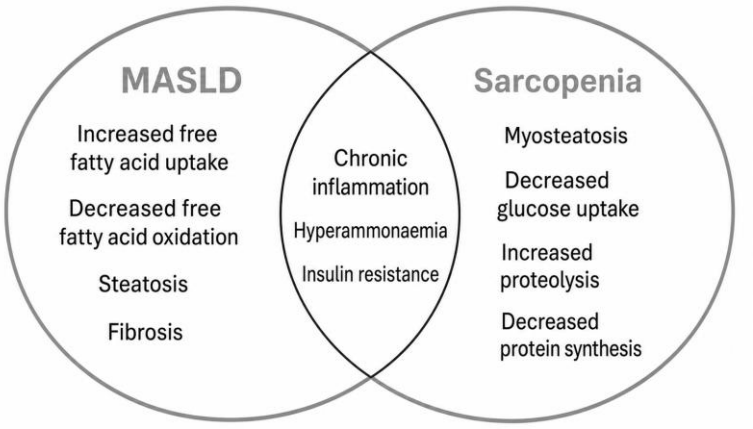


Figure 1.17. Common features of MASLD and sarcopenia.
Sarcopenia commonly coexists with advanced MASLD/MASH and is associated with poorer clinical outcomes, including adverse post-transplant outcomes in patients with advanced liver disease. MASLD and sarcopenia share chronic low-grade inflammation, insulin resistance, and, in advanced liver disease, hyperammonemia, which contribute to a bidirectional liver–muscle axis.

Collectively, these data support the concept that MASLD is frequently accompanied by quantitative and qualitative muscle abnormalities, ranging from reduced muscle mass and strength to fatty infiltration and impaired physical function. Sarcopenia and myosteatosis appear to be both a consequence and a driver of MASLD progression, participating in bidirectional pathophysiological loops that link hepatic steatosis, insulin resistance, and systemic low-grade inflammation to muscle dysfunction and vice versa.

1.3.1 Mechanistic Links between MASLD and Skeletal Muscle

The mechanistic crosstalk between MASLD liver and skeletal muscle organokine networks, shared metabolic perturbations, and chronic inflammation form a “liver–muscle axis” [137,167]. Insulin resistance is a central common denominator because in MASLD, hepatic insulin resistance promotes increased gluconeogenesis and VLDL secretion, while muscle insulin resistance reduces glucose uptake, together driving hyperglycemia, compensatory hyperinsulinemia, and redistribution of lipid flux towards both liver and muscle. Myosteatosis also impairs insulin signaling and excitation–contraction coupling, thereby linking hepatic and muscular steatosis as parallel manifestations of systemic metabolic overload [167–170].

At the endocrine level, hepatokines secreted by steatotic and inflamed liver—such as FGF21, fetuin-A, and others—influence muscular glucose uptake, insulin sensitivity, mitochondrial function, and fatty-acid oxidation. For example, FGF21 is often elevated in MASLD and acts on skeletal muscle to enhance glucose uptake and fatty-acid oxidation, potentially as a compensatory response to metabolic stress, whereas fetuin-A promotes insulin resistance and inflammation in muscle and adipose tissue [171,172]. Conversely, myokines such as IL-6, myostatin, FGF21 from muscle, and others can modulate hepatic gluconeogenesis, lipogenesis, and inflammation, reinforcing the bidirectional nature of liver–muscle communication. Chronic alterations in this hepatokine–myokine network in MASLD are thought to contribute to both hepatic disease progression and muscle wasting, although the relative contribution of individual factors remains to be fully delineated [172–175].

Insights from chronic liver disease and cirrhosis further inform MASLD-related mechanisms. Hyperammonemia, for instance, induces myostatin expression in skeletal muscle, suppresses mTORC1 signaling, enhances autophagy, and impairs mitochondrial function, collectively driving muscle wasting [176–179]. Even though hyperammonemia is less pronounced in early MASLD than in decompensated cirrhosis, similar pathways of impaired protein synthesis, increased autophagy-mediated proteolysis, and mitochondrial dysfunction have been described in metabolic liver disease and may operate at subclinical levels in MASLD-associated muscle wasting. Low-grade systemic inflammation, characterized by elevated IL-6, TNF-α, and other cytokines, further contributes to anabolic resistance in muscle, reduced satellite cell function, and activation of catabolic pathways, while simultaneously promoting hepatic inflammation and fibrogenesis [180,181].

Finally, there is mounting evidence that myosteatosis itself feeds back on the liver. Fat-infiltrated muscle exhibits altered myokine secretion and reduced oxidative capacity, favoring insulin resistance and

increased NEFAs flux, which in turn exacerbate hepatic lipotoxicity and steatohepatitis [180,182]. Systems biology analyses highlight that MASLD and its systemic complications arise from the integrated behavior of multiple organ networks, including liver, muscle, adipose tissue, gut, and brain, rather than from a single organ in isolation [183]. In this context, human-relevant experimental platforms capable of isolating and interrogating liver–muscle crosstalk—such as the modular 3D liver–skeletal muscle system developed in this thesis—are essential for dissecting the causal contribution of MASLD-derived secreted factors to muscle dysfunction and for identifying actionable points of intervention along the liver–muscle axis.

Rather than reducing liver–muscle communication to the study of individual hepatokines, myokines, or isolated soluble mediators, this thesis adopts a broader strategy based on the generation of biologically faithful and disease stage-specific liver CM. In this framework, liver constructs exposed to defined MASLD-relevant stimuli are used to produce CM that captures a more integrated secretory profile of each pathological state, including the combined effects of metabolic stress, inflammatory signaling, and fibrogenic activation. These liver-derived media can then be applied to differentiated and functional skeletal muscle microtissues to assess how stage-specific hepatic dysfunction affects muscle performance and phenotype *in vitro*. The analysis therefore focuses not only on candidate molecular mediators, but also on downstream functional and structural outcomes, including contractility, force generation, myotube size, myogenic regulatory factor expression, and histological alterations. This approach positions the modular platform developed in this thesis as a versatile tool to interrogate multiple dimensions of liver–muscle crosstalk in MASLD, while preserving the flexibility to incorporate additional organ modules and more complex inter-organ communication networks in future studies.

1.4 Rationale of this Work: Modular *In vitro* Study of Liver-Muscle Crosstalk

Despite substantial progress in understanding MASLD as a systemic metabolic disorder, current experimental platforms remain limited in their ability to reproduce disease progression and its extrahepatic consequences under controlled, human-relevant conditions. Conventional *in vitro* liver models can capture selected features of steatosis, inflammation, or fibrogenesis, but they rarely preserve the modularity needed to interrogate how stage-specific hepatic dysfunction affects distal tissues. Conversely, animal models and clinical studies capture systemic complexity but offer limited experimental control over individual organ contributions and are not ideally suited to isolate the causal impact of liver-derived signals on skeletal muscle function. This creates a clear methodological gap, as there is a need for a human, modular platform capable of modeling progressive MASLD-like phenotypes and evaluating their downstream effects on skeletal muscle using functional, structural, and molecular readouts with physiological relevance.

To address this challenge, this thesis presents two complementary and validated tissue-engineered models: a three-dimensional liver model and a three-dimensional skeletal muscle model. Each tissue is first established and characterized, ensuring that the liver model reliably reproduces key features of

MASLD progression and that the skeletal muscle model exhibits the structural organization and contractile functionality required to act as a physiologically relevant target tissue. By building each module independently, it becomes possible to define the contribution of each tissue with greater precision and to create a flexible platform that can later be adapted, expanded, or integrated with additional organ systems.

These models are combined through a modular inter-organ communication strategy. The liver model is used to generate CM representing different stages of disease progression, thereby capturing the complex mixture of soluble factors released by healthy or diseased hepatic tissue. These CM serve as integrated representations of the hepatic secretome and are transferred to the skeletal muscle model, allowing the effects of liver-derived signals to be studied without bias towards any specific mediator involved. In this way, the platform enables the investigation of how progressive hepatic dysfunction influences skeletal muscle biology while maintaining experimental control over both the source and the target tissue.

Using this framework, the effects of liver-derived signals on skeletal muscle can be evaluated through functional, structural, and molecular endpoints, including force generation, myotube morphology, myogenic regulation, and tissue remodeling. The modular platform also establishes the foundation for future dynamic integration into an organ-on-chip system, where liver and muscle tissues could be connected under controlled flow conditions to better reproduce physiological inter-organ communication. The rationale, development, and validation of these experimental modules are presented in the following chapters, particularly Chapter 4 for the liver model, Chapter 5 for the skeletal muscle response, and Chapter 6 for the first step toward organ-on-chip integration.

Chapter 2 | Hypothesis and Objectives

MASLD is a progressive systemic disorder in which hepatic lipid accumulation, inflammatory signaling, and fibrogenic remodeling interact with extrahepatic organs. Although the liver is the central pathological site, disease progression and clinical outcome are strongly influenced by multi-organ metabolic dysfunction. Among these extrahepatic manifestations, skeletal muscle impairment is particularly relevant, as reduced muscle mass, altered muscle quality, and impaired contractile performance are associated with worse prognosis and may contribute to the progression of systemic metabolic dysfunction.

Current experimental approaches are limited in their capacity to reproduce this inter-organ complexity under controlled conditions. Conventional two-dimensional liver and muscle cultures allow mechanistic studies and scalable assays, but they do not adequately reproduce the three-dimensional architecture, matrix-mediated signaling, multicellular interactions, or functional tissue-level readouts required to study MASLD-associated liver–muscle crosstalk. Animal models capture systemic physiology, but their interpretation is constrained by species-specific differences, limited experimental control over individual organ contributions, and difficulty in isolating the causal role of liver-derived signals on skeletal muscle dysfunction. Therefore, there is a need for modular human-relevant *in vitro* platforms that can reproduce defined stages of MASLD progression and allow their downstream impact on functional skeletal muscle tissues to be evaluated.

The hypothesis of this thesis is that human three-dimensional liver constructs combining metabolically competent hepatic cells and HSCs can recapitulate stage-specific features of MASLD progression, including steatosis, inflammatory activation, hepatocellular injury, and early fibrogenic remodeling. Moreover, the CM generated by these liver constructs will contain disease-stage-specific secreted factors capable of inducing measurable functional, structural, and molecular alterations in differentiated three-dimensional skeletal muscle tissues. Finally, the modular integration of these tissue models into a controlled organ-on-chip framework will provide a flexible platform to interrogate liver–muscle crosstalk in MASLD and to support future incorporation of additional organ modules or therapeutic interventions.

Following this rationale, the central hypothesis of this thesis is that a modular human *in vitro* strategy can be used to model MASLD-associated liver–skeletal muscle crosstalk by first establishing independently validated three-dimensional liver and skeletal muscle modules, then connecting them through liver-derived CM, and finally translating this static communication paradigm toward a dynamic organ-on-chip framework. This hypothesis is presented in three parts.

Hepatic module: Human three-dimensional liver constructs combining metabolically competent hepatocyte-like cells and hepatic stellate cells can recapitulate stage-specific features of MASLD progression under controlled *in vitro* conditions. Specifically, exposure to defined lipotoxic and inflammatory stimuli reproduces key features of progressive liver dysfunction, including steatosis, inflammatory activation, hepatocellular injury, hepatic stellate cell activation, and early fibrogenic remodeling.

Skeletal muscle module: CM generated by these stage-specific liver constructs contain integrated hepatic signals sufficient to induce measurable alterations in differentiated three-dimensional skeletal muscle tissues. These signals induce stage-dependent functional, structural, and molecular changes in healthy skeletal muscle, including alterations in contractile force generation, myotube morphology, myogenic regulation, and tissue remodeling.

Organ-on-chip framework: Translating the static liver–muscle communication paradigm into a pressure-driven microfluidic architecture with controlled dilution and mixing will the fluidic basis for future dynamic interrogation of liver–muscle crosstalk, support future integration of the liver and muscle modules into a dynamic multi-organ platform.

According to this hypothesis, the main objective of this thesis is to develop and characterize a modular *in vitro* platform based on human three-dimensional liver and skeletal muscle tissues to model MASLD/MASH-associated liver–muscle crosstalk and evaluate the impact of liver-derived disease-stage-specific signals on skeletal muscle function and phenotype.

The specific objectives are the following:

1. To establish and validate a human three-dimensional liver model capable of reproducing key features of MASLD progression under controlled *in vitro* conditions. This objective includes the calibration of a non-esterified fatty acid stimulus to induce hepatic steatosis, the incorporation of hepatic stellate cells to enable multicellular crosstalk, and the use of lipopolysaccharide as an inflammatory amplifier to generate a MASH-like phenotype.
2. To characterize the stage-specific hepatic phenotypes generated in the three-dimensional liver constructs. This includes the assessment of lipid accumulation, hepatocyte identity and injury, hepatic stellate cell activation, inflammatory and fibrogenic secreted factors, and extracellular matrix remodeling in control, steatotic, MASH-like, and inflammation-only conditions.
3. To generate differentiated and functional three-dimensional skeletal muscle tissues suitable for the study of MASLD-associated muscle dysfunction *in vitro*. This objective includes the fabrication of aligned human skeletal muscle microtissues, their maturation into contractile tissues, and their functional assessment by electrical pulse stimulation.
4. To determine whether CM derived from MASLD-like liver constructs are sufficient to impair skeletal muscle function and phenotype. This includes the optimization of CM exposure

conditions and the evaluation of skeletal muscle contractility, force generation, myotube morphology, myogenic regulatory factor expression, and histological or subcellular changes after exposure to disease-stage-specific liver-derived media.

5. To develop a modular experimental framework for liver–muscle crosstalk studies that can be further adapted to dynamic organ-on-chip integration. This objective includes establishing the conceptual and technical basis for controlled medium exchange, automated inter-organ communication, and future incorporation of additional tissue modules, biosensors, or therapeutic interventions.

Altogether, this thesis aims to provide a human-relevant and modular *in vitro* strategy to study how progressive hepatic dysfunction in MASLD can influence skeletal muscle performance. Rather than focusing on isolated soluble mediators, this work uses biologically generated, stage-specific liver CM as integrated hepatic signals and tests their downstream effects in functional skeletal muscle tissues. This approach is intended to bridge the gap between reductionist cell culture systems and complex animal models, while providing a platform that can be expanded toward more advanced multi-organ models of metabolic disease.

Chapter 3 | Materials and Methods

This chapter describes the experimental pipeline used to establish the three-dimensional liver and skeletal muscle modules, to generate MASLD-like hepatic phenotypes, and to quantify liver–muscle communication. It is organized into: (i) cell sources and culture conditions; (ii) preliminary 2D assays for lipid-challenge optimization; (iii) fabrication, disease induction, and phenotypic characterization of 3D liver constructs; (iv) fabrication and maturation of 3D skeletal muscle tissues; (v) static liver–muscle communication experiments with liver-conditioned media; (vi) shared structural and molecular characterization methods; (vii) organ-on-chip device fabrication and fluidic characterization; and (viii) statistical analysis, reagents, probes, and gene expression assays.

3.1 Cell sources and culture conditions

3.1.1 Immortalized hepatic cells (HepaRG™)

To model hepatocyte-like metabolic responses relevant to MASLD in a controlled *in vitro* setting, HepaRG™ cells were used due to their stable hepatic phenotype and suitability for metabolic challenges. HepaRG™ cells (HPRGC10, Thermo Fisher Scientific, Waltham, MA, USA) were cultured in hepatocyte growth medium (HGM) consisting of William's E Medium + GlutaMAX™ supplement (Gibco, Grand Island, NY, USA), 10% fetal bovine serum (FBS, 10270-106, Gibco), 1% penicillin-streptomycin (10,000 U mL^{-1}, 15140-122, Thermo Fisher Scientific), 5 µg mL^{-1} human insulin (I2643, Sigma-Aldrich, St. Louis, MO, USA), and 50 µM hydrocortisone 21-hemisuccinate sodium salt (H4881, Sigma-Aldrich). Cells were maintained at 37°C in a humidified atmosphere with 5% CO_2. Subculturing was carried out by trypsinization following supplier instructions.

3.1.2 Hepatic stellate cells (LX-2)

To incorporate stromal/pro-fibrotic signaling capacity in liver constructs and enable transition toward steatohepatitis-like phenotypes, LX-2 hepatic stellate cells were used as a human HSC model. LX-2 cells (SCC064, Merck, Darmstadt, Germany) were cultured in DMEM with GlutaMAX™, 4.5 g/L D-glucose, without sodium pyruvate (61965-026, Gibco), supplemented with 1% penicillin-streptomycin (10,000 U mL^{-1}, 15140-122, Thermo Fisher Scientific). For trypsin deactivation and routine growth, 10% and 2% FBS (10270-106, Thermo Fisher Scientific) were used, respectively, as indicated in supplier guidelines.

3.1.3 Human myoblasts (AB1079)

To study distal skeletal muscle responses to liver-derived cues, human primary myoblasts were expanded and differentiated into 3D bioengineered skeletal muscle tissues. The AB1079 human myoblast line (male, 38 years; quadriceps) was provided by Dr. Eduard Gallardo (Hospital de Sant Pau, Barcelona, Spain). Cells were expanded in skeletal muscle cell growth medium (SkM GM; C23060, Promocell, Heidelberg, Germany) supplemented with SupplementMix (Promocell), 10% FBS (10270-106, Thermo Fisher Scientific), and 1% penicillin-streptomycin (10,000 U mL^{-1}, 15140-122, Thermo Fisher Scientific). Differentiation was carried out in DMEM with GlutaMAX™, 4.5 g/L D-glucose, without sodium pyruvate (61965-026, Gibco), supplemented with 1% KnockOut Serum Replacement (KO-SR; 10828028, Thermo Fisher Scientific), 1% penicillin-streptomycin-glutamine (PSG; 10378-016, Gibco), and insulin-transferrin-selenium-ethanolamine (ITS-X; 51500-056, Gibco), referred to as SkM DM.

3.2 Preparation of lipotoxic and inflammatory stimuli

3.2.1 Preparation of non-esterified fatty acids

To recapitulate lipotoxic stress typical of MASLD, palmitate/oleate NEFAs were formulated using albumin as a physiological carrier to facilitate cellular uptake. Palmitic acid (PA; P0500, Sigma-Aldrich, St. Louis, MO, USA) was dissolved in 2-propanol (131090.1212, PanReac AppliChem, ITW Reagents, Darmstadt, Germany) to 400 mM. Oleic acid (OA; O1008, Sigma-Aldrich) was diluted in 2-propanol to 400 mM. Solutions were aliquoted and stored at −20°C. PA and OA were mixed at a 2:1 volume ratio to generate a concentrated PA/OA mixture. The mixture was diluted 1:100 in 1% bovine serum albumin (BSA), fatty acid-free (A8806, Sigma-Aldrich) in PBS 1X to obtain a NEFAs–BSA formulation (NEFAs stock) with a NEFAs/BSA molar ratio of 4:1. Aliquots were stored at −20°C.

3.2.2 High lipid regime for HepaRG in 2D

To establish a rapid 2D lipotoxicity paradigm for assay optimization and comparison with 3D liver constructs, HepaRG™ cells were challenged with a defined PA/OA mixture under serum-free conditions. HepaRG™ cells were seeded in tissue culture-treated 96-well plates at 5.0×10^4 cells cm^{-2} and maintained for 24 h in HGM (37°C, 5% CO_2). Medium was then replaced by serum-free medium (SFM) composed of William's E Medium (GlutaMAX™) supplemented with HepaRG™ Induction Medium Supplement (5X; Gibco, HPRG740). Cells were adapted for 24 h in SFM prior to induction. Cells were then treated with 400 µM PA/OA (2:1) NEFAs mixture, prepared as above and diluted in SFM, and incubated for 24, 48, or 72 h before endpoint assays.

3.3 Preliminary 2D assays for lipid-challenge optimization

3.3.1 Cell culture staining

3.3.1.1 Oil Red O staining

To visualize neutral lipid droplets in 2D HepaRG samples under high-lipid challenge, Oil Red O staining was used as a lipid-soluble dye-based readout commonly applied in liver histology and cell models of steatosis. Cells were washed three times with PBS 1X (5 min each) and fixed with 200 µL neutral buffered formalin solution 10% (HT501128, Sigma-Aldrich) for 15 min. After two washes with ultrapure water (5 min each), cells were rinsed with 60% (v/v) 2-propanol and stained with freshly prepared Oil Red O solution (3:2 dilution in ultrapure water; O1391, Sigma-Aldrich) for 15 min. Excess dye was removed by repeated washing with ultrapure water until the supernatant was clear. Nuclei were counterstained with Harris Modified Hematoxylin Solution (HHS16, Sigma-Aldrich) for 1 min, followed by extensive washing. Samples were maintained in ultrapure water for imaging.

3.3.2 Metabolic activity/viability and lysosomal activity assays

To quantify global metabolic activity and lysosome-dependent uptake capacity under lipid challenge—two complementary readouts frequently altered in lipotoxicity—MTS and Neutral Red assays were performed at multiple timepoints.

3.3.2.1 MTS assay

At 24, 48, and 72 h after lipid challenge, medium was removed and cells were washed three times with PBS 1X for 5 min. Wells were filled with 100 µL fresh SFM plus 20 µL CellTiter 96® AQueous One Solution reagent (G3580, Promega, Madison, WI, USA) and incubated for 2 h (37°C, 5% CO_2). Absorbance at 490 nm was measured using a SPARK microplate reader (Tecan, Männedorf, Switzerland) after shaking for 5 s (1 mm amplitude, 1440 rpm). Reagent-only wells (no cells) were used as blanks for background correction.

3.3.2.2 Neutral Red assay

Neutral Red (NR) uptake was used as a functional proxy for lysosomal/acidic compartment activity. A 1000X NR stock was prepared by dissolving NR powder (N4638, Sigma-Aldrich) at 4 mg mL^{-1} in PBS 1X. One day prior to each timepoint, a 1X NR working solution was prepared by diluting the stock in PBS 1X and incubating overnight at 37°C. At 24, 48, and 72 h after lipid challenge, the working solution was centrifuged (1000 RCF, 5 min) and filtered through a 0.22 µm membrane to remove crystals. Medium was removed and cells were washed three times with PBS 1X for 5 min. Wells were incubated with warm, crystal-free NR working solution (2 h, 37°C, 5% CO_2). Dye solution was discarded, wells were washed twice with PBS 1X, and cells were de-stained with 200 µL de-staining solution (50% v/v ethanol 96%, 49% v/v ultrapure H_2O, 1% v/v glacial acetic acid). Absorbance was measured at 540 nm using a

SPARK microplate reader after shaking for 5 s (1 mm amplitude, 1440 rpm). Reagent-only wells were included as blanks.

3.4 Three-dimensional liver module

3.4.1 Fabrication of 3D liver constructs

To model the liver–muscle axis *in vitro* with controlled cellular composition and matrix mechanics, HepaRG™ hepatocyte-like cells and LX-2 HSCs were co-encapsulated in collagen-based hydrogels that support hepatic function while enabling stromal activation upon inflammatory cues. Collagen type I-based hydrogels were fabricated using the PhotoCol with LAP kit (5170, Advanced BioMatrix, Carlsbad, CA, USA). HepaRG™ and LX-2 were trypsinized, counted per supplier instructions, and combined at a 2:1 ratio (HepaRG™: LX-2). On ice, an encapsulation pre-mix was prepared by sequentially adding neutralizing solution (5205, Advanced BioMatrix), NaOH 1 M (S2770, Sigma-Aldrich), reconstituted collagen solution 5 mg mL^{-1} (5198, Advanced BioMatrix), and LAP solution 17 mg mL^{-1} (5269, Advanced BioMatrix) in William's E Medium, protected from light. The HepaRG™/LX-2 suspension in HGM was added and briefly homogenized. Final cell density was 1.5×10^7 cells mL^{-1}. Thirty-microliter drops were pipetted into cell culture-treated 24-well plates, avoiding bubble formation. Thermal gelation was performed at 37°C for 10 min, followed by UV exposure for 30 s in a UVP Crosslinker (CL-1000, Analytik Jena, Jena, Germany) pre-heated for 30 s. After polymerization (visual change in opacity/color), wells were filled with HGM and incubated at 37°C, 5% CO_2.

3.4.2 Recapitulation of steatosis and steatohepatitis in 3D livers

To mimic progressive MASLD-to-MASH trajectories in a single construct format, two sequential media formulations were used: NEFAs to induce steatosis-like lipotoxicity, followed by NEFAs plus LPS to promote inflammatory/HSC-activating cues consistent with steatohepatitis-like phenotypes. NEFAs treatment medium was prepared by diluting the NEFAs stock 1:100 in SFM. NEFAs+LPS medium was prepared by diluting the NEFAs stock 1:100 in SFM and adding LPS to 0.1 µg mL^{-1} (L8274, Sigma-Aldrich). A carrier control was prepared by diluting BSA in SFM to match the molar concentration present in treatment media; SFM alone served as an untreated control. All constructs were transitioned to SFM for 3 days. Constructs were then incubated for 4 days in their respective treatment medium (control, carrier control, or NEFAs) at 37°C, 5% CO_2. On day 4, media were renewed; only the steatohepatitis group formulation was switched to NEFAs+LPS. Constructs were maintained for 3 additional days until the final timepoint.

3.4.3 AdipoRed™ staining and quantitative analysis

To quantify intracellular neutral lipid content in live 3D liver constructs without fixation-induced artifacts, AdipoRed™ staining was performed and analyzed by standardized projection and segmentation workflows. AdipoRed™ Assay Reagent (PT-7009, Lonza Bioscience, Basel, Switzerland) was diluted to

3% (v/v) in Live Cell Imaging Solution 1X (A14291DJ, Invitrogen, Carlsbad, CA, USA). Five constructs per condition were washed three times with sterile PBS 1X and transferred to µ-Slides (80826, Ibidi, Gräfelfing, Germany) containing diluted AdipoRed™ solution plus 0.1% Hoechst 33342 (H3570, Thermo Fisher Scientific). After incubation (30 min, 37°C, 5% CO_2), Z-stacks (0.81 µm step) were acquired using a Zeiss LSM 800 confocal microscope with a 20X objective (NA = 0.8) and pinhole 1 Airy unit under appropriate incubation conditions. Fiji/ImageJ (DOI: 10.1038/nmeth.2019) was used for processing: Z-stacks were converted to sum projections using a fixed slice number (15 slices). A custom ImageJ macro performed Gaussian background subtraction, thresholding, and mask generation. Mean gray values and areas of segmented lipid droplets and nuclei were quantified, and area-based lipid readouts were normalized to nuclei number.

3.4.4 LIVE/DEAD staining and quantitative analysis

To assess the viability of cell-laden hydrogels under experimental conditions, LIVE/DEAD staining was performed and imaged by confocal microscopy. Constructs were washed three times with PBS 1X under agitation and incubated in a dye solution containing 2 µM calcein AM, 4 µM ethidium homodimer-1, and 0.1% Hoechst (LIVE/DEAD™ Viability/Cytotoxicity Kit, L3224, Invitrogen) for 25 min (37°C, 5% CO_2). Samples were imaged on a Zeiss LSM 800 using a 10X objective (NA = 0.3) and pinhole 1 AU. Image analysis was performed in Fiji/ImageJ.

3.4.5 Picro Sirius Red Staining

To evaluate collagen deposition and organization as a readout of ECM remodeling during MASH-like progression, Picro Sirius Red staining was performed on liver cryosections. Sections were hydrated in distilled water, incubated with Picro Sirius Red solution for 1 h, rinsed twice in 0.5% acetic acid, and rinsed once in absolute ethanol. Two additional ethanol changes were performed to fully dehydrate sections. Slides were mounted using Organo/Limonene Mount™ (O8015, Sigma-Aldrich). Brightfield and polarized imaging were performed on a Leica DMRB upright microscope equipped with a color camera.

3.4.6 Albumin, AST, PINP, and PIIINP measurements

To benchmark liver function and damage (albumin, AST) and quantify soluble collagen propeptides reflecting ECM remodeling (PINP, PIIINP), liver supernatants were analyzed using clinical-grade platforms. Frozen 3D liver supernatants were measured at Hospital Clínic (Barcelona, Spain). Albumin (CPS_000014) and AST (CPS_000040) were measured using a Cobas c 311/501 analyzer as previously reported [184]. PINP and PIIINP were quantified using an IDS-iSYS automated immunoassay analyzer with enzymatic assay-based cartridges.

3.4.7 Cytokine measurements

To quantify inflammatory and remodeling-associated soluble mediators underpinning liver phenotype progression and potential muscle effects, multiplex bead-based immunoassays were performed on

clarified supernatants. Supernatants were collected, centrifuged at 1000 RCF for 5 min, aliquoted, and stored at −80°C. Samples were thawed on ice on the day of assay. Cytokines were quantified using custom ProcartaPlex magnetic bead panels (Thermo Fisher Scientific): 3-plex (human IL-6, IL-1β, TNF-α; PPX-03-MXKA6FD) and 4-plex (human Caspase-3, CRP, IL-8, PDGF-BB; PPX-04-MXMFZDP), following manufacturer instructions. Standards were reconstituted and serially diluted in SFM (8-point curve), with SFM as blank. Fifty microliters of mixed magnetic capture beads were added per well. After washing with a handheld magnetic plate washer, 50 µL of standards/controls/samples (duplicates) were incubated for 2 h at room temperature on a plate shaker (600 rpm), protected from light. After two washes, 25 µL biotinylated detection antibody mix was incubated for 30 min (room temperature, shaking). After two washes, 50 µL streptavidin-PE was incubated for 30 min (room temperature, shaking; light-protected). Beads were washed twice, resuspended in 120 µL reading buffer, and acquired on a Luminex MAGPIX. Median fluorescence intensity (MFI) values were fit to 5-parameter logistic (5-PL) curves using xPONENT and ProcartaPlex Analysis App software, and analyte concentrations were verified to fall within each assay's dynamic range.

3.5 Three-dimensional skeletal muscle module

3.5.1 Fabrication of PDMS casting molds

To generate standardized 3D skeletal muscle tissues suitable for force readouts, PDMS molds incorporating flexible pillars were fabricated to enable tissue self-organization and pillar-deflection-based functional assessment (Figure 5.3). PDMS casting molds were fabricated as described previously [185]. Briefly, 3D-printed master molds were used to generate negative molds, which were silanized with trichloro(1H,1H,2H,2H-perfluorooctyl)-silane (PFOTS). Final PDMS casting molds consisted of a rectangular pool to be filled with a biomaterial and cell mix, with two anchoring posts, around which the tissues will compact (Figure 5.3). PDMS molds were prepared by casting PDMS prepolymer at a 10:1 ratio, curing at 80°C, and thoroughly washing after demolding and punching.

3.5.2 Fabrication and maturation of 3D bioengineered skeletal muscle tissues

To evaluate skeletal muscle functional and catabolic responses to liver-derived signals, human myoblasts were engineered into 3D aligned tissues in pillar-based PDMS molds, enabling both phenotypic readouts and contractility quantification. Tissues were fabricated as described elsewhere [186,187]. Briefly, PDMS molds were cleaned by sequential sonication in water with detergent, 2-propanol, and Milli-Q water, followed by UV sterilization for 15 min. To reduce PDMS-associated adhesion, molds were treated with 1% (w/v) Pluronic® F-127 (Sigma-Aldrich) in cold PBS (100 µL per well) for 2 h at 4°C and rinsed with sterile PBS. AB1079 myoblasts were trypsinized, resuspended in SkM GM, and encapsulated at 2.5×10^7 cells mL^{-1} in a hydrogel consisting of 30% (v/v) Matrigel® Growth Factor Reduced (356231, Corning, NY, USA), 4 mg mL^{-1} fibrinogen (F3879, Sigma-Aldrich), and 2 U mL^{-1} thrombin (T6884, Sigma-Aldrich). Pre-cooled reagents were used to prevent premature

Matrigel polymerization. The mixture was carefully pipetted and distributed between PDMS pillars and polymerized for 30 min at 37°C. SkM GM supplemented with 1 mg mL^{-1} 6-aminocaproic acid (ACA; A2504, Sigma-Aldrich) was added to prevent fibrin degradation. Temperature-driven polymerization promotes 3D tissue compaction around the posts, which was visually monitored to assess alignment and tension development. After 48 h, cultures were switched to SkM DM containing 1 mg mL^{-1} ACA. Half-medium changes were performed every other day until the treatment stage.

3.6 Static liver–muscle communication experiments

3.6.1 Treatment of skeletal muscle tissues with conditioned media from 3D livers

To test liver-to-muscle communication in a controlled and scalable manner, skeletal muscle tissues were exposed to liver CM generated from defined liver phenotypes. On day 16 of differentiation, half of the SkM DM volume was replaced with 2X concentrated CM media such that a final 1X CM concentration was achieved after mixing with the remaining half-volume. Because preliminary experiments indicated toxicity of liver cell culture media, multiple dilutions were evaluated; a final ratio corresponding to 1:50 liver components in SkM DM was selected to minimize functional perturbation unrelated to disease cues. CM were pooled by mixing equal volumes from five liver biological replicates per condition, and the pooled CM was used to treat all skeletal muscle biological replicates.

3.6.2 Functional assessment of 3D skeletal muscle tissues

To quantify muscle function as a clinically relevant endpoint (contractile output), engineered tissues were electrically stimulated, and force was derived from pillar deflection using beam theory. After treatment, differentiated skeletal muscle tissues were stimulated using a custom 24-well EPS platform containing two graphite electrodes per well connected to a pulse generator (Multifunction Generator WF1974, NF Corporation) [188]. The platform was placed in the XL S1 incubation chamber of a Zeiss Axio Observer Z1/7 microscope (37°C, 5% CO_2). Tissues were maintained in fresh DM/ACA during stimulation. Twitch and tetanic contractions were induced using square-wave pulses for 10 s at 1 V mm^{-1} field strength, 1 ms pulse width, and 1–50 Hz with 10% duty cycle. Time series were acquired for 140 s (1 ms exposure time, 82.3 fps) focusing on the top edge of pillars using a 10X objective. Whole tissue brightfield images were acquired using a 2.5X objective.

Pillar displacements were quantified in Fiji/ImageJ [189] by tracking pillar-edge intersections along a user-defined perpendicular line. Forces were computed using Euler–Bernoulli beam bending theory based on PDMS Young's modulus (1.6 MPa), pillar geometry, tissue attachment height, measurement height, and measured displacement. Forces were normalized to tissue cross-sectional areas (CSA) to obtain specific force.

3.6.3 Histological assessment of skeletal muscle tissues

3.6.3.1 LysoTracker™ staining

To quantify acidic compartments (lysosomes/late endosomes) in skeletal muscle tissues following liver-conditioned treatment—an axis relevant to autophagy–lysosome remodeling and muscle wasting—LysoTracker™ staining was combined with myotube segmentation and particle-based quantification. Live skeletal muscle tissues were washed with PBS 1X and incubated with 1 µM LysoTracker™ Red DND-99 (L7528, Invitrogen) for 30 min at 37°C. Tissues were washed three times with PBS 1X and fixed with 10% formalin (Sigma-Aldrich) for 30 min at room temperature. After three PBS washes, tissues were stored at 4°C until cryosectioning (as above). LysoTracker-prestained cryosections were stained with rabbit anti-dystrophin (ab15277, Abcam, Cambridge, UK) followed by donkey anti-rabbit AlexaFluor™ 647. Nuclei were stained using VECTASHIELD® PLUS with DAPI (H-2000, VectorLabs). Imaging was performed on a Zeiss LSM 800 using a 40X oil objective (NA = 1.4) and pinhole 1 AU. Acidic compartments were quantified using a custom ImageJ macro applying sequential background subtraction, convolution filtering, thresholding, and mask generation; particles between 0.1 and 5.0 µm² were analyzed. Segmentation accuracy was verified by overlaying masks on original images. Total particle counts were normalized to myotube area obtained using Cellpose 3 on dystrophin channels [190]. Feret diameters were extracted using the LabelsToRois plugin [191]. Five biological replicates per condition were analyzed in technical triplicates.

3.6.3.2 LC3B immunostaining

To assess autophagy-related structures in skeletal muscle tissues under liver-derived conditions, LC3B immunostaining was performed on cryosections using methanol permeabilization to enhance signal-to-background for punctate structures. A published protocol was followed with modifications [192]. Cryosections were permeabilized in 100% methanol for 15 min at −20°C and blocked in PBS 1X containing 0.5% BSA and 1% normal goat serum (S-1000, VectorLabs) for 1 h at room temperature. Sections were incubated overnight at 4°C with rabbit anti-LC3B (ab51520, Abcam) in blocking buffer. Sections were then incubated with goat anti-rabbit AlexaFluor™ 568 (A-11036, Thermo Fisher Scientific) for 2 h. PBS 1X washes were performed between steps and prior to nuclei counterstaining. Slides were mounted using VECTASHIELD® PLUS with DAPI (H-2000), coverslipped, and sealed for imaging.

3.7 Structural and molecular characterization

3.7.1 Cryosectioning

To enable spatially resolved histology and immunostaining across 3D constructs, tissues were cryoprotected and sectioned at a thickness compatible with confocal imaging and quantitative analysis. Constructs were washed three times with sterile PBS 1X (5 min each) and fixed in 10% formalin (HT501128, Sigma-Aldrich) for 30 min at room temperature. After three PBS washes (5 min each), tissues were incubated in 30% (w/v) sucrose in PBS 1X for 48 h at 4°C. Constructs were embedded in

OCT (P0091, Sigma-Aldrich) in Cryomolds® (VWR) and snap-frozen in pre-cooled isopentane chilled in liquid nitrogen. Blocks were stored at −20°C. Sections (20 µm) were cut using a Leica CM1860 cryostat and collected on SuperFrost Plus™ slides (11950657, Thermo Fisher Scientific), then stored at −20°C until staining.

3.7.2 Standard immunofluorescence staining

To phenotype liver and muscle tissues at the protein level (e.g., structural markers, stress pathways, ECM-associated markers), cryosections were immunostained using permeabilization and blocking conditions compatible with multi-channel confocal imaging. Sections were permeabilized with PBST (PBS 1X + 0.1% Triton X-100) for 15 min at room temperature, washed three times with PBS 1X (5 min each), and blocked with blocking solution (sc-516214, Santa Cruz Biotechnology, Dallas, TX, USA) for 1 h at room temperature. Primary antibodies (Table 3.1) were diluted in blocking buffer and applied overnight at 4°C. After three PBS washes (5 min each), sections were incubated with fluorescent secondary antibodies (Table S1) ± additional probes (Table 3.1) for 45–60 min at room temperature protected from light. Sections were washed three times with PBST (5 min each). Nuclei were counterstained with DAPI (Thermo Fisher Scientific; 15 min) or using VECTASHIELD® PLUS with DAPI (H-2000, VectorLabs, CA, USA). Slides were mounted with antifade medium, coverslipped, and sealed for imaging.

3.7.3 Gene expression analysis by real-time qPCR

To quantify transcriptional programs linked to steatosis/inflammation/fibrosis in liver constructs and atrophy/catabolism/autophagy in skeletal muscle tissues, RT-qPCR was performed on whole-tissue lysates using probe-based detection and validated reference genes. Whole 3D liver and skeletal muscle tissues were homogenized in 1 mL QIAzol using a TissueLyser (50 Hz, 8 min) with stainless steel beads under RNase-free conditions. RNA was purified with the miRNeasy Micro Kit (Qiagen) per manufacturer instructions. RNA concentration and purity were verified by Nanodrop; samples meeting quality criteria were stored at −80°C. Genomic DNA digestion and reverse transcription were performed using QuantiTect Reverse Transcription Kit (Qiagen, 205311) using 1 µg RNA input. qRT-PCR was performed using TaqMan probes (Table 3.2) and TaqMan® Fast Advanced Master Mix (Thermo Fisher Scientific, 4444557). *ACTB* was used as the endogenous control for liver tissues; for skeletal muscle, the geometric mean of *RPLP0* and *B2M* was used after stability verification across conditions. Reactions were run in technical triplicates with five biological replicates per group, including no-amplification controls per probe. Relative expression was calculated by the ΔΔCt method normalized to reference genes and control group.

3.8 Organ-on-chip device fabrication and fluidic characterization

3.8.1 Organ-on-chip device design

To establish the technical basis for future dynamic liver–skeletal muscle co-culture experiments, a first-generation organ-on-chip (OoC) device was designed to connect a liver chamber, a passive diluting–mixing unit, and a skeletal muscle chamber within a single pressure-driven microfluidic circuit (Figure 6.1). The design was guided by the static CM experiments, in which a final 1:50 dilution of liver-derived medium in skeletal muscle differentiation medium was identified as compatible with downstream skeletal muscle exposure. Therefore, the main fluidic requirement of the device was to dilute the liver-derived stream to an approximate liver-medium fraction of 0.02 before entry into the skeletal muscle chamber.

The device was designed using AutoCAD and contained three replicates of the same microfluidic circuit per chip. Each replicate included a liver chamber positioned upstream of a serpentine diluting–mixing region and a downstream skeletal muscle chamber. The liver chamber was designed to host a 3D liver construct, while the skeletal muscle chamber was designed to accommodate a 3D skeletal muscle tissue. The microfluidic layer had a constant channel and chamber height of 100 µm. The liver chamber had a diameter of 3 mm, and the skeletal muscle chamber had a diameter of 8 mm. The liver outlet channel was 10 µm wide, while two skeletal muscle medium channels of 250 µm width merged with the liver outlet stream before entering the serpentine mixing region. The main mixing channel had a width of 510 µm and consisted of repeated upper and lower loops arranged in a serpentine configuration.

Serpentine geometry was selected as a passive mixing strategy to increase the path length and residence time available for diffusion after the convergence of the liver- and muscle-medium streams. This configuration was intended to promote progressive homogenization of the diluted liver-derived stream before the mixture reached the skeletal muscle chamber.

3.8.2 Fabrication and assembly of the microfluidic device

To fabricate the OoC device, a photolithographic master mold was generated on a 5-inch silicon wafer. The wafer was dehydrated at 200°C for 15 min and treated with oxygen plasma for 30 s to improve photoresist adhesion. A SU-8 2010 interlayer was then spin-coated onto the wafer at 500 rpm for 10 s followed by 3000 rpm for 60 s. The wafer was soft-baked at 95°C for 6 min, flood-exposed to UV light at 140 mJ cm^{-2} without a photomask, left to rest for 10 min, and post-exposure baked at 65°C for 1 min and 95°C for 3 min.

The structural layer was fabricated using SU-8 2100. The photoresist was spin-coated twice using a two-step program of 500 rpm followed by 3500 rpm to obtain a final height of approximately 100 µm. The coated wafer was soft-baked at 65°C for 5 min and 95°C for 20 min. The microfluidic pattern was transferred by UV exposure through an acetate photomask at 300 mJ cm^{-2}. After a 10 min resting period, the wafer was baked at 65°C for 5 min and 95°C for 20 min. The wafer was developed in propylene glycol monomethyl ether acetate for 15 min to remove unexposed SU-8, rinsed with isopropanol, and

dried with nitrogen gas. The final mold was silanized in a vacuum chamber for at least 1 h to allow PDMS demolding.

PDMS prepolymer was prepared by mixing base and curing agent at a 10:1 ratio. The mixture was poured over the silicon master, degassed, and cured for 4 h at 65°C. After curing, the PDMS layer was demolded and cleaned before assembly. The final device consisted of three layers: a standard microscope glass slide as the bottom optical layer, the patterned PDMS layer containing the microfluidic channels and chambers, and a PMMA top layer used as the interface for external connectors. The PDMS layer was bonded to the glass substrate by plasma treatment and connected to the PMMA layer using double-sided adhesive tape with a thickness of 170 µm to reduce leakage at the connector interface.

3.8.3 Rhodamine B calibration for fluorescence-based dilution analysis

To enable fluorescence-based visualization and quantification of the liver-medium surrogate, Rhodamine B was used as a fluorescent tracer. A calibration experiment was performed to identify a working concentration within the linear fluorescence range, avoiding signal saturation and self-quenching. Rhodamine B solutions were prepared in Milli-Q water at concentrations ranging from 4×10^{-4} to 4 mg mL^{-1} and transferred to a 96-well plate. Calibration samples were imaged by fluorescence microscopy using identical acquisition settings. Images were analyzed in Fiji/ImageJ [189] by measuring the average pixel intensity in each well. Fluorescence intensity values were plotted as a function of Rhodamine B concentration to identify the concentration range in which intensity remained proportional to concentration. Based on this calibration, a final working concentration of 6×10^{-3} mg mL^{-1} Rhodamine B in Milli-Q water was selected for the fluidic characterization experiments.

3.8.4 Pressure-driven flow setup

To characterize the fluidic behavior of the device, the chip was connected to a pressure-driven flow system. Milli-Q water was used as a substitute for skeletal muscle medium, and Rhodamine B diluted in Milli-Q water was used as a fluorescent surrogate for liver-derived medium. This configuration allowed the liver-derived stream to be visualized after merging with the non-fluorescent muscle-medium surrogate.

The skeletal muscle medium inlet was maintained at a fixed pressure during the characterization experiments, while the pressure applied to the liver inlet was varied across the tested conditions. Liver inlet pressures ranging from 150 to 500 mbar were explored across the experimental series. For each pressure condition, fluorescence microscopy images were acquired at defined locations along the device, including the initial merging region, positions along the serpentine mixing unit, the final location immediately before the skeletal muscle chamber, and the liver and skeletal muscle chambers used for dilution analysis. Fluorescence images were acquired using a 10X microscope objective. Acquisition settings were kept constant within each experimental series to allow comparison between locations and pressure conditions. Images were exported for subsequent quantification in Fiji/ImageJ [189] and custom Python scripts.

3.8.5 Mixing efficiency analysis

To quantify mixing efficiency along the serpentine region, fluorescence intensity profiles were extracted across the channel width at defined locations after the convergence of the liver- and muscle-medium surrogate streams. For each location, a cross-sectional line was drawn perpendicular to the direction of flow, and fluorescence intensity was plotted as a function of channel width. The intensity profiles were fitted using Gaussian functions. The standard deviation obtained from each Gaussian fit was used as an indicator of profile broadening across the channel. Mixing efficiency was then calculated using a mixing index, γ, according to the following equation:

$$\gamma = 1 - \frac{\sigma_{min}}{\sigma} \tag{3.1}$$

Where γ is the mixing index, σ_{min} is the standard deviation of the unmixed reference profile, and σ is the standard deviation of the fluorescence profile at a given downstream location. Mixing-index values were plotted as a function of position along the serpentine channel for each liver inlet pressure condition.

3.8.6 Dilution analysis

To determine whether the device reproduced the 1:50 dilution required for skeletal muscle exposure, fluorescence intensity was compared between the liver chamber and the skeletal muscle chamber under different liver inlet pressure conditions. Because Rhodamine B was used within a concentration range where fluorescence intensity was approximately proportional to concentration, the fluorescence signal was used as a surrogate for Rhodamine B concentration and, therefore, for the relative contribution of the liver-medium surrogate to the final mixture.

Regions of interest were defined in the liver and skeletal muscle chambers using Fiji/ImageJ [189]. Mean fluorescence intensity was extracted from each region of interest, and the decrease in fluorescence signal between the liver chamber and skeletal muscle chamber was used to estimate dilution performance. The target dilution corresponded to a liver-medium fraction of 0.02, equivalent to the 1:50 dilution previously optimized in static skeletal muscle CM experiments. Dilution values were plotted against liver inlet pressure to identify the operating conditions closest to this target.

3.9 Statistical analysis

All statistical analyses and graphing were performed in GraphPad Prism 10 (GraphPad Software, San Diego, CA, USA). Normality was assessed using Shapiro–Wilk. Outliers were identified using the ROUT method (Q = 1%) and excluded when justified. For normally distributed datasets, multi-group comparisons were performed by one-way ANOVA with Tukey's or Dunnett's post hoc tests as appropriate. For non-normal datasets, data were transformed when suitable; otherwise, Kruskal–Wallis

with Dunn's multiple comparisons was used. Data are presented as mean ± SEM unless stated otherwise. Biological replicate numbers are reported in figure legends (technical replicates indicated per assay). Significance was set at $p < 0.05$, with exact p-values and test details reported in text or figure legends.

3.10 Reagents, probes, and gene expression assays

3.10.1 Antibodies and cellular probes

Table 3.1. Antibodies and cellular probes employed throughout experimental work.

Antibody or probe	Target	Supplier data	Dilution
Rabbit anti-Dystrophin IgG antibody	Dystrophin	ab15277, Abcam	1:200
Anti-LC3B antibody from rabbit	LC3B	ab51520, Abcam	
Albumin Polyclonal Antibody from rabbit	Albumin (ALB)	PA5-85166, Invitrogen	1:200
Anti-Vimentin Antibody from mouse	Vimentin	V2258, Sigma-Aldrich	1:200
Anti-Vimentin Antibody from mouse	Vimentin	MAB1681, Sigma-Aldrich	1:200
Anti-α-Smooth Muscle Actin Antibody from mouse	ACTA2	A2547, Sigma-Aldrich	1:200
Anti-ACTN2 Antibody from mouse	ACTN2	A7811, Sigma-Aldrich	1:200
Alexa Fluor 594 Phalloidin	F-actin	A12381, Invitrogen	1:400
Rhodamine-Phalloidin	F-actin	R415, Invitrogen	1:400
Donkey anti-rabbit IgG (H+L), Alexa Fluor 647	Rabbit IgG (secondary)	A31573, Invitrogen	1:200
Goat anti-rabbit IgG (H+L), Alexa Fluor 568	Rabbit IgG (secondary)	A-11036, Invitrogen	1:200

Alexa Fluor 488 goat anti-rabbit IgG (H+L), highly cross-adsorbed	Rabbit IgG (secondary)	A-11034, Invitrogen	1:200
Goat anti-mouse IgG (H+L), Alexa Fluor Plus 647, highly cross-adsorbed	Mouse IgG (secondary)	A32728, Invitrogen	1:200
Goat anti-mouse IgG (H+L), Alexa Fluor Plus 647, highly cross-adsorbed	Mouse IgG (secondary)	A32728, Invitrogen	1:200
Goat anti-mouse IgG (H+L), Alexa Fluor Plus 647, highly cross-adsorbed	Mouse IgG (secondary)	A32728, Invitrogen	1:200
Alexa Fluor 488 goat anti-mouse IgG	Mouse IgG (secondary)	A-11001, Invitrogen	1:200

3.10.2 Gene expression assays

Table 3.2. Reagents for gene expression experiments.

Gene name (aliases)	TaqMan assay ID	Supplier
***ALB* (Albumin)**	Hs00609411_m1, FAM	Thermo Fisher Scientific
***CPS1* (Carbamoyl-phosphate synthase 1)**	Hs00157048_m1, FAM	Thermo Fisher Scientific
***OTC* (Ornithine transcarbamylase)**	Hs00166892_m1, FAM	Thermo Fisher Scientific
***ACTB* (β-actin)**	Hs01060665_g1, FAM	Thermo Fisher Scientific
***HNF4A* (Hepatocyte nuclear factor 4 alpha)**	Hs00230853_m1, FAM	Thermo Fisher Scientific
***CYP3A4* (Cytochrome P450 family 3 subfamily A member 4)**	Hs00604506_m1, FAM	Thermo Fisher Scientific
***COL13A1* (Collagen type XIII alpha 1 chain)**	Hs01103890_m1, FAM	Thermo Fisher Scientific
***MYOG* (Myogenin)**	Hs01072232_m1, FAM	Thermo Fisher Scientific
***MYF5* (Myogenic factor 5)**	Hs00271574_m1, FAM	Thermo Fisher Scientific
***MYF6* (Myogenic factor 6, MRF4)**	Hs00231165_m1, FAM	Thermo Fisher Scientific
***MYH7* (Myosin heavy chain 7, β-MHC)**	Hs01110632_m1, FAM	Thermo Fisher Scientific
***MYOD1* (Myogenic differentiation 1)**	Hs00159528_m1, FAM	Thermo Fisher Scientific

TRIM63 **(Tripartite motif containing 63, MuRF1)**	Hs00822397_m1, FAM	Thermo Fisher Scientific
FBXO32 **(F-box protein 32, Atrogin-1)**	Hs01041408_m1, FAM	Thermo Fisher Scientific
GAPDH **(Glyceraldehyde-3-phosphate dehydrogenase)**	Hs02786624_g1, VIC	Thermo Fisher Scientific
B2M **(Beta-2-microglobulin)**	Hs00187842_m1, VIC	Thermo Fisher Scientific
RPLP0 **(Ribosomal protein lateral stalk subunit P0, also known as 36B4)**	Hs00420895_gH, VIC	Thermo Fisher Scientific

Chapter 4 | Bioengineered Liver Module

4.1 Chapter rationale and modeling framework

The MASLD field has advanced through the combined use of clinical studies, animal models, conventional *in vitro* systems, and emerging organ-on-chip technologies. Each of these strategies contributes distinct information. While clinical studies define disease phenotypes and therapeutic endpoints in patients, animal models provide access to systemic physiology and time-resolved tissue analysis. More recently, *in vitro* models allow finely controlled interrogation of cellular mechanisms and microphysiological systems offer a route toward dynamic, human-relevant multi-organ modeling. However, none of these approaches alone fully addresses the experimental needs of this thesis. Clinical and animal studies capture systemic complexity but provide limited control over individual organ contributions, whereas reductionist *in vitro* systems often lack the three-dimensional architecture, multicellular interactions, extracellular matrix context, and modularity required to model progressive MASLD and its downstream extrahepatic effects.

In this context, the development of a modular human *in vitro* platform based on three-dimensional liver constructs is particularly valuable. By combining metabolically competent hepatocyte-like cells with HSCs in a collagen-based microenvironment, the liver module developed in this chapter is designed to recapitulate key features of MASLD progression, including steatosis, lipotoxic stress, inflammatory activation, hepatocellular injury, and early fibrogenic remodeling. Importantly, the model is conceived as the hepatic component of a broader modular strategy to study liver–skeletal muscle crosstalk. The stage-specific CM generated by these liver constructs provide integrated hepatic signals that can be later transferred to functional three-dimensional skeletal muscle tissues, while the same modular logic establishes the basis for future integration into a dynamic organ-on-chip framework.

4.2 Aims and scope

The introductory section of this chapter does not repeat the biological background of MASLD presented in Chapter 1. Instead, it focuses on the practical experimental strategies currently used to study MASLD and MASH, with emphasis on their respective strengths and limitations as modeling platforms. For this reason, the following sections are organized around four major approaches: clinical studies, animal models, *in vitro* models, and organ-on-chip systems. This structure is intended to identify the methodological gap that motivates the experimental work presented in this chapter, which is the lack of

a human-relevant, mechanistically controlled, three-dimensional, and modular liver model that can reproduce defined features of MASLD progression while remaining compatible with downstream liver–muscle communication studies.

Accordingly, the aim of this chapter is to present, characterize, and validate a three-dimensional human liver model capable of generating stage-specific MASLD-like phenotypes under controlled *in vitro* conditions. The chapter first situates this model within the broader landscape of MASLD modeling strategies, then describes the experimental development of the liver construct, the preparation of lipotoxic and inflammatory stimuli, and the assessment of disease-relevant endpoints including lipid accumulation, hepatocellular dysfunction and injury, inflammatory mediator release, hepatic stellate cell activation, and extracellular matrix remodeling. Together, these elements establish the liver module as the first experimental component of the modular liver–skeletal muscle platform developed in this thesis.

4.3 Introduction: Preclinical Modelling Strategies for Metabolic Dysfunction-Associated Steatotic Liver Disease

4.3.1 Clinical Studies

Clinical studies are golds standards to define the phenotypes of a disease and for validating therapeutic targets. In MASLD, they employ observational cohorts, prospective studies, and randomized controlled trials (RCTs) designed to study disease burden, identify prognostic factors, and test potential interventions. Large epidemiological cohorts and registry-based studies define prevalence, incidence, and mortality, while biopsy-based cohorts allow matching of histological features to clinical outcomes and validation of non-invasive diagnostic tools. Interventional trials—like pharmacological and lifestyle RCTs—assess effects on histological endpoints, non-invasive biomarkers, and clinical outcomes such as regression, transplantation, and mortality. For the scope of this thesis work, relevant outputs from MASLD clinical research include testing of potential interventions, biomarker identification, stratification features that correlate with disease severity, and identification of fibrosis stages as the primary histological predictor of liver-related outcomes.

The very recent MAESTRO-NASH and ESSENCE trials exemplify how late-phase MASLD-MASH trials are now designed and what they aim to deliver. In MAESTRO-NASH, adults with biopsy-confirmed MASH and F1b–F3 fibrosis were randomized to once-daily resmetirom or placebo. After 52 weeks, resmetirom achieved resolution of steatohepatitis without fibrosis worsening (26–30% vs 10% with placebo) and ≥1-stage fibrosis improvement without worsening of necro inflammatory activity (24–26% vs 14% with placebo). It also showed meaningful reductions in LDL-cholesterol, which led to the first drug approval specific to MASH [193]. The ongoing phase 3 ESSENCE trial tests a GLP-1 receptor agonist strategy in patients with biopsy-proven MASH and F2–F3 fibrosis, randomizing them to once-weekly semaglutide 2.4 mg or placebo, with primary endpoints of MASH resolution and fibrosis improvement assessed on repeat biopsy after 72 weeks of treatment [194]. Together, these studies

illustrate how MASLD-MASH drug development integrates biopsy-based histological endpoints, weight loss, lipid lowering, and long-term outcome modeling to move from mechanism to tangible clinical benefit for a population that previously had no approved pharmacotherapy.

Clinical studies provide direct evidence in the target species, capturing the full complexity of human physiology, including multi-organ crosstalk, microbiome effects, and comorbidity patterns. They enable long-term follow-up over years or even decades, allowing quantification of progression rates, and evaluation of interventions on clinically meaningful hard endpoints that cannot be modeled faithfully in animals or *in vitro*. Large-scale cohorts can include thousands of patients across diverse ethnicities and healthcare systems, enabling the study of sub-phenotypes such as lean MASLD or sarcopenic MASLD. Nevertheless, clinical studies are time-consuming and costly, often requiring years to recruit, take biopsies, treat, and follow patients to capture histological change or clinical events, which delays feedback to basic research and drug development. The reliance on liver biopsy for definitive diagnosis and trial endpoints leads to high screen failure rates, limits inclusion of patients unwilling or unable to undergo biopsy and introduces sampling and inter-reader variability that can dilute treatment effects. Moreover, clinical studies are largely correlative, and they are not suited to dissecting molecular pathways or testing causal roles of individual genes or molecular circuits in isolation. Furthermore, even clinical trials are not designed to account for some extrahepatic outcomes.

4.3.2 Animal Models

Animal models, primarily in rodents, aim to reproduce selected aspects of human MASLD through genetic manipulation, dietary interventions, or with toxins, thereby enabling controlled interrogation of disease mechanisms and preclinical testing of candidate therapies. These models are used to study the sequence from steatosis to steatohepatitis, fibrosis, and sometimes hepatocarcinogenesis, as well as to evaluate systemic metabolic perturbations and multi-organ interactions under experimental conditions that are not feasible in humans.

Dietary excess models like high-fat (HFD), high-fat–high-fructose (HFHF), and high-cholesterol (HCD) allow the replication of obesity, insulin resistance, and dyslipidemia, whereas nutrient-deficient (methionine–choline-deficient) and toxin-augmented models (commonly CCl_4) are used to accelerate inflammation and fibrosis. Genetic models with a deficiency or gene knockout (for instance leptin- or leptin-receptor–deficient mice, or strains with altered lipid metabolism) help study the contribution of specific pathways to steatosis and steatohepatitis [195,196].

Animal studies provide access to whole organs and tissues for detailed histological, transcriptomic, proteomic, and metabolomic analyses across disease stages, enabling mechanistic links between cellular pathways and histological or biochemical phenotypes. They have been instrumental in defining the roles of TLR4-mediated innate immune activation, ER stress, mitochondrial dysfunction, lipotoxic species, and hepatic stellate cell activation in MASH pathogenesis, and in testing pharmacological modulation of these pathways *in vivo* [197]. Since animals can be sacrificed at predefined time points,

investigators construct time-resolved trajectories of steatosis, inflammation, and fibrosis that are difficult to obtain from human clinical biopsies. Animal models also allow systematic evaluation of lifestyle interventions—mainly diet and exercise— along with dose–response and drug interaction studies, under rigorously controlled environmental conditions.

Relative to clinical trials, rodent studies are faster and less expensive, compressing decades of human disease into months while still capturing milestones such as steatohepatitis and bridging fibrosis. They enable invasive sampling and organ harvesting that would be impossible or unethical in humans. From a scope perspective, animals can be bred or engineered to carry specific mutations or reporter constructs, allowing precise testing of gene responses and enabling cell lineage tracing, *in vivo* imaging, and functional genomics screens. The ability to standardize diet and housing conditions reduces environmental noise and increases statistical power for detecting mechanistic effects.

Despite the advantages, no current animal model fully recapitulates the human MASLD phenotype, especially the combination of metabolic syndrome, heterogeneous histological patterns, and long-term cardiovascular and malignant outcomes. Nutrient-deficient models such as MCD diets rapidly induce severe steatohepatitis and fibrosis but paradoxically cause weight loss and improved insulin sensitivity, which is opposite to the typical human MASLD phenotype. Diet-induced models reproduce obesity and insulin resistance but often develop only mild fibrosis even after prolonged feeding and show resistance to hepatocellular ballooning and advanced necroinflammation [197–199]. Behind these observations lay numerous species differences in lipoprotein handling, bile acid composition, immune system, and xenobiotic metabolism, which frequently yield drugs that show efficacy in rodents but fail in human trials. Finally, maintaining large cohorts of specialized mice on complex diets in barrier facilities is costly, and the ethical imperative to reduce animal use (3R principle) motivates the development of complementary human-based experimental systems.

4.3.3 *In vitro* Models

Liver models *in vitro* provide a controllable, scalable platform for mechanistic dissection and drug screening, complementing data from *in vivo* experiments and enabling high-content measurements even at single-cell resolution. They range from simple 2D monocultures of liver cell types to 3D spheroids or organoids. More sophisticated liver-on-chip systems that incorporate flow, zonation, and multi-organ interactions are also included in these approaches *in vitro*.

4.3.3.1 2D in vitro models

2D models in MASLD typically consist of hepatocyte cell lines (commonly HepG2 and Huh7), differentiated human hepatic cell lines (notably HepaRG), or primary hepatocytes cultured as monolayers on rigid plastic or coated surfaces that enhance cell adhesion [200–202]. They are sometimes in co-culture with non-parenchymal cells such as macrophages using membrane separation

systems. Steatosis is induced by exposure to free fatty acid mixtures—often PA and OA—, high glucose, lipogenic media, or methionine–choline-deficient conditions.

2D systems are inexpensive, technically straightforward, and readily miniaturized into 96-/384-well formats, making them well suited to high-throughput screening of large compound libraries. They allow precise control of extracellular conditions, with chemically defined media and culture substrate stiffness among the most relevant, and enable easy imaging, biochemical assays, and omics readouts. However, primary human hepatocytes rapidly dedifferentiate in 2D, losing key functions such as CYP450 activity and albumin secretion within days, while immortalized cell lines display cancer-like metabolic wiring especially glycolytic bias and altered urea cycle that diverges from healthy hepatocytes *in vivo* [200,203]. Often overlooked, the stiffness of tissue-culture plastic lies in the realm of GPa, while the soft healthy liver microenvironment is around 2–12 kPa. This consistently activates HSCs and fails to model mechanotransduction in MASLD progression [204,205]. Moreover, classical 2D monocultures lack spatial gradients, native-like intercellular interactions, and the full set of non-parenchymal cells, limiting their capacity to recapitulate complex liver architecture and MASLD features such as zonated lipotoxicity, multicellular inflammatory loops, and ECM remodeling.

4.3.3.2 3D in vitro models

Unlike their conventional monolayer counterparts, 3D liver models include spheroids and organoids formed by self-aggregated hepatocytes often co-cultured with HSCs, ECs, and macrophages, as well as scaffold-based constructs in natural or synthetic hydrogels based on collagen, gelatin, and alginate matrices that provide a tunable ECM. Human induced pluripotent stem cells (iPSCs) liver organoids and multi-lineage spheroids are increasingly used to model chronic liver injury, fibrosis, and genetic susceptibility to MASLD.

In this configuration, 3D architecture improves intercellular and cell–matrix interactions of biochemical and physical nature, promoting more stable hepatocyte polarization, grouping for bile canaliculi formation, and long-term maintenance of metabolic and synthetic functions compared with 2D monolayers [204,206]. Hydrogels can be engineered to match physiological or fibrotic liver stiffness, allowing experimental interrogation of mechanosensitive pathways during fibrosis progression [205]. Multiple cell types can also be incorporated into 3D systems. Besides hepatocytes, HSCs, Kupffer cells, and LECs help better recapitulate the inflammatory and fibrogenic crosstalk characteristic of MASH and support more physiologically relevant responses to candidate drugs.

Despite their many benefits, 3D models demand technical expertise in biology, tissue engineering and biomaterial science to establish and standardize. Spatially, diffusion limitations are common issues that can lead to hypoxic or necrotic cores in large constructs, which complicate phenotype characterization. As significantly more cell numbers are needed to fabricate these constructs, imaging and high-content analysis are more challenging than in 2D. In organoids and hydrogel-based systems, batch-to-batch variability originated during differentiation periods or due to hydrogel composition can affect

reproducibility and throughput. Additionally, many 3D models still lack full representation of the complex sinusoidal niche and extrahepatic organ interactions that shape MASLD pathophysiology *in vivo*.

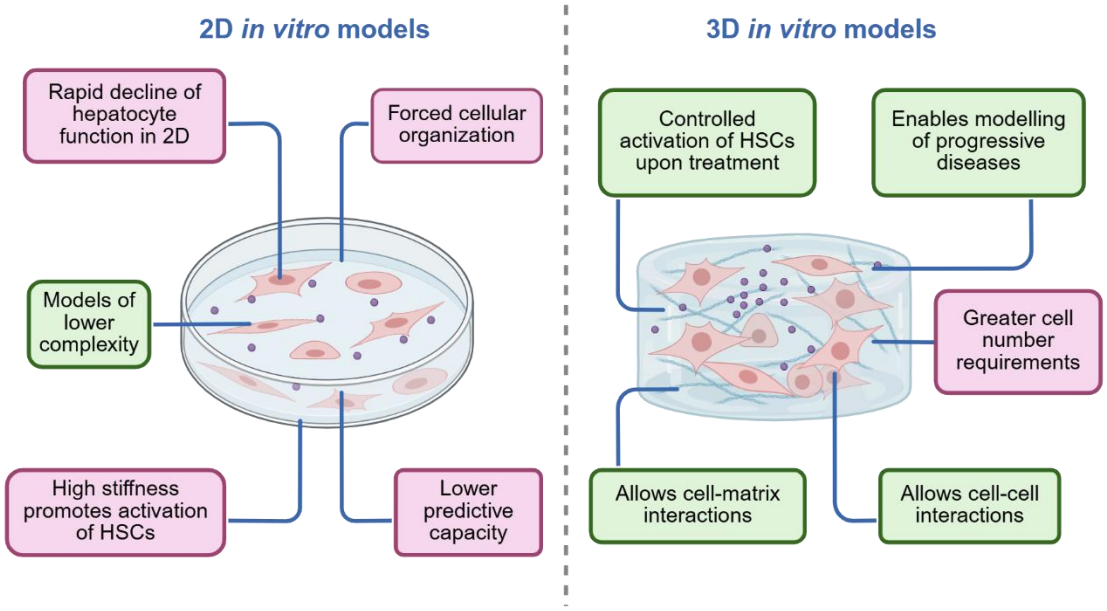


Figure 4.1. Comparison of two-dimensional and three-dimensional *in vitro* strategies for MASLD modeling. Schematic summary of the main advantages and limitations of 2D and 3D *in vitro* liver models used to study MASLD progression. Conventional 2D cultures provide lower-complexity and experimentally accessible systems, but they are limited by rapid decline of hepatocyte function, forced cellular organization, non-physiological substrate stiffness that can promote hepatic stellate cell activation, and reduced predictive capacity. In contrast, 3D *in vitro* models better support cell–cell and cell–matrix interactions, allow controlled activation of HSCs upon treatment, and enable modeling of progressive disease phenotypes. However, these systems require higher cell numbers and greater technical complexity than 2D cultures. Created in BioRender. (2026). https://BioRender.com/3w9jpp1

4.3.3.3 Organ-on-chip models

Liver-on-chip and related microphysiological systems (MPS) incorporate liver cells in microfluidic devices under perfusion, often in layered or compartmentalized settings that try to reproduce structural features of the liver, including oxygen and nutrient gradients. These platforms range from liver-only chips focusing on steatosis or fibrosis to interconnected multi-organ systems like gut–liver or adipose–liver chips that model inter-organ crosstalk in MASLD [207,208].

Relevant examples include devices that generate hepatic zonation using gradient generators or dual-channel flows, multi-channel systems with co-cultured hepatocytes, stellate cells, Kupffer cells, and endothelial cells to model steatohepatitis, and microphysiological platforms such as Liver-Chip® by Emulate Inc. and OrganoPlate LiverTox™ by Mimetas for high-content toxicity and disease studies. Recent integrated gut–liver-on-chip platforms have successfully recapitulated FFA-induced MASLD initiation and progression, highlighting the contribution of the gut [209–212].

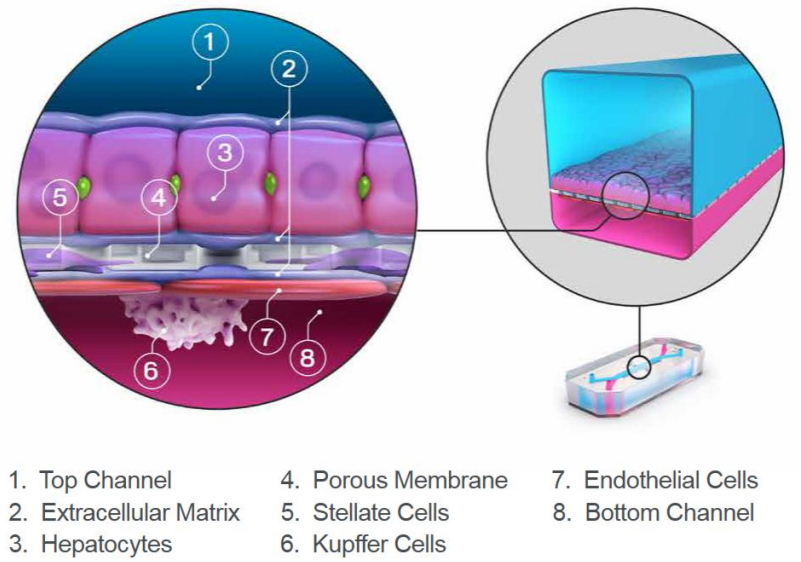


Figure 4.2. Representative architecture of a commercial liver-on-chip platform.
Liver-Chip developed by Emulate Inc., showing a two-channel microfluidic configuration separated by a porous membrane. The upper parenchymal channel contains species-specific hepatocytes embedded within an extracellular matrix and co-cultured with HSCs and KCs, while the lower vascular channel is lined with liver sinusoidal ECs. This compartmentalized architecture enables controlled perfusion, parenchymal–vascular communication, and multicellular modeling of liver physiology and disease-relevant responses. Adapted from the Emulate Liver-Chip Technical Note, July 2020.

Organ-on-chip (OoC) models maintain liver-specific functions for extended periods under dynamic flow, support zonation, and allow real-time monitoring of oxygen consumption, metabolic fluxes, and secreted cytokines, thereby providing a highly human-relevant environment to study MASLD pathophysiology and drug responses [208]. They can also reproduce steatosis, lipotoxic cell death, inflammatory cytokine secretion, stellate cell activation, and fibrogenesis. Moreover, they have been successfully used to evaluate candidate therapeutics such as pioglitazone, obeticholic acid, elafibranor, and others in a human context [213–215]. Commercial organ-on-chip providers now offer standardized liver-on-chip systems and services specifically designed towards MASLD drug discovery, which facilitates broader adoption in preclinical pipelines.

Despite their promising performance, liver-on-chip systems are relatively low-throughput compared with simple 2D assays, require bulky, specialized microfluidic equipment and expertise, and remain expensive on a sample basis, limiting their use for compound screening. Commonly used device materials are being constantly improved to date due to small molecule absorption or permeability—with PDMS as the hallmark example—, which can potentially confound pharmacokinetics and dose–response relationships. Since research laboratories specialized in OoC tend to develop each their own approach, standardization across field is still limited, and there is no consensus yet on which readouts or configurations will best predict clinical efficacy in MASLD. This author thinks these models currently complement rather than replace traditional animal studies and clinical trials.

4.4 Results

4.4.1 Strategy for model induction

4.4.1.1 2D Optimization

To ensure a robust transition into a three-dimensional environment, it was first necessary to calibrate the lipotoxic stimulus in a controlled 2D setting, using hepatocyte-like cells only. We selected the HepaRG cell line as our parenchymal foundation because, unlike other immortalized lines, they retain a highly differentiated human hepatocyte-like phenotype and demonstrate a well-documented responsiveness to both metabolic and inflammatory stressors [200].

Our initial engineering goal was to identify a concentration of NEFAs that could reliably induce steatosis without triggering immediate cell death. NEFAs were prepared at three increasing concentrations and diluted in SFM. HepaRG cells were cultured in 2D at equal cell density of 5.0×10^4 cells cm^{-2} and maintained in hepatocyte growth medium (HGM) for 24 hours. After the adaptation time, the medium was replaced with SFM for additional 24 hours before lipid challenge. This strategy was chosen to make HepaRG preserve the differentiated hepatocyte-like features over proliferation. Since the NEFAs formulation contains albumin protein as a lipid carrier, this serum-free approach is ideal to account for the effect of albumin and consider it a true, absolute, and vehicle control. The lipid challenge was initiated by incubating HepaRG in 2D in increasing concentrations of the 2:1 PA/OA NEFAs mix —namely 40 µM, 100 µM, and 400 µM— for 24, 48 or 72 hours (Figure 4.3).

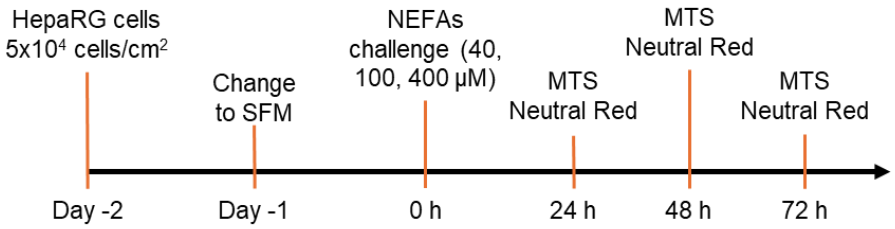


Figure 4.3. Experimental timeline for the characterization of steatosis in response to lipid load.
Three concentrations of 2:1 PA/OA NEFAs mix were used: 40, 100, 400 µM.

Metabolic Response and Lysosomal Activity

We monitored metabolic activity/viability and lysosomal activity by MTS and Neutral Red assays. Hepatocytes under high lipid load exhibit high metabolism that in sustained regimes becomes a driver of damage. Lysosome homeostasis is impaired in steatosis and progression to MASH.

In the MTS assay, metabolically active cells reduce the MTS tetrazolium salt into a colored formazan product, making the Abs_{490} signal directly proportional to the metabolic activity of the live cell sample.

Neutral Red assay, on the other hand, employs a cationic dye that penetrates cells and accumulates in lysosomes of viable cells, making Abs_{540} directly proportional to lysosomal activity of viable cells.

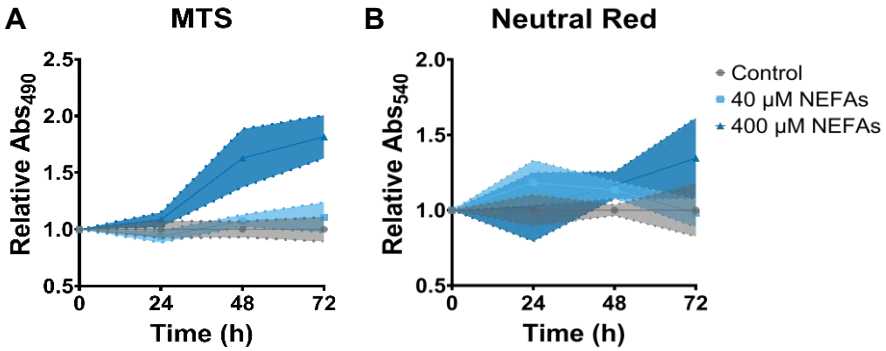


Figure 4.4. Validation of lipid internalization by HepaRG cells in 2D culture.
A) Metabolic activity measured by MTS assay at 24, 48, and 72 h following exposure to NEFAs (n=3). B) Lysosomal activity assessed by Neutral Red assay at 24, 48, and 72 h after NEFAs treatment (n=3).

The exposure to increasing NEFAs concentrations (PA/OA 2:1, 40 µM, 100 µM, and 400 µM) elicited a time- and dose-dependent increase in metabolic activity. Interestingly, the two lowest concentrations did not trigger significant changes in metabolism or lysosomal activity. However, at 400 µM NEFAs, we observed an 81% increase in MTS signal (p=0.03) and a 34.6% increase in Neutral Red uptake from 24 h to 72 h. Even though the trend of Neutral Red uptake was clear, it did not reach statistical significance (Figure 4.4).

Lipid Internalization

MASLD starts with the onset of hepatic steatosis, defined as the excess lipid accumulation in hepatocytes, inside structures called lipid droplets (LDs). After the lipid challenge, HepaRG samples in 2D were fixed and stained with Oil Red O dye, a common stain in hepatology for the observation of LDs in histology samples.

The metabolic surge we observed after the treatment with the highest concentration of NEFAs (400 µM) corresponded with histological lipid accumulation. While lower dose of NEFAs (40 µM) was histologically indistinguishable from vehicle controls, the 400 µM treatment yielded robust lipid droplet formation, as visualized by Oil Red O staining. The middle concentration (100 µM) yielded low lipid accumulation, far from the robust overload observed in clinical diagnosis criteria of hepatic steatosis. Moreover, some replicate experiments failed to demonstrate consistent observations for this moderate concentration (Figure 4.5).

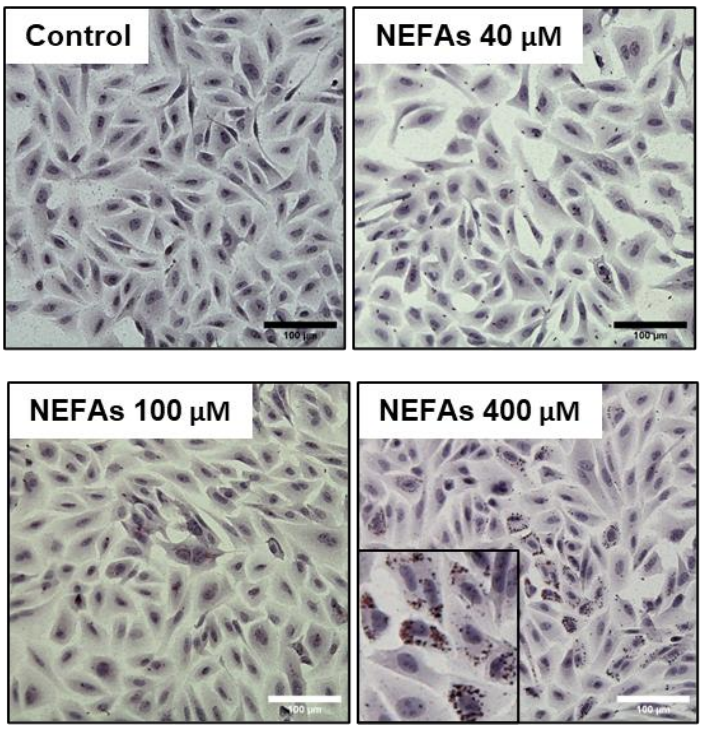


Figure 4.5. Histological validation of lipid internalization by HepaRG cells in 2D culture.
Representative brightfield images showing intracellular lipid droplets in HepaRG cells stained with Oil Red O and counterstained with Harris-modified hematoxylin. Scale bar = 100 µm.

These observations in 2D HepaRG cells established that at least 72 hours incubation under 400 µM NEFAs were required to drive a steatotic phenotype, providing the baseline for the more complex 3D constructs.

4.4.2 Fabrication of 3D Liver Constructs and Structural Stability

Transitioning to 3D allowed us to incorporate the multicellular crosstalk essential for modelling disease progression. To better capture the nuances of MASLD, we chose to use co-culture models in 3D. This way, liver parenchymal cells were encapsulated in presence of HSCs, key drivers of disease progression that react to a variety of cues from damaged hepatocytes [117]. We encapsulated HepaRG and LX-2— a human hepatic stellate cell line— at a 2:1 ratio within a methacrylated collagen type I-based hydrogel. This proportion ensures sufficient hepatocyte number while providing enough stellate cells to model the inflammatory and fibrotic hallmarks of MASH.

The experimental timeline was designed to encapsulate cell mix in HGM, followed by an adaptation period in SFM. After allowing cells to adapt, steatosis was induced in the 3D constructs. Then, we stimulated HSCs with LPS to induce activated phenotype along with its characteristic signaling. Unlike HepaRG in 2D, HepaRG in 3D needed longer exposure to the NEFAs 400 µM formulation to achieve distinguishable differences in lipid internalization. Therefore, incubation under high lipid regime was

extended to 96 hours (4 days). Next, HSC stimulation with LPS was carried out by renewing media containing NEFAs 400 µM and adding LPS 0.1 µg mL^{-1}. The timeline for 3D constructs is described in Figure 4.6.

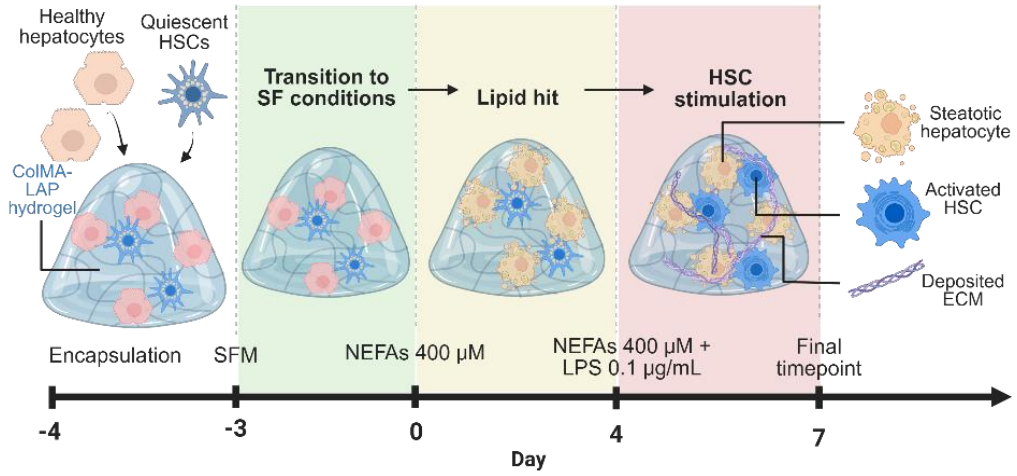


Figure 4.6. Fabrication and disease-induction timeline of the 3D MASLD/MASH liver model.
Schematic representation of the experimental workflow used to generate 3D liver constructs and induce progressive MASLD-like phenotypes *in vitro*. HepaRG and LX-2 cells were co-encapsulated in a collagen methacrylate/LAP hydrogel and maintained in hepatocyte growth conditions before transition to SFM. After adaptation, constructs were exposed to 400 µM NEFAs to induce a steatotic lipid hit. At day 4, selected constructs were further stimulated with 400 µM NEFAs plus 0.1 µg/mL LPS to promote inflammatory activation of HSCs and generate a MASH-like phenotype. Final analysis was performed on day 7 to assess lipid accumulation, hepatocellular injury, HSC activation, and extracellular matrix remodeling. Created in BioRender. (2026) https://BioRender.com/gd5e7hk

Structural Integrity

Biomaterial stability is key for 3D tissue constructs, as it supports a variety of biological, biochemical, and physical interactions between encapsulated cells. Size shrinkage can be a sign of the hydrogel components losing structure or undergoing biochemical changes. Since the 3D constructs presented in this work are thought to support many types of readouts at the evaluated timepoints, size and tissue clarity was monitored throughout the experimental timeline. The constructs demonstrated excellent structural stability throughout the 11-day experimental timeline. Brightfield microscopy confirmed a homogeneous cell distribution across the hydrogel matrix, with no evident signs of compaction or degradation (Figure 4.7). Even though some cells escaped the hydrogel matrix 24 hours after fabrication, the whole constructs were transferred to a new culture plate with each change of medium to avoid any contribution of the escaping cells in monolayers to the readouts.

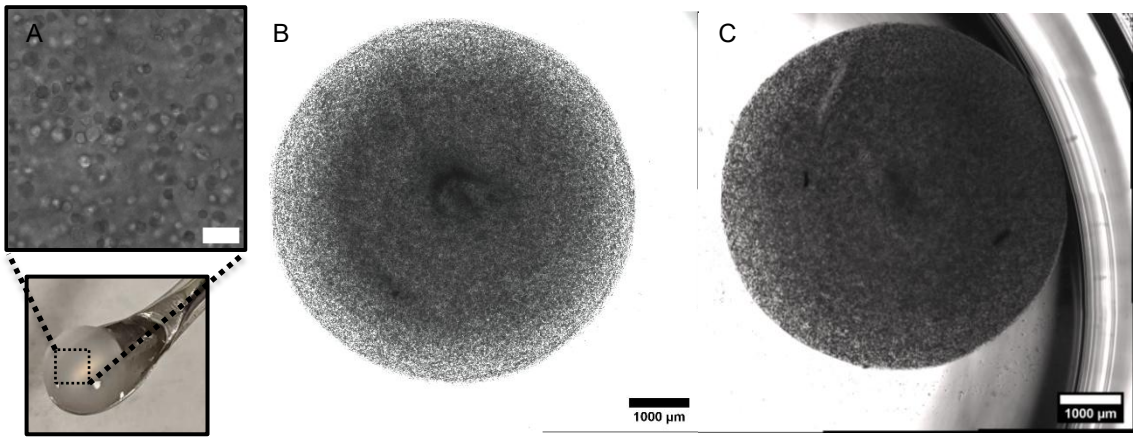


Figure 4.7. Macroscopic appearance of 3D liver constructs at different timepoints, evaluated by brightfield microscopy to assess hydrogel integrity.

A) Representative image of a freshly fabricated construct and its cell distribution. Scale bar = 50 µm. B) Representative image at day 0 (before incubation under high lipid regime). Scale bar = 1000 µm. C) Representative image on day 7 (final timepoint). Scale bar = 1000 µm.

4.4.3 Phenotypic Preservation

A preserved hepatocyte-like phenotype is crucial to replicating steatosis and the metabolic changes elicited by lipid overload. Before initiating disease induction, we confirmed that the 3D environment supported hepatocyte identity. Albumin protein is expressed in hepatocytes and is a common marker of hepatocyte health and differentiated state. Immunofluorescence was performed after the adaptation period in SFM (day 0) and at the end of experiment. Immunofluorescence revealed albumin-positive clusters on day 0 and in control constructs at day 7, demonstrating that the encapsulation process and the hydrogel environment did not impair the cells' differentiated state and albumin synthetic capabilities (Figure 4.8).

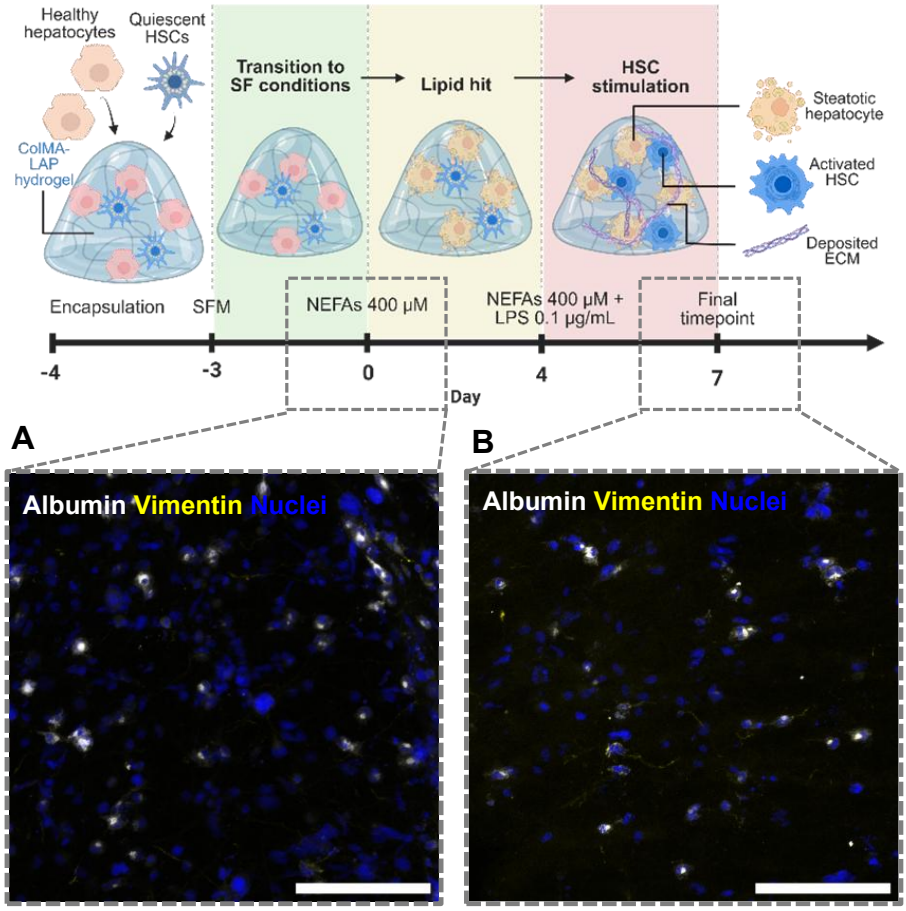


Figure 4.8. Assessment of phenotypic preservation in 3D liver constructs by confocal microscopy. Representative images of albumin-positive hepatocytes and vimentin-expressing HSCs. A) Day 0. B) Day 7. Scale bars = 100 µm. Created with BioRender. (2026). https://BioRender.com/gd5e7hk

4.4.4 Steatosis and The Synergistic Transition to MASH

Under steatosis, excess lipids are compartmentalized in LDs, triggering hepatocyte ballooning. At the final timepoint, brightfield microscopy revealed subcellular structures resembling lipid droplets, which were consistently present in all NEFAs- and NEFAs+LPS-treated constructs. Similar structures were not observed with this microscopy technique in control and LPS-treated groups (Figure 4.9).

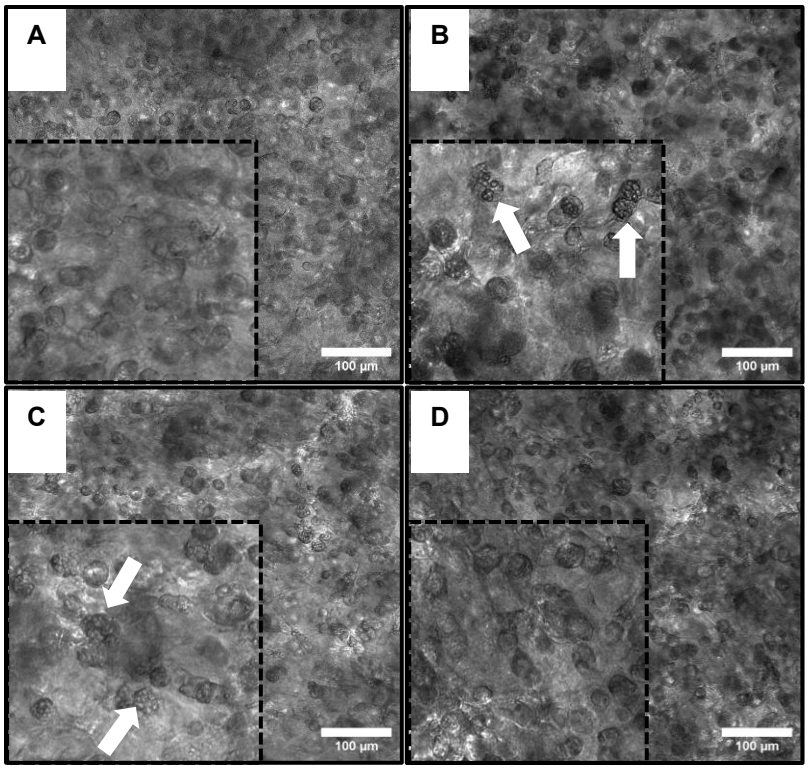


Figure 4.9. First observations of steatosis in 3D liver constructs by brightfield microscopy
Constructs imaged at the final timepoint (day 7). White arrows point at subcellular structures resembling lipid droplets in ballooned hepatocytes. A) Control group. B) NEFAs-treated group. C) NEFAs+LPS co-treated group. D) LPS group. Scale bar = 100 µm.

Moreover, brightfield microscopy revealed large structures resembling apoptotic bodies, especially in the co-treated group. Like LDs and ballooning, structures resembling apoptotic bodies were not observed with this microscopy technique in control and LPS-treated groups (Figure 4.10).

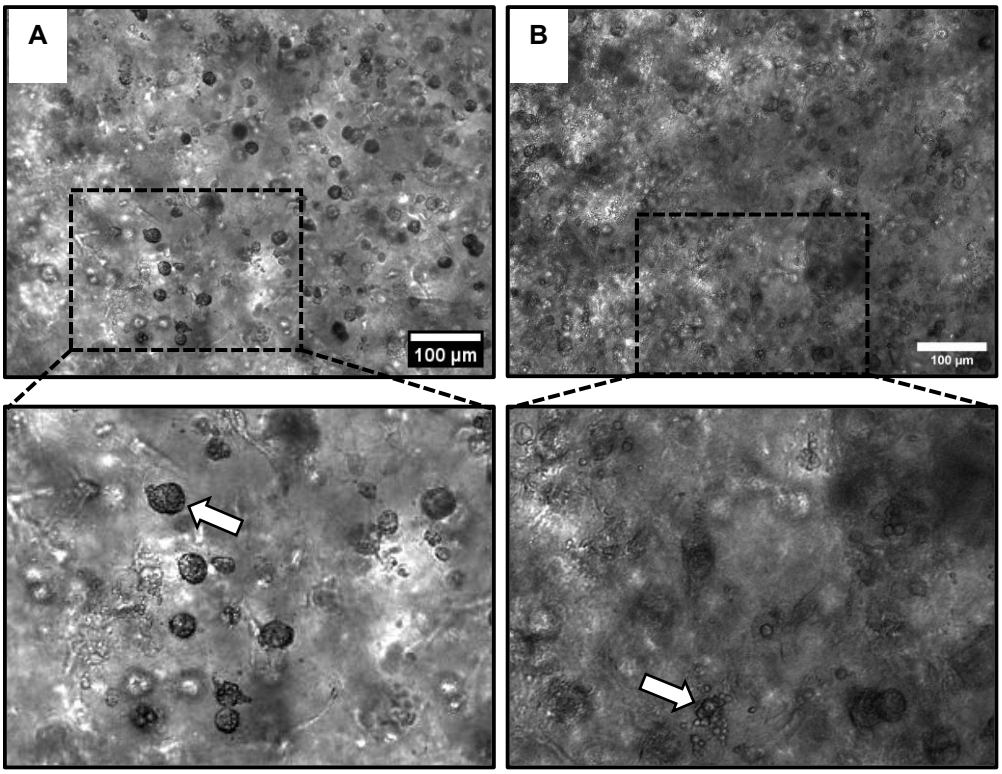


Figure 4.10. Representative brightfield images of structures resembling apoptotic bodies.
Pointed at with white arrows, these structures were found in NEFAs-treated constructs (A) and NEFAs+LPS co-treated constructs (B). Scale bars = 100 µm.

Oil Red O staining was tested on cryosections of 3D liver constructs, as is common in liver histology. Unfortunately, good quality staining was not achieved with these collagen-based hydrogels, as particulate dye precipitates appeared consistently inside cryosections. Alternatively, a fluorescent probe approach was chosen to test image-based quantification of steatosis.

The 3D constructs were imaged at the end of experiment by confocal microscopy to assess the degree of lipid accumulation after the induction of steatosis and stimulation of HSCs. AdipoRed™ stain is Nile Red dye commercially available for staining of neutral lipids in live cell samples. This lipophilic dye partitions into the intracellular fat droplets and is commonly used to assess adipocyte differentiation. Since hepatocytes are fat-storing cells—even in healthy conditions, this dye was employed to detect baseline and abnormal levels of intracellular LDs in the 3D liver constructs. At the final timepoint, live 3D constructs were incubated with diluted dye as per manufacturer instructions, followed by Z-stack confocal acquisition for the 572 nm emission wavelength of Nile Red. Baseline lipid content was observed as expected in the control group as diffuse signal with few defined LDs. In contrast, the constructs treated with NEFAs exhibited brighter and larger LDs in greater number, morphologically similar to the structures initially observed by brightfield microscopy (Figure 4.9). Surprisingly, lipid accumulation in NEFAs+LPS co-treated constructs was consistently exacerbated both in LD number

and size. Finally, the intracellular lipid content of LPS-treated constructs was diffuse like the control group, though bigger droplets were observed compared to the control (Figure 4.11).

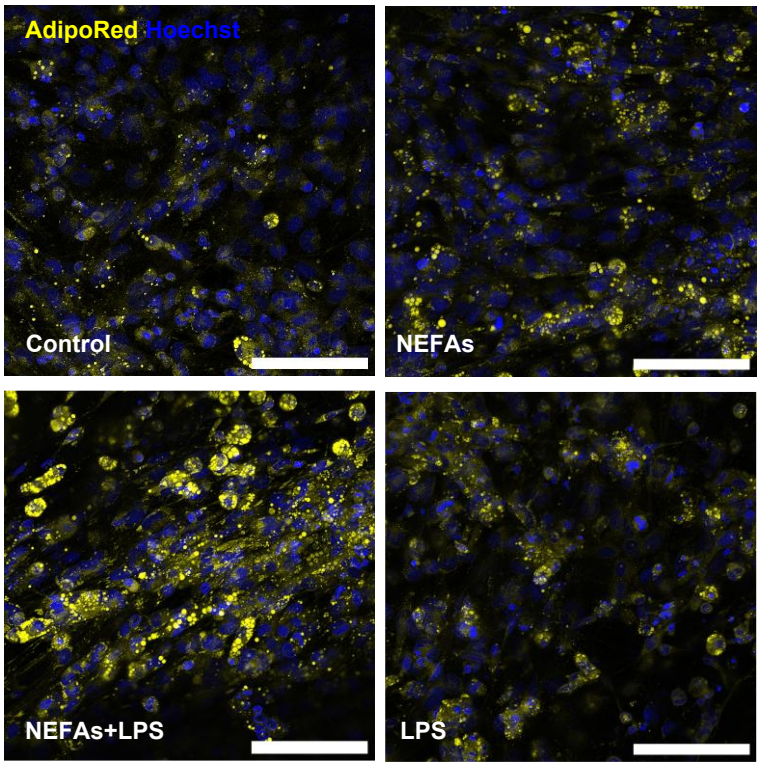


Figure 4.11. Assessment of steatosis in live 3D liver constructs.
Representative confocal Z-projections of live constructs stained with AdipoRed™ at the final timepoint. Nuclei were stained with Hoechst 33342. Scale bar = 100 µm.

Using AdipoRed™ staining and confocal Z-stack analysis, we detected a significant 70.6% increase in mean fluorescence intensity ($p=0.027$) in the NEFAs group, with a massive 479.4% expansion in lipid droplet area ($p=0.01$) compared to controls. Interestingly, while the total area and intensity increased significantly, the droplet count only rose by 63.1% without reaching statistical significance ($p>0.05$). This suggested that the high-lipid challenge only primarily drives the growth and coalescence of existing droplets rather than just creating new ones, a feature that closely mimics the macrovesicular steatosis observed in patients (Figure 4.12).

To model the transition from simple steatosis to the more aggressive MASH, we incorporated an experimental group co-treated with NEFAs 400 µM + LPS 0.1 µg mL^{-1}, on day 4 and stimulate the inflammatory potential of the LX-2 cells. The co-treatment (NEFAs+LPS) triggered a dramatic synergistic response. We observed a 141.7% increase in AdipoRed intensity ($p<0.0001$) and a 118.1% increase in droplet count ($p=0.0007$). Droplet area showed a striking 506% increase (0.007). The huge differences in all metrics observed in the co-treated group suggested some synergistic effect. Significant differences

between NEFAs and NEFAs+LPS groups (p=0.035 for intensity) were observed, supporting a potential synergy. Notably, LPS alone did not induce lipid accumulation reflected in intensity or droplet area, suggesting that the observed phenotype is a result of metabolic-inflammatory synergy rather than individual stimuli effects, and that lipid loading is necessary to induce steatosis. This quantification is consistent with observations from projections of AdipoRed™ staining (Figure 4.11).

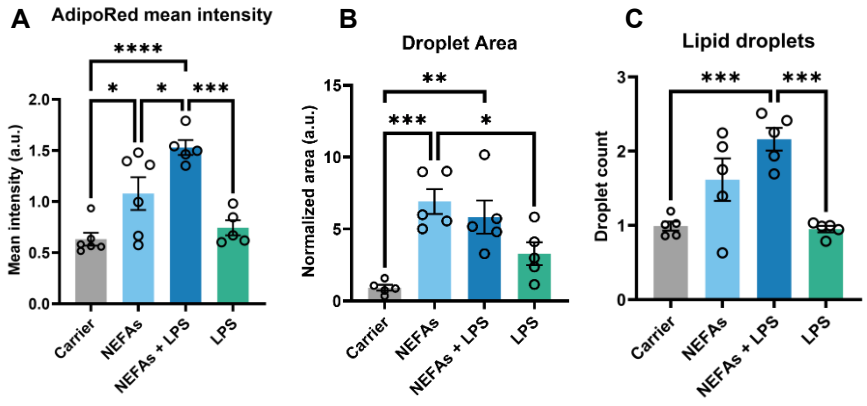


Figure 4.12. Quantitative assessment of steatosis in live 3D liver constructs.
A) Quantification of AdipoRed™ mean fluorescence intensity normalized to Hoechst 33342 intensity signal. B) Lipid droplet area normalized to nuclei number. C) Lipid droplet count normalized to nuclei number. Results are expressed as mean ± SEM and compared using one-way analysis of variance (ANOVA) followed by Tukey's post hoc tests when appropriate. * $p < 0.05$; ** $p < 0.01$; *** $p < 0.001$; **** $p < 0.0001$.

4.4.5 Hepatocellular Dysfunction and Damage

Hepatocytes are damage under sustained lipid stress. These effects are monitored through markers of hepatocellular function and damage. We monitored albumin (*ALB*) mRNA expression in all experimental groups to assess hepatocyte integrity and function. Immunofluorescence staining was performed on 3D construct cryosections to visualize albumin-positive clusters of differentiated hepatocytes. Like the previous observations in steatosis, a potential synergistic effect emerged. This synergistic stress caused by the co-treatment directly impaired liver function.

NEFAs alone did not significantly reduce *ALB* mRNA expression, although a clear downward trend of 0.56-fold was observed compared to the control group (p>0.05). In contrast, *ALB* expression decreased significantly in the NEFAs+LPS co-treated group, showing a 0.23-fold change compared to the control (p=0.02) at the final timepoint. LPS alone also significantly reduced *ALB* expression (0.30-fold change compared to control, p=0.02).

Qualitatively, confocal images closely replicated the quantification of relative expression. Numerous albumin-positive clusters were observed, along with bright confocal signal. Marked reductions in the signal intensity and number of albumin-positive cells were observed in both NEFAs and NEFAs+LPS

groups, though the latter showed the strongest decrease. This observation may indicate a significant loss of hepatocyte identity or health under MASH conditions (Figure 4.13).

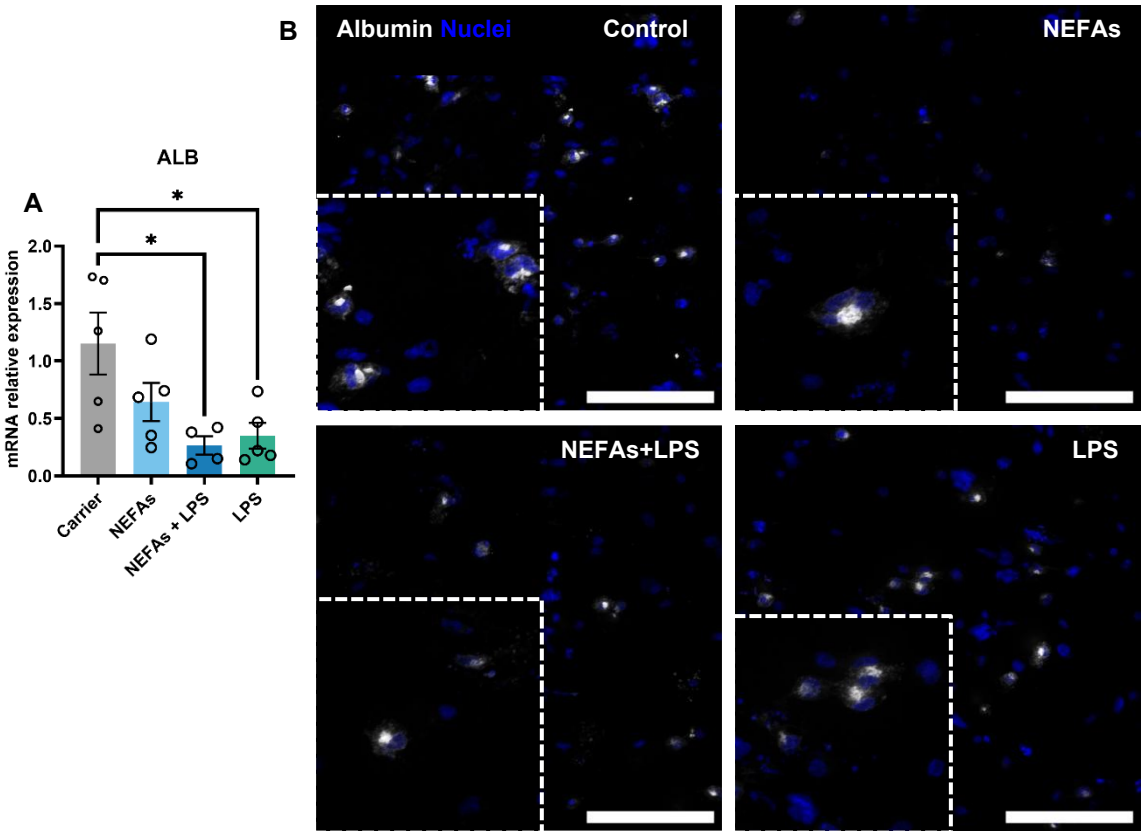


Figure 4.13. Evaluation of albumin expression and synthesis as a marker of hepatocyte identity.
A) Relative mRNA expression of *ALB* (albumin) at the final time point, using the carrier condition as the reference group and *ACTB* (actin β) as the housekeeping gene. Expression levels were calculated by the ΔΔCt method. B) Albumin immunostaining on construct cryosections at the final timepoint. Nuclei were stained with Hoechst 33342. Scale bar = 100 µm. Results are expressed as mean ± SEM and compared using one-way analysis of variance (ANOVA) followed by Tukey's post hoc tests when appropriate. * $p < 0.05$; ** $p < 0.01$; *** $p < 0.001$; **** $p < 0.0001$.

To further evaluate hepatocellular damage, we monitored aspartate aminotransferase (AST) activity in supernatants from 3D liver constructs. AST is an enzyme involved in amino acid metabolism and is employed as canonical marker of hepatocellular damage, as it is released into circulation when cell disassembly of ballooned hepatocytes occurs.

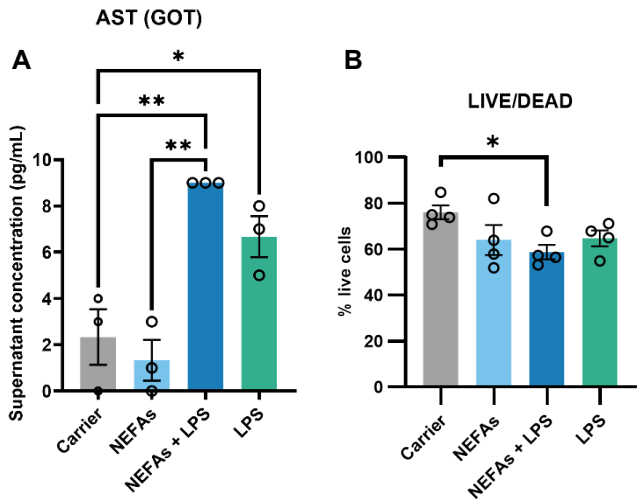


Figure 4.14. Hepatocellular damage and overall cell viability of 3D constructs.
A) Supernatant analysis of aspartate aminotransferase (AST) levels at the final timepoint. B) Percentage of live cells over total cells from LIVE/DEAD™ staining. Results are expressed as mean ± SEM and compared using one-way analysis of variance (ANOVA) followed by Tukey's or Dunnett's post hoc tests when appropriate. * $p < 0.05$; ** $p < 0.01$; *** $p < 0.001$; **** $p < 0.0001$.

Although significant differences in AST concentration were not detected in the NEFAs-treated group, AST activity rose by 285.7% (p=0.002) in the NEFAs+LPS co-treated group. Supernatants from LPS treated constructs showed a significant 185.7% rise in AST concentration as well (p=0.03) (Figure 4.14A). The behavior of AST release into the supernatants occurred along with a significant 22.9% reduction in cell viability (p=0.03) of the NEFAs+LPS co-treated constructs, as confirmed by LIVE/DEAD staining. Interestingly, NEFAs-alone (-15.9%) and LPS-alone (-14.9%) treatments caused apparent but not significant drops in cell viability compared to the control group (Figure 4.14B).

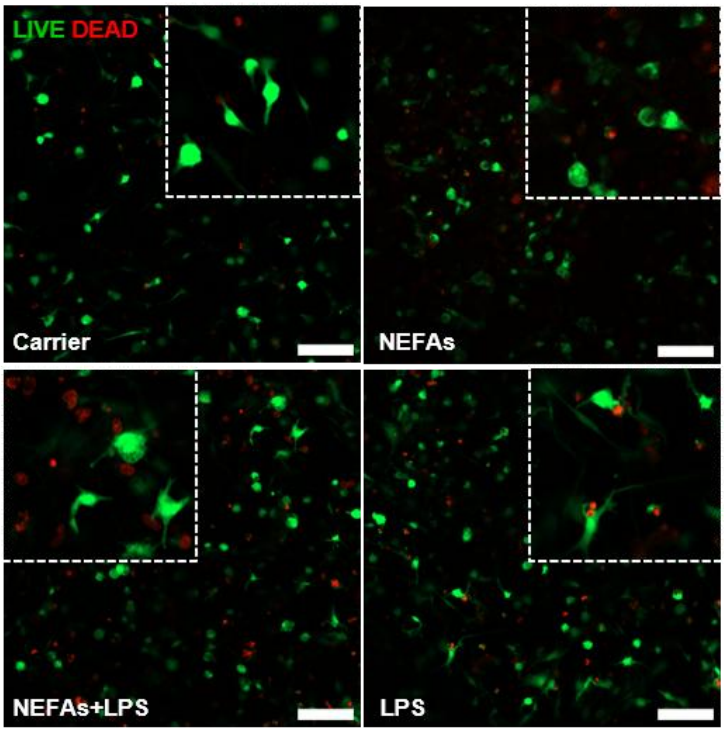


Figure 4.15. Representative confocal images of LIVE/DEAD™ staining at the final timepoint.
Scale bar = 100 µm.

Live and dead cells were visualized by confocal microscopy. Dead cells (red) were more frequently observed in both the NEFAs and NEFAs+LPS groups than in control images, and treatment exposure was associated with clear morphological changes. In these groups, many cells appeared more rounded, consistent with hepatocyte rounding/ballooning and an apparent increase in cell size. In contrast, the LPS-only group showed no obvious changes in hepatocyte size; however, dead cells were more numerous and were accompanied by elongated, branched cells suggestive of activated HSCs (Figure 4.15).

4.4.6 Markers of apoptosis and MASLD progression

Caspase-3 is a key effector of apoptosis, mediating irreversible cellular dismantling and commonly used as a readout of apoptotic activity. Here, caspase-3 was quantified in construct supernatants to capture extracellular levels of the active enzyme at the downstream end of the caspase cascade. NEFAs induced an early increase in caspase-3 as soon as day 4 (post–lipid hit), reaching +79.5% versus controls ($p=0.007$). By day 7, following the HSC stimulation phase, caspase-3 remained elevated relative to controls (+37.1%, $p>0.05$), although absolute concentrations were lower than at day 4. In contrast, the NEFAs+LPS co-treatment group displayed significantly increased caspase-3 on day 7 (+70.1%, $p=0.01$) compared to controls. LPS treatment alone produced only a modest, non-significant increase (+17.5%,

p>0.05). Overall, these results suggest a model in which lipotoxicity initiates apoptotic signaling, which is subsequently maintained or reinforced by the inflammatory second hit (Figure 4.16).

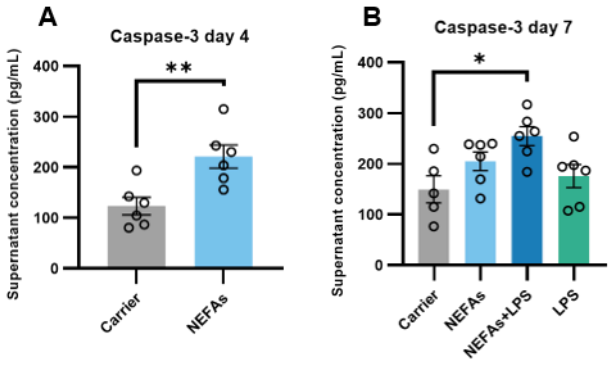


Figure 4.16. Apoptotic effector caspase-3 in supernatants from 3D liver constructs.
A) Day 4 (after incubation in high-lipid regime). B) Day 7 (after incubation in HSC-stimulating conditions). Results are expressed as mean ± SEM. Groups at day 4 were compared with unpaired tests with Welch's correction. Groups on day 7 were compared using one-way ANOVA followed by Tukey's, Dunnett's, or Kruskal-Wallis post hoc tests when appropriate. * p < 0.05; ** p < 0.01; *** p < 0.001; **** p < 0.0001.

IL-6 is a pleiotropic cytokine that contributes to hepatocyte homeostasis and inflammatory signaling, and it also functions as an inter-organ mediator. In line with the trends observed for other readouts, IL-6 changed minimally to day 4 following NEFAs exposure. By day 7, however, a pronounced inflammatory response became evident: NEFAs alone elicited only a modest, non-significant increase in IL-6 (+18.24%, p>0.05), whereas NEFAs+LPS co-treatment induced a marked elevation in IL-6 supernatant levels (+323.2%, p<0.0001). LPS alone produced a smaller, non-significant increase (+38.3%, p>0.05). IL-6 levels in the co-treated group were significantly higher than in all other conditions, consistent with a synergistic effect of lipotoxicity and the HSC-stimulation phase (Figure 4.17A-B).

IL-8 (CXCL8) is a chemotactic protein involved in the progression to MASH stage, a very strong predictor of fibrosis and correlates with poor outcomes for MASLD patients. Like IL-6 expression pattern, IL-8 expression trended upward on day 4 (+22.5%) but without statistical significance. After the HSC stimulation phase at day 7, supernatant levels of IL-8 showed a 6.0% increase in the NEFAs-treated group and reached significance only in NEFAs+LPS group with a 55.8% rise (p=0.007) and LPS-alone group with a 46.5% increase (p=0.03) (Figure 4.17C-D).

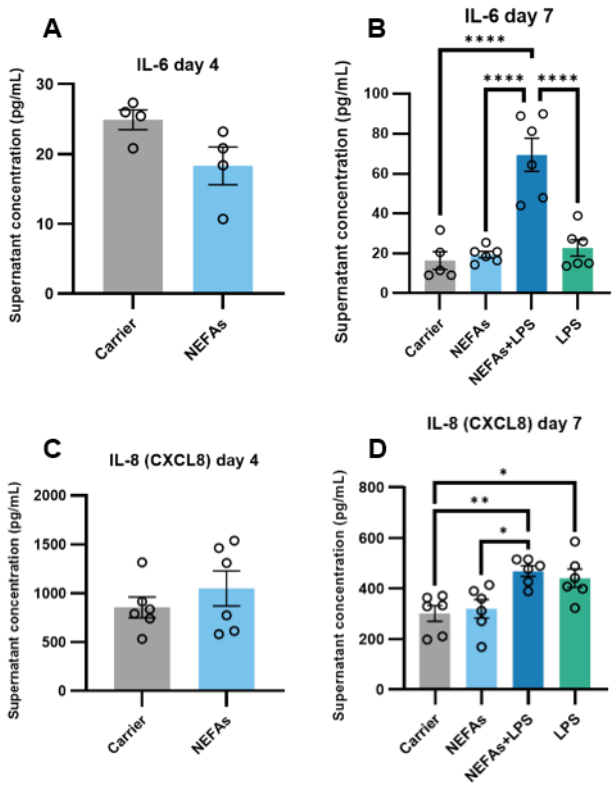


Figure 4.17. Inflammatory cytokines related to MASH progression in supernatants from 3D liver constructs. Measured at day 4 and day 7. A) – B) IL-6. C) – D) IL-8 (CXCL8). Results are expressed as mean ± SEM. Groups at day 4 were compared with unpaired tests with Welch's correction. Groups on day 7 were compared using one-way ANOVA followed by Tukey's, Dunnett's, or Kruskal-Wallis post hoc tests when appropriate. * $p < 0.05$; ** $p < 0.01$; *** $p < 0.001$; **** $p < 0.0001$.

4.4.7 Pro-fibrotic Remodeling

ECM remodeling is a hallmark of the disease progression to MASH, where activated HSCs actively deposit collagen, among other components, contributing to the onset of fibrosis and an overall change in the physical properties of the liver tissue. We investigated ECM remodeling through histological, biochemical, and molecular approaches.

PDGF-BB isoform is a strong mitogen and activator of HSCs, promoting HSC proliferation and fibrogenesis. Despite a mild 17.6% increase in the NEFAs-treated group, PDGF-BB in 3D liver constructs supernatants showed no significant changes on day 4. However, on day 7, NEFAs+LPS co-treatment significantly upregulated PDGF-BB by 279% (p=0.02), suggesting the activation of pro-fibrotic pathways, specifically under combined metabolic and inflammatory stress (Figure 4.18).

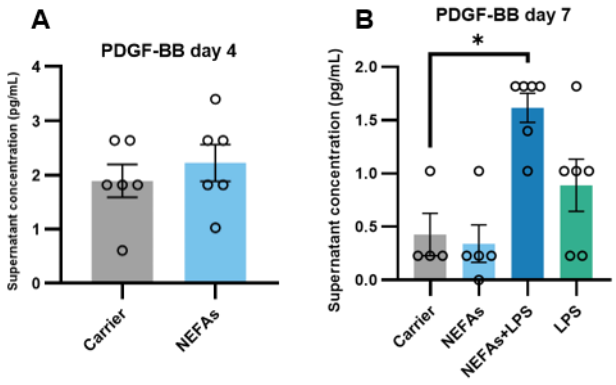


Figure 4.18. PDGF-BB isoform in supernatants from 3D liver constructs.
A) Day 4 (after incubation in high-lipid regime). B) Day 7 (after incubation in HSC-stimulating conditions). Results are expressed as mean ± SEM. Groups at day 4 were compared with unpaired tests with Welch's correction. Groups at day 7 were compared using one-way ANOVA followed Kruskal-Wallis post hoc tests when appropriate. * $p < 0.05$; ** $p < 0.01$; *** $p < 0.001$; **** $p < 0.0001$.

Vimentin is an intermediate filament protein that is upregulated during hepatic stellate cell (HSC) activation, marking the transition from a quiescent state toward a myofibroblast-like, fibrogenic phenotype. In addition to its association with activation, vimentin contributes to cell shape, motility, and migration, making it a useful indicator of cytoskeletal remodeling in activated HSCs. In control cryosections, vimentin staining was faint and sparse. In contrast, NEFAs-treated samples displayed brighter, more elongated, and branched vimentin-positive structures. The strongest signal and most extensive branching were observed in NEFAs+LPS co-treated constructs, whereas the LPS-only group showed a milder, less interconnected network, consistent with LPS acting as a direct HSC stimulus (Figure 4.19). Overall, these qualitative patterns support treatment-induced HSC activation, with vimentin network intensity and architectural complexity increasing with induction severity.

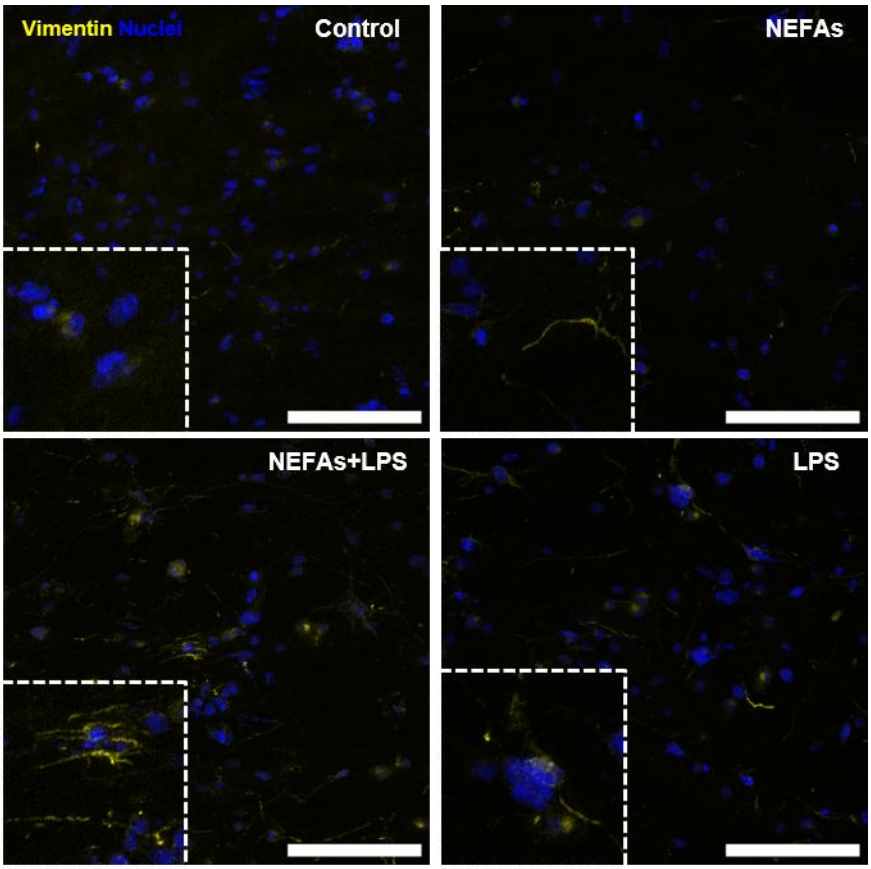


Figure 4.19. Vimentin immunostaining at the final timepoint.
Representative confocal Z-projections of construct cryosections stained with antibodies against intermediate filament protein vimentin, and DAPI (nuclei). Scale bar = 100 µm.

Picro Sirius Red staining was used to visualize collagen networks in tissue cryosections. In brightfield images, the staining revealed collagen fiber deposition forming pericellular halos around cell clusters, a pattern reminiscent of early pericellular fibrosis reported in MASH (Figure 4.20A). Because cytoplasmic components are counterstained in yellow/golden tones, overall cellular morphology could also be qualitatively assessed by brightfield microscopy. Compared with controls, NEFAs-treated constructs displayed more rounded cells with irregular outlines, consistent with lipid overload–associated hepatocyte swelling and ballooning-like morphology. In NEFAs+LPS co-treated constructs, fragmented and dismantled-looking cells were frequently observed surrounded by debris-like material, indicating pronounced structural disruption (Figure 4.20A).

Under polarized light, collagen fibers exhibited birefringence consistent with a mixed fiber composition, including yellow/orange signals typically associated with thicker, more densely packed fibers often attributed to type I collagen and green signals typically associated with thinner fibers often attributed to type III collagen (Figure 4.20B). Control sections showed weaker, more diffuse and sparse birefringence with predominantly yellow signal distributed across the section. In the NEFAs group, collagen appeared

more organized, with brighter and more continuous birefringent fibers. The NEFAs+LPS co-treatment group displayed the highest degree of fiber organization and an increased contribution of red/orange birefringence, consistent with a shift toward thicker and/or more compact collagen fibers. In these samples, fibers frequently extended between neighboring clusters, producing bridging-like patterns, consistent with those described in progressive fibrotic disease. In contrast, LPS-treated constructs showed predominantly yellow birefringence with comparatively thinner-appearing fibers and with a marked level of organization (Figure 4.20B).

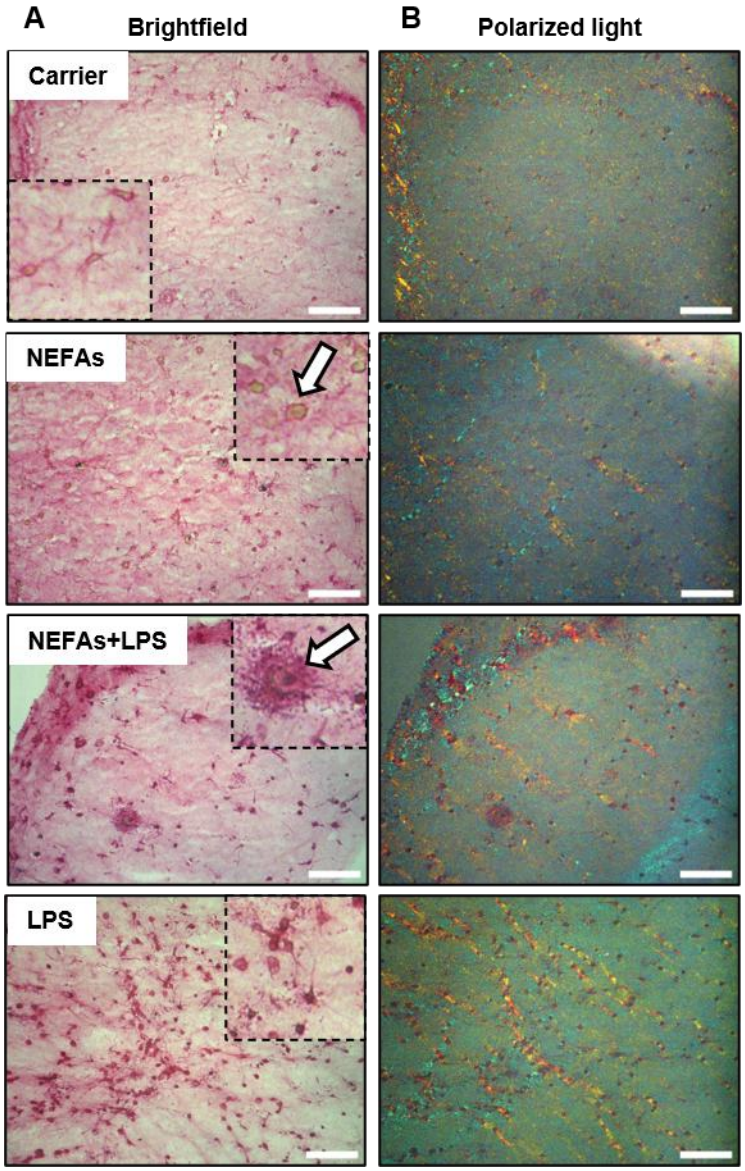


Figure 4.20. Histological characterization of 3D liver construct cryosections with Picro Sirius Red staining. A) Representative brightfield images of cryosections stained with the dye. Staining interpretation: Collagen fibers – red. Cytoplasm – yellow/gold. White arrows point at notable structures discussed above. Scale bar = 100 µm. B) Polarized light microscopy on the same construct cryosections stained with the dye. Staining interpretation: Type-I collagen fibers – yellow/orange birefringence. Type-III collagen fibers – green birefringence. Scale bar = 100 µm.

This structural remodeling was further supported by the assessment of collagen type-I relative expression. Despite a mild non-significant increase (1.09-fold, p>0.05), NEFAs treatment did not upregulate *COL1A1* relative expression compared to the reference group. However, a 2.50-fold increase in *COL1A1* expression (p=0.03) was expressed in the NEFAs+LPS co-treated group. LPS treatment alone upregulated *COL1A1* relative expression, though to a lesser extent (2.06-fold, p>0.05). These results suggest an active collagen deposition in response to treatments (Figure 4.21).

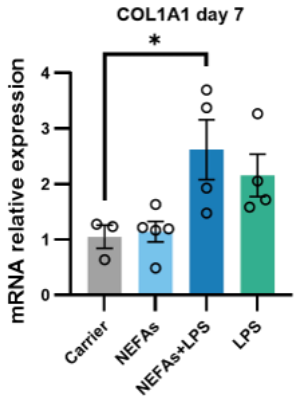


Figure 4.21. Relative mRNA expression of *COL1A1* gene at the final timepoint.
Carrier condition is the reference group and *ACTB* (actin β) is the housekeeping gene. Expression levels were calculated by the ΔΔCt method. Results are expressed as mean ± SEM. Groups were compared using one-way ANOVA followed by Dunnett's post hoc tests when appropriate. * $p < 0.05$; ** $p < 0.01$.

Procollagen serum biomarkers reflect collagen turnover, specifically collagen type-I (PINP) and collagen type-III (PIIINP) synthesis, and serve as non-invasive indicators of fibrosis in heart, liver, and lungs. The supernatant concentrations of both propeptides were measured as soluble indicators of collagen deposition inside the 3D constructs. Interestingly, PINP and PIIINP propeptides in the supernatants did not show significant increases on day 4. On day 7, however, PIIINP levels trended downward with both NEFAs (-6.1%, p>0.05) and NEFAs+LPS (-14.7%, p>0.05) treatments, while LPS alone significantly reduced PIIINP levels (-51.2%, p=0.001). PINP showed non-significant upward trends under NEFAs and NEFAs+LPS treatment at the same timepoint (Figure 4.22).

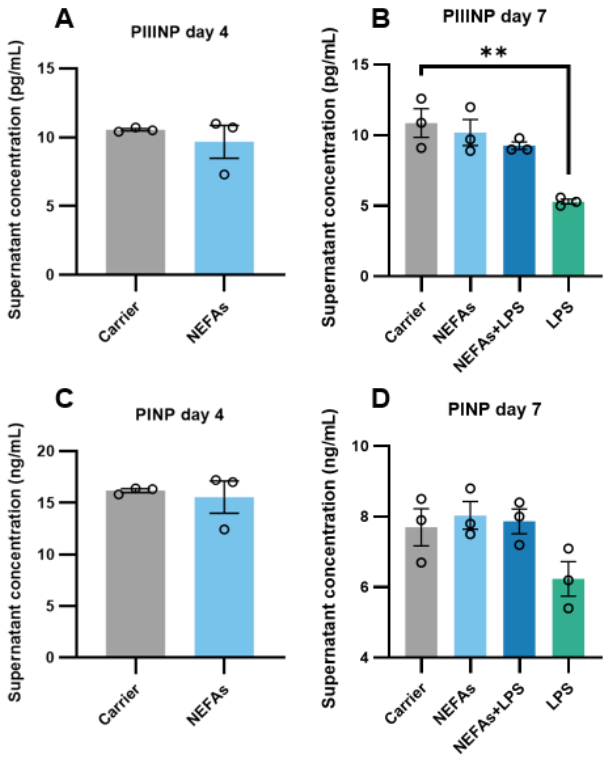


Figure 4.22. PIIINP and PINP in supernatants from 3D liver constructs at day 4 (after lipid hit) and 7 (after lipid hit and hepatic stellate cell stimulation).

A) – B) procollagen type-III. C) – D) Procollagen type-I. Results are expressed as mean ± SEM. Groups at day 4 were compared with unpaired tests with Welch's correction. Groups at day 7 were compared using one-way ANOVA followed by Tukey's or Dunnett's post hoc tests when appropriate. * $p < 0.05$; ** $p < 0.01$.

The lack of elevated propeptides in supernatants may reflect either propeptide retention within the dense 3D matrix or a shift in collagen temporal dynamics not captured by these circulating markers. These observations further emphasize the importance of the 3D scaffold for capturing these architectural changes.

4.5 Discussion

4.5.1 The balance between biological faithfulness, scalability and modularity of the 3D liver constructs

MASLD is increasingly recognized not as a static condition, but as a pathobiological continuum. This progression spans from relatively indolent hepatic triglyceride sequestration to MASH, a critical junction where lipotoxicity, chronic inflammation, and active fibrogenesis become the primary drivers of liver injury [41,216]. Recapitulating this transition *in vitro* remains a formidable challenge due to its multifactorial and nonlinear nature. In the *in vivo* environment, the shift toward a MASH phenotype is governed by a sophisticated reciprocal crosstalk between parenchymal hepatocytes—the primary hubs for lipid metabolism and proteotoxic stress responses—and non-parenchymal cells, most notably HSCs, alongside systemic influences such as immune cell infiltration and endocrine signaling.

Traditional *in vitro* methodologies struggle to encapsulate this systemic complexity. While 2D monocultures offer a scalable platform for quantifying intracellular lipid droplet dynamics, they are fundamentally limited by their inability to maintain the quiescent state of HSCs or reproduce the polarized tissue-level architecture essential for physiological signaling. Conversely, while advanced organoid and microfluidic organ-on-a-chip systems significantly enhance cellular complexity and biomimetic interactions, they often introduce substantial biological variability or lack the throughput necessary for extensive secretome analysis [217–219].

Addressing these limitations, the 3D liver constructs developed in this thesis were not designed to simulate the entirety of the metabolic syndrome, but rather to serve as a high-fidelity, stage-specific hepatic surrogate. By establishing distinct steatosis-like and MASH-like phenotypes within a multicellular framework, this model prioritizes the stabilization of hepatocyte-HSC interactions. Crucially, the platform is engineered as a standardized generator of stage-specific secreted factors. This modularity allows for the causal investigation of liver-derived factors on distal tissues—specifically skeletal muscle, as explored in Chapter 5—under the automated dynamic control systems detailed in Chapter 6. Consequently, this liver module functions as a controlled biological engine, enabling the functional dissection of organ-organ crosstalk in a way that traditional, closed-system models cannot.

4.5.2 Cell types and 3D hydrogel architecture

The selection of HepaRG cells as the parenchymal backbone of this model is key due to their exceptional metabolic longevity and unique dual differentiation capacity. Unlike PHHs, which suffer from rapid phenotypic decay and significant donor-to-donor variability, HepaRG cells maintain stable metabolic profiles over extended culture periods [200]. For the purposes of this work, reproducible experiments to assess downstream effects on skeletal muscle and phenotypic durability are prerequisites. It ensures that the secreted factors used for inter-organ signaling (Chapter 5) are derived from a consistent and well-characterized metabolic state rather than being an artifact of primary cell dedifferentiation.

To simulate the inflammatory and pro-fibrotic signaling characteristic of MASH, LX-2 HSCs were integrated as the primary non-parenchymal component. While LX-2 cells are an immortalized line and may not encapsulate the full spectrum of primary HSC heterogeneity, they remain the gold standard for modeling paracrine signaling and fibrogenic activation *in vitro*. Their high transfectability and ability to retain key features of the HSC activation make them superior to earlier immortalized lines [220,221]. Within the scope of this research, the LX-2 line provides the minimal functional unit necessary to drive the transition from simple steatosis to a MASH-like state, prioritizing platform scalability without sacrificing the essential biochemical outputs required for subsequent modular integration.

The decision to transition from 2D culture to a 3D type-I collagen-based hydrogel architecture addresses a fundamental limitation in liver modeling: the high sensitivity of HSCs to substrate stiffness. In conventional 2D systems, the high and non-biological rigidity of plastic or glass surfaces triggers spontaneous non-physiological HSC activation, confounding the study of disease-driven fibrosis. By embedding the HepaRG/LX-2 co-culture within a 3D matrix of tunable stiffness, we provide a more biomimetic mechanical environment that better maintains HSCs in a representative state.

Furthermore, this 3D arrangement allows for dynamic matrix remodeling to be assessed. While complex microfluidic "liver-on-a-chip" platforms offer high-resolution control over cellular interfaces, they often necessitate cumbersome peripheral equipment that limits throughput. Our hydrogel-based approach strikes a strategic balance; it captures the essential crosstalk between cells and their environment while remaining compatible with multiplexed endpoint assays and standardized liquid handling. This ensures the model is not only biologically relevant but also practically robust for the automated dynamic control systems discussed in Chapter 6.

4.5.3 Disease induction strategy

To simulate the progression from simple steatosis to MASH, this model utilizes a precisely defined induction strategy rather than a multifactorial metabolic cocktail. While more complex mixtures—simulating hyperinsulinemic or hyperglycemic conditions—might offer broader physiological inclusivity, they frequently introduce significant batch variability and obscure the causal attribution of specific phenotypes. In the context of this work, where the liver's secreted factors are subsequently applied to skeletal muscle (Chapter 5), maintaining a defined chemical environment is paramount to isolating the effects of liver-derived factors from the baseline induction components.

The choice of NEFAs, specifically a 2:1 ratio of PA and OA conjugated to albumin, provides a high-fidelity surrogate for the primary hepatic lipid influx observed in patients. Clinical evidence suggests that approximately 60% of the hepatic lipid pool in MASLD originates from peripheral lipolysis in adipose tissue, with an additional 15% coming from dietary intake [64,222–224]. By prioritizing NEFAs-mediated lipotoxicity over DNL, the model still accurately reflects the dominant drivers of lipid overload while ensuring the metabolic input remains quantifiable and reproducible.

To transition the phenotype toward MASH, LPS was utilized as a second hit. This reflects the clinical impairment of the gut-liver axis, where increased intestinal permeability leads to systemic endotoxemia and the subsequent activation of innate immune pathways within the liver [225]. By using LPS as a controlled inflammatory amplifier, we successfully recapitulate the transition from passive lipid sequestration to an active, pathological state characterized by inflammatory signaling. This defined, modular approach avoids the variability often associated with serum-based or poorly defined medium supplements [226]. Ultimately, this strategy ensures that the disease-stage secreted factors generated are sufficiently robust for downstream testing in skeletal muscle models and for the automated, dynamic integration covered in Chapter 6.

4.5.4 The synergy in steatosis and hepatocellular injury

A consistent pattern emerged across all readouts: the co-treatment of NEFAs and LPS elicited the most significant phenotypic changes. Quantitative microscopy revealed that while NEFAs alone induced steatosis, the effect was markedly intensified when combined with LPS. Critically, LPS administration in the absence of NEFAs did not induce lipid accumulation. This suggests that the exacerbated steatosis in the co-treated group is not a technical artifact of HSC activation, but rather a functional synergy where inflammatory signaling impairs hepatocellular lipid handling. These findings support the emerging consensus that MASH is not merely the additive result of two independent insults, but a complex interaction of multiple impaired pathways.

The observed decline in albumin (*ALB*) expression provides significant insight into the progression toward a MASH-like phenotype *in vitro*. The most pronounced reduction occurred in the NEFAs+LPS group, although LPS alone also exerted a significant inhibitory effect. While further selection of reference genes may help refine the specific contribution of LPS to *ALB* suppression, the downward trend aligns with clinical observations where reduced albumin synthesis serves as a hallmark of deteriorating liver function and correlates inversely with Child-Pugh and MELD scores [227,228].

Mechanistically, *ALB* expression is tightly linked to the broader hepatocyte identity program, which is largely orchestrated by the master regulator Hepatocyte Nuclear Factor 4 Alpha (*HNF4A*) [228]. Previous studies have demonstrated that *HNF4A* activity is significantly inhibited under lipotoxic conditions [229]. We hypothesize that under the combined stress of lipid overload and inflammatory signaling, hepatocytes may undergo a shift in biological priorities, favoring survival pathways over the maintenance of specialized metabolic functions. This hypothesis is consistent with previous findings from our laboratory in 3D murine models, where Hnf4a expression decreased in a dose-dependent manner with NEFAs exposure [184]. In the context of this thesis, this shift is critical: the secreted factors generated by these constructs reflect the altered hepatocyte state and not merely a consequence of increased lipid content.

The elevation of AST in the co-treated condition further corroborates the observed loss of hepatocyte identity and suggests that cellular injury contributes to the decline in albumin production. This increase

in AST mirrors clinical patterns in MASH patients, where elevated transaminases are associated with lobular inflammation and hepatocyte ballooning [230]. Although AST levels can be variable and influenced by various hepatic events, it remains a robust and clinically relevant marker of hepatocellular damage within this *in vitro* framework. To further validate these findings, additional markers specifically involved in programmed cell death and irreversible injury are explored in the subsequent sections to confirm the recapitulation of key MASH progression events.

4.5.5 Apoptosis

Caspase-3 serves as a pivotal effector caspase within the apoptotic cascade. Synthesized as an inactive zymogen, it is proteolytically activated by initiator caspases 8, 9, and 10 to execute cell death through the cleavage of essential structural and regulatory proteins [231]. In this model, active caspase-3 levels rose significantly by day 4 following the initial lipid challenge. This early elevation likely reflects the onset of hepatocyte apoptosis in response to lipotoxic stress. Mechanistically, this is consistent with palmitate-induced activation of the c-Jun N-terminal kinase (JNK) pathway—a primary stress response regulator of apoptosis—and subsequent ERK phosphorylation [232].

The persistence of this apoptotic signal through day 7 underscores the role of caspase-3 as both a marker and a mediator of sustained injury in MASH. The early emergence of these cues aligns with the established pathological sequence: lipotoxicity triggers hepatocyte apoptosis, leading to the release of apoptotic bodies and DAMPs. These factors, in turn, activate HSCs and initiate an inflammatory response that further exacerbates hepatocellular injury, establishing a pathogenic feed-forward loop [117].

Interestingly, the absolute concentration of active caspase-3 in the supernatants was lower on day 7 than on day 4. This observation may be attributed to a reduction in the total pool of viable, active hepatocytes following sustained exposure to lipid overload and paracrine inflammatory signaling from activated HSCs. Crucially, the temporal behavior of caspase-3 helps distinguish a MASH-like progression from simple, acute lipotoxicity. If inflammatory cytokines had peaked on day 4 prior to apoptotic markers, the model would primarily reflect an immune-driven response. Instead, the early appearance of apoptosis followed by the later prominence of inflammatory mediators supports a staged progression that is highly consistent with the known pathophysiology of human MASLD, further validating the induction strategy employed in this work.

4.5.6 HSC activation as a driver of a MASH-like progression

A robust MASLD platform must capture the activation of HSCs, as these non-parenchymal cells are central responders and executors of fibrogenic remodeling. During MASLD progression, quiescent vitamin A-storing HSCs transition into proliferative, chemotactic myofibroblasts in response to paracrine cues—including hepatocyte stress signals, PAMPs, and DAMPs [117].

In this model, the histological evidence of vimentin remodeling—characterized by increased intensity and the formation of network-like morphologies, particularly in the NEFAs+LPS group—aligns with an activated phenotype. This structural transformation provides a cellular correlation to the changes in the secreted factors discussed below, reinforcing the model's ability to simulate the transition from a metabolic storage state to an active pathological state.

4.5.7 Temporal resolution of cytokine and growth factor responses

The measurement of biomarkers on day 4 and day 7 allows for a sequential interpretation of disease development. Interestingly, NEFAs exposure alone did not significantly elevate inflammatory biomarkers by day 4, suggesting that lipid loading is insufficient to trigger immediate paracrine activation within 96 hours. This observation is consistent with the clinical behavior of early MASLD, which often remains silent regarding systemic inflammatory markers [233,234]. Other *in vitro* co-culture studies have similarly noted that inflammatory cytokines typically emerge in later phases rather than the initial steatotic stage [235,236]. This reflects the high buffering capacity of hepatocytes, which can tolerate substantial lipid accumulation before manifesting severe stress [234]. However, by day 7, the MASH-like group (NEFAs+LPS) demonstrated a clear elevation in inflammatory and growth factor outputs.

IL-6 served as a key indicator of this chronic inflammatory shift. While IL-6 can support regeneration in acute settings [237–239], its sustained elevation is a hallmark of metabolic dysregulation and clinical severity in MASH, even acting as a driver for hepatocellular carcinoma [239]. In our model, the sustained elevation of IL-6 without corresponding changes in C-reactive protein (CRP) suggests a transition toward chronic inflammation rather than an acute-phase response. This correlates with the previously noted decline in albumin synthesis, suggesting that IL-6 may drive hepatocytes to prioritize survival over specialized metabolic functions [240].

Interleukin-8 (IL-8/CXCL8) is a potent pro-inflammatory chemokine and a primary mediator of neutrophil recruitment. In the context of MASH, IL-8 expression is closely linked to lipotoxicity and the activation of the gut-liver axis. Clinical data indicate that serum IL-8 levels reflect the severity of cirrhosis and correlate more strongly with fibrotic liver injury and poor clinical outcomes than many established fibrosis markers [241,242]. In this model, the significant upregulation of IL-8 in the NEFAs+LPS group on day 7 suggests that the platform successfully recapitulates the transition to an active inflammatory state. Beyond its role in leukocyte recruitment, recent reports suggest that IL-8 possesses potent pro-angiogenic properties that may link chronic MASH to hepatocarcinogenesis [243]. The presence of IL-8 in the construct supernatants indicates that the model is producing a chemotactic phenotype capable of signaling to the immune system. This functionality is a key requirement for future modular experiments where immune cell recruitment could be integrated into the platform.

Platelet-Derived Growth Factor-BB (PDGF-BB) is recognized as the most potent mitogen for activated HSCs and a central driver of hepatic fibrosis. The importance of this pathway is highlighted by *in vivo* studies where PDGFRβ-deficient mice exhibit significantly reduced fibrosis and chronic inflammation,

even when steatosis remains unchanged [244,245]. This underscores that PDGF signaling is a specific requirement for the progression from simple lipid accumulation to fibrotic tissue remodeling. In this 3D model, the elevated levels of PDGF-BB in the MASH-like group provide robust evidence of LX-2 activation. While HSCs are the primary source of PDGF isoforms in the liver, the use of HepaRG cells adds another layer of physiological relevance; their cholangiocyte-like features allow the production of additional PDGF isoforms, potentially creating a more complex signaling environment than a simple hepatocyte-HSC co-culture. The detection of PDGF-BB in the supernatants is particularly valuable for the downstream studies in Chapter 5. It confirms that the liver module is not only secreting inflammatory cytokines but also potent growth factors that can fundamentally alter the metabolic and structural environment of distal tissues like skeletal muscle.

4.5.8 Pro-fibrotic remodeling and ECM markers

The histological analysis provides strong evidence of active ECM remodeling. The observation of collagen fibers extending between cell clusters resembles the bridging fibrosis patterns seen in clinical biopsies [245]. This is further supported by Picro Sirius Red staining and the upregulation of COL1A1.

However, we observed an unexpected reduction in the soluble propeptides PIIINP and PINP on day 7. This should not be interpreted as a downregulation of fibrosis, but rather as a reflection of the complex regulation and post-translational modifications (PTMs) inherent to collagen processing [246]. In MASLD progression, type III collagen typically appears early in the remodeling phase, while type I peaks later [247]. It is possible that day 7 captures a specific window where collagen deposition is occurring rapidly, but the release of soluble propeptides into the supernatant is hindered.

Furthermore, the 3D hydrogel environment likely influences the bioavailability of these markers. As the matrix becomes denser due to fibrotic remodeling, cleaved propeptides may become sequestered within the construct or locally degraded rather than diffusing into the supernatant. This mechanical confinement highlights a fundamental difference between clinical plasma biomarkers—which represent a systemic balance of synthesis and clearance—and a simplified *in vitro* model. Therefore, imaging-based characterization of collagen architecture remains the most reliable indicator of active fibrotic remodeling in this platform.

4.5.9 Summary of the model performance

Taken together, the 3D liver model successfully reproduces multiple hallmarks of the MASLD-MASH progression: steatosis, hepatocyte injury, early apoptosis, stellate cell activation, and the release of stage-specific inflammatory and pro-fibrotic mediators. The primary value of this platform is not in capturing every clinical nuance of the disease, but in its ability to function as a standardized generator of stage-specific secreted factors. This allows for the functional testing of liver-derived factors on distal

tissues, providing a robust foundation for the inter-organ experiments and automated control paradigms detailed in Chapters 5 and 6.

Chapter 5 | Bioengineered Skeletal Muscle Module

5.1 Chapter rationale and modeling framework

The liver–skeletal muscle axis is a central component of MASLD-associated systemic dysfunction. Although the liver is the primary site of steatosis, inflammation, and fibrogenic remodeling, skeletal muscle is a major determinant of whole-body metabolic homeostasis and a clinically relevant target of wasting. In MASLD and MASH, muscle impairment can manifest not only as reduced mass, but also as altered tissue quality, impaired contractile performance, and reduced functional reserve. Therefore, modeling the extrahepatic consequences of progressive liver dysfunction requires a skeletal muscle platform that can report tissue-level function, rather than relying only on molecular or morphological markers.

In this thesis, we adopt a fibrin-Matrigel-based human 3D skeletal muscle construct anchored between PDMS posts, serving as the receiving module for MASLD stage-specific CM. This configuration supports myoblast alignment, tissue compaction, myotube formation, and force generation under electrical pulse stimulation, allowing skeletal muscle performance to be quantified as a functional endpoint. The muscle construct represents the functional counterpart to the hepatic module developed in Chapter 4: while the liver model generates stage-specific signals, the skeletal muscle model enables evaluation of whether those signals are sufficient to induce measurable contractile, structural, and molecular alterations. This modular arrangement provides a controlled human *in vitro* framework to interrogate liver-derived effects on skeletal muscle while maintaining independent control over the source and target tissues.

5.2 Aims and scope

The introductory section of this chapter focuses on the experimental requirements for modeling MASLD-associated skeletal muscle dysfunction *in vitro* and on the rationale for selecting a functional 3D skeletal muscle module as the target tissue for liver-derived signals. Accordingly, the following sections are organized around three main points: (i) the native complexity of skeletal muscle and the limitations of conventional models, particularly for studying contractile dysfunction; (ii) the main classes of *in vitro* skeletal muscle models, with emphasis on why 3D tissues compatible with electrical pulse stimulation provide tissue-level readouts that are not accessible in 2D cultures; and (iii) the relevance of liver–muscle platforms for studying hepatically driven muscle impairment.

The aim of this chapter is to establish, characterize, and apply a functional human 3D skeletal muscle model as the receiving module. Specifically, this chapter describes the fabrication and maturation of aligned skeletal muscle tissues, their exposure to CM generated by the 3D liver constructs described in Chapter 4, and the assessment of liver-induced muscle alterations through contractile, morphological, histological, and molecular endpoints. By doing so, this chapter tests whether MASLD-like signals from the liver are sufficient to impair skeletal muscle phenotype and function under controlled *in vitro* conditions, while providing the biological basis for future dynamic integration with the liver module in an organ-on-chip framework.

5.3 Introduction: Models of Skeletal Muscle

5.3.1 Native complexity of liver–muscle crosstalk

Skeletal muscle modeling for MASLD/MASH-associated sarcopenia sits at the intersection of multi-organ pathophysiology and bioengineering. In this context, functional 3D in-vitro muscle systems—particularly those compatible with EPS and organ-on-chip integration—offer a way to bridge the gap between mechanistic reductionism in 2D cultures and the systemic but poorly controllable complexity of animal models [151,248,249].

Native skeletal muscle is a hierarchically organized, highly vascularized and innervated tissue in which multinucleated myofibers are bundled into fascicles and embedded in a multilayered extracellular matrix ECM. This environment is rich in collagens I, III, IV and VI, laminins, glycoproteins and proteoglycans, which collectively support force transmission, mechanotransduction and satellite-cell niche function. Myogenesis and regeneration are governed by a tightly regulated transcriptional hierarchy of transcription factors *PAX7*, *MYF5*, *MYOD1*, *MYOG*, and *MYF6*) and by an immune–metabolic milieu in which cytokines and myokines couple muscle to systemic metabolic status [140,142].

As discussed in depth in Chapter 1, sarcopenia arises from an imbalance between muscle protein synthesis and breakdown driven by hyperammonemia in MASLD, chronic inflammation and physical inactivity. Hyperammonemia induces NF-κB–dependent upregulation of myostatin, impairs mTORC1 signaling, activates autophagy and impairs the TCA cycle anaplerosis and mitochondrial energetics, all of which converge on reduced muscle protein synthesis and increased proteolysis. This liver–muscle axis makes skeletal muscle a target of hepatically driven toxicity—an inter-organ relationship that is difficult to dissect mechanistically in either conventional 2D cultures or whole-animal models [151,250].

5.3.2 Limitations of conventional models

Classical 2D myotube cultures on plastic or simple ECM-coated substrates are invaluable for studying myogenic signaling, toxicology and high-throughput screening, but they lack key features of adult muscle, especially the 3D architecture, matrix-supported alignment, passive tension, realistic stiffness,

and multicellular interactions. These cultures often exhibit fetal-like gene expression, immature sarcomeric organization and limited force-generating capacity, which constrains their utility for modelling contractile dysfunction and metabolic defects in sarcopenia [250,251].

Rodent models capture systemic influences such as hormonal milieu, neural input, physical activity and whole-organ metabolism, and they have been extensively used to study muscle wasting in chronic liver disease and cirrhosis. However, species differences in immune responses, mitochondrial biology, ECM composition and fiber type distribution limit translational fidelity, and *in vivo* it is nearly impossible to isolate the contribution of specific hepatic signals—for instance steatotic hepatocyte secretome—from confounders such as diet, activity and ageing [251]. These limitations have motivated a shift toward bioengineered 3D skeletal muscle models that aim to recapitulate human tissue architecture and function while retaining experimental control and modularity.

5.3.3 In-vitro skeletal muscle models

5.3.3.1 2D systems with engineered topographical cues

Several intermediate systems enhance 2D cultures by imposing geometric or topographical cues that promote myotube alignment and partial maturation. Micropatterning using microcontact printing, microgrooved hydrogels or crumpled graphene can guide C2C12 and human myoblasts into highly aligned myotubes with improved sarcomeric organization and increased expression of contractile genes. Electrospun fiber mats and patterned conductive substrates like PEG–PEDOT hydrogels, and graphene oxide–polyacrylamide also combine anisotropy with enhanced electrical properties to foster myogenic differentiation [142,252].

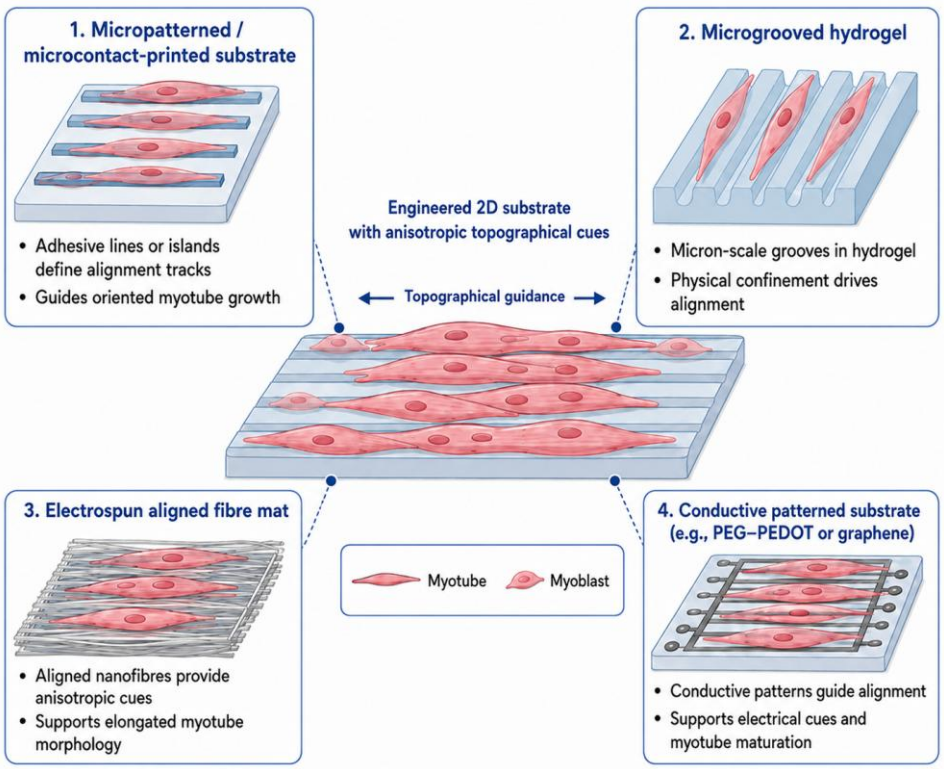


Figure 5.1. Engineered 2D skeletal muscle culture systems with topographical cues.
Schematic representation of engineered 2D platforms designed to impose spatial guidance on myogenic cells and promote oriented myotube formation. Although these platforms improve alignment, sarcomeric organization and early differentiation compared with conventional 2D cultures, they remain simplified systems that do not fully reproduce 3D architecture, passive tension or tissue-level contractility.

These aligned 2D systems are relatively simple and high-throughput, and they are useful for studying cell–substrate interactions, and early differentiation. However, they still lack true 3D architecture, physiological stiffness, long-range force transmission and tissue-level contractility, making them suboptimal for functional sarcopenia modelling or for probing liver–muscle biochemical crosstalk at the tissue scale.

5.3.3.2 3D myobundles

Three-dimensional myobundles generated by encapsulating myogenic cells in hydrogels between anchor points have become the workhorse of functional skeletal muscle modelling. Collagen type I, fibrin and decellularized ECM (dECM) are commonly used scaffolds; compaction around posts or frames generates uniaxial alignment, multinucleated myofibers and measurable twitch and tetanic forces under EPS [253–257].

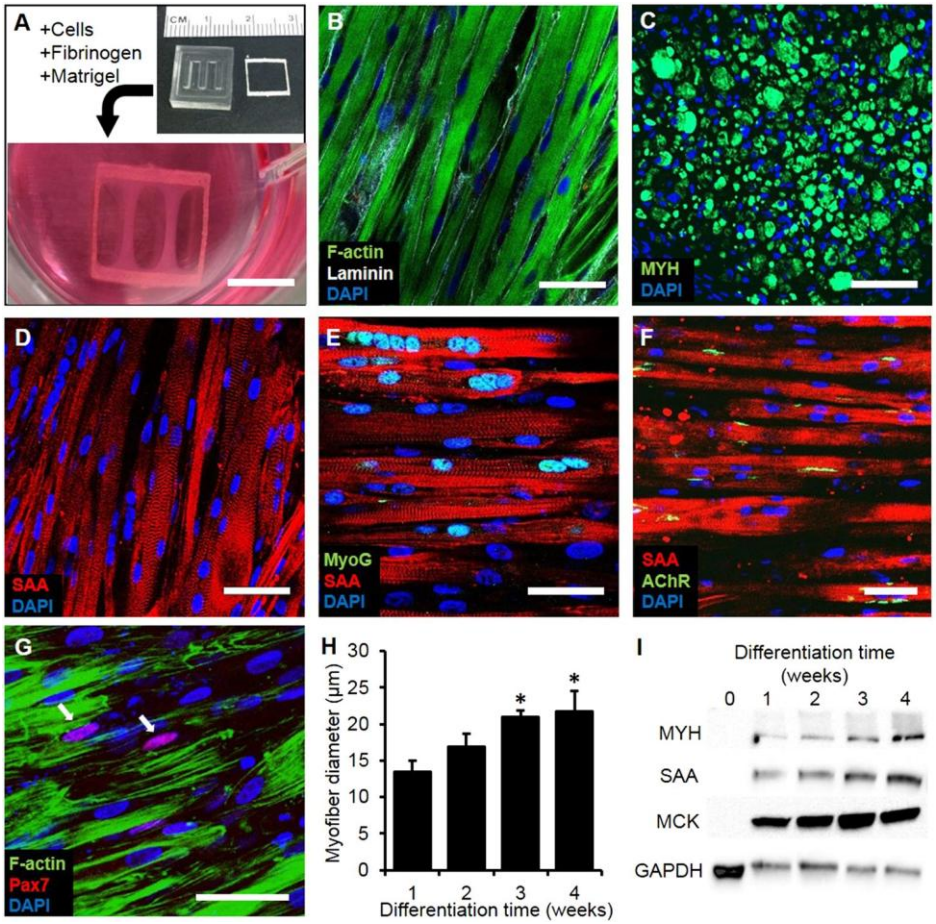


Figure 5.2. Bioengineered myobundles as 3D *in vitro* skeletal muscle models.
A) Representative fabrication and characterization of bioengineered human myobundles generated from primary human myogenic cells. The figure illustrates myobundle formation within a fibrin/Matrigel matrix anchored to a supporting frame, followed by structural characterization of aligned myofibers (B-C), sarcomeric organization (D), myogenic marker expression (E), acetylcholine receptor localization (F), Pax7-positive cells (G), and progressive maturation during culture (H-I). Reproduced from Madden *et al*. (2015) under the Creative Commons Attribution License. © 2015 Madden *et al*. [253]

Fibrin-based constructs with primary human myoblasts or hiPSC-derived progenitors can form highly aligned, cross-striated myofibers that respond predictably to drugs, cytokines and electrical training, and they can maintain cultures for weeks while retaining a PAX7+ satellite cell pool. Electrical stimulation protocols increase myotube diameter, metabolic flux and specific force, approaching fetal–neonatal human muscle phenotypes. Co-culture with stem cell-derived motor neurons yields innervated 3D neuromuscular tissues that develop functional neuromuscular junctions, further boosting maturity and making adult-like contractile phenotypes accessible *in vitro* [256].

5.3.3.3 *Microphysiological muscle-on-chip systems*

Microfluidic muscle-on-chip systems integrate 3D myobundles into perfused devices with controlled flow, oxygen, nutrient gradients and built-in sensors. The 3D skeletal muscles used in this work are considered under this classification. Pioneering platforms suspend fibrin– or collagen–Matrigel–based micro-bundles between flexible micropillars or posts, allowing continuous readout of passive tension and active force via pillar deflection under EPS. Newer devices incorporate magnetic or optical force sensing, enabling high-throughput, real-time monitoring of contractility in response to drugs or disease-related stimuli [250,252,258,259].

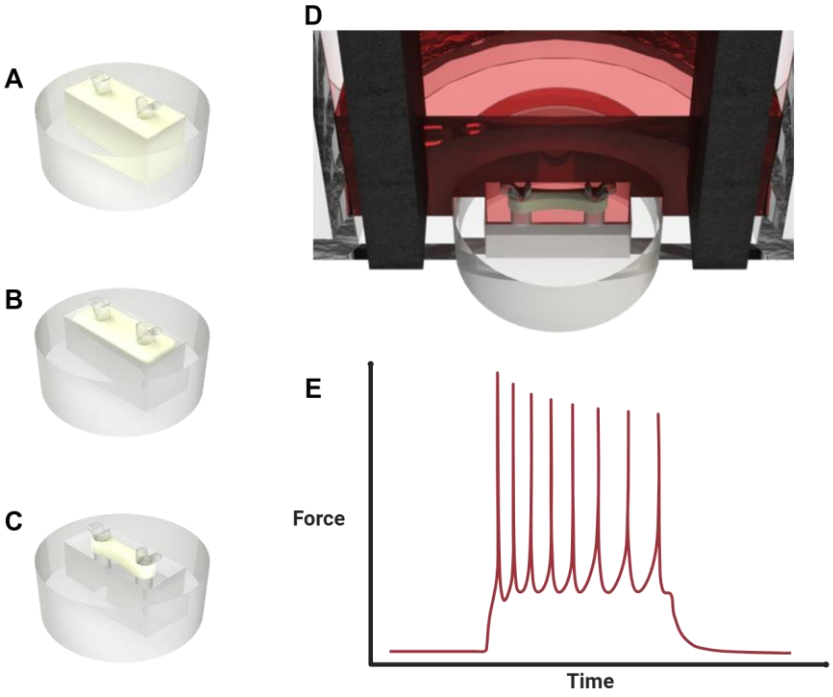


Figure 5.3. Fabrication and functional assessment workflow of 3D skeletal muscle-on-chip constructs. A) A polymeric casting mold is filled with a liquid cell–biomaterial suspension to generate the initial skeletal muscle precursor construct. B) During early culture, hydrogel compaction begins as embedded myogenic cells remodel the extracellular matrix and experience passive mechanical constraints imposed by the anchoring posts. C) Progressive matrix remodeling and cell-mediated tension lead to the formation of a compacted, suspended 3D skeletal muscle tissue aligned between the posts. D) Mature skeletal muscle constructs are transferred to an electrical pulse stimulation (EPS) platform, enabling controlled stimulation of individual tissues. E) Contractile function is quantified from each stimulated construct by recording force–time traces, allowing assessment of force generation. Created with BioRender.com. (2026). https://BioRender.com/ob3dqto

These microphysiological systems are particularly attractive for modelling sarcopenia and chronic liver disease-associated muscle wasting because they combine human-cell relevance with precise control over biochemical and mechanical loading and allow long-term exposure to defined hepatic or systemic factors. Donor-specific satellite-cell–derived myobundles in microfluidic chips have already been used

to compare contractile phenotypes of young active versus old sedentary muscle and to evaluate candidate interventions for age-related sarcopenia [249].

5.3.4 Functional readouts in models of skeletal muscle

A distinctive strength of 3D skeletal muscle constructs is their ability to generate measurable contractile forces under controlled stimulation, providing functional information that cannot be inferred from morphology alone. *In vitro* muscle platforms commonly use electrical pulse stimulation (EPS) to bypass the neuromuscular junction and directly depolarize the engineered tissue, allowing contractility to be assessed independently of motor neuron input. By applying EPS at defined frequencies, these systems can elicit twitch-like or tetanic contractions and quantify parameters such as peak force, passive tension, fatigue resistance and recovery. Depending on the platform design, force generation can be measured using flexible posts, cantilevers, magnetic sensing or optical readouts, enabling systematic interrogation of how disease-associated factors affect excitation–contraction coupling and mechanical output [185,253,254,260].

EPS also has a dual role in engineered skeletal muscle systems: it can be used both as a maturation stimulus and as an assay input. Repeated stimulation protocols promote larger fibre diameter, mitochondrial biogenesis and oxidative metabolism, shifting engineered muscles toward a more mature and oxidative phenotype that is closer to the clinical context of MASLD-associated sarcopenia. In multi-organ platforms, EPS further provides a means to model exercise-like activity and study its interactions with the liver, pancreas or adipose compartments through soluble secreted factors. This is particularly relevant given the central role of exercise in the clinical management of both MASLD and sarcopenia [185,253,254].

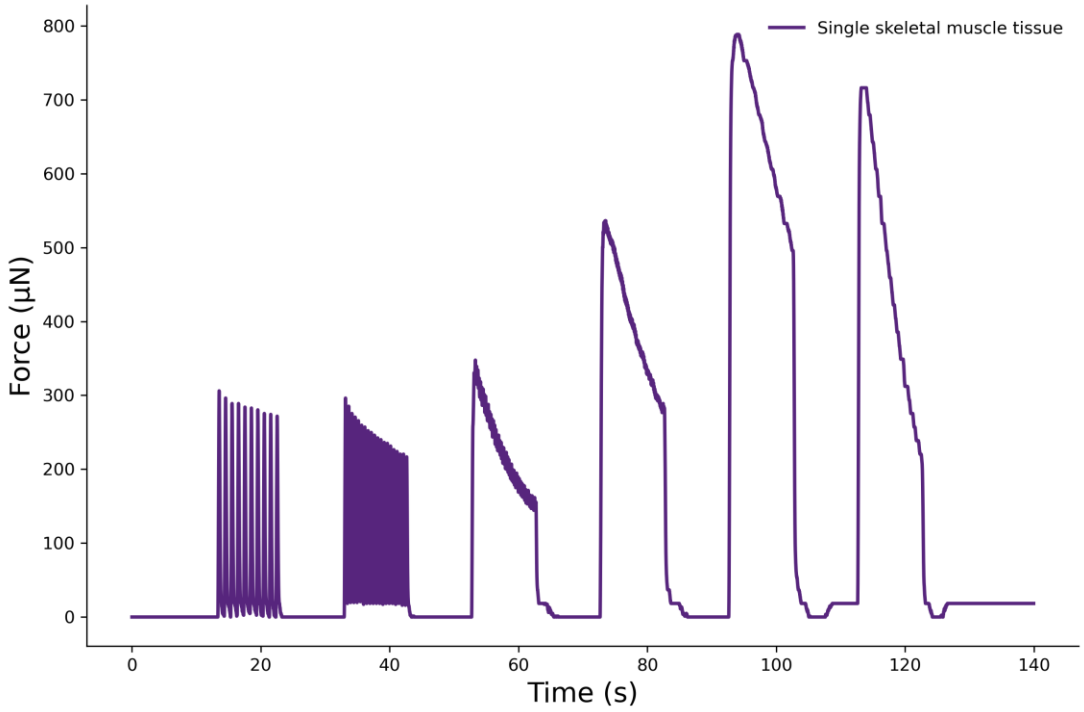


Figure 5.4. Representative contractile response of a 3D engineered skeletal muscle tissue under EPS. Force–time plot showing the contractile spectrum generated by one *in vitro* skeletal muscle tissue exposed to increasing EPS frequencies. Low-frequency stimulation produced discrete twitch-like contractions, whereas higher-frequency stimulation induced tetanic contractions with greater peak force. This frequency-dependent response enables functional assessment of tissue performance, including twitch force, tetanic force, relaxation behavior, and fatigue-related phenotypes.

In the context of MASLD-associated sarcopenia, functional 3D muscle models allow controlled evaluation of how liver-derived stressors, including hyperammonemia, inflammatory cytokines and fatty hepatocyte-derived secretomes, alter force generation, contractile reserve, fatigue resistance and recovery under standardized EPS regimes. Frequency-dependent reductions in force may reveal impaired tissue quality even when gross morphology or myotube size appear only modestly affected. In the present work, EPS is therefore used as a central functional readout to determine whether liver-derived CM are sufficient to impair the performance of mature engineered skeletal muscle tissues, and to establish a platform that could later be used to test pharmacological, nutritional or exercise-mimetic countermeasures.

5.3.5 Improvement of conventional models by advanced *in vitro* skeletal muscles

Compared with rodent models, 3D human skeletal muscle tissues—especially in organ-on-chip and multi-organ configurations—offer several advantages for studying MASLD-associated sarcopenia. Besides being compatible with a human cellular context, including primary or iPSC-derived myogenic progenitors and patient-specific cells, which better reflect human genetics and mitochondrial–metabolic

phenotypes, 3D skeletal muscles allow quantitative, high-content functional readouts and integrated biosensing for real-time monitoring of muscle homeostasis and injury. Compatibility with scalable, semi-automated platforms that reduce reagent and cell requirements facilitate screening and support rigorous statistics. Relative to conventional 2D cultures, 3D functional models restore matrix-supported alignment, passive tension, more physiological stiffness and tissue-level contractility, which are essential for accurately capturing sarcomeric remodeling, mechano-sensitive signaling and the interplay between contractile dysfunction and metabolism.

Nonetheless, current 3D and chip-based models still face challenges, including incomplete maturation to fully adult phenotypes, limited incorporation of non-myogenic stromal and immune populations, and the practical complexity of multi-organ integration and standardization. Continued refinement of biomaterials, fabrication strategies and cell sources should progressively increase their relevance for MASLD-associated sarcopenia.

This conceptual landscape positions 3D functional skeletal muscle constructs—particularly EPS-responsive muscle-on-chip and multi-organ systems—as a powerful complement to both 2D cultures and animal models for disentangling liver–muscle crosstalk and for testing targeted countermeasures against MASLD-associated muscle wasting.

5.3.6 Design remarks for the skeletal muscle module

The skeletal muscle module used in this thesis was selected to provide a functional and experimentally tractable receiving tissue for liver-derived signals. Engineering skeletal muscle *in vitro* requires a biomaterial environment that supports myoblast viability, alignment, fusion, differentiation, and force transmission, while maintaining sufficient structural integrity during culture. Natural hydrogels such as fibrin, collagen, and Matrigel are frequently used for this purpose because they provide biochemical and adhesive cues that favor myogenesis, although their mechanical properties and biological variability must be considered carefully [142,261]. In this work, a fibrin/Matrigel-based matrix was used because this combination supports myoblast remodeling, tissue compaction, and the formation of aligned multinucleated myotubes, while remaining compatible with long-term culture and downstream histological, molecular, and functional readouts.

The tissues were fabricated by hydrogel molding between flexible PDMS posts, a strategy widely used to produce 3D muscles with uniaxial alignment and passive tension. As the cell-laden hydrogel compacts between the anchoring posts, the embedded myogenic cells experience geometric and mechanical constraints that promote longitudinal organization and tissue-level force transmission. Importantly, the same post-based configuration enables quantitative contractile assessment by measuring pillar deflection during electrical pulse stimulation, thereby providing a direct functional readout of skeletal muscle performance [253,256–258]. This feature is central to the objective of Chapter 5, because it allows the impact of MASLD stage-specific liver-conditioned media to be evaluated not only through

molecular or morphological changes, but also through force generation as a physiologically meaningful endpoint.

For the aims of this thesis, the fibrin/Matrigel hydrogel molded between PDMS posts offered an appropriate balance between biological relevance, experimental robustness, compatibility with CM exposure, and functional quantification. Therefore, this platform was selected as the skeletal muscle counterpart to the 3D liver module described in Chapter 4 and as a modular component that could later be adapted to organ-on-chip integration.

5.4 Results

5.4.1 Fabrication of 3D skeletal muscle tissues

Skeletal muscle is a major effector of whole-body metabolism and a central target of MASLD-associated muscle wasting. Impairments in contractile performance and muscle quality can occur even in the absence of evident loss of mass. To interrogate whether secreted factors (SFs) from diseased livers are sufficient to disturb skeletal muscle function, we employed a previously established human 3D skeletal muscle platform based on encapsulation of immortalized myoblasts in Matrigel®–fibrin hydrogels [186,187]. This configuration supports myoblast fusion into aligned, multinucleated myotubes that generate force under electrical pulse stimulation (EPS), providing a quantitative functional readout that closely reflects physiological muscle performance.

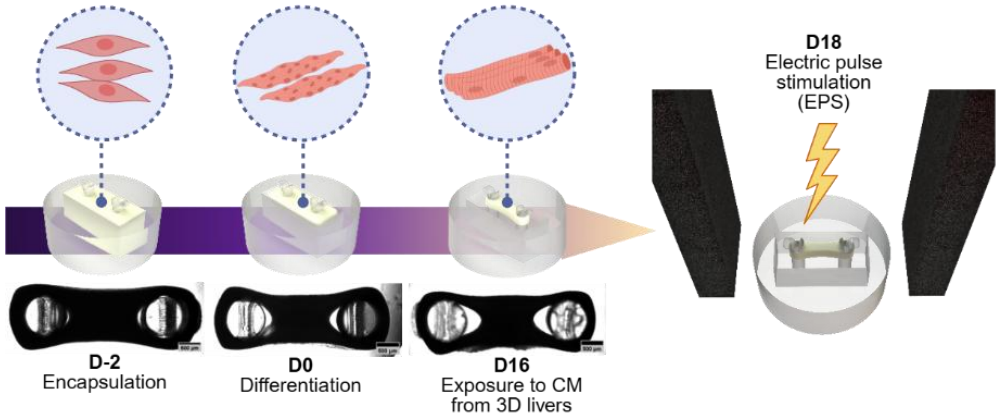


Figure 5.5. Schematic representation of 3D skeletal muscle fabrication, maturation, and experimental timeline. AB1079 immortalized myoblasts were encapsulated in a Matrigel®-fibrin matrix and seeded in PDMS chips with pillars. After encapsulation, the biomaterial compacts due to incubation at 37ºC and favors tension and alignment. Tissues undergo a 48-hour growth/adaptation and a 16-day differentiation phase before being exposed to CM from 3D liver constructs for 48 hours. Created in BioRender. (2025) https://BioRender.com/4sv98s2

Human myoblasts were encapsulated between flexible PDMS pillars (Figure 5.5) and left to adapt to the 3D environment for 2 days, during which compaction of the biomaterial occurred. Then, the tissues were cultured for 16 days under a defined differentiation medium to obtain mature 3D skeletal muscle tissues.

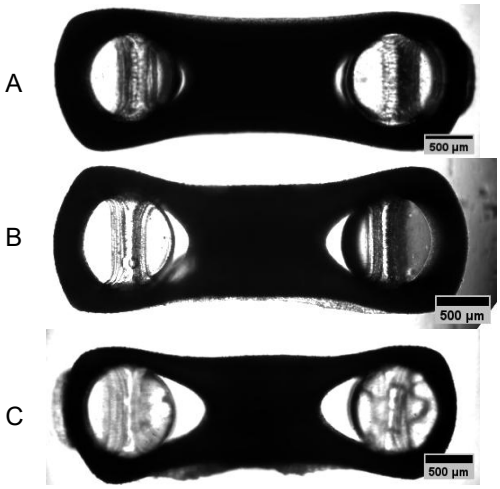


Figure 5.6. Skeletal muscle tissues imaged by brightfield microscopy at different timepoints.
Performed as assessment of biomaterial compaction and adequate hanging from the pillars. A) Day -2. B) Day 0. C) Day 16. Scale bar = 500 µm.

By the end of the maturation stage, tissues exhibited consistent compaction, visible tension by hanging from the pillars (Figure 5.6), and a dense network of longitudinally aligned, multinucleated myotubes, as confirmed by whole-mount imaging and confocal microscopy (Figure 5.7).

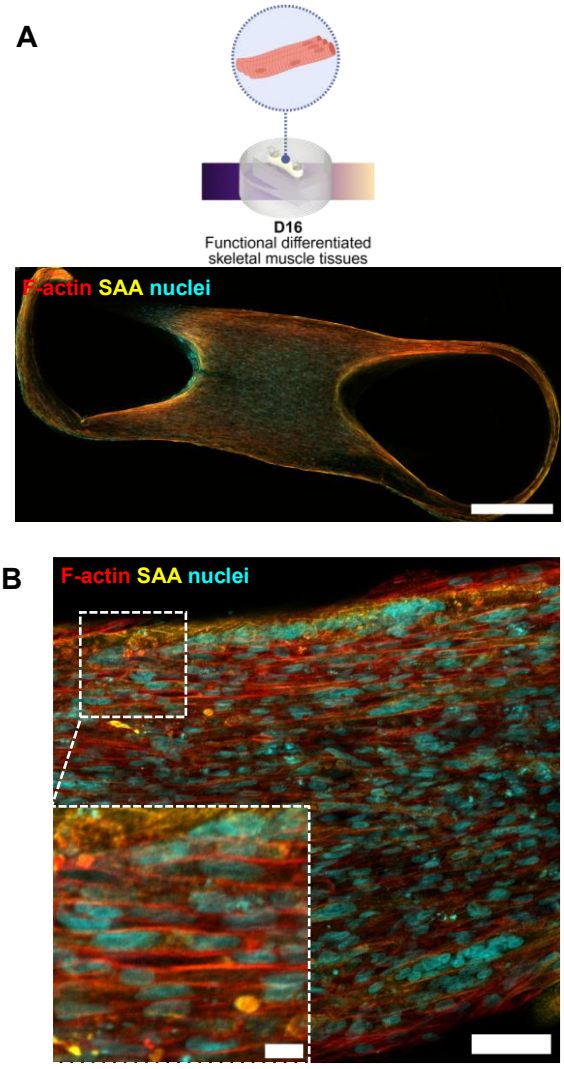


Figure 5.7. Inspection of 3D skeletal muscle whole mounts.
A) 3D tissues at the end of the maturation stage. Scale bar = 500 µm. B) Representative confocal image of myotubes in a longitudinal view. Scale bar = 100 µm. Inset scale bar = 20 µm.

5.4.2 Exposure to MASLD-conditioned media

To model liver-induced muscle dysfunction, differentiated muscles were exposed for 48 h to CM collected from the 3D liver constructs developed in Chapter 4, corresponding to four hepatic conditions: healthy untreated (Control), steatotic liver constructs under NEFAs only (SL), MASH-like livers under co-treatment with NEFAs+LPS (MASH), and liver constructs stimulated with LPS only (LPS liver).

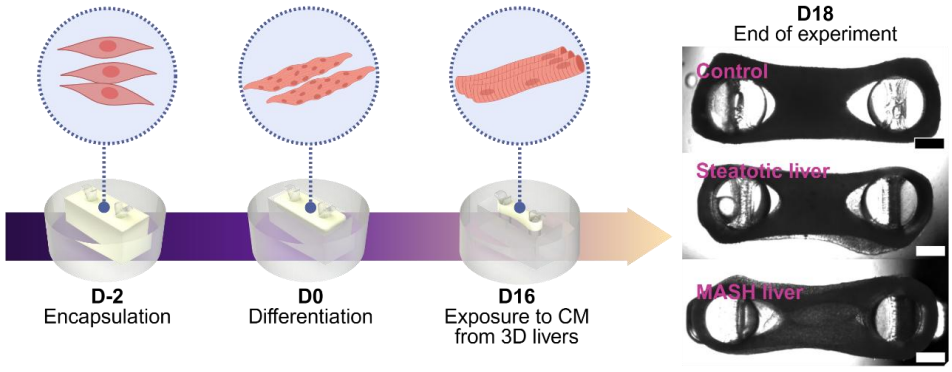


Figure 5.8. Representative brightfield images of 3D tissues after exposure to CM from the liver model.
Scale bar = 500 µm. Created in BioRender. (2025) https://BioRender.com/5tcj1t8

Because preliminary tests showed that undiluted liver culture medium was toxic to skeletal muscle tissues (Figure 5.9A), CM was diluted into skeletal muscle differentiation medium, and a final volumetric ratio of 1:50 liver CM in SkM medium was selected as the highest dose that did not compromise baseline viability or contractile capacity in control conditions (Figure 5.9B).

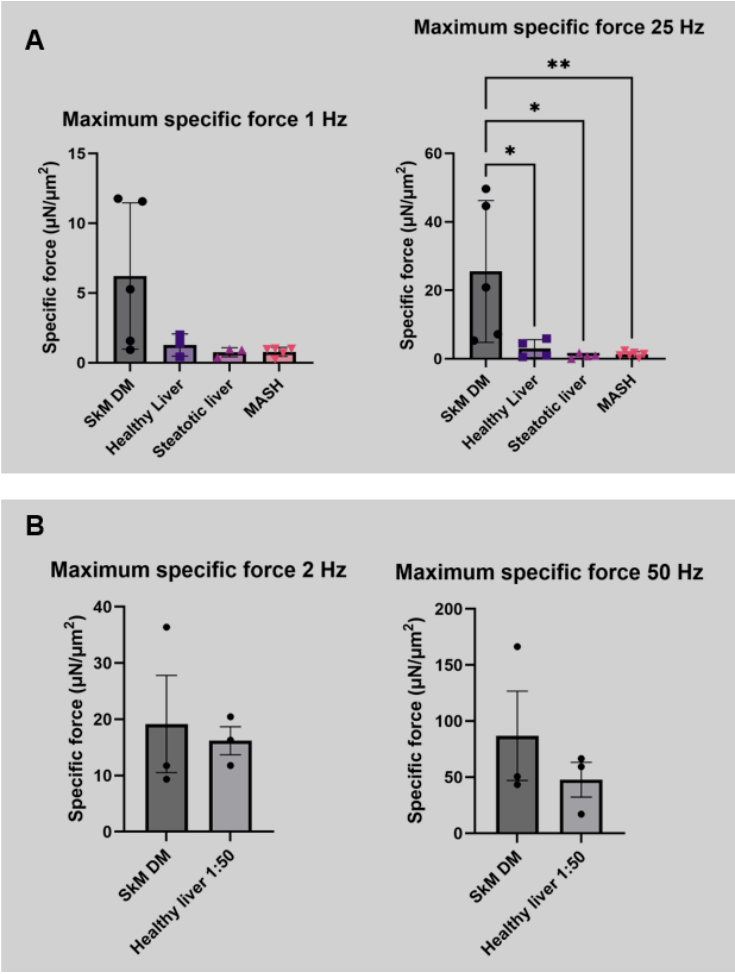


Figure 5.9. Optimization of liver CM dilution for functional testing in 3D skeletal muscle tissues.
A) Maximum specific force generated by 3D skeletal muscle tissues after exposure to liver CM diluted 1:2. CM from healthy, steatotic and MASH-like liver constructs markedly reduced contractile output compared with standard SkM DM, indicating that this dilution was not suitable for functional interrogation of liver-derived effects. B) Comparison of skeletal muscle tissues maintained in SkM DM or exposed to healthy liver CM diluted 1:50. At this higher dilution, healthy liver CM preserved measurable contractile responses upon EPS, supporting its use for subsequent experiments evaluating disease-stage-specific effects of liver on skeletal muscle function. Results are expressed as mean ± SEM. Differences between means tested by Student's t-test or one-way ANOVA followed by Tukey's post-hoc tests when appropriate. *$p < 0.05$; **$p < 0.01$.

Additional controls were evaluated to assess the effect of the clean liver serum-free medium (clean SFM) and CM from healthy liver constructs (Control), compared to normal SkM DM. No statistically significant differences were found between the first two conditions, indicating that the previous contact with the liver constructs is not detrimental to the functional capabilities of skeletal muscle tissues. The decline in contractility is most likely due to the presence of the volumetric fraction of liver medium diluted in the SkM DM (Figure 5.10).

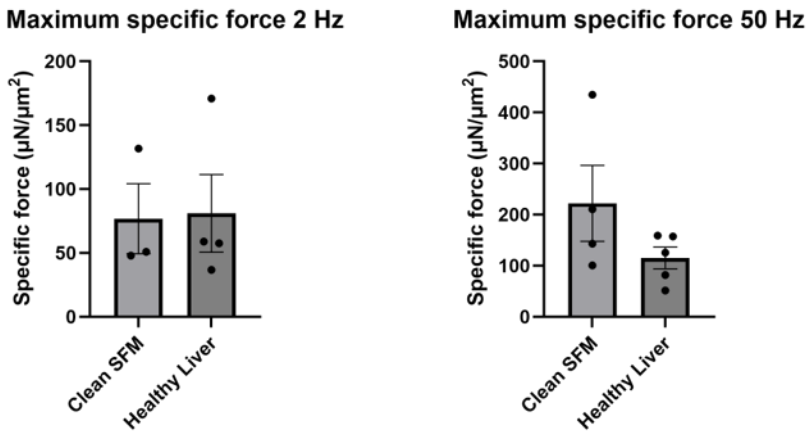


Figure 5.10. Control comparison for CM exposure in 3D skeletal muscle tissues.
Maximum specific force generated by 3D skeletal muscle tissues exposed to either unused liver serum-free medium (Clean SFM) or CM collected from healthy liver constructs (Healthy Liver), both diluted 1:50 in SkM DM. This control experiment was performed to assess whether the basal liver culture medium or the secretome from non-diseased liver constructs affected skeletal muscle contractile function under the selected dilution conditions. Data are shown as individual tissue values with mean ± SEM. Results are expressed as mean ± SEM. Differences between means evaluated by unpaired Student's t-test.

5.4.3 MASLD-conditioned media induce a severity-dependent decline in muscle contractility

In MASLD patients, reduced muscle strength and early fatigue are prominent functional manifestations that have been associated with adverse outcomes and do not always correlate with muscle mass. To determine whether liver-derived SFs can reproduce such functional impairments *in vitro*, we subjected 3D skeletal muscle tissues to EPS after exposure to the different liver-derived CM. The EPS protocol consisted of square-wave pulses (1 V mm^{-1}, 1 ms pulse width) delivered at increasing frequencies (Figure 5.11A), allowing us to assess both twitch-type (2 Hz) and tetanic-type (50 Hz) contractions while tracking pillar deflection to compute specific forces normalized to tissue cross-sectional area (CSA), which is termed as specific force (Figure 5.11B).

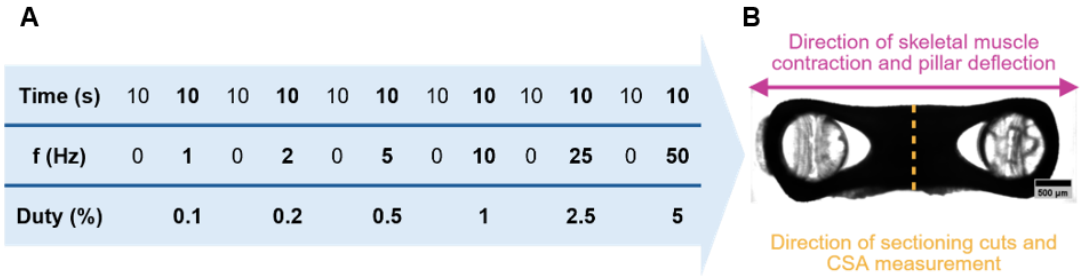


Figure 5.11. Electrical stimulation and visualization of measured variables.
A) EPS protocol. B) Brightfield image of a 3D tissue with depicted pillar deflection (purple) upon electrical stimulation and representation of sectioning cuts (yellow) for CSA measurement. Scale bar = 500 µm. Created in BioRender. Fernández Costa, J. (2026) https://BioRender.com/m2ip7ac

Though more evident at some stimulation frequencies than others, specific forces exerted by SL-treated tissues were lower than controls, and MASH-treated tissues appeared even weaker throughout the EPS regime. Across the EPS protocol, we observed a clear severity-dependent decline in muscle contractility as liver disease stage worsened. Tissues treated with CM from steatotic livers (SL-CM) already showed a marked reduction in force generation compared to controls, while MASH-derived CM further exacerbated the functional deficit (Figure 5.12).

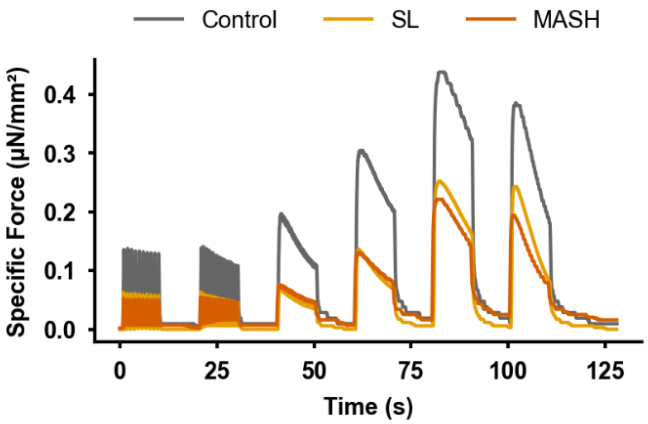


Figure 5.12. Representative contractile profiles of skeletal muscle tissues after exposure to CM from the liver constructs.

From the EPS regime, 2 Hz and 50 Hz were selected to compare conditions, since they normally show the lowest inter-group variability. At 2 Hz stimulation (twitch contractions), SL-treated muscles contracted 29% weaker and MASH-treated muscles exhibited a 60% reduction in specific force relative to controls, although these differences did not reach statistical significance ($p=0.06$), indicating a trend toward impaired twitch performance under MASLD-like conditions (Figure 5.13).

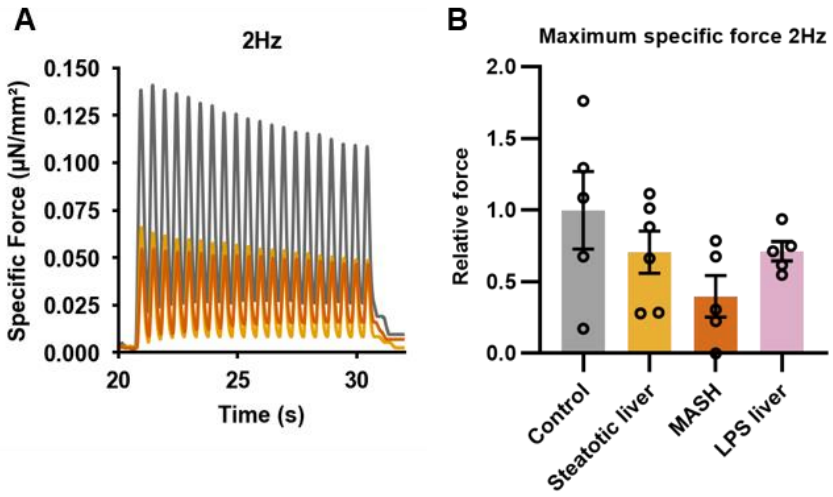


Figure 5.13. Functional evaluation at 2 Hz after exposure to CM from the liver constructs.
A) Twitch-type contractions at 2Hz. B) Specific contractile forces at 2Hz relative to the control mean. Results are expressed as mean ± SEM. Differences between means tested by one-way ANOVA.

The deficit became more pronounced under high-frequency stimulation. At 50 Hz tetanic contractions, SL-treated tissues exerted 53.1% less force but the difference compared to the control group was not significant. However, MASH-treated muscles displayed a significant and severe contractile deficit with a 77.2% reduction in specific force compared to controls (p=0.01) (Figure 5.14). CM from LPS-only livers appeared to influence skeletal muscle tissues, with twitch and tetanic forces comparable to SL-treated tissues but not significantly different from controls, suggesting that the full MASH-like milieu—rather than NEFAs or LPS alone—is required to elicit the most severe functional phenotype.

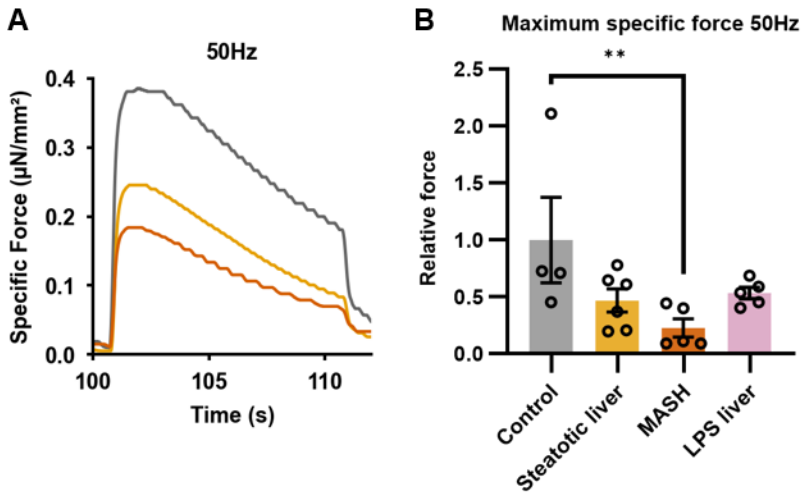


Figure 5.14. Functional evaluation at 50 Hz after exposure to CM from the liver constructs.
A) Tetanic-type contractions at 50 Hz. B) Specific contractile forces at 50 Hz relative to the control mean. Results are expressed as mean ± SEM. Differences between means tested by Kruskal-Wallis test. * $p < 0.05$; ** $p < 0.01$.

Together, these data demonstrate that MASLD-derived SFs are sufficient to induce a decline in contractile performance in human 3D skeletal muscle tissues, with the most pronounced deficits observed under MASH-like conditions and at higher stimulation frequencies that more closely model intense or prolonged muscle activity. The frequency-dependent nature of this impairment is consistent with clinical reports of exercise intolerance and early fatigue in MASLD, supporting the physiological relevance of the observed functional changes [262].

5.4.4 Myotube size and morphology under MASLD-conditioned media

At the clinical level characterization of sarcopenia and muscle wasting, muscle CSA is used to monitor muscle mass and can reflect changes in muscle quality as well. In clinical cohorts, muscle mass and strength can behave differently under MASLD and related liver diseases, with patients exhibiting normal or mildly reduced muscle mass but disproportionate functional impairment [262]. To determine whether the contractile decline observed in our 3D model was accompanied by overt structural wasting, we examined myotube size and morphology in cross-sections of skeletal muscle tissues. Cryosections were stained for sarcomeric α-actinin (SAA) and F-actin, revealing the architecture of individual myotubes and allowing us to quantify diameter and cross-sectional area distributions (Figure 5.15).

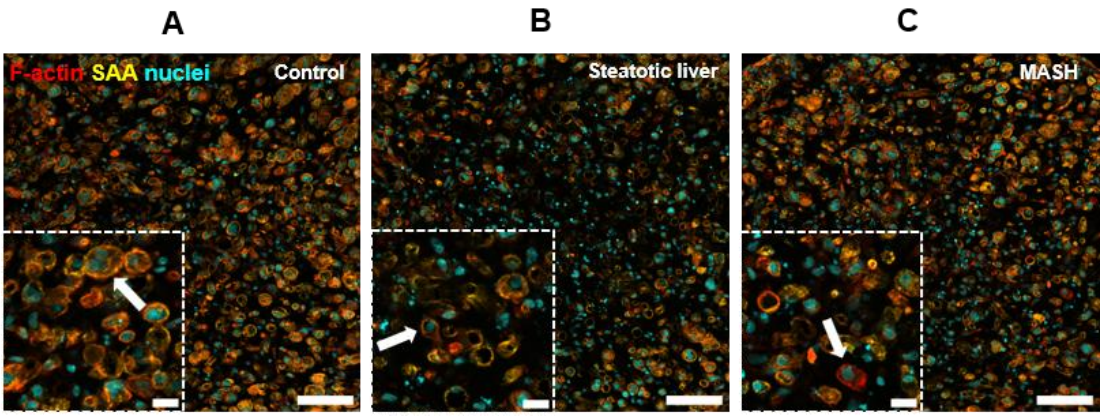


Figure 5.15. Histological examination of myotube morphology and size.
Representative confocal images of 3D skeletal muscle tissue cryosections stained against sarcomeric α-actinin (SAA), f-actin, and nuclei. A) Treated with CM from healthy livers. B) Treated with CM from steatotic livers. C) Treated with CM from MASH-like livers. White arrows point at representative myotube sizes. Scale bar = 50 µm. Inset scale bar = 10 µm.

Qualitatively, both SL- and MASH-treated tissues displayed compromised myotube integrity relative to controls, with more heterogeneous fiber calibers and regions of apparent thinning (Figure 5.15B-C). Histogram analysis of myotube diameters showed an overall shift towards smaller myotubes in size distribution for both SL- and MASH-treated tissues, indicating a greater proportion of smaller fibers compared to control tissues, which were treated with CM from healthy liver constructs (Figure 5.16).

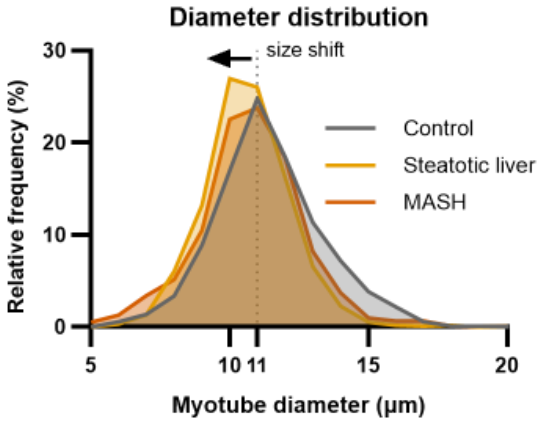


Figure 5.16. Overlapped distribution of myotube size across experimental groups.
Diameter distribution of myotubes observed by confocal microscopy. Biological replicates: n = 6 per experimental group.

Quantitatively, SL-CM induced the most pronounced structural atrophy. Myotube median diameter decreased by 6.5% (p=0.003), and myotube cross-sectional area declined by 10.0% (p=0.02) relative to

control muscles. In contrast, MASH-CM caused only modest, non-significant reductions in diameter (-2.8%, p>0.05) and area (-6.0%, p>0.05), despite producing the largest functional impairment (Figure 5.17).

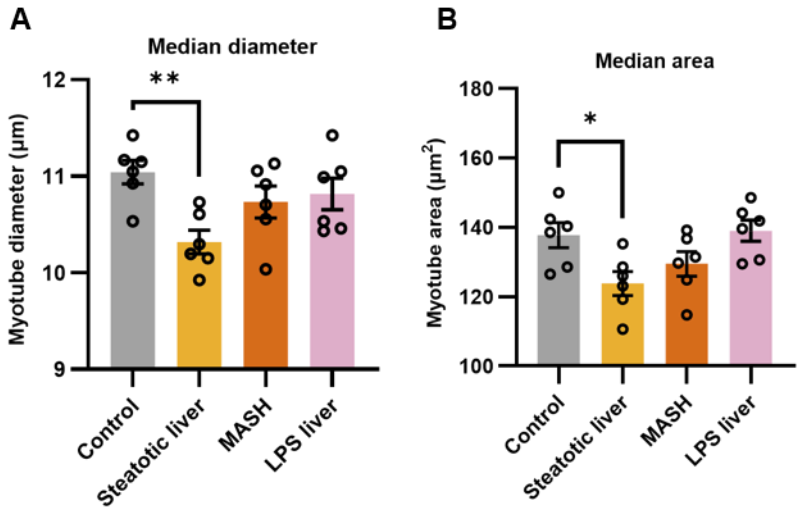


Figure 5.17. Morphometric evaluation of skeletal muscle tissues after exposure to CM from the liver model. A) Median myotube diameter. B) Median myotube area. Results are expressed as mean ± SEM. Differences between means tested by one-way ANOVA followed by Dunnett's post-hoc tests when appropriate. * p < 0.05; ** p < 0.01.

These findings indicate that while MASLD-derived SFs can directly trigger myotube atrophy—most clearly under SL-like conditions—structural changes visible in myotube size alone do not fully account for the severity of the contractile deficit observed under MASH-like exposure.

5.4.5 MASLD-derived factors repress canonical atrogenes and alter the myogenic program

Given the reduction in myotube size under SL-CM, we next examined whether classical proteolytic pathways associated with muscle atrophy were engaged. The ubiquitin–proteasome system, particularly the muscle-specific E3 ligases atrogin-1 (*FBXO32*) and MuRF1 (*TRIM63*), are well-established effectors of muscle wasting in diverse catabolic states. We therefore quantified the relative expression of *FBXO32* and *TRIM63* by qRT-PCR in 3D skeletal muscle tissues after exposure to liver-derived CM.

Contrary to our initial expectation that atrophy would be accompanied by atrogene induction, both *FBXO32* and *TRIM63* were significantly downregulated in muscles exposed to diseased-liver CM. SL-CM reduced *FBXO32* expression by 29.6% (p=0.02) and *TRIM63* expression by 4.0% (p>0.05), whereas MASH-CM elicited a more pronounced suppression of both *FBXO32* (-57.6%, p<0.001) and

TRIM63 (-46.8%, p=0.02) (Figure 5.18). This pattern suggests that MASLD-induced muscle dysfunction in this model does not rely on the canonical ubiquitin–proteasome–mediated atrophy program and instead engages alternative pathways of muscle remodeling and protein balance.

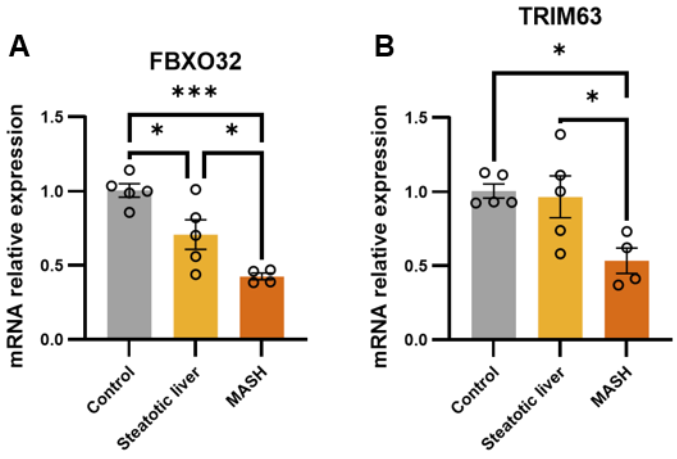


Figure 5.18. Relative expression of atrogenes in 3D skeletal muscle tissues after exposure to CM from the liver constructs.

A) *FBXO32*. B) *TRIM63*. Genes RPL0P and *B2M* were used as the housekeeping genes. Expression levels were calculated by the ΔΔCt method. Results are expressed as mean ± SEM and compared using one-way ANOVA followed by Tukey's or Dunnett's post hoc tests when appropriate. * p < 0.05; ** p < 0.01; *** p < 0.001.

To better understand how MASLD-derived SFs influence muscle regeneration and differentiation, we also profiled myogenic regulatory factors (MRFs) and a marker of terminal differentiation in skeletal muscle. *MYOG* and *MYOD1* work sequentially to drive skeletal muscle formation and regeneration. Under SL-CM, both genes showed non-significant upward trends (+35.5% and +82.5%, respectively; p>0.05), suggesting an early response to the stimulus provided by the SL environment. Under the MASH-like environment, expression levels of *MYOG* and *MYOD1* returned to levels closer to the control condition, showing no statistically significant differences to them (Figure 5.19).

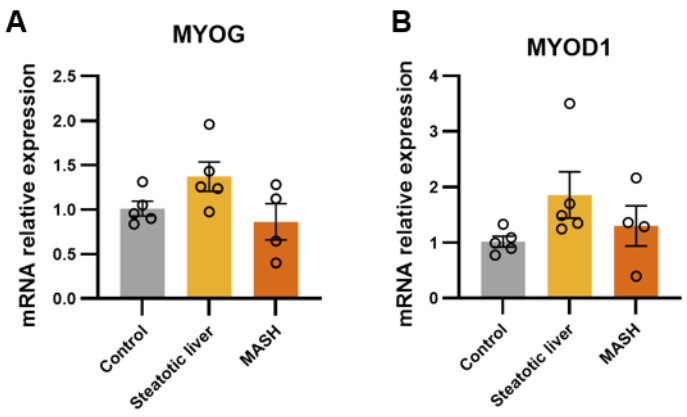


Figure 5.19. Relative expression of MRFs in 3D skeletal muscle tissues after exposure to CM from the liver constructs.

A) *MYOG*. B) *MYOD1*. Genes RPL0P and *B2M* were used as the housekeeping genes. Expression levels were calculated by the ΔΔCt method. Results are expressed as mean ± SEM and compared using one-way ANOVA followed by Tukey's or Dunnett's post hoc tests when appropriate. * $p < 0.05$; ** $p < 0.01$; *** $p < 0.001$.

Further examination of the MRFs revealed decreases proportional to liver disease severity, a behavior observed often in several phenotypes. Both *MYF5* and *MYF6* genes code for crucial transcription factors involved in muscle differentiation. While *MYF5* initiates myoblast specification, determination, and proliferation during embryonic development, *MYF6* operates during later muscle formation, facilitating terminal differentiation and adult muscle maturation. SL-CM triggered a 37.7% decrease ($p=0.07$) in *MYF5* expression and a very mild, non-significant 9.8% decrease ($p>0.05$) in *MYF6* expression. In contrast, under the MASH-like environment, the exposure significantly downregulated *MYF5* (-57.4%, $p=0.01$) and *MYF6* (-46.9%, $p=0.01$), indicating suppression of early and intermediate myogenic programs in the context of severe liver-derived injury (Figure 5.20).

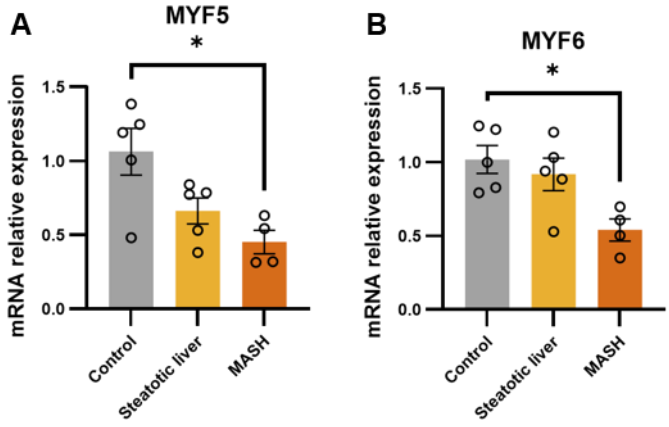


Figure 5.20. Relative expression of MRFs in 3D skeletal muscle tissues after exposure to CM from the liver constructs.

A) *MYF5*. B) *MYF6*. Genes RPL0P and *B2M* were used as the housekeeping genes. Expression levels were calculated by the ΔΔCt method. Results are expressed as mean ± SEM and compared using one-way ANOVA followed by Tukey's or Dunnett's post hoc tests when appropriate. * $p < 0.05$.

The terminal differentiation marker *MYH7* (β-myosin heavy chain) encodes for a protein essential for muscle contraction. It exhibited progressive downregulation across conditions, with a 29.0% ($p>0.05$) non-significant reduction in SL-treated tissues and reaching significance in MASH-treated muscles (-58.9%, $p=0.008$) (Figure 5.21).

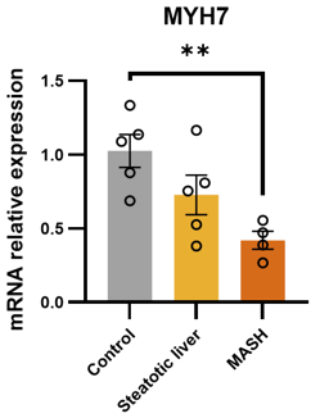


Figure 5.21. Relative expression of terminal differentiation marker *MYH7* in 3D skeletal muscle tissues after exposure to CM from the liver constructs.

Genes RPL0P and *B2M* were used as the housekeeping genes. Expression levels were calculated by the ΔΔCt method. Results are expressed as mean ± SEM and compared using one-way ANOVA followed by Tukey's or Dunnett's post hoc tests when appropriate. * $p < 0.05$; ** $p < 0.01$.

Altogether, these data reveal that MASLD-derived SFs induce changes in the myogenic landscape, characterized by repression of canonical atrogenes and a severity-dependent disruption of myogenic regulatory factors, particularly under MASH-like conditions. SL-like exposure appears to trigger a mixed phenotype combining moderate atrophy with compensatory myogenic signaling, whereas MASH-like exposure suppresses key myogenic drivers and terminal differentiation markers.

5.4.6 MASLD-conditioned media enhance autophagy and lysosomal activity in skeletal muscles

Autophagy and lysosome pathways are central to muscle protein homeostasis and are increasingly implicated in both metabolic diseases and muscle wasting syndromes. Given the previous observations regarding the unexpected suppression of well-established atrogenes, we wanted to determine whether autophagy dysregulation contributes to the MASLD-induced decrease in myotube size in our model. We evaluated lysosomal and autophagosomal compartments at the histological level using LysoTracker staining and LC3B immunostaining on skeletal muscle tissue cryosections, respectively. LysoTracker Red DND-99 (LTR99) dye labels acidic organelles, including lysosomes and autophagolysosomes, whereas LC3B puncta reflect autophagosome formation via accumulation of the lipidated LC3-II form on autophagosomal membranes [263].

Control muscles displayed a low, diffuse LTR99 signal distributed throughout the sarcoplasm, consistent with basal lysosomal activity in homeostatic conditions. In contrast, tissues treated with SL- or MASH-derived CM exhibited prominent punctate LTR99 patterns, indicative of increased acidic compartment formation and clustering (Figure 5.22).

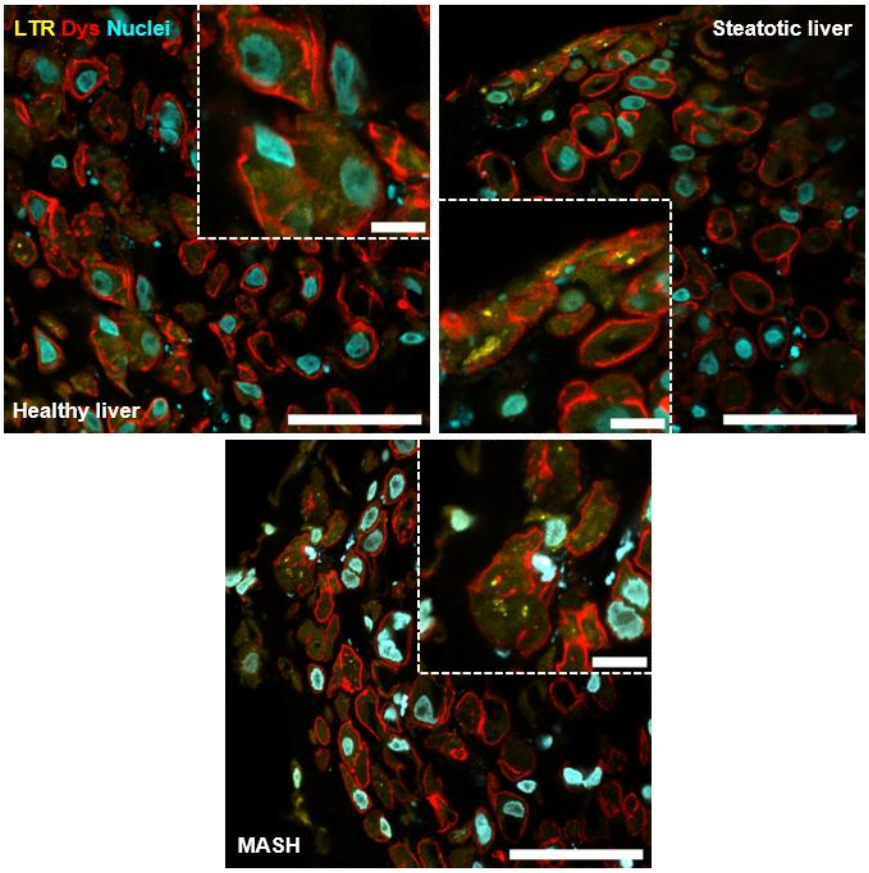


Figure 5.22. Acidic compartments on tissue cryosections after exposure to CM from liver constructs.
Representative confocal images of cryosections stained with an antibody against dystrophin, LysoTracker™ Red DND-99 (LTR), and DAPI. Scale bar = 50 µm. Inset scale bar = 10 µm.

Quantitative analysis confirmed a progressive increase of lysosome-associated structures: SL-CM induced a non-significant rise in puncta density, whereas MASH-CM triggered a robust 153.5% increase in LTR99-positive puncta (p=0.005), with significant differences between SL and MASH groups (p=0.01) (Figure 5.23). This pattern suggests enhanced lysosomal biogenesis or accumulation under MASH-like conditions.

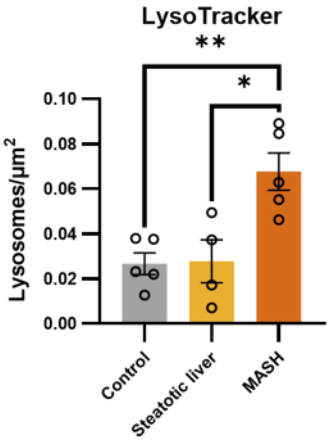


Figure 5.23. Quantification of acidic compartments on tissue cryosections.
Stained with LysoTracker™ Red DND-99 (LTR) after exposure to CM from liver constructs. Results are expressed as mean ± SEM and compared using one-way ANOVA followed by Tukey's or Dunnett's post hoc tests when appropriate. * $p < 0.05$; ** $p < 0.01$.

LC3B staining further supported the presence of an altered autophagic response. Control samples showed diffuse, cloud-like staining patterns of LC3B protein. In tissues exposed to the environment from diseased liver constructs, LC3B puncta were visibly elevated in both intensity and number per myotube compared to controls (Figure 5.24).

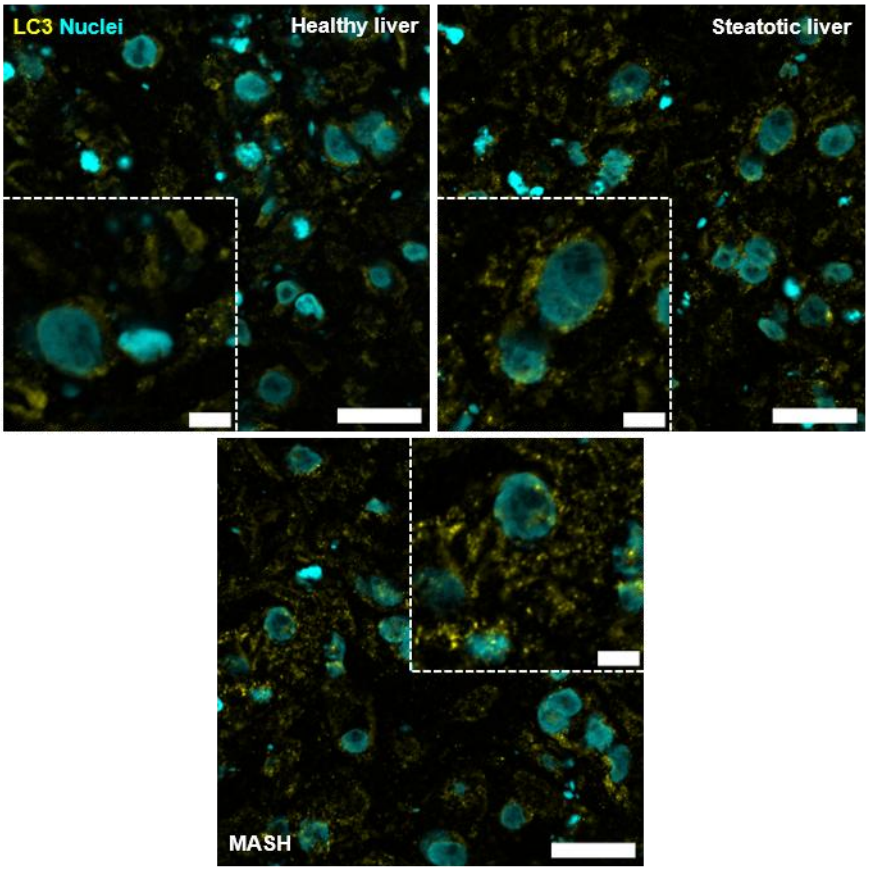


Figure 5.24. LC3 puncta on tissue cryosections after exposure to CM from liver constructs.
Representative confocal images of cryosections stained against LC3B protein and DAPI. Scale bar = 20 µm. Inset scale bar = 50 µm.

Quantification revealed that SL-CM increased LC3B puncta by 46.8% (p=0.03), while MASH-CM produced a 59.0% increase (p=0.01), behaving similar to the LysoTracker findings and indicating a stage-dependent enhancement of autophagosome formation with increasing liver disease severity (Figure 5.25).

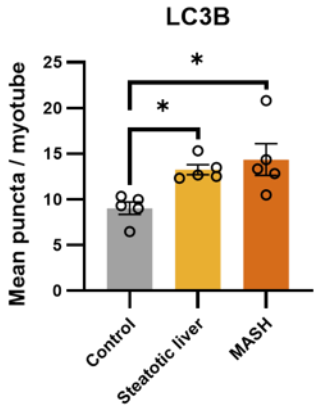


Figure 5.25. Quantification of LC3 puncta on tissue cryosections.
Staining against LC3B protein after exposure to CM from liver constructs. Results are expressed as mean ± SEM and compared using one-way ANOVA followed by Tukey's or Dunnett's post hoc tests when appropriate. * $p < 0.05$.

Overall, the autophagy–lysosome data indicate that MASLD-derived SFs induce a progressive activation of autophagy-related pathways in skeletal muscle, with the strongest alterations observed under MASH-like exposure. Coupled with the repression of canonical atrogenes and disruption of myogenic regulators, these findings support that muscle wasting may arise from a complex imbalance in protein homeostasis that integrates altered lysosomal/autophagosomal dynamics, non-canonical protein turnover programs, and impaired myogenic differentiation rather than from a simple activation of classical ubiquitin–proteasome–mediated atrophy.

5.5 Discussion

MASLD has emerged as a paradigmatic multi-organ condition in which hepatic lipid overload, inflammation, and fibrosis converge with systemic metabolic dysregulation to impair distant tissues, including skeletal muscle. Clinical studies consistently report reduced muscle strength, exercise intolerance, and altered body composition across the MASLD spectrum. Furthermore, sarcopenia and muscle-wasting phenotypes affect up to 43% of patients, often with disproportionate functional impairment relative to muscle mass [262]. In this chapter, building on the MASLD–MASH liver platform presented previously in Chapter 4, we used a human 3D skeletal muscle model to investigate if stage-specific liver SFs drive muscle dysfunction. We integrated functional, structural, transcriptional, and autophagy–lysosome readouts. Our findings support a model in which progressive MASLD-like injury elicits a muscle quality–dominated phenotype characterized by severity-dependent contractile deficits, partial dissociation between mass and function, repression of canonical atrogenes, disruption of myogenic programs, and graded activation of autophagy-related pathways.

5.5.1 MASLD-derived factors reproduce severity-dependent functional impairment and dissociation between muscle mass and strength

The first key observation is that CM from diseased liver constructs is sufficient to induce a graded decline in contractile performance of mature 3D skeletal muscle tissues. Exposure to SL-CM already caused a marked reduction in twitch and tetanic forces, and CM from MASH-like livers further exacerbated this deficit, particularly at higher stimulation frequencies that approximate intense or sustained muscle activity. This severity-dependent pattern recapitulates clinical observations linking more advanced MASLD to lower muscle strength and greater fatigability, suggesting that the milieu of cytokines, growth factors, and metabolic byproducts secreted by the diseased liver can compromise contractility in a stage-dependent manner [262].

We observed a non-linear relationship between disease severity and functional decline in the skeletal muscles. The largest drop in function occurred between control and SL-treated samples. Even though the MASH-treated muscles showed further decrements in function, the drop was relatively more modest, despite a clear worsening of several liver injury markers in this stage. These findings are consistent with reported dissociations between muscle mass and performance in patients [264].

This plateau-like behavior is consistent with the notion that muscle becomes progressively less responsive to incremental hepatotoxic stress once key signaling and metabolic pathways are affected, resulting in a ceiling effect for functional decline like that described clinically in advanced chronic liver disease [262]. Together, these data underscore that liver-derived factors alone are sufficient to produce a MASLD-like functional phenotype in 3D skeletal muscles.

5.5.2 Myotube structural changes contribute to, but do not fully explain, contractile deficits

Histological analysis revealed that MASLD-CM altered myotube integrity and size, but these structural changes did not fully account for the severity of functional impairment. SL-CM produced the greatest reduction in myotube diameter and cross-sectional area, consistent with true wasting driven by catabolic cues, whereas MASH-CM caused smaller, non-significant decreases in fiber size despite inducing the most severe contractile deficit. This uncoupling between gross morphometry and force generation reinforces clinical observations that muscle quality—encompassing fiber composition, excitation–contraction coupling, mitochondrial function, and intracellular organization—is a more informative determinant of outcomes than raw muscle mass in MASLD and related liver diseases.

Our data therefore support a model in which MASLD-derived factors exert at least two partially overlapping effects in muscle. The first is dominated by a marked decrease in muscle mass and only subtle contractile impairment, as captured by SL-CM. The second is consistent with a more advanced phase in which intrinsic muscle dysfunction predominates over further changes in fiber size, as captured by MASH-CM. While the present work cannot resolve all underlying mechanisms, subsequent analyses

of protein homeostasis regulators, myogenic transcription factors, and autophagy–lysosome dynamics point to a complex remodeling of muscle homeostasis beyond canonical catabolic pathways.

5.5.3 Downregulation of canonical atrogenes suggests non-classical mechanisms of muscle wasting

Muscle weakness can arise from reduced fiber size, impaired contractile machinery, or metabolic and energetic dysfunction. In MASLD–associated sarcopenia and muscle wasting, circulating factors are thought to mediate these impairments, and our findings support this paradigm. Among the mediators elevated in our system, IL-6 trans-signaling appears particularly relevant. While transient IL-6 production by muscle supports regeneration and adaptation, systemic chronic elevation—as observed in MASH—disrupts myogenic differentiation and promotes catabolism via JAK/STAT3 and related pathways [265,266], leading to upregulation of muscle-specific E3 ubiquitin ligases such as atrogin-1 (*FBXO32*) and MuRF1 (*TRIM63*) [267,268]. Sustained IL-6 exposure can also interfere with IGF1 signaling, impairing muscle growth and shifting the balance toward protein degradation [269].

Beyond its effects on protein turnover, IL-6–driven metabolic disruption may contribute to functional impairment through redox and mitochondrial stress. Elevated circulating IL-6 in mice disrupts skeletal muscle redox balance by altering nuclear factor erythroid 2–related factor 2 (Nrf2) signaling, suppressing antioxidant defense genes and activating autophagy and ubiquitin–proteasome pathways [270]. Consistent with this, we observe increased lysosomal biogenesis and autophagic bodies in MASH-treated tissues.

To assess whether canonical atrogene upregulation could underlie the decline in myotube size, we measured the relative expression of *FBXO32* and *TRIM63*. However, we observed an unexpected downregulation of both atrogenes, despite the evidence of fiber size reduction under SL-CM and MASH-CM. These ligases are prototypical mediators of proteasome-dependent protein degradation in diverse atrophy models, including denervation, cancer cachexia, and glucocorticoid excess, and their upregulation is often used as a molecular hallmark of catabolic signaling [271]. In our system, however, both genes were significantly repressed by diseased-liver CM, with the strongest suppression under MASH-like conditions.

This pattern aligns with emerging data indicating that *FBXO32* and *TRIM63* are not uniformly upregulated across all forms of muscle wasting, particularly in metabolic disorders and aging-associated sarcopenia. Increasing evidence has demonstrated that atrogene expression profiles can vary substantially across types of atrophy models, most of them rodent models. Different pathological contexts appear to engage distinct combinations of proteolytic systems and adaptive responses [272]. The repression of atrogenes observed here suggests that MASLD-associated muscle wasting is mediated by other non-classical protein homeostasis programs, potentially involving altered autophagy–lysosome flux, impaired myofibrillar turnover, or shifts in protein synthesis rather than a simple activation of ubiquitin–proteasome degradation. This interpretation is supported by the autophagy-related findings

discussed below and highlights the value of human, disease-relevant models for revealing atypical molecular signatures that might be obscured in generic atrophy paradigms.

One potential contributor to this atypical response is IL-8, which was markedly elevated in CM from MASH-like liver constructs. While IL-8 acts in the liver as a chemoattractant with strong pro-inflammatory effects, its systemic actions on skeletal muscle appear more complex. IL-8 has been reported to exert anti-catabolic effects by enhancing Akt phosphorylation, inactivating FoxO3 transcription factor, and reducing its levels in rat skeletal muscle cells, leading to decreased expression of atrogin-1 and MuRF1 and increased myotube diameter [273]. In our human cell system, elevated IL-8 may therefore contribute to the paradoxical preservation of myotube size in MASH-treated muscles despite pronounced functional impairment. This suggests that IL-8 could be part of a liver–muscle strategy aimed at delaying atrophy during early stages of sustained hepatic stress. However, we speculate that prolonged exposure to a MASH-like environment (>48 h) may eventually overwhelm this compensation, resulting in activation of canonical atrogenes and more pronounced muscle wasting. This is an interesting direction for future work modeling the time-dependent effect of diseased liver on healthy differentiated skeletal muscle.

5.5.4 Myogenic program remodeling under steatotic liver- and MASH-like conditions

To further understand how MASLD-derived factors reshape muscle homeostasis, we examined the expression of key myogenic regulatory factors and a marker of terminal differentiation. Myogenin (*MYOG*) and myogenic differentiation 1 (*MYOD1*) are central transcriptional regulators of myogenic commitment and differentiation. Under SL-CM, *MYOG* and *MYOD1* exhibited non-significant upward trends, suggesting an early compensatory attempt to sustain or enhance myogenic commitment and differentiation in the face of catabolic stress. Similar dysregulation of myogenic regulators, deviating from healthy groups, has been reported in sarcopenia, where such changes are thought to partially counteract protein degradation and functional decline [274–277]. This is consistent with observations in other settings of subclinical or early muscle injury, where modest elevations of IL-6 and other cytokines can transiently promote myoblast activation and fusion by initiating transcription of *MYOD1* and *MYOG*, and this potentially preserves muscle structure. In line with this interpretation, *MYF5* expression showed a slight, non-significant decrease, suggesting that *MYF5* activity may give way to *MYOD1*-driven differentiation.

However, this compensatory response appears insufficient under exposure to MASH-like secreted factors. In MASH-treated tissues, *MYOG* and *MYOD1* expression returned toward control levels, while *MYF5* and *MYF6* expression declined further, consistent with a repression of early myogenic programs in a chronic inflammatory environment [274]. Supporting this interpretation, expression of myosin heavy chain 7 (*MYH7*), a key sarcomeric motor protein and marker of myogenic maturation, was significantly reduced in MASH-treated muscles, indicating impaired terminal differentiation. Such differentiation blockade has been observed following exposure to pro-inflammatory CM from obese individuals, which impairs the nuclear fusion index (NFI), a direct indicator of myoblast differentiation [278]. Similar effects

have been described in murine cells responding to LPS treatment by downregulating *MYH7* expression, supporting the presence of muscle wasting and dedifferentiation processes in response to circulating factors from peripheral tissues [279], as in MASLD-associated leaky gut.

Elevated PDGF-BB in the MASH-CM is likely another contributing factor to this phenotype. Beyond its established role in fibrogenic signaling, PDGF-BB is a potent mitogen that actively inhibits myogenic differentiation and promotes a more proliferative, less differentiated state [280,281]. Together, these findings suggest that early stage MASLD-derived signals initially trigger compensatory myogenic programs, but exposure to a MASH-like inflammatory and growth factor milieu suppresses differentiation, contributing to impaired muscle quality despite relatively preserved myotube size.

Taken together, these data support a two-stage view of myogenic remodeling under MASLD-like exposure: SL-derived signals induce a mixed phenotype combining moderate atrophy with compensatory myogenic activation, whereas MASH-like signals suppress key myogenic regulators and terminal markers, undermining regenerative capacity and contributing to functional decline even when myotube size appears partially preserved.

5.5.5 Autophagy–lysosome remodeling as a central axis of MASLD-induced muscle dysfunction

The lysosome and autophagy experiments emerged as an alternative to canonical atrogene activation, and as a key node in MASLD-induced muscle pathology. We examined acidic compartment abundance as a marker of intracellular degradative activity. LysoTracker staining revealed a progressive increase in acidic compartment density across conditions, with a significant 153.5% rise in puncta under MASH-CM and a clear shift toward clustered lysosomal structures, phenotypes that have been associated with metabolic stress and altered lysosomal function in other systems [263], reflecting altered cargo flux, organelle turnover, and cellular homeostasis. In parallel, LC3B puncta were increased under both SL- and MASH-CM, consistent with enhanced autophagosome formation.

We also observed increased LC3B (microtubule-associated protein light chain 3B) puncta following exposure to SL and MASH environments. LC3B puncta accumulation may indicate enhanced autophagosome formation. Metabolic cues such as elevated FFAs and other lipid derivatives have been shown to disrupt autophagosome–lysosome cooperation, leading to cytoplasmic accumulation of autophagosomes [263,282,283].

These findings indicate that MASLD-derived factors influence autophagy-related pathways in skeletal muscle, but the directionality—adaptive versus maladaptive—remains outside the scope of this work. On one hand, increased autophagosome formation and lysosomal biogenesis may represent an attempt to clear damaged organelles and protein aggregates in response to lipotoxic and inflammatory insults. On the other, persistent LC3B accumulation and expansion of lysosomal compartments can reflect impaired autophagic flux, particularly in the presence of elevated free fatty acids from damaged

hepatocytes and cytokine exposure, which have been shown to disrupt autophagosome–lysosome cooperation. In such a scenario, autophagy initiation is uncoupled from effective degradation, leading to accumulation of intermediate structures that may themselves interfere with other biological functions like contraction, calcium handling, or mitochondrial dynamics.

Our results therefore point to autophagy–lysosome dysregulation as one of the mechanisms underlying MASLD-associated muscle quality decline, complementing the observed repression of atrogenes and disruption of myogenic programs. Future work will be required to distinguish whether the predominant defect lies in autophagy initiation, cargo recognition, vesicle trafficking, or lysosomal degradative capacity, and to map how these alterations intersect mitochondrial integrity and oxidative stress in this context.

5.5.6 Integration with liver module: a multi-layered liver–muscle axis

The integrated liver–muscle platform developed across Chapters 4 and 5 provides a mechanistic framework for understanding how staged MASLD-like injury is translated into muscle dysfunction through circulating factors. The liver constructs used to generate CM exhibit well-characterized phenotypes from steatosis and MASH-like states. The hepatic signatures are mirrored in the muscle module by severity-dependent contractile decline, partial mass–function dissociation, repression of canonical atrogenes, remodeling of the myogenic program, and influence in autophagy–lysosome systems.

Among the mediators implicated in this axis, IL-6 and IL-8 are particularly notable. Chronic IL-6 elevation has been linked to impaired myogenesis, increased catabolism, and activation of autophagy–proteasome pathways, whereas IL-8 can exert anti-catabolic effects on muscle by enhancing Akt signaling and suppressing FoxO3-dependent atrogene expression. The paradoxical combination of severe functional impairment with relatively preserved myotube size under MASH-CM may therefore reflect a complex balance between IL-6–driven protein homeostasis stress and IL-8–mediated anti-atrophic compensation, superimposed on a background of PDGF-BB-induced differentiation decrease. In this view, MASLD-associated muscle wasting is not a simple monotonic process of atrophy, but rather a dynamic competition between injury and potentially compensatory signals that collectively shape muscle quality and regenerative potential under CM exposure.

5.5.7 Limitations and future directions

While this chapter demonstrates that MASLD-derived factors can recapitulate key aspects of clinical muscle impairment in a human 3D model, several limitations should be acknowledged to contextualize the findings and guide future experiments. First, the exposure design relied on a 48-hour CM treatment at a fixed dilution chosen to avoid overt toxicity of liver culture medium on muscle tissues. Although this was sufficient to uncover robust functional and molecular changes, it does not capture the chronicity of

MASLD-associated systemic exposure, and longer treatment paradigms will be necessary to model cumulative, potentially irreversible damage in the context of unresolved MASLD.

Second, the skeletal muscle module incorporates immortalized myoblasts only and lacks communication with additional tissue models other than the liver, which are increasingly recognized as critical regulators of muscle homeostasis in metabolic disease. The absence of well-characterized satellite cell and fibroadipogenic progenitor (FAP) pools likely simplifies clinical phenotypes of MASLD-associated sarcopenia and muscle wasting, particularly with respect to myogenesis and myosteatosis. Incorporating these additional cell types or combining the current platform with adipose components would enable more comprehensive analysis of MASLD-driven muscle pathology, at the expense of further optimizations like the one carried out with culture media.

Third, our autophagy assessment relied on static imaging of LC3B and LysoTracker-positive compartments, which cannot definitively distinguish between enhanced autophagy initiation and impaired degradation. Flux assays using lysosomal inhibitors, live-cell reporters, or complementary readouts of mitochondrial quality control will be required to dissect the precise nature of autophagy–lysosome alterations and to test whether targeted modulation of this pathway can rescue skeletal muscle mass and function.

Finally, as with the liver module, our platform currently uses immortalized cell lines and defined NEFAs+LPS insults, which offer standardization and reproducibility but do not fully recapitulate the genetic, dietary, and microbiome-related drivers of MASLD in patients. Outside the scope of this work, more complex explorations incorporating patient-derived myogenic cells from individuals with distinct MASLD phenotypes, would enable stratification of muscle responses by genotype, metabolic profile, or clinical stage and supporting more personalized mechanistic and therapeutic investigations.

5.5.8 Implications for MASLD-associated muscle wasting and translational opportunities

The present work provides several conceptual advances for understanding and targeting MASLD-associated muscle wasting while presenting a modular *in vitro* platform for the study of its extra-hepatic implications. First, it establishes that stage-specific hepatic secreted factors in the absence of systemic confounders, are sufficient to produce severity-dependent functional decline, partial structural atrophy, non-canonical protein balance signatures, and autophagy–lysosome remodeling. Second, it highlights that classical atrogenes may not fully explain muscle wasting in metabolic liver disease, emphasizing the need to broaden therapeutic strategies beyond inhibition of ubiquitin–proteasome pathways. Third, by employing functional readouts in a modular multi-tissue platform, the system provides a useful tool to evaluate either liver or muscle interventions. For this author, anti-inflammatory or anti-fibrotic agents pose the most interesting and best suited strategies to explore in the future with this MASLD model. On the muscle side, exercise mimetics that resemble clinical treatment of

sarcopenia, autophagy modulators, or myogenic enhancers can offer quantifiable data on performance, structure, and molecular signatures.

In summary, Chapter 5 situates skeletal muscle as an active, dynamically regulated target of MASLD-derived signals, whose fate is shaped by the interplay between inflammatory, growth factor, and protein homeostasis pathways influenced by the liver. The human 3D liver–muscle platform described here offers a mechanistically grounded, ethically aligned, and scalable approach to disentangle these interactions and to identify actionable nodes for preventing or reversing liver-driven muscle wasting in MASLD and related conditions.

Chapter 6 | Organ-on-Chip Device for Liver-Skeletal Muscle Interrogation

6.1 Introduction

Organs-on-chips are micro engineered culture systems in which human cells are organized within perfused microfluidic architectures designed to reproduce a minimal functional unit of an organ. They combine controlled flow, defined 3D geometry, mechanical and electrical stimulation, and often multiple cell types and extracellular matrix components to recapitulate organ-level functions with far greater physiological relevance than 2D culture, while avoiding many interspecies differences of animal models. Recent syntheses have emphasized the role of these systems as engineered tissue constructs built using the tools of tissue engineering and microfluidics [284].

Over the last decade, organs-on-chips have moved from proof-of-concept devices to broadly used platforms for biological research and preclinical testing. Comprehensive reviews highlight how cardiac, liver, gut, kidney, lung, vascular and tumor chips are now used to study human development and pathophysiology, to predict drug efficacy and toxicity, and to model complex systemic phenomena when multiple compartments are fluidically coupled. At the same time, clinical translation will stress the need for industry-compatible materials, integrated sensing, higher-throughput and more standardized operation, and formal validation against clinical and *in vivo* data, framing organs-on-chips as a promising route to more predictive human models for drug development and, eventually, personalized medicine [285–287].

6.1.1 Contribution statement and collaborative framework

The organ-on-chip work presented in this chapter was developed in collaboration with Dr. Carolina Rodríguez-Gallo, whose background in condensed matter physics, colloidal systems, and microfluidic flow provided essential physical and mathematical expertise for the engineering component of this thesis. Her contribution was central to the microfluidic design process, chip fabrication, characterization strategy, experimental design, mixing and dilution experiments. I gratefully acknowledge her work, technical guidance, and conceptual contribution to the development and characterization of the first-generation liver–skeletal muscle microfluidic device.

My contribution consisted of defining the biological rationale and overall design requirements of the device within the context of the modular liver–muscle platform developed in this thesis. Specifically, I contributed to the device conceptualization, material selection, initial CAD design iterations, definition of physical dimensions and required microfluidic elements, arrangement of the 3D tissue culture chambers, dilution/mixing unit, the experimental characterization needed to translate the static CM experiments into a pressure-driven microfluidic format. I also contributed to the experimental design throughout the pipeline and to the interpretation of the fluidic characterization results in relation to MASLD-associated liver–skeletal muscle crosstalk. Therefore, this chapter is a collaborative engineering step that establishes the fluidic basis for future dynamic organ-on-chip integration of the liver and skeletal muscle modules.

6.1.2 Positioning of the Organ-on-Chip device

OoC devices have emerged as powerful *in vitro* systems that integrate microfluidics, biomaterials, and tissue engineering to recreate key aspects of human organ physiology and pathophysiology under controlled flow. In contrast to conventional static cultures, these platforms aim to reproduce tissue-level structure, mechanical cues, and dynamic exposure to soluble factors, thereby improving the predictive value of preclinical models for disease mechanisms and drug responses [285,288–294]. Within this technological landscape, the present thesis explores MASLD-associated liver–skeletal muscle crosstalk using human 3D bioengineered tissues, and Chapter 6 represents the first engineering step toward a dynamic multi-organ-on-chip implementation of this axis.

The preceding chapters established that 3D collagen-based liver constructs combining hepatocyte-like and HSCs can generate disease-stage–specific CM, and that exposure of differentiated 3D skeletal muscle tissues to these media under static conditions can induce structural and functional alterations consistent with muscle dysfunction. However, static conditioned-medium transfer does not capture continuous inter-organ communication, time-dependent concentration profiles, or flow-dependent phenomena that are central to systemic metabolic diseases [285]. Chapter 6 is therefore deliberately framed as a technical bridge. It does not yet present a fully validated dynamic MASLD liver–muscle OoC, but rather a first-generation liver–skeletal-muscle device that establishes the fluidic basis for future live-tissue co-culture under flow (Figure 6.1).

6.1.3 Biological motivation behind the Organ-on-Chip device

Metabolic dysfunction-associated steatotic liver disease (MASLD), including its progressive inflammatory and fibrogenic form MASH, has become one of the most prevalent chronic liver diseases worldwide, tightly linked to obesity, insulin resistance, and type 2 diabetes. Beyond its intrahepatic manifestations, MASLD is increasingly recognized as a systemic disorder that affects extrahepatic organs, including skeletal muscle, via complex metabolic, endocrine, and inflammatory mechanisms.

Clinical and experimental studies have documented a high prevalence of sarcopenia—defined as loss of skeletal muscle mass and function—in MASLD patients and suggest a bidirectional relationship in which muscle dysfunction both contributes to and results from hepatic steatosis and fibrosis [295,296].

Skeletal muscle is a major site of glucose disposal and lipid oxidation, and its impairment exacerbates insulin resistance, fat accumulation, and systemic inflammation, thereby promoting MASLD progression. Conversely, hepatic steatosis, lipotoxicity, and low-grade inflammation can alter circulating metabolite and cytokine profiles, impacting muscle protein turnover, mitochondrial function, and regenerative capacity. This interdependence has led to the conceptualization of a “liver–muscle axis” in metabolic disease, in which hepatokines, myokines, and metabolic intermediates cooperatively shape disease trajectories [296,297]. The thesis focuses not on isolated candidate factors, but on disease-stage–specific liver CM as integrated hepatic signals that modulate engineered skeletal muscle tissues.

6.1.4 From conditioned medium transfer to dynamic organ-on-chip

In the static 3D platform developed in earlier chapters, CM from 3D MASLD-like liver constructs were collected, diluted with skeletal muscle differentiation medium, and then applied in batch to differentiated 3D skeletal muscle tissues for defined exposure periods. This strategy enabled precise control of exposure concentration and duration, and it revealed that insufficiently diluted liver media were strongly disruptive to muscle tissues, whereas a 1:50 dilution in skeletal muscle differentiation medium was compatible with maintaining viable tissues and revealing disease-stage–specific phenotypes. Nevertheless, static CM transfer inherently lacks continuous inflow and outflow, does not reproduce physiologic perfusion patterns, and cannot capture dynamic feedback between coupled tissues.

Organ-on-chip technology offers a natural route to address these limitations by integrating the existing 3D liver and functional differentiated skeletal muscle modules into a microfluidic architecture that supports continuous, pressure-driven flow of liver-derived secretomes toward the muscle compartment. In this configuration, liver constructs can be perfused in real time, and the resulting effluent can be diluted, mixed, and delivered to skeletal muscle tissues. This would allow the investigation of time-dependent responses and repeated challenges in future multi-organ setups. The central challenge, however, is to translate the empirically determined static exposure condition—a 1:50 dilution of liver medium—into a microfluidic environment where flow rate, channel geometry, and diffusion together govern the composition experienced by muscle tissues.

6.1.5 Organ-on-chip and microfluidic background

OoC systems are built on microfluidic principles: at the typical length scales of microchannels, flows usually operate at low Reynolds numbers, where viscous forces dominate over inertial forces and laminar flow is commonly achieved. Under laminar conditions, when two liquids are brought into contact within a channel, they tend to flow as parallel streams separated by a relatively stable interface. Under

this condition, mixing is then governed primarily by molecular diffusion across this interface rather than by turbulence. The characteristic diffusion time depends on the diffusion coefficient of the solute and on the square of the diffusion distance, so efficient mixing over short channel lengths often requires strategies to reduce the effective diffusion path or to continually deform the interface [298,299].

Micromixers are broadly classified as active, which rely on external energy inputs to stir or perturb the flow, and passive, which use only geometric features and pressure-driven flow to enhance interface stretching and folding. Active micromixers can achieve high mixing efficiency but typically require integrated actuators or fields, increasing device complexity and potentially imposing constraints on cell culture compatibility. Passive micromixers—such as serpentine, herringbone, or spiral channels—offer a simpler and more robust solution, particularly suitable for long-term biological experiments, because they rely solely on channel geometry to generate secondary flows and increase residence time. In curved channels, centrifugal effects shift the velocity maximum toward the outer wall and generate transverse Dean vortices, which drive fluid elements across streamlines and thereby enhance mixing without requiring moving parts. Serpentine designs with repeated bends exploit this mechanism to progressively homogenize solutes along the channel length while maintaining moderate pressure drops compatible with microfluidic perfusion [299,300].

OoC systems are built on microfluidic principles. At the typical length scales of microchannels, fluid behavior differs substantially from that observed at the macroscale. Inertia is strongly reduced, viscous forces dominate, and flow is commonly laminar. This regime is usually described by the Reynolds number, which compares inertial and viscous forces and provides a useful criterion to anticipate whether flow will remain ordered within the channel. These characteristics are fundamental to the operation of microphysiological systems and have been extensively described in the microfluidics literature [301].

$$Re = \frac{\rho U L}{\eta} \tag{6.1}$$

The equation 6.1 shows the definition of the non-dimensional Reynolds number, where ρ is the fluid density, U is the characteristic fluid velocity, L is the characteristic length scale of the channel, and η is the dynamic viscosity. Under low Reynolds number conditions, fluid streams do not mix by turbulence. Instead, when two liquids are brought into contact within a microchannel, they tend to flow as parallel streams separated by a relatively stable interface. Consequently, homogenization depends primarily on molecular diffusion across this interface and on the degree to which the device geometry increases the interfacial area between streams. This diffusion-dominated transport regime is one of the defining features of microfluidic systems and strongly influences mixer design [302].

The pressure-driven operation of the device can be understood from the simplified form of the Navier–Stokes equation. This equation assumes an incompressible, Newtonian fluid and a steady and

predominantly unidirectional flow. Under these conditions, the inertial terms become negligible, and the equation reduces to a balance between the pressure gradient and viscous resistance.

$$\vec{\nabla} p = \eta \nabla^2 \vec{u} \tag{6.2}$$

In equation 6.2, $\overrightarrow{\nabla p}$ is the pressure gradient driving fluid motion through the microchannel, η is the dynamic viscosity of the fluid, and $\vec{u}$ is the fluid velocity field. The operator ∇^2 describes how the velocity field varies spatially across the channel. In physical terms, this simplified expression states that, under low Reynolds number conditions, the pressure gradient imposed by the external pump is dictated by viscous stresses generated by the resistance of the fluid to deformation. Therefore, fluid motion in the channel is governed primarily by applied pressure and by viscous dissipation rather than by inertial effects. For pressure-driven flow in a channel, the resulting velocity profile is parabolic in straight regions, with higher velocities toward the center of the channel and lower velocities near the walls. The volumetric flow rate is therefore determined by the applied pressure difference and the hydraulic resistance of the channel, as summarized by the Hagen–Poiseuille relation:

$$Q = \frac{\Delta p}{R_H} \tag{6.3}$$

Here, Q is the volumetric flow rate, Δp is the pressure difference, and R_H is the hydraulic resistance, which depends on channel geometry and fluid viscosity. This relationship is key to the present device because the contributions of the liver-derived and skeletal muscle inlet streams are controlled by their pressure-driven flow rates. In practical terms, modifying the inlet pressure changes the velocity of the corresponding stream and therefore changes both the dilution ratio and the residence time available for mixing before the mixture reaches the skeletal muscle chamber. Pressure-driven flow and hydraulic resistance are routinely used to simulate and control flow distribution in microfluidic networks [303].

Under laminar flow, diffusion becomes the main mechanism by which molecules move across the interface between adjacent streams. The characteristic diffusion time increases with the square of the diffusion distance and decreases with the diffusion coefficient of the solute. Therefore, reducing the effective diffusion distance, increasing residence time, or increasing the interfacial area between streams can improve mixing efficiency. To illustrate this, diffusion time and distance are governed by the following equations 6.4 to 6.6:

$$t_D \approx \frac{d^2}{D} \tag{6.4}$$

$$L_D = Ut_d \approx U\frac{d^2}{D} \tag{6.5}$$

Or

$$L_D \approx U\frac{w^2}{D} \tag{6.6}$$

where t_D is the diffusion time, d is the diffusion distance, D is the diffusion coefficient, L_D is the minimum length required to approach diffusive mixing, U is the average fluid velocity, and w can be used as the relevant channel width. These relationships explain why pressure and channel geometry are key in the design of passive microfluidic mixers. Increasing pressure increases velocity and can enhance throughput, but it also reduces residence time and can therefore reduce the time available for diffusion. Conversely, lower inlet pressures can favor mixing by allowing molecules more time to diffuse across the channel width. The interplay between convection and diffusion is a key consideration in the design of microfluidic mixing systems.

Micromixers are broadly classified as active or passive. Active micromixers rely on external energy inputs, such as acoustic, magnetic, electrical, or mechanical perturbations, to stir or disturb the flow. Although they can achieve high mixing efficiency, their integration increases device complexity and may impose additional constraints on biological compatibility. Passive micromixers rely only on channel geometry and pressure-driven flow. They are therefore attractive for long-term biological experiments, where simplicity, robustness, optical accessibility, and minimal perturbation of the culture environment are desirable. Passive mixing strategies are particularly common in organ-on-chip platforms because they facilitate fabrication and operation while maintaining biocompatibility [304].

The device developed in this chapter uses a passive serpentine diluting–mixing unit. Serpentine geometries increase the path length available for diffusion and introduce repeated curved regions that alter the local velocity field. In curved channels, centrifugal effects displace the velocity maximum toward the outer wall and can generate transverse secondary flows, often described as Dean-type vortices. These secondary flows promote movement across streamlines and help deform the interface between adjacent liquids, thereby enhancing homogenization without requiring moving parts or external actuation. This is particularly relevant for the liver–skeletal muscle OoC because the liver-derived stream must be diluted and homogenized with skeletal muscle differentiation medium before entering the muscle chamber. Dean-flow-enhanced mixing in curved microchannels has been widely reported as an effective passive mixing mechanism [305].

In this chapter, mixing performance was evaluated experimentally using Rhodamine B as a fluorescent liver-medium surrogate. Fluorescence intensity profiles were extracted across the channel width at defined locations along the serpentine region. These profiles were fitted with Gaussian functions, and their standard deviation was used to calculate a mixing index. This index approaches 1 as the fluorescence profile becomes broader and more homogeneous across the channel width, as detailed:

$$\gamma = 1 - \frac{\sigma_{min}}{\sigma} \tag{6.7}$$

Here, γ is the mixing index, σ_{min} is the standard deviation of the unmixed reference profile, and σ is the standard deviation of the fluorescence profile at a given downstream location. This analysis provides a bridge between the microfluidic theory described above and the characterization presented in the Results section. Specifically, it allows the pressure-dependent progression of mixing along the serpentine channel to be evaluated and related to the operating conditions required to reproduce the 1:50 liver-medium dilution previously optimized in the static skeletal muscle exposure experiments.

6.1.6 Biological modules for future integration

The OoC device developed in this chapter is designed as an engineering tool for future integration of the biological modules established in Chapters 4 and 5, rather than as a fully implemented co-culture system. The first module consists of 3D collagen-based liver constructs that combine hepatocyte-like HepaRG cells and LX-2 HSCs, cultured under lipotoxic and inflammatory conditions to reproduce progressive MASLD-like features, including steatosis, hepatocellular dysfunction, inflammatory cytokine production, stellate cell activation, and early fibrogenic remodeling. These constructs generate CM that contain liver-derived secreted factors, reflecting specific disease stages.

The second module consists of human 3D bioengineered skeletal muscle tissues formed in flexible-post PDMS chips, which support aligned myofibers and functional readouts via EPS and force measurements. This platform enables the characterization of muscle contractility, morphology, and molecular markers in response to liver-derived signals, and it has already demonstrated that stage–specific CM can induce muscle alterations under static exposure. In the context of Chapter 6, these modules are not yet physically integrated into the microfluidic device; instead, they define chamber dimensions, imaging requirements, and the target dilution of liver-derived medium that must be achieved before the mixture reaches the muscle compartment.

6.1.7 Translating dilution requirements into engineering constraints

A central finding from the static conditioned-medium experiments is that skeletal muscle tissues tolerated liver-derived media only when diluted 1:50 in skeletal muscle differentiation medium, while more concentrated conditions were associated with severe functional disruption. In quantitative terms, this corresponds to a liver-medium fraction of 0.02 in the final mixture applied to muscle tissues, and this value was adopted as the primary biological design constraint for the microfluidic device. The engineering problem addressed in this chapter was to design a microfluidic configuration and operating

regime that deliver a homogenized mixture with a liver-medium fraction close to 0.02 at the entrance of the muscle chamber.

In a pressure-driven microfluidic system, this requirement translates into constraints on channel cross-section, flow-rate ratios, and mixing efficiency along the path from the liver outlet to the muscle compartment. The relative contributions of the liver and muscle inlets are determined by the applied pressures, which set the volumetric flow rates and thus the nominal dilution factor, while the geometry of the mixing region controls how the two streams achieve homogeneity. Importantly, the design must also remain compatible with future live-tissue culture, adding constraints on overall device height, optical accessibility, and chamber layout. Designs were made accounting for the real size of both biological components, which are to be placed inside the OoC device in their functional differentiated state.

6.2 Aims and scope

In summary, the aim of Chapter 6 is to establish the fluidic foundation for future dynamic liver–muscle co-culture experiments within an OoC device. Specifically, the objectives are:

1. Design and fabricate a first-generation microfluidic device that connects a liver chamber, a passive serpentine diluting–mixing unit, and a skeletal muscle chamber in a configuration compatible with 3D human liver and muscle constructs
2. Characterize mixing along the serpentine using Rhodamine B fluorescence imaging and a quantitative mixing index derived from cross-sectional intensity profiles
3. Determine the inlet pressure conditions under which the liver-medium surrogate is diluted to a fraction close to 0.02 before entering the muscle chamber, thereby reproducing the static 1:50 exposure condition under flow
4. Identify technical limitations and practical constraints that must be addressed before integrating live tissues.

By achieving these goals, this chapter positions a first-generation OoC device that already fulfills flow, mixing, and dilution requirements for dynamic liver-to-muscle studies while clearly delineating the remaining steps needed to realize a fully functional MASLD liver–muscle co-culture model under physiologically relevant flow conditions.

6.3 Results

6.3.1 Design rationale for a liver–skeletal muscle organ-on-chip platform

The static CM experiments described in Chapter 5 demonstrated that secreted factors released by the 3D liver constructs were sufficient to impair skeletal muscle function *in vitro*. However, this experimental configuration relied on manual medium collection, dilution, and transfer between independently cultured tissues. Although this approach allowed controlled testing of liver-derived CM, it did not reproduce continuous inter-tissue communication under flow. Therefore, the next step of the platform consisted of designing a first-generation organ-on-chip (OoC) device capable of integrating one 3D liver construct and one 3D skeletal muscle tissue within a shared microfluidic circuit.

The main design requirement was determined by the biological constraints identified in the static experiments. Undiluted liver CM was not compatible with differentiated skeletal muscle tissues, whereas a 1:50 dilution in skeletal muscle differentiation medium preserved muscle tissue function while still allowing the detection of liver-disease-dependent effects (see Chapter 5). Consequently, the OoC device was designed not only as a physical co-culture platform, but also as a fluidic dilution and mixing system capable of reducing the concentration of liver-derived medium before its arrival to the skeletal muscle chamber.

The resulting device contained two tissue regions connected through a passive diluting and mixing unit. The upstream chamber was designed to host the 3D liver construct, while the downstream chamber was designed to host the 3D skeletal muscle tissue. Two independent inlets allowed the introduction of liver medium and skeletal muscle medium, respectively. Liver medium exiting the liver chamber entered a narrow outlet channel and merged with the skeletal muscle medium stream before passing through a serpentine mixing region. The mixed medium was then directed into the skeletal muscle chamber, thereby reproducing the conceptual workflow of the static CM experiments under continuous flow.

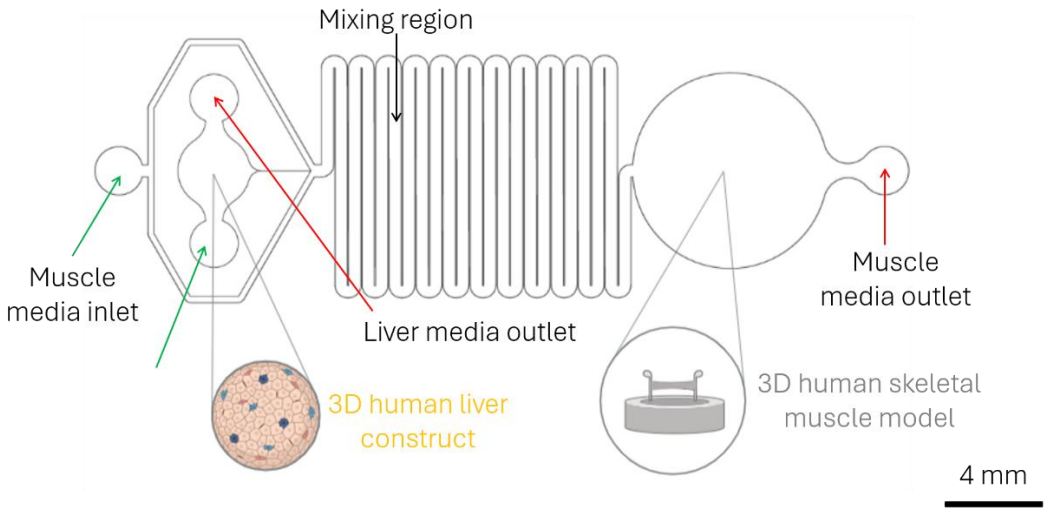


Figure 6.1. General design of the liver–skeletal muscle organ-on-chip device.
Schematic top view of the microfluidic device developed to support controlled communication between a 3D human liver construct and a 3D human skeletal muscle tissue. The design includes independent liver and muscle medium inlets and outlets, a dedicated liver chamber, a downstream skeletal muscle chamber, and an intermediate serpentine diluting/mixing unit. This configuration enables liver-derived medium to be diluted and homogenized with skeletal muscle medium before reaching the muscle compartment, allowing controlled exposure of the muscle tissue to liver-derived soluble factors while preserving independent fluidic access to each organ module.

6.3.2 Fabrication and layering of the first-generation device

The first prototype was fabricated as a multilayer microfluidic chip. The bottom layer consisted of a standard glass slide to allow optical inspection of the channels and tissue regions. The microfluidic architecture was defined in a PDMS layer, while a PMMA top layer provided mechanical support and access for external connectors. A double-sided adhesive layer was used between PDMS and PMMA to facilitate assembly and reduce leakage at the connector interface.

The microfluidic design incorporated three replicas of the same device within a single chip. Each replica contained a liver chamber, a serpentine diluting/mixing unit, and a skeletal muscle chamber. The chamber and channel height was 100 µm. The liver chamber had a diameter of 3 mm, while the skeletal muscle chamber had a diameter of 8 mm. The liver outlet channel was considerably narrower than the main mixing channel, which created a strong hydraulic-resistance imbalance between the liver and muscle medium streams and contributed to the intended dilution of liver-derived medium. After merging with the skeletal muscle medium, both streams entered a 510 µm-wide serpentine mixing channel composed of repeated upper and lower loops.

This architecture was selected to address two requirements simultaneously. First, the device had to dilute the liver-derived medium to approximately 1:50 before skeletal muscle exposure. Second, it had to promote sufficient mixing before the medium reached the skeletal muscle chamber. Because flow in microchannels occurs predominantly under laminar conditions, the design relied on passive mixing rather than turbulent mixing. The serpentine geometry increased the length of the fluidic path and

promoted secondary flow components in curved regions, thereby increasing the opportunity for diffusion and homogenization between the liver-derived stream and the skeletal muscle medium stream.

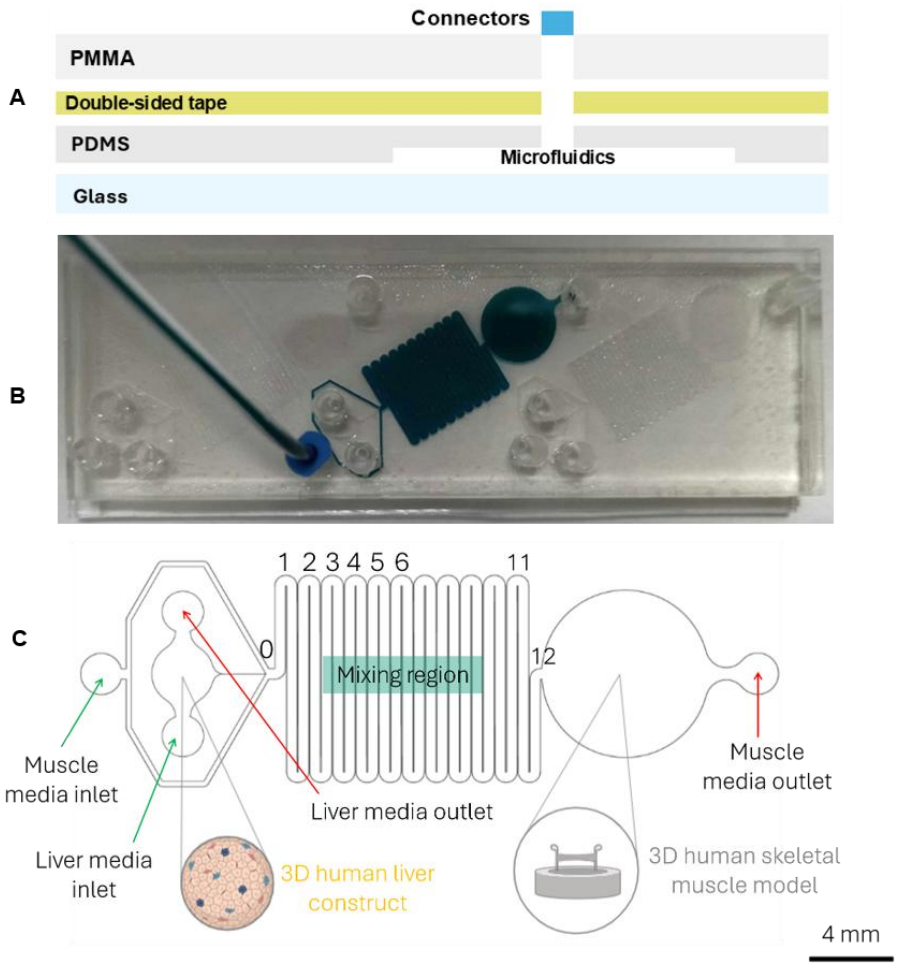


Figure 6.2. Layered structure, assembled prototype, and mixing-analysis regions of the liver–skeletal muscle organ-on-chip device.

A) Schematic cross-section of the chip architecture, showing the glass substrate, patterned PDMS microfluidic layer, double-sided adhesive tape, PMMA top layer, and external connectors for fluidic access. B) Top-view image of the assembled chip. Blue ink was injected into the central replicate to visualize the microfluidic circuit, including the liver chamber, serpentine diluting/mixing unit, and downstream muscle chamber. C) Schematic top view of the liver–skeletal muscle microfluidic circuit. Numbered positions indicate the locations along the dilution/mixing unit where fluorescence intensity profiles were acquired to evaluate progressive mixing before the fluid reached the skeletal muscle chamber.

6.3.3 Integration constraints for microscopy-compatible multi-tissue culture

In addition to fluidic dilution and mixing, the device had to remain compatible with practical tissue culture and imaging requirements. The maximum device height was constrained to approximately 1 cm to allow positioning under standard microscopy configurations. The liver and skeletal muscle tissue regions were also spatially separated to allow independent optical access to both chambers. The final layout placed

the two tissue regions at a lateral center-to-center distance of approximately 42.2 mm, allowing the liver and skeletal muscle regions to be visualized independently.

This constraint was particularly relevant for future biological implementation. The liver chamber needed to accommodate a 3D liver construct without obstructing the fluidic route, while the skeletal muscle chamber needed to host an anchored 3D skeletal muscle tissue compatible with downstream functional or structural assessment. Although live tissues were not ultimately introduced into the chip within the timeframe of this thesis, the first-generation design established the geometrical and optical basis for a future dynamic liver–muscle co-culture system.

6.3.4 Fluorescence-based characterization of mixing along the serpentine channel

After fabrication, the fluidic behavior of the device was characterized using a fluorescence-based assay. Rhodamine B diluted in Milli-Q water was used to simulate liver-derived medium, whereas Milli-Q water without fluorophore was used to simulate skeletal muscle medium. This approach allowed visualization of the liver-derived stream and quantification of its progressive dilution and mixing after merging with the skeletal muscle medium stream.

Before the main characterization experiments, Rhodamine B concentration was calibrated to identify a concentration range in which fluorescence intensity remained proportional to fluorophore concentration. This step was necessary because high Rhodamine B concentrations can produce self-quenching, thereby disrupting the linear relationship between concentration and fluorescence signals. Based on this calibration, a working concentration of 6 × 10^-3 mg/mL Rhodamine B was selected for the mixing and dilution experiments.

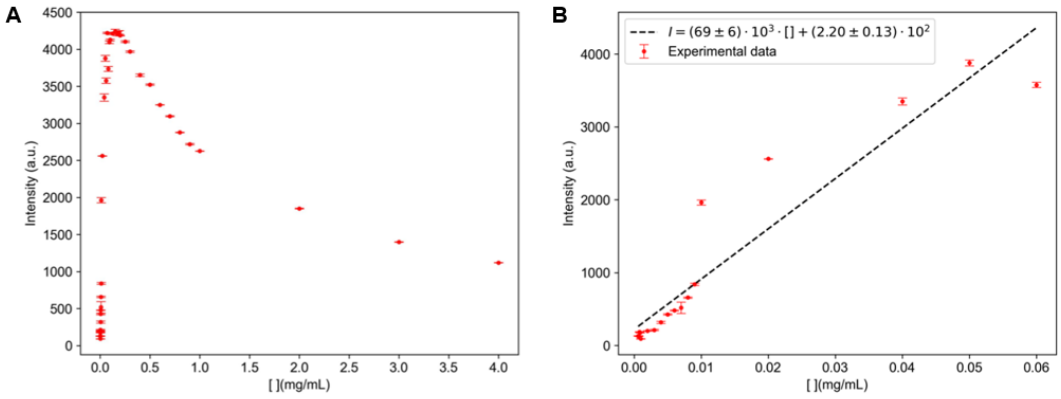


Figure 6.3. Rhodamine B calibration for fluorescence-based dilution and mixing analysis.
A) Fluorescence intensity measured across a broad range of Rhodamine B concentrations, showing a non-linear response at higher concentrations due to self-quenching. Maximum signal was observed around 0.5 mg·mL^{-1}, after which fluorescence intensity decreased despite increasing dye concentration. B) Linear fluorescence region selected for quantitative analysis. Intensity values plotted against Rhodamine B concentration and fitted by linear regression.

The chip was then connected to a pressure-driven flow system. Skeletal muscle medium flow was maintained through the muscle inlet, while the pressure applied to the liver inlet was varied across a broad range of conditions between 150 and 500 mbar, depending on the experimental series. Fluorescence microscopy images were acquired at defined positions along the serpentine channel to monitor the distribution of the Rhodamine B signal after the convergence of the liver-derived and skeletal muscle medium streams.

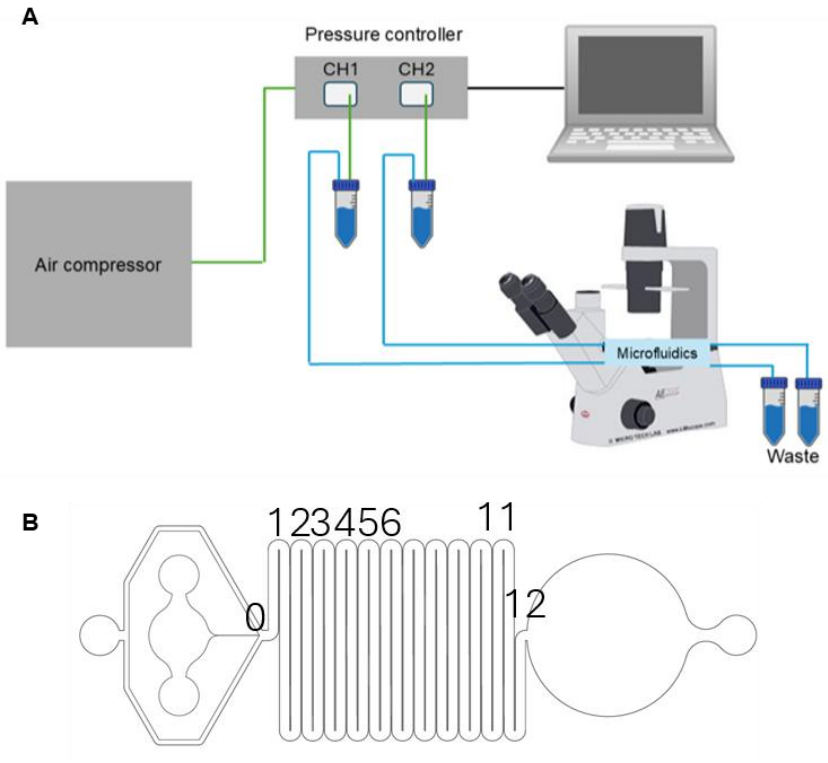


Figure 6.4. Experimental setup for pressure-driven microfluidic dilution and mixing characterization.
A) Schematic representation of the fluorescence microscopy setup used to characterize the liver–skeletal muscle organ-on-chip device. An air compressor supplies pressure to a two-channel pressure controller, which independently drives the muscle medium and liver medium streams into the microfluidic chip. The chip is positioned on the stage of a fluorescence microscope to enable real-time imaging of Rhodamine B transport, dilution, and mixing along the microfluidic circuit. Outlet tubing collects the effluent into waste reservoirs. B) Specific fluorescence imaging locations.

At the initial merging region, fluorescence intensity was spatially concentrated, indicating that the Rhodamine B-containing liver stream and the non-fluorescent muscle medium stream were not yet fully mixed. As the fluids progressed through the serpentine channel, the fluorescence profile broadened across the channel width, indicating progressive dispersion of Rhodamine B into the initially non-fluorescent stream. This qualitative observation confirmed that the serpentine region promoted gradual mixing before the fluid reached the skeletal muscle chamber.

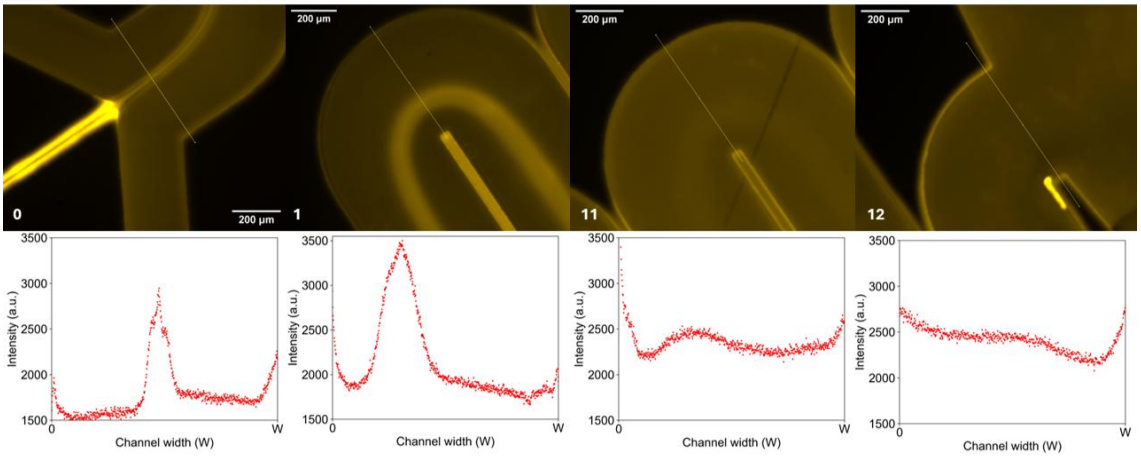


Figure 6.5. Fluorescence-based evaluation of progressive mixing along the serpentine channel. Representative fluorescence microscopy images acquired at selected positions along the microfluidic diluting/mixing region, with the corresponding transverse line-intensity profiles measured across the channel width. At the initial intersection point, the Rhodamine B stream appears spatially confined, producing a sharp intensity peak. As the fluids progress through the serpentine channel, the intensity profile broadens and becomes progressively flat. The final position before the muscle chamber shows a more homogeneous fluorescence distribution across the channel width.

6.3.5 Pressure-dependent mixing efficiency in the serpentine region

To quantify mixing along the device, fluorescence intensity profiles were extracted across the channel width at defined positions of the serpentine region. These profiles were fitted using Gaussian distributions, and the standard deviation of each fitted profile was used to calculate a mixing index. This index increased as the fluorescence profile broadened and approached a more homogeneous distribution across the channel width.

The mixing analysis showed that the device promoted progressive homogenization of the Rhodamine B-containing liver stream with the muscle medium stream along the serpentine region. However, mixing efficiency depended on the pressure applied at the liver inlet. Lower liver inlet pressures produced faster convergence of the mixing index toward complete mixing, whereas higher liver inlet pressures delayed homogenization. This behavior was consistent with the expected relationship between pressure, flow velocity, and residence time in laminar microfluidic systems. Higher pressures increase fluid velocity, reducing the time available for molecular diffusion across the interface between the two streams. Conversely, lower pressures prolong residence time within the serpentine region and therefore favor diffusive mixing.

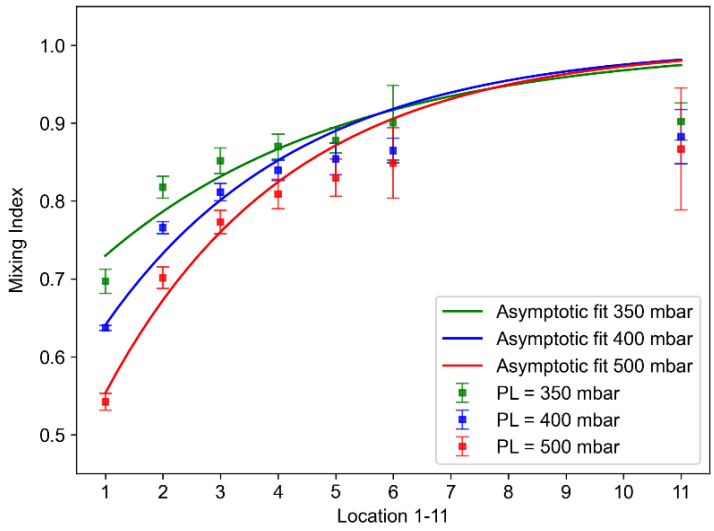


Figure 6.6. Mixing efficiency along the serpentine diluting/mixing unit at different liver inlet pressures. Mixing index values measured at sequential positions along the serpentine channel for three liver inlet pressures, while maintaining the muscle inlet pressure constant. Experimental data are shown with error bars, and asymptotic fits were used to describe the progression toward complete mixing. Lower liver inlet pressures produced higher mixing index values at earlier positions. In all tested conditions, the mixing index progressively approached 1 along the channel, consistent with increasing homogenization before the fluid reached the skeletal muscle chamber.

Among the tested conditions, the highest-pressure conditions showed the slowest approach toward complete mixing. In contrast, lower-to-intermediate liver pressures improved the progression of mixing along the serpentine channel. Importantly, despite pressure-dependent differences in the rate of mixing, the fluorescence intensity profile measured immediately before the skeletal muscle chamber was nearly flat across the channel width. This indicated that, under the tested conditions, the two fluid streams were substantially homogenized before entering the skeletal muscle chamber.

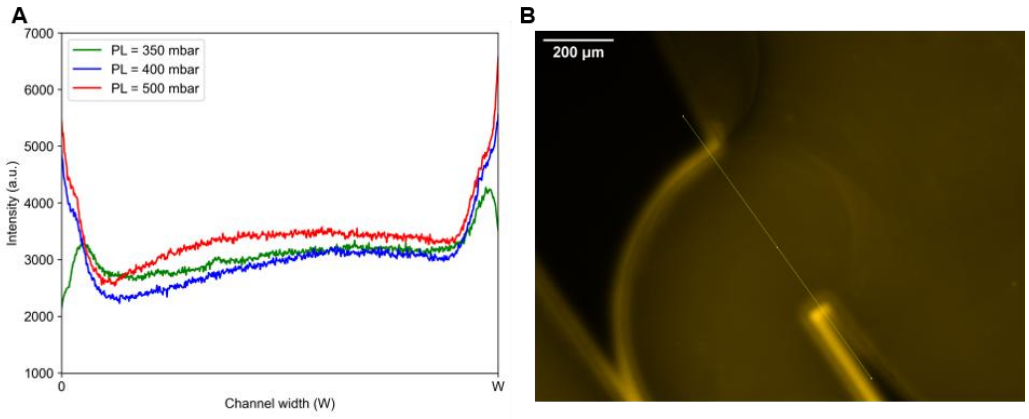


Figure 6.7. Fluorescence intensity profiles at the outlet of the serpentine diluting/mixing unit. A) Cross-channel fluorescence intensity profiles measured immediately before the skeletal muscle chamber, corresponding to location 12 of the microfluidic circuit. Profiles are shown for different liver inlet pressures while

maintaining the muscle inlet pressure constant. B) Representative fluorescence microscopy image of location 12 at a liver inlet pressure of 500 mbar, showing the analyzed cross-sectional line used to extract the intensity profile. Scale bar = 200 µm.

6.3.6 Identification of pressure conditions compatible with the target 1:50 liver-medium dilution

In addition to mixing, the device was evaluated for its ability to reproduce the 1:50 dilution of liver-derived medium that had been optimized in the static CM experiments. For this purpose, fluorescence intensity was compared between the liver chamber and the skeletal muscle chamber under different liver inlet pressures. Because Rhodamine B was used within a concentration range where fluorescence intensity was approximately proportional to concentration, the decrease in signal between both chambers was used as a directly proportional indicator for liver-medium dilution.

The dilution analysis showed that the liver-derived fluorescent signal was strongly reduced before reaching the skeletal muscle chamber, confirming that the device could dilute the liver stream through its convergence with the muscle medium stream. The extent of dilution was pressure dependent. Lower-to-intermediate liver inlet pressures produced a larger difference between the liver chamber signal and the skeletal muscle chamber signal, whereas higher liver inlet pressures increased the relative contribution of the liver-derived stream to the final mixture.

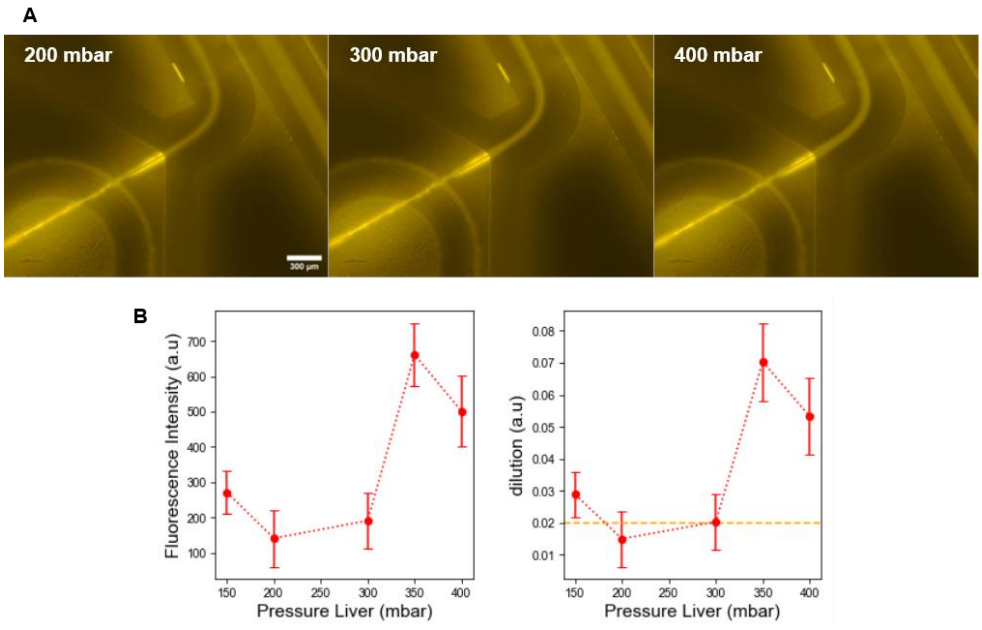


Figure 6.8. Pressure-dependent dilution of Rhodamine B in unlabeled fluid before entry into the skeletal muscle chamber.

A) Representative fluorescence microscopy images at location 0, showing the fluidic profile generated at different liver inlet pressures. B) Quantification of fluorescence intensity and corresponding dilution ratio in the skeletal muscle chamber across the tested liver inlet pressures. The dashed horizontal line indicates the target dilution of 0.02, corresponding to a

1:50 liver-to-muscle medium ratio. Pressures around 200–300 mbar produced dilution values close to the target range, whereas higher liver inlet pressures increased the relative contribution of liver-derived medium reaching the skeletal muscle compartment. Data are shown as mean ± SD.

The target 1:50 dilution corresponds to a final liver-medium fraction of approximately 0.02. Under the tested conditions, the dilution profile intersected this target range most consistently around 300 mbar, indicating that this pressure condition was the closest to the biologically required dilution. This result was particularly relevant because the 1:50 dilution was not an arbitrary engineering target, but the dilution previously identified as compatible with functional skeletal muscle exposure to liver CM. Therefore, the fluidic characterization supported the feasibility of translating the static CM protocol into a continuous-flow OoC configuration.

6.4 Discussion

The work presented in this chapter is the first engineering step toward translating the static liver-CM transfer strategy developed in previous chapters into a dynamic liver–skeletal muscle OoC platform. The preceding experiments demonstrated that CM generated by 3D MASLD-like liver constructs altered the phenotype and contractile performance of differentiated 3D skeletal muscle tissues. However, those experiments relied on manual collection, dilution, and batch exposure of skeletal muscle tissues to liver-derived media. While this strategy was appropriate to isolate the contribution of liver-derived soluble factors under controlled conditions, it did not reproduce continuous inter-organ communication under flow. Therefore, the purpose of this chapter was to establish the fluidic basis required for future dynamic integration of the two biological modules.

6.4.1 Design constraints and engineering goal of the fluidic characterization

The main design constraint was defined by static skeletal muscle experiments. Preliminary exposure studies showed that concentrated liver culture media were not compatible with skeletal muscle tissue function, whereas dilution of liver CM at 1:50 in skeletal muscle differentiation medium preserved tissue viability and enabled the detection of disease-stage-specific effects. This empirical condition was used as engineering requirement, since the OoC device had to dilute the liver-derived stream to an approximate final liver-medium fraction of 0.02 before reaching the skeletal muscle chamber. If medium exchange is not properly adjusted, downstream phenotypes may reflect culture incompatibility or nutrient imbalance rather than inter-tissue signaling.

The first-generation device successfully incorporated a liver chamber, a downstream skeletal muscle chamber, a stream intersection, and a passive serpentine diluting–mixing unit positioned between both compartments. Pressure-driven configuration allowed independent control of the liver- and muscle-medium surrogate streams, while the serpentine geometry was intended to promote progressive homogenization before entry into the muscle chamber. Although live tissues were not ultimately introduced into the chip during the timeframe of this thesis, the resulting platform provides a physical route for future dynamic liver-to-muscle communication.

The progressive flattening of the cross-sectional fluorescence intensity profiles confirmed that the serpentine unit promoted mixing of fluorophore Rhodamine B with the non-fluorescent muscle-medium surrogate. Evaluation of mixing index at multiple positions along the microfluidic circuit was consistent with the pressure dependence of the mixing behavior, as lower and intermediate pressures allowed earlier mixing, compared to the higher-pressure regimes. In microchannels, flow is typically characterized by low Reynolds numbers, meaning that viscous forces dominate and turbulence is absent. Under these conditions, adjacent fluid streams mix primarily by molecular diffusion, and mixing efficiency depends strongly on residence time, diffusion distance, and channel geometry. Higher liver inlet pressures increased fluid velocity and therefore reduced the time available for molecular diffusion across the interface between streams. Consequently, higher pressure conditions, particularly the highest tested liver pressures, showed slower convergence toward complete mixing. Conversely, lower-to-intermediate liver pressures favored more efficient homogenization along the serpentine channel. From a biological perspective, using low to intermediate pressures in microfluidic devices protects cells from excessive shear stress and pressure inside the culture chambers. We also hypothesize that 3D models should offer greater protection against adverse physical stimuli than conventional monolayer OoC devices. Together, these results support the use of a passive serpentine geometry and demonstrate that pressure selection is not merely a matter of achieving flow, but a key parameter controlling both dilution and mixing towards reliable multi OoC platforms, where culture media compatibility is considered.

Fluorescence intensity profiles acquired immediately before the skeletal muscle chamber appeared nearly flat across the channel width, indicating substantial homogenization before the mixture entered the downstream tissue compartment. Skeletal muscle tissue would otherwise be exposed to spatially heterogeneous medium composition, with different regions receiving different concentrations of liver-derived factors. For future live-tissue implementation, homogeneous delivery will be essential to ensure that any observed contractile, morphological, or molecular phenotype can be attributed to the intended liver-derived exposure rather than to local concentration gradients within the chamber.

The dilution analysis further demonstrated that the device could approach the biologically required 1:50 liver-medium dilution under selected pressure conditions. Since Rhodamine B fluorescence was used within a concentration range where intensity was approximately proportional to concentration, the decrease in fluorescence signal from the liver chamber to the skeletal muscle chamber provided an alternative for dilution measurement. The target liver-medium fraction of 0.02 was reached most closely around the lower-to-intermediate pressure range, particularly near 300 mbar.

6.4.2 Limitations of the microfluidic characterization towards biological translation

Nevertheless, the interpretation of the dilution results should remain cautious. The fluorescence-based dilution analysis was affected by variability, especially in some intermediate pressure conditions. This variability likely reflected a combination of experimental factors, including pixel-level heterogeneity, differences in focus, local background fluorescence, and the complexity of the tubing configuration. Fluorescence imaging was sensitive to the complexity of the experimental setup. The device required several tubing connections to the pressure controller and collection outlets, and Rhodamine B-containing tubes occasionally generated background fluorescence when positioned close to the microscope objective. This artifact could increase the apparent fluorescence intensity in selected regions and affect quantitative analysis. Some images were partially unfocused, which complicated Gaussian fitting of the fluorescence intensity profiles. This limitation was particularly relevant for the mixing-index analysis, because the calculated index depended on accurate extraction of the cross-channel intensity distribution. Third, the dilution analysis showed variability in the fluorescence intensity measured in the skeletal muscle chamber, especially at some intermediate pressures. This variability likely reflected a combination of optical background, local pixel-intensity heterogeneity, and experimental differences between replicates.

In addition, Rhodamine B in Milli-Q water represents a simplified surrogate of liver-CM and skeletal muscle differentiation medium. Actual biological media contains proteins, salts, metabolites, and other components that may alter viscosity, surface interactions, and adsorption behavior. Therefore, while the current results support the feasibility of pressure-controlled dilution, the final operating parameters should be revalidated using standards and finally the real media formulations before live-tissue experiments. Liver-derived CM also contains a complex mixture of proteins, metabolites, extracellular vesicles, lipids, and cytokines with different diffusion coefficients and surface-interaction properties. Larger biomolecules may diffuse more slowly and may interact differently with PDMS or other device materials. Therefore, future work should consider validating transport using fluorescently labeled proteins or biologically relevant molecular tracers with diffusion properties closer to those of cytokines or secreted factors. This would help determine whether the mixing behavior observed with Rhodamine B accurately predicts the spatial distribution of liver-derived bioactive components.

The previous points bring the choice of PDMS as the microfluidic material to discussion, which is also relevant for future optimization. PDMS remains widely used in organ-on-chip prototyping because it is optically transparent, gas-permeable, biocompatible, and compatible with soft lithography. These properties make it highly suitable for first-generation device fabrication and microscopy-based characterization. However, PDMS can absorb small hydrophobic molecules and interact with proteins, potentially altering the effective concentration of bioactive compounds delivered to cells. This is particularly important in MASLD modeling, where lipids, lipotoxic species, cytokines, and metabolic mediators contribute to the skeletal muscle phenotype. Although this issue does not invalidate the

present fluidic proof-of-concept, it should be addressed before biological implementation, either by surface treatment or material substitution with newer polymers like Flexdym™.

A further limitation is that live tissues were not introduced into the device in this thesis. Whether live constructs can remain viable inside the chambers under perfusion remains to be demonstrated. Moreover, the replication of phenotypes observed in the static experimental configuration should be consistent inside the OoC as well.

These steps are essential for converting the current platform into a functional liver–muscle OoC model. Skeletal muscle integration will require careful consideration of tissue anchoring, chamber geometry, flow-induced shear exposure, access for electrical pulse stimulation, and compatibility with post-flow contractility measurements. Similarly, liver construct integration will require assessment of tissue retention, perfusion around or through the hydrogel, maintenance of hepatic phenotype, and preservation of disease-stage-specific secretome generation under dynamic conditions. Extensive work is being carried out by other authors in the Biosensors for Bioengineering group as a follow-up to this present study, to advance a reliable multi OoC for the study of MASLD-associated muscle wasting.

Despite these limitations, the present device addresses a key bottleneck in the development of multi-organ systems, which is the translation of empirically optimized static exposure conditions into a controllable microfluidic format. Multi-organ chips often fail not because individual tissue modules are unavailable, but because their integration introduces mismatched medium requirements, dilution artifacts, inappropriate flow rates, or poorly defined inter-compartment scaling. In the present work, the static 1:50 liver-CM exposure condition provided a rational quantitative target for fluidic design. By approaching this target under flow, the device establishes a more controlled starting point for future biological experiments than a simple direct liver-to-muscle connection would provide.

The liver and skeletal muscle models were first developed and characterized independently, allowing each module to be optimized according to its own biological requirements. Chapter 6 then introduces a connecting architecture that can, in future iterations, allow liver-derived cues to be delivered dynamically to the muscle compartment. This modular approach is advantageous because it enables stepwise troubleshooting. Fluidic routing, dilution, mixing, liver viability, muscle viability, and functional response can each be evaluated separately before attempting fully coupled long-term experiments.

6.4.3 Future work

Future work should proceed in the following manner. Fluidic characterization should be repeated using the actual culture media used for liver and skeletal muscle tissues to account for differences in fluid properties. Then, the dilution behavior should be validated using tracers that better approximate the transport of proteins or cytokines. Next, live 3D liver constructs should be loaded into the liver chamber and maintained under flow to assess viability, structural stability, and phenotype preservation. Skeletal muscle tissues should also be integrated into the downstream chamber, with particular attention to compatibility with EPS-based contractility assessment. Finally, the complete dynamic liver–muscle

experiment should compare whether exposure under flow reproduces the functional impairment, myotube remodeling, and molecular alterations previously observed under static CM transfer.

Chapter 7 | Conclusions

The work presented in this thesis aimed to develop a modular human *in vitro* platform for the study of liver–skeletal muscle crosstalk in the context of MASLD. The main conclusions derived from this work are the following:

1. A three-dimensional human liver model was established that reproduces coordinated features of MASLD progression under controlled *in vitro* conditions. HepaRG hepatocyte-like cells and LX-2 hepatic stellate cells embedded in collagen-based hydrogels provided a multicellular hepatic microenvironment suitable for modeling hepatocyte–stromal interactions in disease conditions. A chemically defined NEFAs challenge induced steatosis and altered hepatocyte function, while the incorporation of LPS intensified hepatocellular injury, inflammatory activation, hepatic stellate cell activation, and early fibrogenic remodeling. These phenotypes were supported by changes in albumin expression, inflammatory cytokine secretion, and collagen expression. Thus, the model reproduced a set of phenotypes consistent with current evidence of MASLD as a progressive disease driven by lipid overload, inflammatory amplification, and matrix remodeling.

2. The liver constructs functioned both as disease models and as generators of biologically active hepatic signals for downstream liver–skeletal muscle crosstalk studies. Conditioned media collected from defined liver phenotypes transmitted pathological cues generated by the liver constructs under controlled experimental conditions. This approach preserved the complexity of the liver-derived secretome while maintaining control over disease stage, exposure time, and dilution. The liver model therefore provided a source of integrated hepatic signals, instead of relying in isolated candidate mediators.

3. Functional three-dimensional human skeletal muscle tissues were fabricated as a platform to evaluate MASLD-associated muscle impairment. Human myoblasts were engineered into aligned and differentiated constructs capable of contracting in response to electrical pulse stimulation, enabling quantification of skeletal muscle performance. The combination of contractile force measurements with myotube morphology, myogenic gene expression, and subcellular markers provided a multidimensional assessment of muscle phenotype.

Tissues allowed liver-derived pathological cues to be tested at the functional, structural, molecular, and cellular levels within the same bioengineered tissue system.

4. Conditioned media derived from MASLD-like liver constructs impaired skeletal muscle function and phenotype. Exposure of differentiated 3D skeletal muscle tissues to liver conditioned media produced measurable reductions in contractile performance, with MASH-like conditioned media inducing the most marked force impairment. These functional alterations were accompanied by changes in myotube size, myogenic regulatory factor expression, and autophagy–lysosomal markers. These findings support the hypothesis that soluble factors generated by diseased liver constructs during MASLD progression independently induce skeletal muscle dysfunction in a controlled human *in vitro* system.

5. The skeletal muscle response to liver-derived pathological cues involved alterations beyond canonical atrophy defined by reduced mass alone. Although changes in myotube diameter and area were observed, the magnitude and pattern of contractile impairment were not fully explained by morphological reduction. The combination of impaired force generation, the altered autophagy–lysosomal markers, and modulation of myogenic gene expression indicates that MASLD-associated muscle dysfunction in this platform involved deterioration of muscle quality as well as changes in tissue structure.

6. The independent development and characterization of the liver and skeletal muscle models demonstrated the value of modular bioengineered tissues for dissecting inter-organ interactions in complex diseases. By validating each tissue module separately, this work established defined hepatic disease phenotypes, functional skeletal muscle maturation, and tissue-specific readouts before coupling both systems by conditioned medium transfer. This modular strategy made it possible to isolate the contribution of stage-specific signals to skeletal muscle impairment, while retaining the flexibility to adjust exposure conditions, integrate additional assays, and expand the system toward more complex multi-organ configurations. The resulting framework is particularly suited for systemic disorders such as MASLD.

7. A first generation liver–skeletal muscle OoC device was designed, fabricated, and fluidically characterized as a technical bridge toward dynamic inter-organ integration. The device incorporated independent liver and skeletal muscle compartments connected through a passive mixing unit, addressing the culture medium incompatibility identified during static conditioned medium experiments. Fluorescence-based characterization using Rhodamine B demonstrated that pressure-driven flow modulates the relative contribution of liver-derived and skeletal muscle media streams, and that serpentine architecture supports progressive and effective mixing before entry into the skeletal muscle chamber.

Although live-tissue co-culture under flow was not implemented within the timeframe of this thesis, the device established the fluidic basis for future dynamic liver–muscle communication studies.

Overall, this thesis establishes a modular human-relevant *in vitro* strategy to model MASLD-associated liver–skeletal muscle crosstalk. The work integrates a multicellular 3D liver model capable of generating MASLD-like phenotypes, a functional 3D skeletal muscle model suitable for multiple readout assessment, and a first-generation microfluidic device designed to support future dynamic coupling of both tissues. By demonstrating that pathological liver conditioned media impair engineered skeletal muscle function, this thesis provides experimental evidence that hepatic disease signals can contribute directly to muscle dysfunction in a controlled human bioengineered system. Altogether, the platform bridges reductionist cell culture and complex animal models and provides a foundation for future studies incorporating continuous perfusion, additional organ modules, secretome profiling, and therapeutic interventions.

Chapter 8 | References

1. Younossi ZM, Kalligeros M, Henry L. Epidemiology of metabolic dysfunction-associated steatotic liver disease. Clin Mol Hepatol. 2025 Feb 1;31(Suppl):32–50. doi:10.3350/CMH.2024.0431 PubMed PMID: 39159948.

2. Xu B, Li H, Pi Y, Li K. Global, regional and national burden of Metabolic dysfunction-associated steatotic liver disease in adolescents and adults aged 15–49 years from 1990 to 2021: results from the 2021 Global Burden of Disease study. Front Med (Lausanne). 2025 Jun 25;12. doi:10.3389/fmed.2025.1568211

3. Rinella ME, Lazarus J V., Ratziu V, Francque SM, Sanyal AJ, Kanwal F, et al. A multisociety Delphi consensus statement on new fatty liver disease nomenclature. J Hepatol. 2023 Dec 1;79(6):1542–56. doi:10.1016/j.jhep.2023.06.003 PubMed PMID: 37363821.

4. Li Y, Yang P, Ye J, Xu Q, Wu J, Wang Y. Updated mechanisms of MASLD pathogenesis. Lipids Health Dis. 2024 Apr 22;23(1):117. doi:10.1186/s12944-024-02108-x

5. Sandireddy R, Sakthivel S, Gupta P, Behari J, Tripathi M, Singh BK. Systemic impacts of metabolic dysfunction-associated steatotic liver disease (MASLD) and metabolic dysfunction-associated steatohepatitis (MASH) on heart, muscle, and kidney related diseases. Front Cell Dev Biol. 2024 Jul 16;12. doi:10.3389/fcell.2024.1433857

6. Azam MM, Mukhtar S, Haris M, Laique F, Amir S, Mohiuddin M, et al. FDA's approval of resmetirom (Rezdiffra): a breakthrough in MASH management. Exploration of Drug Science. 2024 Dec 3;867–74. doi:10.37349/eds.2024.00078

7. Wang D, Miao J, Zhang L, Zhang L. Research advances in the diagnosis and treatment of MASLD/MASH. Ann Med. 2025 Dec 31;57(1). doi:10.1080/07853890.2024.2445780

8. Mousa AM, Mahmoud M, AlShuraiaan GM. Resmetirom: The First Disease-Specific Treatment for MASH. Rajpal A, editor. Int J Endocrinol. 2025 Jan 26;2025(1). doi:10.1155/ije/6430023

9. Li Y, Li L, Zhang Y, Lu J, Tang X, Bi C, et al. Clinical and pathological characteristics of metabolic dysfunction-associated steatotic liver disease and the key role of epigenetic regulation: implications for molecular mechanism and treatment. Ther Adv Endocrinol Metab. 2025 Oct 17;16. doi:10.1177/20420188251321602

10. Lauridsen MM, Ravnskjaer K, Gluud LL, Sanyal AJ. Disease classification, diagnostic challenges, and evolving clinical trial design in MASLD. J Clin Invest. 2025 May 15;135(10):e189953. doi:10.1172/JCI189953 PubMed PMID: 40371650.

11. Kostrzewski T, Maraver P, Ouro-Gnao L, Levi A, Snow S, Miedzik A, et al. A Microphysiological System for Studying Nonalcoholic Steatohepatitis. Hepatol Commun. 2020 Jan 13;4(1):77–91. doi:10.1002/hep4.1450

12. Kozlitina J, Sookoian S. Global Epidemiological Impact of <scp> *PNPLA3* I148M </scp> on Liver Disease. Liver International. 2025 Mar 7;45(3). doi:10.1111/liv.16123

13. Sherman DJ, Liu L, LaGory EL, Fordstrom P, Pruitt D, Barreda J, et al. PNPLA3-I148M is a neomorph that interferes with two primary hepatic triglyceride clearance pathways. Cell Rep. 2025 Oct;44(10):116371. doi:10.1016/j.celrep.2025.116371

14. Lee NH, Jeong SJ, Wang JH, Choi YJ, Oh HM, Cho JH, et al. The Clinical Diagnosis-Based Nationwide Epidemiology of Metabolic Dysfunction-Associated Liver Disease in Korea. J Clin Med. 2023 Dec 12;12(24):7634. doi:10.3390/jcm12247634

15. Liu J, Li C, Yang Y, Li J, Sun X, Zhang Y, et al. Special correlation between diet and MASLD: positive or negative? Cell Biosci. 2025 Apr 12;15(1):44. doi:10.1186/s13578-025-01382-1

16. Huang M, Chen H, Wang H, Zhang Y, Li L, Lan Y, et al. Global burden and risk factors of MASLD: trends from 1990 to 2021 and predictions to 2030. Intern Emerg Med. 2025 Jun 28;20(4):1013–24. doi:10.1007/s11739-025-03895-6

17. Heyens LJM, Innocenti F, Van Steenkiste C, Struyve M, Francque SM, Koek GH, et al. Prevalence and Risk Factors of MASLD in Prediabetes and Type 2 Diabetes Mellitus in Belgium and The Netherlands. Biomedicines. 2025 Nov 19;13(11):2821. doi:10.3390/biomedicines13112821

18. Quek J, Chan KE, Wong ZY, Tan C, Tan B, Lim WH, et al. Global prevalence of non-alcoholic fatty liver disease and non-alcoholic steatohepatitis in the overweight and obese population: a systematic review and meta-analysis. Lancet Gastroenterol Hepatol. 2023 Jan;8(1):20–30. doi:10.1016/S2468-1253(22)00317-X

19. Younossi ZM, Golabi P, Price JK, Owrangi S, Gundu-Rao N, Satchi R, et al. The Global Epidemiology of Nonalcoholic Fatty Liver Disease and Nonalcoholic Steatohepatitis Among Patients With Type 2 Diabetes. Clinical Gastroenterology and Hepatology. 2024 Oct;22(10):1999-2010.e8. doi:10.1016/j.cgh.2024.03.006

20. Yuan J, He X, Lu Y, Pu X, Liu L, Zhang X, et al. Triglycerides/high-density lipoprotein-cholesterol ratio outperforms traditional lipid indicators in predicting metabolic dysfunction-associated steatotic liver disease among U.S. adults. Front Endocrinol (Lausanne). 2025 Apr 15;16. doi:10.3389/fendo.2025.1591241

21. Sun Y, Miao X, Hu M, Xie X, Liu S, Song Z, et al. Remnant cholesterol and its variability independent of low density lipoprotein cholesterol predict metabolic dysfunction associated steatotic liver disease. Sci Rep. 2025 Feb 6;15(1):4455. doi:10.1038/s41598-025-88000-9

22. Tang C, Peng D, Zong K, Wu Z, Gong M, Li H, et al. Association between the lymphocyte-to-high-density lipoprotein ratio and metabolic dysfunction-associated steatotic liver disease among US adults: a cross-sectional study from NHANES 2017 to 2020. BMC Gastroenterol. 2024 Dec 23;24(1):470. doi:10.1186/s12876-024-03565-5

23. Basil B, Myke-Mbata BK, Eze OE, Akubue AU. From adiposity to steatosis: metabolic dysfunction-associated steatotic liver disease, a hepatic expression of metabolic syndrome – current insights and future directions. Clin Diabetes Endocrinol. 2024 Dec 2;10(1):39. doi:10.1186/s40842-024-00187-4

24. Boulos M, Mousa RS, Jeries N, Simaan E, Alam K, Bulus B, et al. Hidden in the Fat: Unpacking the Metabolic Tango Between Metabolic Dysfunction-Associated Steatotic Liver Disease and Metabolic Syndrome. Int J Mol Sci. 2025 Apr 7;26(7):3448. doi:10.3390/ijms26073448

25. Younossi ZM, Koenig AB, Abdelatif D, Fazel Y, Henry L, Wymer M. Global epidemiology of nonalcoholic fatty liver disease—Meta-analytic assessment of prevalence, incidence, and outcomes. Hepatology. 2016 Jul 22;64(1):73–84. doi:10.1002/hep.28431

26. Jinjuvadia R, Antaki F, Lohia P, Liangpunsakul S. The Association Between Nonalcoholic Fatty Liver Disease and Metabolic Abnormalities in The United States Population. J Clin Gastroenterol. 2017 Feb;51(2):160–6. doi:10.1097/MCG.0000000000000666

27. Zhang F, Liu L, Li W. Correlation of sarcopenia with progression of liver fibrosis in patients with metabolic dysfunction-associated steatotic liver disease: a study from two cohorts in China and the United States. Nutr J. 2025 Jan 14;24(1):6. doi:10.1186/s12937-025-01081-0

28. Bhanji RA, Narayanan P, Allen AM, Malhi H, Watt KD. Sarcopenia in hiding: The risk and consequence of underestimating muscle dysfunction in nonalcoholic steatohepatitis. Hepatology. 2017 Dec 30;66(6):2055–65. doi:10.1002/hep.29420

29. Bhanji RA, Carey EJ, Yang L, Watt KD. The Long Winding Road to Transplant: How Sarcopenia and Debility Impact Morbidity and Mortality on the Waitlist. Clinical Gastroenterology and Hepatology. 2017 Oct;15(10):1492–7. doi:10.1016/j.cgh.2017.04.004

30. Wong R, Yuan LY. Sarcopenia and metabolic dysfunction associated steatotic liver disease: Time to address both. World J Hepatol. 2024 Jun 27;16(6):871–7. doi:10.4254/wjh.v16.i6.871

31. Golabi P, Owrangi S, Younossi ZM. Global perspective on nonalcoholic fatty liver disease and nonalcoholic steatohepatitis - prevalence, clinical impact, economic implications and management strategies. Aliment Pharmacol Ther. 2024 Jun 30;59(S1). doi:10.1111/apt.17833

32. Younossi ZM, Paik JM, Henry L, Yang J, Fernandes G, Stepanova M, et al. The Growing Economic and Clinical Burden of Nonalcoholic Steatohepatitis (NASH) in the United States. J Clin Exp Hepatol. 2023 May;13(3):454–67. doi:10.1016/j.jceh.2022.12.005

33. Paik JM, Eberly KE, Kabbara K, Harring M, Younossi Y, Henry L, et al. Non-alcoholic fatty liver disease is associated with greater risk of 30-day hospital readmission in the United States (U.S.). Ann Hepatol. 2023 Jul;28(4):101108. doi:10.1016/j.aohep.2023.101108

34. Day CP, James OFW. Steatohepatitis: A tale of two “Hits”? Gastroenterology. 1998 Apr 1;114(4 I):842–5. doi:10.1016/S0016-5085(98)70599-2 PubMed PMID: 9547102.

35. Buzzetti E, Pinzani M, Tsochatzis EA. The multiple-hit pathogenesis of non-alcoholic fatty liver disease (NAFLD). Metabolism. 2016 Aug 1;65(8):1038–48. doi:10.1016/j.metabol.2015.12.012 PubMed PMID: 26823198.

36. Benedé-Ubieto R, Cubero FJ, Nevzorova YA. Breaking the barriers: the role of gut homeostasis in Metabolic-Associated Steatotic Liver Disease (MASLD). Gut Microbes. 2024 Dec 31;16(1). doi:10.1080/19490976.2024.2331460

37. Petta S, Armandi A, Bugianesi E. Impact of <scp>PNPLA3 I148M</scp> on Clinical Outcomes in Patients With <scp>MASLD</scp>. Liver International. 2025 Mar 16;45(3). doi:10.1111/liv.16133

38. Soto A, Spongberg C, Martinino A, Giovinazzo F. Exploring the Multifaceted Landscape of MASLD: A Comprehensive Synthesis of Recent Studies, from Pathophysiology to Organoids and Beyond. Biomedicines. 2024 Feb 8;12(2):397. doi:10.3390/biomedicines12020397

39. Syed-Abdul MM. Lipid Metabolism in Metabolic-Associated Steatotic Liver Disease (MASLD). Metabolites [Internet]. Multidisciplinary Digital Publishing Institute (MDPI); 2024 [cited 2025 Dec 1]. p. 12. Available from: https://pmc.ncbi.nlm.nih.gov/articles/PMC10818604/ doi:10.3390/metabo14010012 PubMed PMID: 38248815.

40. Dicker D, Frühbeck G, Vettor R, Gastaldelli A, Yki-Järvinen H, Schick F, et al. Correction to: EASL–EASD–EASO Clinical Practice Guidelines on the management of metabolic dysfunction-associated steatotic liver disease (MASLD): Executive Summary (Diabetologia, (2024), 67, 11, (2375-2392), 10.1007/s00125-024-06196-3). Diabetologia. 2024;67(11):2608. doi:10.1007/s00125-024-06258-6 PubMed PMID: 39352523.

41. Tacke F, Horn P, Wong VWSS, Ratziu V, Bugianesi E, Francque S, et al. EASL–EASD–EASO Clinical Practice Guidelines on the management of metabolic dysfunction-associated steatotic liver disease (MASLD): Executive Summary. Diabetologia. 2024 Jun 13;67(11):2375–92. doi:10.1007/s00125-024-06196-3 PubMed PMID: 38869512.

42. Tilg H, Adolph TE, Tacke F. Therapeutic modulation of the liver immune microenvironment. Hepatology. 2023 Nov;78(5):1581–601. doi:10.1097/HEP.0000000000000386

43. Meyer M, Schwärzler J, Jukic A, Tilg H. Innate Immunity and MASLD. Biomolecules. 2024 Apr 1;14(4):476. doi:10.3390/BIOM14040476 PubMed PMID: 38672492.

44. Talari NK, Mattam U, Rahman AP, Hemmelgarn BK, Wyder MA, Sylvestre PB, et al. Functional compartmentalization of hepatic mitochondrial subpopulations during MASH progression. Communications Biology 2025 8:1. 2025 Feb 18;8(1):258-. doi:10.1038/s42003-025-07713-9 PubMed PMID: 39966593.

45. Ekstedt M, Hagström H, Nasr P, Fredrikson M, Stål P, Kechagias S, et al. Fibrosis stage is the strongest predictor for disease-specific mortality in NAFLD after up to 33 years of follow-up. Hepatology. 2015 May 23;61(5):1547–54. doi:10.1002/hep.27368

46. Dulai PS, Singh S, Patel J, Soni M, Prokop LJ, Younossi Z, et al. Increased risk of mortality by fibrosis stage in nonalcoholic fatty liver disease: Systematic review and meta-analysis. Hepatology. 2017 May 31;65(5):1557–65. doi:10.1002/hep.29085

47. Kim D, Kim RW, Kim HJ, Therneau TM. Association between noninvasive fibrosis markers and mortality among adults with nonalcoholic fatty liver disease in the United States. Hepatology. 2013 Apr;57(4):1357–65. doi:10.1002/hep.26156

48. Gandhi CR. Hepatic stellate cell activation and pro-fibrogenic signals. J Hepatol. 2017 Nov;67(5):1104–5. doi:10.1016/j.jhep.2017.06.001

49. Garbuzenko DV. Pathophysiological mechanisms of hepatic stellate cells activation in liver fibrosis. World J Clin Cases. 2022 Apr 26;10(12):3662–76. doi:10.12998/wjcc.v10.i12.3662

50. Robert S, Gicquel T, Bodin A, Lagente V, Boichot E. Characterization of the MMP/TIMP Imbalance and Collagen Production Induced by IL-1β or TNF-α Release from Human Hepatic Stellate Cells. Avila MA, editor. PLoS One. 2016 Apr 5;11(4):e0153118. doi:10.1371/journal.pone.0153118

51. Shen W, Middleton MS, Cunha GM, Delgado TI, Wolfson T, Gamst A, et al. Changes in abdominal adipose tissue depots assessed by MRI correlate with hepatic histologic improvement in non-alcoholic steatohepatitis. J Hepatol. 2023 Feb;78(2):238–46. doi:10.1016/j.jhep.2022.10.027

52. Houghton D, Thoma C, Hallsworth K, Cassidy S, Hardy T, Burt AD, et al. Exercise Reduces Liver Lipids and Visceral Adiposity in Patients With Nonalcoholic Steatohepatitis in a Randomized Controlled Trial. Clinical Gastroenterology and Hepatology. 2017 Jan;15(1):96-102.e3. doi:10.1016/j.cgh.2016.07.031

53. Lee E, Korf H, Vidal-Puig A. An adipocentric perspective on the development and progression of non-alcoholic fatty liver disease. J Hepatol. 2023 May;78(5):1048–62. doi:10.1016/j.jhep.2023.01.024

54. Kobayashi T, Iwaki M, Nakajima A, Nogami A, Yoneda M. Current Research on the Pathogenesis of NAFLD/NASH and the Gut–Liver Axis: Gut Microbiota, Dysbiosis, and Leaky-Gut Syndrome. Int J Mol Sci. 2022 Oct 2;23(19):11689. doi:10.3390/ijms231911689

55. Liu J, Wu A, Cai J, She ZG, Li H. The contribution of the gut-liver axis to the immune signaling pathway of NAFLD. Front Immunol. 2022 Aug 31;13. doi:10.3389/fimmu.2022.968799

56. Rao G, Peng X, Li X, An K, He H, Fu X, et al. Unmasking the enigma of lipid metabolism in metabolic dysfunction-associated steatotic liver disease: from mechanism to the clinic. Front Med (Lausanne). 2023 Nov 27;10. doi:10.3389/fmed.2023.1294267

57. Ueki K, Kondo T, Kahn CR. Suppressor of Cytokine Signaling 1 (SOCS-1) and SOCS-3 Cause Insulin Resistance through Inhibition of Tyrosine Phosphorylation of Insulin Receptor Substrate Proteins by Discrete Mechanisms. Mol Cell Biol. 2004 Jun 27;24(12):5434–46. doi:10.1128/MCB.24.12.5434-5446.2004

58. Rui L, Yuan M, Frantz D, Shoelson S, White MF. SOCS-1 and SOCS-3 Block Insulin Signaling by Ubiquitin-mediated Degradation of IRS1 and IRS2. Journal of Biological Chemistry. 2002 Nov;277(44):42394–8. doi:10.1074/jbc.C200444200

59. Hançer NJ, Qiu W, Cherella C, Li Y, Copps KD, White MF. Insulin and Metabolic Stress Stimulate Multisite Serine/Threonine Phosphorylation of Insulin Receptor Substrate 1 and Inhibit Tyrosine Phosphorylation. Journal of Biological Chemistry. 2014 May;289(18):12467–84. doi:10.1074/jbc.M114.554162

60. Shi H, Tzameli I, Bjørbæk C, Flier JS. Suppressor of Cytokine Signaling 3 Is a Physiological Regulator of Adipocyte Insulin Signaling. Journal of Biological Chemistry. 2004 Aug;279(33):34733–40. doi:10.1074/jbc.M403886200

61. Carli F, Della Pepa G, Sabatini S, Vidal Puig A, Gastaldelli A. Lipid metabolism in MASLD and MASH: From mechanism to the clinic. JHEP Reports. 2024 Dec;6(12):101185. doi:10.1016/j.jhepr.2024.101185

62. Mejía-Guzmán JE, Belmont-Hernández RA, Chávez-Tapia NC, Uribe M, Nuño-Lámbarri N. Metabolic-Dysfunction-Associated Steatotic Liver Disease: Molecular Mechanisms, Clinical Implications, and Emerging Therapeutic Strategies. Int J Mol Sci. 2025 Mar 25;26(7):2959. doi:10.3390/ijms26072959

63. Pohl J, Ring A, Hermann T, Stremmel W. Role of FATP in parenchymal cell fatty acid uptake. Biochimica et Biophysica Acta (BBA) - Molecular and Cell Biology of Lipids. 2004 Nov;1686(1–2):1–6. doi:10.1016/j.bbalip.2004.06.004

64. Lambert JE, Ramos-Roman MA, Browning JD, Parks EJ, Ramos–Roman MA, Browning JD, et al. Increased de novo lipogenesis is a distinct characteristic of individuals with nonalcoholic fatty liver disease. Gastroenterology. 2014 Mar;146(3):726–35. doi:10.1053/j.gastro.2013.11.049 PubMed PMID: 24316260.

65. Mitsuyoshi H, Yasui K, Harano Y, Endo M, Tsuji K, Minami M, et al. Analysis of hepatic genes involved in the metabolism of fatty acids and iron in nonalcoholic fatty liver disease. Hepatology Research. 2009 Apr 26;39(4):366–73. doi:10.1111/j.1872-034X.2008.00464.x

66. Kohjima M, Enjoji M, Higuchi N, Kato M, Kotoh K, Yoshimoto T, et al. Re-evaluation of fatty acid metabolism-related gene expression in nonalcoholic fatty liver disease. Int J Mol Med. 2007 Sep 1. doi:10.3892/ijmm.20.3.351

67. Horton JD, Goldstein JL, Brown MS. SREBPs: activators of the complete program of cholesterol and fatty acid synthesis in the liver. Journal of Clinical Investigation. 2002 May 1;109(9):1125–31. doi:10.1172/JCI0215593

68. Ferré P, Foufelle F. Hepatic steatosis: a role for de novo lipogenesis and the transcription factor SREBP-1c. Diabetes Obes Metab. 2010 Oct;12(s2):83–92. doi:10.1111/j.1463-1326.2010.01275.x

69. Liao Y, Chen Q, Liu L, Huang H, Sun J, Bai X, et al. Amino acid is a major carbon source for hepatic lipogenesis. Cell Metab. 2024 Nov;36(11):2437-2448.e8. doi:10.1016/j.cmet.2024.10.001

70. Chappell DA, Medh JD. Receptor-mediated mechanisms of lipoprotein remnant catabolism. Prog Lipid Res. 1998 Dec;37(6):393–422. doi:10.1016/S0163-7827(98)00017-4

71. Xiang M, Tian X, Wang H, Gan P, Zhang Q. Inappropriate Diet Exacerbates Metabolic Dysfunction-Associated Steatotic Liver Disease via Abdominal Obesity. Nutrients. 2024 Dec 5;16(23):4208. doi:10.3390/nu16234208

72. Hassani Zadeh S, Mansoori A, Hosseinzadeh M. Relationship between dietary patterns and non-alcoholic fatty liver disease: A systematic review and meta-analysis. J Gastroenterol Hepatol. 2021 Jun 14;36(6):1470–8. doi:10.1111/jgh.15363

73. Burger K, Trauner M, Bergheim I. Pathogenic aspects of fructose consumption in metabolic dysfunction-associated steatotic liver disease (MASLD): A narrative review. Cell Stress. 2025 Jun 24;9:49–64. doi:10.15698/cst2025.06.305

74. Herman MA, Birnbaum MJ. Molecular aspects of fructose metabolism and metabolic disease. Cell Metab. 2021 Dec;33(12):2329–54. doi:10.1016/j.cmet.2021.09.010

75. Peyman M, Babin-Ebell A, Rodríguez-Rodríguez R, Rigon M, Aguilar-Recarte D, Villarroya J, et al. SIRT1 regulates hepatic vldlr levels. Cell Communication and Signaling. 2024 May 28;22(1):297. doi:10.1186/s12964-024-01666-y

76. Huerta-Ávila EE, Ramírez-Silva I, Torres-Sánchez LE, Díaz-Benítez CE, Orbe-Orihuela YC, Lagunas-Martínez A, et al. High Relative Abundance of Lactobacillus reuteri and Fructose Intake are Associated with Adiposity and Cardiometabolic Risk Factors in Children from Mexico City. Nutrients. 2019 May 28;11(6):1207. doi:10.3390/nu11061207

77. Chou CL, Li CH, Fang TC. Benefits of Valsartan and Amlodipine in Lipolysis through PU.1 Inhibition in Fructose-Induced Adiposity. Nutrients. 2022 Sep 12;14(18):3759. doi:10.3390/nu14183759

78. Park JW, Kim SE, Lee NY, Kim JH, Jung JH, Jang MK, et al. Role of Microbiota-Derived Metabolites in Alcoholic and Non-Alcoholic Fatty Liver Diseases. Int J Mol Sci. 2021 Dec 31;23(1):426. doi:10.3390/ijms23010426

79. Lambertz J, Weiskirchen S, Landert S, Weiskirchen R. Fructose: A Dietary Sugar in Crosstalk with Microbiota Contributing to the Development and Progression of Non-Alcoholic Liver Disease. Front Immunol. 2017 Sep 19;8. doi:10.3389/fimmu.2017.01159

80. Jarmakiewicz-Czaja S, Sokal-Dembowska A, Filip R. Effects of Selected Food Additives on the Gut Microbiome and Metabolic Dysfunction-Associated Steatotic Liver Disease (MASLD). Medicina (B Aires). 2025 Jan 22;61(2):192. doi:10.3390/medicina61020192

81. Singh A, Buckholz A, Kumar S, Newberry C. Implications of Protein and Sarcopenia in the Prognosis, Treatment, and Management of Metabolic Dysfunction-Associated Steatotic Liver Disease (MASLD). Nutrients. 2024 Feb 26;16(5):658. doi:10.3390/nu16050658

82. Venkatesan N, Doskey LC, Malhi H. The Role of Endoplasmic Reticulum in Lipotoxicity during Metabolic Dysfunction–Associated Steatotic Liver Disease (MASLD) Pathogenesis. Am J Pathol. 2023 Dec;193(12):1887–99. doi:10.1016/j.ajpath.2023.08.007

83. Rada P, González-Rodríguez Á, García-Monzón C, Valverde ÁM. Understanding lipotoxicity in NAFLD pathogenesis: is CD36 a key driver? Cell Death Dis. 2020 Sep 25;11(9):802. doi:10.1038/s41419-020-03003-w

84. Walter P, Ibrahimi I, Blobel G. Translocation of proteins across the endoplasmic reticulum. II. Signal recognition protein (SRP) mediates the selective binding to microsomal membranes of in-vitro-assembled polysomes synthesizing secretory protein. J Cell Biol. 1981 Nov 1;91(2):545–50. doi:10.1083/jcb.91.2.551

85. Ruggiano A, Foresti O, Carvalho P. ER-associated degradation: Protein quality control and beyond. Journal of Cell Biology. 2014 Mar 17;204(6):869–79. doi:10.1083/jcb.201312042

86. Jacquemyn J, Cascalho A, Goodchild RE. The ins and outs of endoplasmic reticulum-controlled lipid biosynthesis. The EMBO Reports. 2017 Nov 1;18(11):1905–21. doi:10.15252/embr.201643426

87. Radanović T, Ernst R. The Unfolded Protein Response as a Guardian of the Secretory Pathway. Cells. 2021 Oct 31;10(11):2965. doi:10.3390/cells10112965

88. Savage DB, Petersen KF, Shulman GI. Disordered Lipid Metabolism and the Pathogenesis of Insulin Resistance. Physiol Rev. 2007 Apr;87(2):507–20. doi:10.1152/physrev.00024.2006

89. Kakisaka K, Cazanave SC, Fingas CD, Guicciardi ME, Bronk SF, Werneburg NW, et al. Mechanisms of lysophosphatidylcholine-induced hepatocyte lipoapoptosis. American Journal of Physiology-Gastrointestinal and Liver Physiology. 2012 Jan;302(1):G77–84. doi:10.1152/ajpgi.00301.2011

90. Cazanave SC, Elmi NA, Akazawa Y, Bronk SF, Mott JL, Gores GJ. CHOP and AP-1 cooperatively mediate PUMA expression during lipoapoptosis. American Journal of Physiology-Gastrointestinal and Liver Physiology. 2010 Jul;299(1):G236–43. doi:10.1152/ajpgi.00091.2010

91. Brown M V., Compton SA, Milburn M V., Lawton KA, Cheatham B. Metabolomic signatures in lipid-loaded HepaRGs reveal pathways involved in steatotic progression. Obesity. 2013 Dec 13;21(12). doi:10.1002/oby.20440

92. Sunny NE, Parks EJ, Browning JD, Burgess SC. Excessive Hepatic Mitochondrial TCA Cycle and Gluconeogenesis in Humans with Nonalcoholic Fatty Liver Disease. Cell Metab. 2011 Dec;14(6):804–10. doi:10.1016/j.cmet.2011.11.004

93. Li X, Chen W, Jia Z, Xiao Y, Shi A, Ma X. Mitochondrial Dysfunction as a Pathogenesis and Therapeutic Strategy for Metabolic-Dysfunction-Associated Steatotic Liver Disease. Int J Mol Sci. 2025 Apr 30;26(9):4256. doi:10.3390/ijms26094256

94. Clare K, Dillon JF, Brennan PN. Reactive Oxygen Species and Oxidative Stress in the Pathogenesis of MAFLD. J Clin Transl Hepatol. 2022 Oct 28;10(5):939–46. doi:10.14218/JCTH.2022.00067

95. Svobodová G, Horní M, Velecká E, Boušová I. Metabolic dysfunction-associated steatotic liver disease-induced changes in the antioxidant system: a review. Arch Toxicol. 2025 Jan 23;99(1):1–22. doi:10.1007/s00204-024-03889-x

96. Kim MJ, Park YR, Jang G, Han YK, Ishii I, Jang SY, et al. Cystathionine γ-Lyase Protects Against Choline-Deficient High-Fat Diet-Induced Metabolic Dysfunction-Associated Steatotic Liver Disease Through the Cysteine–Glutathione Axis in Mice. Antioxid Redox Signal. 2025 Sep 15. doi:10.1177/15230864251377735

97. Chaurasia B, Summers SA. Ceramides – Lipotoxic Inducers of Metabolic Disorders. Trends in Endocrinology & Metabolism. 2015 Oct;26(10):538–50. doi:10.1016/j.tem.2015.07.006

98. Duan Y, Pan X, Luo J, Xiao X, Li J, Bestman PL, et al. Association of Inflammatory Cytokines With Non-Alcoholic Fatty Liver Disease. Front Immunol. 2022 May 6;13. doi:10.3389/fimmu.2022.880298

99. Wree A, McGeough MD, Peña CA, Schlattjan M, Li H, Inzaugarat ME, et al. NLRP3 inflammasome activation is required for fibrosis development in NAFLD. J Mol Med. 2014 Oct 28;92(10):1069–82. doi:10.1007/s00109-014-1170-1

100. Remmerie A, Martens L, Thoné T, Castoldi A, Seurinck R, Pavie B, et al. Osteopontin Expression Identifies a Subset of Recruited Macrophages Distinct from Kupffer Cells in the Fatty Liver. Immunity. 2020 Sep;53(3):641-657.e14. doi:10.1016/j.immuni.2020.08.004

101. Tran S, Baba I, Poupel L, Dussaud S, Moreau M, Gélineau A, et al. Impaired Kupffer Cell Self-Renewal Alters the Liver Response to Lipid Overload during Non-alcoholic Steatohepatitis. Immunity. 2020 Sep;53(3):627-640.e5. doi:10.1016/j.immuni.2020.06.003

102. Takeda K. Toll-like receptors in innate immunity. Int Immunol. 2004 Nov 22;17(1):1–14. doi:10.1093/intimm/dxh186

103. Akira S, Uematsu S, Takeuchi O. Pathogen Recognition and Innate Immunity. Cell. 2006 Feb;124(4):783–801. doi:10.1016/j.cell.2006.02.015

104. Watanabe A, Hashmi A, Gomes DA, Town T, Badou A, Flavell RA, et al. Apoptotic hepatocyte DNA inhibits hepatic stellate cell chemotaxis via toll-like receptor 9. Hepatology. 2007 Nov;46(5):1509–18. doi:10.1002/hep.21867

105. Aoyama T, Paik YH, Seki E. Toll-Like Receptor Signaling and Liver Fibrosis. Gastroenterol Res Pract. 2010;2010:1–8. doi:10.1155/2010/192543

106. Arrese M, Cabrera D, Kalergis AM, Feldstein AE. Innate Immunity and Inflammation in NAFLD/NASH. Dig Dis Sci. 2016 May 3;61(5):1294–303. doi:10.1007/s10620-016-4049-x

107. Ganz M, Szabo G. Immune and inflammatory pathways in NASH. Hepatol Int. 2013 Dec 30;7(S2):771–81. doi:10.1007/s12072-013-9468-6

108. Zhang Q, Raoof M, Chen Y, Sumi Y, Sursal T, Junger W, et al. Circulating mitochondrial DAMPs cause inflammatory responses to injury. Nature. 2010 Mar;464(7285):104–7. doi:10.1038/nature08780

109. Szabo G, Dolganiuc A, Mandrekar P. Pattern recognition receptors: A contemporary view on liver diseases. Hepatology. 2006 Aug;44(2):287–98. doi:10.1002/hep.21308

110. Seki E, Tsutsui H, Nakano H, Tsuji NM, Hoshino K, Adachi O, et al. Lipopolysaccharide-Induced IL-18 Secretion from Murine Kupffer Cells Independently of Myeloid Differentiation Factor 88 That Is Critically Involved in Induction of Production of IL-12 and IL-1β. The Journal of Immunology. 2001 Feb 15;166(4):2651–7. doi:10.4049/jimmunol.166.4.2651

111. Rossato M, Di Vincenzo A, Pagano C, Hadi H El, Vettor R. The P2X7 Receptor and NLRP3 Axis in Non-Alcoholic Fatty Liver Disease: A Brief Review. Cells. 2020 Apr 22;9(4):1047. doi:10.3390/cells9041047

112. Alisi A, Carsetti R, Nobili V. Pathogen- or damage-associated molecular patterns during nonalcoholic fatty liver disease development. Hepatology. 2011 Nov;54(5):1500–2. doi:10.1002/hep.24611

113. Garcia-Martinez I, Santoro N, Chen Y, Hoque R, Ouyang X, Caprio S, et al. Hepatocyte mitochondrial DNA drives nonalcoholic steatohepatitis by activation of TLR9. Journal of Clinical Investigation. 2016 Jan 25;126(3):859–64. doi:10.1172/JCI83885

114. Yu L, Gao F, Li Y, Su D, Han L, Li Y, et al. Role of pattern recognition receptors in the development of MASLD and potential therapeutic applications. Biomedicine & Pharmacotherapy. 2024 Jun;175:116724. doi:10.1016/j.biopha.2024.116724

115. Paik YH, Schwabe RF, Bataller R, Russo MP, Jobin C, Brenner DA. Toll–Like Receptor 4 Mediates Inflammatory Signaling by Bacterial Lipopolysaccharide in Human Hepatic Stellate Cells. Hepatology. 2003 May;37(5):1043–55. doi:10.1053/jhep.2003.50182

116. Seki E, Brenner DA. Toll-like receptors and adaptor molecules in liver disease. Hepatology. 2008 Jul;48(1):322–35. doi:10.1002/hep.22306

117. Tsuchida T, Friedman SL. Mechanisms of hepatic stellate cell activation. Nat Rev Gastroenterol Hepatol. 2017 Jul 10;14(7):397–411. doi:10.1038/nrgastro.2017.38 PubMed PMID: 28487545.

118. Min K, Karuppannan SK, Tae G. The impact of matrix stiffness on hepatic cell function, liver fibrosis, and hepatocellular carcinoma—Based on quantitative data. Biophys Rev. 2024 Jun 1;5(2). doi:10.1063/5.0197875

119. Wen D, Gao Y, Ho C, Yu L, Zhang Y, Lyu G, et al. Focusing on Mechanoregulation Axis in Fibrosis: Sensing, Transduction and Effecting. Front Mol Biosci. 2022 Mar 11;9. doi:10.3389/fmolb.2022.804680

120. McPherson S, Stewart SF, Henderson E, Burt AD, Day CP. Simple non-invasive fibrosis scoring systems can reliably exclude advanced fibrosis in patients with non-alcoholic fatty liver disease. Gut. 2010 Sep 26;59(9):1265–9. doi:10.1136/gut.2010.216077

121. Kanwal F, Shubrook JH, Adams LA, Pfotenhauer K, Wai-Sun Wong V, Wright E, et al. Clinical Care Pathway for the Risk Stratification and Management of Patients With Nonalcoholic Fatty Liver Disease. Gastroenterology. 2021 Nov;161(5):1657–69. doi:10.1053/j.gastro.2021.07.049

122. Kantartzis K, Stefan N. Clustering NAFLD: phenotypes of nonalcoholic fatty liver disease and their differing trajectories. Hepatol Commun. 2023 Apr;7(4). doi:10.1097/HC9.0000000000000112

123. Raverdy V, Tavaglione F, Chatelain E, Lassailly G, De Vincentis A, Vespasiani-Gentilucci U, et al. Data-driven cluster analysis identifies distinct types of metabolic dysfunction-associated steatotic liver disease. Nat Med. 2024 Dec 9;30(12):3624–33. doi:10.1038/s41591-024-03283-1

124. Babu AF. Metabolic Signatures in Lean MASLD: Current Insights and Future Directions. Metabolites. 2025 Aug 31;15(9):583. doi:10.3390/metabo15090583

125. Mahdessian H, Taxiarchis A, Popov S, Silveira A, Franco-Cereceda A, Hamsten A, et al. TM6SF2 is a regulator of liver fat metabolism influencing triglyceride secretion and hepatic lipid droplet content. Proceedings of the National Academy of Sciences. 2014 Jun 17;111(24):8913–8. doi:10.1073/pnas.1323785111

126. Buch S, Stickel F, Trépo E, Way M, Herrmann A, Nischalke HD, et al. A genome-wide association study confirms PNPLA3 and identifies TM6SF2 and MBOAT7 as risk loci for alcohol-related cirrhosis. Nat Genet. 2015 Dec 19;47(12):1443–8. doi:10.1038/ng.3417

127. Motomura T, Amirneni S, Diaz-Aragon R, Faccioli L, Malizio M, Coard M, et al. Is HSD17B13 Genetic Variant a Protector for Liver Dysfunction? Future Perspective as a Potential Therapeutic Target. J Pers Med. 2021 Jun 30;11(7):619. doi:10.3390/jpm11070619

128. Wattacheril JJ, Abdelmalek MF, Lim JK, Sanyal AJ. AGA Clinical Practice Update on the Role of Noninvasive Biomarkers in the Evaluation and Management of Nonalcoholic Fatty Liver Disease: Expert Review. Gastroenterology. 2023 Oct;165(4):1080–8. doi:10.1053/j.gastro.2023.06.013

129. Sohn W. Essential tools for assessing advanced fibrosis in metabolic dysfunction-associated steatotic liver disease: Editorial on “Optimal cut-offs of vibration-controlled transient elastography and magnetic resonance elastography in diagnosing advanced liver fib. Clin Mol Hepatol. 2025 Jan 1;31(1):277–80. doi:10.3350/cmh.2024.0823

130. López Tórrez SM, Ayala CO, Ruggiro PB, Costa CAD, Wagner MB, Padoin AV, et al. Accuracy of prognostic serological biomarkers in predicting liver fibrosis severity in people with metabolic dysfunction-associated steatotic liver disease: a meta-analysis of over 40,000 participants. Front Nutr. 2024 Feb 14;11. doi:10.3389/fnut.2024.1284509

131. Verschuren L, Mak AL, van Koppen A, Özsezen S, Difrancesco S, Caspers MPM, et al. Development of a novel non-invasive biomarker panel for hepatic fibrosis in MASLD. Nat Commun. 2024 May 29;15(1):4564. doi:10.1038/s41467-024-48956-0

132. Iruzubieta P, Mayo R, Mincholé I, Martínez-Arranz I, Arias-Loste MT, Ibañez-Samaniego L, et al. One-step non-invasive diagnosis of metabolic dysfunction-associated steatohepatitis and fibrosis in high-risk population. United European Gastroenterol J. 2024 Sep 4;12(7):919–29. doi:10.1002/ueg2.12589

133. Tsai CH, Hung TH, Wong TS, Lin CY, Hsu CL, Ko PH, et al. Extrahepatic manifestations of metabolic dysfunction-associated steatotic liver disease: An updated clinical overview. Tzu Chi Med J. 2025 Oct;37(4):378–85. doi:10.4103/tcmj.tcmj_158_25

134. Krishnan SM, Sobey CG, Latz E, Mansell A, Drummond GR. <scp>IL</scp> -1β and <scp>IL</scp> -18: inflammatory markers or mediators of hypertension? Br J Pharmacol. 2014 Dec;171(24):5589–602. doi:10.1111/bph.12876

135. Sinha RA, Singh BK, Yen PM. Direct effects of thyroid hormones on hepatic lipid metabolism. Nat Rev Endocrinol. 2018 May 23;14(5):259–69. doi:10.1038/nrendo.2018.10

136. Harring M, Golabi P, Paik JM, Shah D, Racila A, Cable R, et al. Sarcopenia Among Patients With Nonalcoholic Fatty Liver Disease (NAFLD) Is Associated With Advanced Fibrosis. Clinical Gastroenterology and Hepatology. 2023 Oct;21(11):2876-2888.e5. doi:10.1016/j.cgh.2023.02.013

137. Merz KE, Thurmond DC. Role of Skeletal Muscle in Insulin Resistance and Glucose Uptake. In: Comprehensive Physiology [Internet]. Wiley; 2020. p. 785–809. Available from: https://onlinelibrary.wiley.com/doi/10.1002/cphy.c190029 doi:10.1002/cphy.c190029

138. Skeletal muscle structure, physiology, and function. In. 2023. p. 3–16. Available from: https://linkinghub.elsevier.com/retrieve/pii/B9780323988186000133 doi:10.1016/B978-0-323-98818-6.00013-3

139. Frontera WR, Ochala J. Skeletal Muscle: A Brief Review of Structure and Function. Calcif Tissue Int. 2015 Mar 8;96(3):183–95. doi:10.1007/s00223-014-9915-y

140. Mukund K, Subramaniam S. Skeletal muscle: A review of molecular structure and function, in health and disease. WIREs Systems Biology and Medicine. 2020 Jan 13;12(1). doi:10.1002/wsbm.1462

141. Allen J, Ramsden M, Nisar S. Skeletal muscle structure, function and pathology. Orthop Trauma. 2024 Jun;38(3):137–44. doi:10.1016/j.mporth.2024.03.004

142. Fernández-Costa JM, Fernández-Garibay X, Velasco-Mallorquí F, Ramón-Azcón J. Bioengineered in vitro skeletal muscles as new tools for muscular dystrophies preclinical studies. J Tissue Eng. 2021;12:10–2. doi:10.1177/2041731420981339

143. Scott W, Stevens J, Binder–Macleod SA. Human Skeletal Muscle Fiber Type Classifications. Phys Ther. 2001 Nov 1;81(11):1810–6. doi:10.1093/ptj/81.11.1810

144. Talbot J, Maves L. Skeletal muscle fiber type: using insights from muscle developmental biology to dissect targets for susceptibility and resistance to muscle disease. WIREs Developmental Biology. 2016 Jul 19;5(4):518–34. doi:10.1002/wdev.230

145. Murgia M, Toniolo L, Nagaraj N, Ciciliot S, Vindigni V, Schiaffino S, et al. Single Muscle Fiber Proteomics Reveals Fiber-Type-Specific Features of Human Muscle Aging. Cell Rep. 2017 Jun;19(11):2396–409. doi:10.1016/j.celrep.2017.05.054

146. Qaisar R, Bhaskaran S, Van Remmen H. Muscle fiber type diversification during exercise and regeneration. Free Radic Biol Med. 2016 Sep;98:56–67. doi:10.1016/j.freeradbiomed.2016.03.025

147. Orioli L, Thissen JP. Myokines as potential mediators of changes in glucose homeostasis and muscle mass after bariatric surgery. Front Endocrinol (Lausanne). 2025 Mar 18;16. doi:10.3389/fendo.2025.1554617

148. Milani I, Codini M, Guarisco G, Chinucci M, Gaita C, Leonetti F, et al. Hepatokines and MASLD: The GLP1-Ras-FGF21-Fetuin-A Crosstalk as a Therapeutic Target. Int J Mol Sci. 2024 Oct 8;25(19):10795. doi:10.3390/ijms251910795

149. Schiaffino S, Mammucari C. Regulation of skeletal muscle growth by the IGF1-Akt/PKB pathway: insights from genetic models. Skelet Muscle. 2011;1(1):4. doi:10.1186/2044-5040-1-4

150. Foletta VC, White LJ, Larsen AE, Léger B, Russell AP. The role and regulation of MAFbx/atrogin-1 and MuRF1 in skeletal muscle atrophy. Pflugers Arch. 2011 Mar 11;461(3):325–35. doi:10.1007/s00424-010-0919-9

151. Allen SL, Quinlan JI, Dhaliwal A, Armstrong MJ, Elsharkawy AM, Greig CA, et al. Sarcopenia in chronic liver disease: mechanisms and countermeasures. American Journal of Physiology-Gastrointestinal and Liver Physiology. 2021 Mar 1;320(3):G241–57. doi:10.1152/ajpgi.00373.2020

152. Rodney GG, Pal R, Abo-Zahrah R. Redox regulation of autophagy in skeletal muscle. Free Radic Biol Med. 2016 Sep;98:103–12. doi:10.1016/j.freeradbiomed.2016.05.010

153. Birchmeier C, Brohmann H. Genes that control the development of migrating muscle precursor cells. Curr Opin Cell Biol. 2000 Dec;12(6):725–30. doi:10.1016/S0955-0674(00)00159-9

154. Pownall ME, Gustafsson MK, Emerson CP. Myogenic Regulatory Factors and the Specification of Muscle Progenitors in Vertebrate Embryos. Annu Rev Cell Dev Biol. 2002 Nov;18(1):747–83. doi:10.1146/annurev.cellbio.18.012502.105758

155. Bentzinger CF, Wang YX, Rudnicki MA. Building Muscle: Molecular Regulation of Myogenesis. Cold Spring Harb Perspect Biol. 2012 Feb 1;4(2):a008342–a008342. doi:10.1101/cshperspect.a008342

156. Yin H, Price F, Rudnicki MA. Satellite Cells and the Muscle Stem Cell Niche. Physiol Rev. 2013 Jan;93(1):23–67. doi:10.1152/physrev.00043.2011

157. Kaczmarek A, Kaczmarek M, Ciałowicz M, Clemente FM, Wolański P, Badicu G, et al. The Role of Satellite Cells in Skeletal Muscle Regeneration—The Effect of Exercise and Age. Biology (Basel). 2021 Oct 18;10(10):1056. doi:10.3390/biology10101056

158. Han X, Zhang G Sen, Li QR, Zhang Z. Current approach to the diagnosis of sarcopenia in cardiovascular diseases. Front Nutr. 2024 Nov 15;11. doi:10.3389/fnut.2024.1422663

159. Cruz-Jentoft AJ, Baeyens JP, Bauer JM, Boirie Y, Cederholm T, Landi F, et al. Sarcopenia: European consensus on definition and diagnosis. Age Ageing. 2010 Jul 1;39(4):412–23. doi:10.1093/ageing/afq034

160. Sayer AA, Cruz-Jentoft A. Sarcopenia definition, diagnosis and treatment: consensus is growing. Age Ageing. 2022 Oct 6;51(10). doi:10.1093/ageing/afac220

161. Cruz-Jentoft AJ, Bahat G, Bauer J, Boirie Y, Bruyère O, Cederholm T, et al. Sarcopenia: Revised European consensus on definition and diagnosis. Age and Ageing. 2019. p. 16–31. doi:10.1093/ageing/afy169 PubMed PMID: 30312372.

162. Hsieh YC, Joo SK, Koo BK, Lin HC, Lee DH, Chang MS, et al. Myosteatosis, but not Sarcopenia, Predisposes NAFLD Subjects to Early Steatohepatitis and Fibrosis Progression. Clinical Gastroenterology and Hepatology. 2023 Feb;21(2):388-397.e10. doi:10.1016/j.cgh.2022.01.020

163. Kim HK, Bae SJ, Lee MJ, Kim EH, Park H, Kim HS, et al. Association of Visceral Fat Obesity, Sarcopenia, and Myosteatosis with Non-Alcoholic Fatty Liver Disease without Obesity. Clin Mol Hepatol. 2023 Oct 1;29(4):987–1001. doi:10.3350/cmh.2023.0035

164. Koo BK, Kim D, Joo SK, Kim JH, Chang MS, Kim BG, et al. Sarcopenia is an independent risk factor for non-alcoholic steatohepatitis and significant fibrosis. J Hepatol. 2017 Jan;66(1):123–31. doi:10.1016/j.jhep.2016.08.019

165. Ohara M, Ogawa K, Suda G, Kimura M, Maehara O, Shimazaki T, et al. L-Carnitine Suppresses Loss of Skeletal Muscle Mass in Patients With Liver Cirrhosis. Hepatol Commun. 2018 Aug 6;2(8):910–22. doi:10.1002/hep4.1207

166. Li X, He J, Sun Q. The prevalence and effects of sarcopenia in patients with metabolic dysfunction-associated steatotic liver disease (MASLD): A systematic review and meta-analysis. Clinical Nutrition. 2024 Sep;43(9):2005–16. doi:10.1016/j.clnu.2024.07.006

167. Chakravarthy M V., Siddiqui MS, Forsgren MF, Sanyal AJ. Harnessing Muscle–Liver Crosstalk to Treat Nonalcoholic Steatohepatitis. Front Endocrinol (Lausanne). 2020;11(December):1–15. doi:10.3389/fendo.2020.592373

168. Altajar S, Baffy G. Skeletal Muscle Dysfunction in the Development and Progression of Nonalcoholic Fatty Liver Disease. J Clin Transl Hepatol. 2020 Dec 28;8(4):1–10. doi:10.14218/JCTH.2020.00065

169. Zhao ZH, Zou J, Huang X, Fan YC, Wang K. Assessing causal relationships between sarcopenia and nonalcoholic fatty liver disease: A bidirectional Mendelian randomization study. Front Nutr. 2022 Nov 9;9. doi:10.3389/fnut.2022.971913

170. Mikolasevic I, Pavic T, Filipec Kanizaj T, Bender DV, Domislovic V, Krznaric Z. Nonalcoholic Fatty Liver Disease and Sarcopenia: Where Do We Stand? Filipović B, editor. Can J Gastroenterol Hepatol. 2020 Nov 2;2020:1–12. doi:10.1155/2020/8859719

171. Ke Y, Xu C, Lin J, Li Y. Role of hepatokines in non-alcoholic fatty liver disease. J Transl Int Med. 2019 Dec 1;7(4):143–8. doi:10.2478/jtim-2019-0029

172. Meex RCR, Watt MJ. Hepatokines: linking nonalcoholic fatty liver disease and insulin resistance. Nat Rev Endocrinol. 2017 Sep 9;13(9):509–20. doi:10.1038/nrendo.2017.56

173. Miao X, Alidadipour A, Saed V, Sayyadi F, Jadidi Y, Davoudi M, et al. Hepatokines: unveiling the molecular and cellular mechanisms connecting hepatic tissue to insulin resistance and inflammation. Acta Diabetol. 2024 Jul 20;61(11):1339–61. doi:10.1007/s00592-024-02335-9

174. Yang B, Lu L, Zhou D, Fan W, Barbier-Torres L, Steggerda J, et al. Regulatory network and interplay of hepatokines, stellakines, myokines and adipokines in nonalcoholic fatty liver diseases and nonalcoholic steatohepatitis. Front Endocrinol (Lausanne). 2022 Sep 30;13. doi:10.3389/fendo.2022.1007944

175. Bucarey JL, Trujillo-González I, Paules EM, Espinosa A. Myokines and Their Potential Protective Role Against Oxidative Stress in Metabolic Dysfunction-Associated Steatotic Liver Disease (MASLD). Antioxidants. 2024 Nov 7;13(11):1363. doi:10.3390/antiox13111363

176. Dasarathy S, Hatzoglou M. Hyperammonemia and proteostasis in cirrhosis. Curr Opin Clin Nutr Metab Care. 2018 Jan;21(1):30–6. doi:10.1097/MCO.0000000000000426

177. Qiu J, Thapaliya S, Runkana A, Yang Y, Tsien C, Mohan ML, et al. Hyperammonemia in cirrhosis induces transcriptional regulation of myostatin by an NF-κB–mediated mechanism. Proceedings of the National Academy of Sciences. 2013 Nov 5;110(45):18162–7. doi:10.1073/pnas.1317049110

178. Qiu J, Tsien C, Thapalaya S, Narayanan A, Weihl CC, Ching JK, et al. Hyperammonemia-mediated autophagy in skeletal muscle contributes to sarcopenia of cirrhosis. American Journal of Physiology-Endocrinology and Metabolism. 2012 Oct 15;303(8):E983–93. doi:10.1152/ajpendo.00183.2012

179. Kumar A, Davuluri G, Silva RN e, Engelen MPKJ, Ten Have GAM, Prayson R, et al. Ammonia lowering reverses sarcopenia of cirrhosis by restoring skeletal muscle proteostasis. Hepatology. 2017 Jun 28;65(6):2045–58. doi:10.1002/hep.29107

180. Zambon Azevedo V, Silaghi CA, Maurel T, Silaghi H, Ratziu V, Pais R. Impact of Sarcopenia on the Severity of the Liver Damage in Patients With Non-alcoholic Fatty Liver Disease. Front Nutr. 2022 Jan 17;8. doi:10.3389/fnut.2021.774030

181. Severinsen MCK, Pedersen BK. Muscle–Organ Crosstalk: The Emerging Roles of Myokines. Endocr Rev. 2020 Aug 1;41(4):594–609. doi:10.1210/endrev/bnaa016

182. Kim H, Lee S, Jeong C, Han Y, Lee M. RORα–GABP–TFAM axis alleviates myosteatosis with fatty atrophy through reinforcement of mitochondrial capacity. J Cachexia Sarcopenia Muscle. 2024 Apr 25;15(2):615–30. doi:10.1002/jcsm.13432

183. Zeybel M, Arif M, Li X, Altay O, Yang H, Shi M, et al. Multiomics Analysis Reveals the Impact of Microbiota on Host Metabolism in Hepatic Steatosis. Advanced Science. 2022 Apr 7;9(11). doi:10.1002/advs.202104373

184. De Chiara F, Ferret-Miñana A, Fernández-Costa JM, Senni A, Jalan R, Ramón-Azcón J. Fatty Hepatocytes Induce Skeletal Muscle Atrophy In Vitro: A New 3D Platform to Study the Protective Effect of Albumin in Non-Alcoholic Fatty Liver. Biomedicines. 2022 May 1;10(5). doi:10.3390/biomedicines10050958 PubMed PMID: 35625696.

185. Fernández-Costa JM, Ortega MA, Rodríguez-Comas J, Lopez-Muñoz G, Yeste J, Mangas-Florencio L, et al. Training-on-a-Chip: A Multi-Organ Device to Study the Effect of Muscle Exercise on Insulin Secretion in Vitro. Adv Mater Technol. 2023 Apr 23;8(7). doi:10.1002/admt.202200873

186. Tejedera-Villafranca A, Montolio M, Ramón-Azcón J, Fernández-Costa JM. Mimicking sarcolemmal damage in vitro: a contractile 3D model of skeletal muscle for drug testing in Duchenne muscular dystrophy. Biofabrication. 2023 Oct 1;15(4):045024. doi:10.1088/1758-5090/acfb3d

187. Mughal S, Sabater-Arcis M, Artero R, Ramón-Azcón J, Fernández-Costa JM. Taurine activates the AKT–mTOR axis to restore muscle mass and contractile strength in human 3D in vitro models of steroid myopathy. Dis Model Mech. 2024 Apr 1;17(4). doi:10.1242/dmm.050540

188. Ruiz-Gutiérrez M, Tejedera-Villafranca A, Pujol-Pinto S, Ramón-Azcón J, Fernández-Costa JM. Myo-MOVES: a custom electrical stimulation system for functional studies of 3D bioengineered muscle. Lab Chip. 2025;25(21):5677–90. doi:10.1039/D5LC00614G

189. Schindelin J, Arganda-Carreras I, Frise E, Kaynig V, Longair M, Pietzsch T, et al. Fiji: an open-source platform for biological-image analysis. Nat Methods. 2012 Jul 28;9(7):676–82. doi:10.1038/nmeth.2019

190. Stringer C, Wang T, Michaelos M, Pachitariu M. Cellpose: a generalist algorithm for cellular segmentation. Nat Methods. 2021 Jan 14;18(1):100–6. doi:10.1038/s41592-020-01018-x

191. Waisman A, Norris AM, Elías Costa M, Kopinke D. Automatic and unbiased segmentation and quantification of myofibers in skeletal muscle. Sci Rep. 2021 Jun 3;11(1):11793. doi:10.1038/s41598-021-91191-6

192. Sabater-Arcis M, Bargiela A, Moreno N, Poyatos-Garcia J, Vilchez JJ, Artero R. Musashi-2 contributes to myotonic dystrophy muscle dysfunction by promoting excessive autophagy through miR-7 biogenesis repression. Mol Ther Nucleic Acids. 2021 Sep 3;25:652–67. doi:10.1016/J.OMTN.2021.08.010

193. Brennan PN, Kopka CJ, Agirre-Garrido L, Hansen CD, Alkhouri N, Schattenberg JM, et al. Reviewing MAESTRO-NASH and the implications for hepatology and health systems in implementation/accessibility of Resmetirom. npj Gut and Liver. 2025 Jan 22;2(1):3. doi:10.1038/s44355-024-00017-5

194. Sanyal AJ, Newsome PN, Kliers I, Østergaard LH, Long MT, Kjær MS, et al. Phase 3 Trial of Semaglutide in Metabolic Dysfunction–Associated Steatohepatitis. New England Journal of Medicine. 2025 Jun 5;392(21):2089–99. doi:10.1056/NEJMoa2413258

195. Flessa CM, Nasiri-Ansari N, Kyrou I, Leca BM, Lianou M, Chatzigeorgiou A, et al. Genetic and Diet-Induced Animal Models for Non-Alcoholic Fatty Liver Disease (NAFLD) Research. Int J Mol Sci. 2022 Dec 13;23(24):15791. doi:10.3390/ijms232415791

196. Suriano F, Vieira-Silva S, Falony G, Roumain M, Paquot A, Pelicaen R, et al. Novel insights into the genetically obese (ob/ob) and diabetic (db/db) mice: two sides of the same coin. Microbiome. 2021 Dec 28;9(1):147. doi:10.1186/s40168-021-01097-8

197. KIRSCH R, CLARKSON V, SHEPHARD EG, MARAIS DA, JAFFER MA, WOODBURNE VE, et al. Rodent nutritional model of non-alcoholic steatohepatitis: Species, strain and sex difference studies. J Gastroenterol Hepatol. 2003 Nov 13;18(11):1272–82. doi:10.1046/j.1440-1746.2003.03198.x

198. Stöppeler S, Palmes D, Fehr M, Hölzen JP, Zibert A, Siaj R, et al. Gender and strain-specific differences in the development of steatosis in rats. Lab Anim. 2013 Jan 1;47(1):43–52. doi:10.1177/0023677212473717

199. Van Herck M, Vonghia L, Francque S. Animal Models of Nonalcoholic Fatty Liver Disease—A Starter's Guide. Nutrients. 2017 Sep 27;9(10):1072. doi:10.3390/nu9101072

200. Andersson TB, Kanebratt KP, Kenna JG. The HepaRG cell line: A unique in vitro tool for understanding drug metabolism and toxicology in human. Expert Opin Drug Metab Toxicol. 2012;8(7):909–20. doi:10.1517/17425255.2012.685159 PubMed PMID: 22568886.

201. Gerets HHJ, Tilmant K, Gerin B, Chanteux H, Depelchin BO, Dhalluin S, et al. Characterization of primary human hepatocytes, HepG2 cells, and HepaRG cells at the mRNA level and CYP activity in response to inducers and their predictivity for the detection of human hepatotoxins. Cell Biol Toxicol. 2012 Apr 19;28(2):69–87. doi:10.1007/s10565-011-9208-4

202. Samanez CH, Caron S, Briand O, Dehondt H, Duplan I, Kuipers F, et al. The human hepatocyte cell lines IHH and HepaRG: models to study glucose, lipid and lipoprotein metabolism. Arch Physiol Biochem. 2012 Jul 18;118(3):102–11. doi:10.3109/13813455.2012.683442

203. Ramboer E, De Craene B, De Kock J, Vanhaecke T, Berx G, Rogiers V, et al. Strategies for immortalization of primary hepatocytes. J Hepatol. 2014 Oct;61(4):925–43. doi:10.1016/j.jhep.2014.05.046

204. Ali M, Payne SL. Biomaterial-based cell delivery strategies to promote liver regeneration. Biomater Res. 2021 Feb 12;25(1). doi:10.1186/s40824-021-00206-w

205. Kostallari E, Wei B, Sicard D, Li J, Cooper SA, Gao J, et al. Stiffness is associated with hepatic stellate cell heterogeneity during liver fibrosis. American Journal of Physiology-Gastrointestinal and Liver Physiology. 2022 Feb 1;322(2):G234–46. doi:10.1152/ajpgi.00254.2021

206. Peters KM, Wilson RB, Borradaile NM. Non-parenchymal hepatic cell lipotoxicity and the coordinated progression of non-alcoholic fatty liver disease and atherosclerosis. Curr Opin Lipidol. 2018 Oct;29(5):417–22. doi:10.1097/MOL.0000000000000535

207. Deng J, Zhang X, Chen Z, Luo Y, Lu Y, Liu T, et al. A cell lines derived microfluidic liver model for investigation of hepatotoxicity induced by drug-drug interaction. Biomicrofluidics. 2019 Mar 1;13(2). doi:10.1063/1.5070088

208. Esch MB, Prot JM, Wang YI, Miller P, Llamas-Vidales JR, Naughton BA, et al. Multi-cellular 3D human primary liver cell culture elevates metabolic activity under fluidic flow. Lab Chip. 2015;15(10):2269–77. doi:10.1039/C5LC00237K

209. Moradi E, Jalili-Firoozinezhad S, Solati-Hashjin M. Microfluidic organ-on-a-chip models of human liver tissue. Acta Biomater. 2020 Oct;116:67–83. doi:10.1016/j.actbio.2020.08.041

210. Bircsak KM, DeBiasio R, Miedel M, Alsebahi A, Reddinger R, Saleh A, et al. A 3D microfluidic liver model for high throughput compound toxicity screening in the OrganoPlate®. Toxicology. 2021 Feb;450:152667. doi:10.1016/j.tox.2020.152667

211. Lee SY, Kim D, Lee SH, Sung JH. Microtechnology-based in vitro models: Mimicking liver function and pathophysiology. APL Bioeng. 2021 Dec 1;5(4). doi:10.1063/5.0061896

212. Yang J, Hirai Y, Iida K, Ito S, Trumm M, Terada S, et al. Integrated-gut-liver-on-a-chip platform as an in vitro human model of non-alcoholic fatty liver disease. Commun Biol. 2023 Mar 23;6(1):310. doi:10.1038/s42003-023-04710-8

213. Kostrzewski T, Cornforth T, Snow SA, Ouro-Gnao L, Rowe C, Large EM, et al. Three-dimensional perfused human in vitro model of non-alcoholic fatty liver disease. World J Gastroenterol. 2017;23(2):204. doi:10.3748/wjg.v23.i2.204

214. Kostrzewski T, Snow S, Battle AL, Peel S, Ahmad Z, Basak J, et al. Modelling human liver fibrosis in the context of non-alcoholic steatohepatitis using a microphysiological system. Commun Biol. 2021 Sep 15;4(1):1080. doi:10.1038/s42003-021-02616-x

215. Freag MS, Namgung B, Reyna Fernandez ME, Gherardi E, Sengupta S, Jang HL. Human Nonalcoholic Steatohepatitis on a Chip. Hepatol Commun. 2021 Feb;5(2):217–33. doi:10.1002/hep4.1647

216. Devasia AG, Ramasamy A, Leo CH, Devasia AG, Ramasamy A, Leo CH. Current Therapeutic Landscape for Metabolic Dysfunction-Associated Steatohepatitis. International Journal of Molecular Sciences 2025, Vol 26,. 2025 Feb 19;26(4). doi:10.3390/IJMS26041778 PubMed PMID: 40004240.

217. Gatzios A, Rombaut M, Buyl K, De Kock J, Rodrigues RM, Rogiers V, et al. From NAFLD to MAFLD: Aligning Translational In Vitro Research to Clinical Insights. Biomedicines. 2022 Jan 1;10(1):161. doi:10.3390/biomedicines10010161 PubMed PMID: 35052840.

218. Polidoro MA, Ferrari E, Marzorati S, Lleo A, Rasponi M. Experimental liver models: From cell culture techniques to microfluidic organs-on-chip. Liver International. 2021 Aug 26;41(8):1744–61. doi:10.1111/liv.14942

219. Boeckmans J, Natale A, Buyl K, Rogiers V, De Kock J, Vanhaecke T, et al. Human-based systems: Mechanistic NASH modelling just around the corner? Pharmacol Res. 2018 Aug 1;134:257–67. doi:10.1016/j.phrs.2018.06.029 PubMed PMID: 29964161.

220. Xu L, Hui AY, Albanis E, Arthur MJ, O'Byrne SM, Blaner WS, et al. Human hepatic stellate cell lines, LX-1 and LX-2: new tools for analysis of hepatic fibrosis. Gut. 2005 Jan;54(1):142–51. doi:10.1136/gut.2004.042127

221. Zahmatkesh E, Othman A, Braun B, Aspera R, Ruoß M, Piryaei A, et al. In vitro modeling of liver fibrosis in 3D microtissues using scalable micropatterning system. Arch Toxicol. 2022 Jun 2;96(6):1799–813. doi:10.1007/s00204-022-03265-7 PubMed PMID: 35366062.

222. Ress C. Mechanisms of intrahepatic triglyceride accumulation. World J Gastroenterol. 2016;22(4):1664. doi:10.3748/wjg.v22.i4.1664

223. Donnelly KL, Smith CI, Schwarzenberg SJ, Jessurun J, Boldt MD, Parks EJ. Sources of fatty acids stored in liver and secreted via lipoproteins in patients with nonalcoholic fatty liver disease. Journal of Clinical Investigation. 2005 May 2;115(5):1343–51. doi:10.1172/JCI23621

224. Tamura S, Shimomura I. Contribution of adipose tissue and de novo lipogenesis to nonalcoholic fatty liver disease. Journal of Clinical Investigation. 2005 May 2;115(5):1139–42. doi:10.1172/JCI24930

225. Schilcher K, Dayoub R, Kubitza M, Riepl J, Klein K, Buechler C, et al. Saturated Fat-Mediated Upregulation of IL-32 and CCL20 in Hepatocytes Contributes to Higher Expression of These Fibrosis-Driving Molecules in MASLD. Int J Mol Sci. 2023 Aug 25;24(17):13222. doi:10.3390/ijms241713222 PubMed PMID: 37686029.

226. Bronsard J, Savary C, Massart J, Viel R, Moutaux L, Catheline D, et al. 3D multi-cell-type liver organoids: A new model of non-alcoholic fatty liver disease for drug safety assessments. Toxicology in Vitro. 2024 Feb;94(March 2023):105728. doi:10.1016/j.tiv.2023.105728 PubMed PMID: 37951556.

227. Amouzandeh M, Sundstr€om A, Wahlin S, Wernerman J, Rooyackers O, Norberg Å, et al. Albumin and fibrinogen synthesis rates in advanced chronic liver disease. Am J Physiol Gastrointest Liver Physiol. 2023 Nov 1;325(5):G391–7. doi:10.1152/ajpgi.00072.2023 PubMed PMID: 37605837.

228. Guzman-Lepe J, Cervantes-Alvarez E, Collin de l'Hortet A, Wang Y, Mars WM, Oda Y, et al. Liver-enriched transcription factor expression relates to chronic hepatic failure in humans. Hepatol Commun. 2018 May 23;2(5):582–94. doi:10.1002/hep4.1172

229. Takagi S, Nakajima M, Kida K, Yamaura Y, Fukami T, Yokoi T. MicroRNAs regulate human hepatocyte nuclear factor 4α, modulating the expression of metabolic enzymes and cell cycle. Journal of Biological Chemistry. 2010 Feb;285(7):4415–22. doi:10.1074/jbc.M109.085431 PubMed PMID: 20018894.

230. Ampuero J, Aller R, Gallego-Durán R, Crespo J, Calleja JL, García-Monzón C, et al. The biochemical pattern defines MASLD phenotypes linked to distinct histology and prognosis. J Gastroenterol. 2024 Jul 15;59(7):586–97. doi:10.1007/s00535-024-02098-8

231. Porter AG, Jänicke RU. Emerging roles of caspase-3 in apoptosis. Cell Death Differ. 1999 Feb 28;6(2):99–104. doi:10.1038/sj.cdd.4400476

232. Dong J, Viswanathan S, Adami E, Singh BK, Chothani SP, Ng B, et al. Hepatocyte-specific IL11 cis-signaling drives lipotoxicity and underlies the transition from NAFLD to NASH. Nat Commun. 2021 Jan 4;12(1):66. doi:10.1038/s41467-020-20303-z PubMed PMID: 33397952.

233. Lindenmeyer CC, McCullough AJ. The Natural History of Nonalcoholic Fatty Liver Disease—An Evolving View. Clin Liver Dis. 2018 Feb;22(1):11–21. doi:10.1016/j.cld.2017.08.003

234. Rennert C, Heil T, Schicht G, Stilkerich A, Seidemann L, Kegel-Hübner V, et al. Prolonged Lipid Accumulation in Cultured Primary Human Hepatocytes Rather Leads to ER Stress than Oxidative Stress. Int J Mol Sci. 2020 Sep 26;21(19):7097. doi:10.3390/ijms21197097

235. Hasui N, Sakaguchi K, Ogawa T, Sakamoto Y, Shimizu T. In vitro ballooned hepatocytes can be produced by primary human hepatocytes and hepatic stellate cell sheets. Sci Rep. 2022 Mar 29;12(1):5341. doi:10.1038/s41598-022-09428-x

236. Feaver RE, Cole BK, Lawson MJ, Hoang SA, Marukian S, Blackman BR, et al. Development of an in vitro human liver system for interrogating nonalcoholic steatohepatitis. JCI Insight. 2016 Dec 8;1(20). doi:10.1172/jci.insight.90954

237. Tachibana S, Zhang X, Ito K, Ota Y, Cameron AM, Williams GM, et al. Interleukin-6 is required for cell cycle arrest and activation of DNA repair enzymes after partial hepatectomy in mice. Cell Biosci. 2014 Dec 3;4(1):6. doi:10.1186/2045-3701-4-6

238. STREETZ KL, LUEDDE T, MANNS MP, TRAUTWEIN C. Interleukin 6 and liver regeneration. Gut. 2000 Aug 1;47(2):309–12. doi:10.1136/gut.47.2.309

239. Aleksandrova K, Boeing H, Nöthlings U, Jenab M, Fedirko V, Kaaks R, et al. Inflammatory and metabolic biomarkers and risk of liver and biliary tract cancer. Hepatology. 2014 Sep;60(3):858–71. doi:10.1002/hep.27016

240. Li L, Cui L, Lin P, Liu Z, Bao S, Ma X, et al. Kupffer-cell-derived IL-6 is repurposed for hepatocyte dedifferentiation via activating progenitor genes from injury-specific enhancers. Cell Stem Cell. 2023 Mar;30(3):283-299.e9. doi:10.1016/j.stem.2023.01.009

241. Liu G, Wang X, Yang T, Yan Y, Xiang T, Yang L, et al. High Interleukin-8 Levels Associated With Decreased Survival in Patients With Cirrhosis Following Transjugular Intrahepatic Portosystemic Shunt. Front Med (Lausanne). 2022 Feb 28;9. doi:10.3389/fmed.2022.829245

242. Glass O, Henao R, Patel K, Guy CD, Gruss HJ, Syn WK, et al. Serum Interleukin-8, Osteopontin, and Monocyte Chemoattractant Protein 1 Are Associated With Hepatic Fibrosis in Patients With Nonalcoholic Fatty Liver Disease. Hepatol Commun. 2018 Nov 1;2(11):1344–55. doi:10.1002/HEP4.1237

243. Kubo T, Nishimura N, Kaji K, Tomooka F, Shibamoto A, Iwai S, et al. Role of Epiregulin on Lipopolysaccharide-Induced Hepatocarcinogenesis as a Mediator via EGFR Signaling in the Cancer Microenvironment. Int J Mol Sci. 2024 Apr 17;25(8):4405. doi:10.3390/ijms25084405 PubMed PMID: 38673992.

244. Wada T, Takeda Y, Okekawa A, Komatsu G, Iwasa Y, Onogi Y, et al. Deletion of platelet-derived growth factor receptor β suppresses tumorigenesis in metabolic dysfunction-associated steatohepatitis (MASH) mice with diabetes. Sci Rep. 2024 Oct 11;14(1):23829. doi:10.1038/s41598-024-75713-6

245. Wells RG. Hepatic fibrosis in children and adults. Clin Liver Dis (Hoboken). 2017 Apr 20;9(4):99–101. doi:10.1002/cld.623

246. Pereira RO, Abel ED. BATokines in metabolic liver disease: good cops or bad cops? EMBO J. 2024 Sep 25;43(21):4807–9. doi:10.1038/s44318-024-00239-6

247. Hall A, Cotoi C, Luong TV, Watkins J, Bhathal P, Quaglia A. Collagen and elastic fibres in acute and chronic liver injury. Sci Rep. 2021 Jul 15;11(1):14569. doi:10.1038/s41598-021-93566-1

248. Mughal S, López-Muñoz GA, Fernández-Costa JM, Cortés-Reséndiz A, De Chiara F, Ramón-Azcón J. Organs-on-Chips: Trends and Challenges in Advanced Systems Integration. Adv Mater Interfaces. 2022 Nov 25;9(33). doi:10.1002/admi.202201618

249. Giza S, Mojica-Santiago JA, Parafati M, Malany LK, Platt D, Schmidt CE, et al. Microphysiological system for studying contractile differences in young, active, and old, sedentary adult derived skeletal muscle cells. Aging Cell. 2022 Jul 2;21(7). doi:10.1111/acel.13650

250. Fernández-Costa JM, Tejedera-Vilafranca A, Fernández-Garibay X, Ramón-Azcón J. Muscle-on-a-chip devices: a new era for in vitro modelling of muscular dystrophies. Dis Model Mech. 2023 Jun 1;16(6). doi:10.1242/dmm.050107

251. Santoso JW, McCain ML. Neuromuscular disease modeling on a chip. Dis Model Mech. 2020 Jul 1;13(7). doi:10.1242/dmm.044867

252. Agrawal G, Aung A, Varghese S. Skeletal muscle-on-a-chip: an in vitro model to evaluate tissue formation and injury. Lab Chip. 2017;17(20):3447–61. doi:10.1039/C7LC00512A

253. Madden L, Juhas M, Kraus WE, Truskey GA, Bursac N. Bioengineered human myobundles mimic clinical responses of skeletal muscle to drugs. Elife. 2015 Jan 9;4. doi:10.7554/eLife.04885

254. Khodabukus A, Madden L, Prabhu NK, Koves TR, Jackman CP, Muoio DM, et al. Electrical stimulation increases hypertrophy and metabolic flux in tissue-engineered human skeletal muscle. Biomaterials. 2019 Apr;198:259–69. doi:10.1016/j.biomaterials.2018.08.058

255. Ebrahimi M, Lad H, Fusto A, Tiper Y, Datye A, Nguyen CT, et al. De novo revertant fiber formation and therapy testing in a 3D culture model of Duchenne muscular dystrophy skeletal muscle. Acta Biomater. 2021 Sep;132:227–44. doi:10.1016/j.actbio.2021.05.020

256. Afshar Bakooshli M, Lippmann ES, Mulcahy B, Iyer N, Nguyen CT, Tung K, et al. A 3D culture model of innervated human skeletal muscle enables studies of the adult neuromuscular junction. Elife. 2019 May 14;8. doi:10.7554/eLife.44530

257. Rao L, Qian Y, Khodabukus A, Ribar T, Bursac N. Engineering human pluripotent stem cells into a functional skeletal muscle tissue. Nat Commun. 2018 Jan 9;9(1):126. doi:10.1038/s41467-017-02636-4

258. Ortega MA, Fernández-Garibay X, Castaño AG, De Chiara F, Hernández-Albors A, Balaguer-Trias J, et al. Muscle-on-a-chip with an on-site multiplexed biosensing system for: In situ monitoring of secreted IL-6 and TNF-α. Lab Chip. 2019;19(15):2568–80. doi:10.1039/c9lc00285e PubMed PMID: 31243422.

259. Hernández-Albors A, Castaño AG, Fernández-Garibay X, Ortega MA, Balaguer J, Ramón-Azcón J. Microphysiological sensing platform for an in-situ detection of tissue-secreted cytokines. Biosens Bioelectron X. 2019 Oct;2:100025. doi:10.1016/j.biosx.2019.100025

260. Vandenburgh H, Shansky J, Benesch-Lee F, Barbata V, Reid J, Thorrez L, et al. Drug-screening platform based on the contractility of tissue-engineered muscle. Muscle Nerve. 2008 Apr 19;37(4):438–47. doi:10.1002/mus.20931

261. Alheib O, da Silva LP, Caballero D, Pires RA, Kundu SC, Correlo VM, et al. Micropatterned gellan gum-based hydrogels tailored with laminin-derived peptides for skeletal muscle tissue engineering. Biomaterials. 2021 Dec;279:121217. doi:10.1016/j.biomaterials.2021.121217

262. Kumbaroğlu BF, Balaban YH, Düger T. Muscle Strength and Cardiovascular Health in MASLD: A Prospective Study. Medicina (Lithuania). 2025 Feb 1;61(2):1–15. doi:10.3390/medicina61020247 PubMed PMID: 40005364.

263. de Araujo MEGG, Liebscher G, Hess MW, Huber LA. Lysosomal size matters. Traffic. 2020 Jan 1;21(1):60–75. doi:10.1111/TRA.12714/ PubMed PMID: 31808235.

264. Henrot P, Blervaque L, Dupin I, Zysman M, Esteves P, Gouzi F, et al. Cellular interplay in skeletal muscle regeneration and wasting: insights from animal models. Journal of Cachexia, Sarcopenia and Muscle [Internet]. John Wiley and Sons Inc; 2023 Apr 1. p. 745–57. Available from: https://pubmed.ncbi.nlm.nih.gov/36811134/ doi:10.1002/jcsm.13103 PubMed PMID: 36811134.

265. Tandon P, Montano-Loza AJ, Lai JC, Dasarathy S, Merli M. Sarcopenia and frailty in decompensated cirrhosis. J Hepatol. 2021 Jul 1;75(Suppl 1):S147–62. doi:10.1016/j.jhep.2021.01.025 PubMed PMID: 34039486.

266. Visser M, Pahor M, Taaffe DR, Goodpaster BH, Simonsick EM, Newman AB, et al. Relationship of interleukin-6 and tumor necrosis factor-α with muscle mass and muscle strength in elderly men and women: The health ABC study. Journals of Gerontology - Series A Biological Sciences and Medical Sciences. 2002 May 1;57(5):326–32. doi:10.1093/gerona/57.5.M326 PubMed PMID: 11983728.

267. Yakabe M, Ogawa S, Ota H, Iijima K, Eto M, Ouchi Y, et al. Inhibition of interleukin-6 decreases atrogene expression and ameliorates tail suspension-induced skeletal muscle atrophy. Asakura A, editor. PLoS One. 2018 Jan 19;13(1):e0191318. doi:10.1371/journal.pone.0191318

268. Huang Z, Zhong L, Zhu J, Xu H, Ma W, Zhang L, et al. Inhibition of IL-6/JAK/STAT3 pathway rescues denervation-induced skeletal muscle atrophy. Ann Transl Med. 2020 Dec;8(24):1681–1681. doi:10.21037/atm-20-7269 PubMed PMID: 29351340.

269. De Benedetti F, Alonzi T, Moretta A, Lazzaro D, Costa P, Poli V, et al. Interleukin 6 causes growth impairment in transgenic mice through a decrease in insulin-like growth factor-I. A model for stunted growth in children with chronic inflammation. Journal of Clinical Investigation. 1997 Feb 15;99(4). doi:10.1172/JCI119207 PubMed PMID: 9045866.

270. Forcina L, Miano C, Scicchitano BM, Rizzuto E, Berardinelli MG, De Benedetti F, et al. Increased Circulating Levels of Interleukin-6 Affect the Redox Balance in Skeletal Muscle. Oxid Med Cell Longev. 2019 Nov 16;2019. doi:10.1155/2019/3018584 PubMed PMID: 31827671.

271. Bonaldo P, Sandri M. Cellular and molecular mechanisms of muscle atrophy. DMM Disease Models and Mechanisms. 2013 Jan;6(1):25–39. doi:10.1242/DMM.010389, PubMed PMID: 23268536.

272. Hunt LC, Graca FA, Pagala V, Wang YD, Li Y, Yuan ZF, et al. Integrated genomic and proteomic analyses identify stimulus-dependent molecular changes associated with distinct modes of skeletal muscle atrophy. Cell Rep. 2021 Nov;37(6):109971. doi:10.1016/j.celrep.2021.109971

273. Milewska M, Domoradzki T, Majewska A, Błaszczyk M, Gajewska M, Hulanicka M, et al. Interleukin-8 enhances myocilin expression, Akt-FoxO3 signaling and myogenic differentiation in rat skeletal muscle cells. J Cell Physiol. 2019;234(11):19675–90. doi:10.1002/jcp.28568 PubMed PMID: 30945300.

274. Brzeszczyńska J, Meyer A, McGregor R, Schilb A, Degen S, Tadini V, et al. Alterations in the in vitro and in vivo regulation of muscle regeneration in healthy ageing and the influence of sarcopenia. J Cachexia Sarcopenia Muscle. 2018 Feb 6;9(1):93–105. doi:10.1002/jcsm.12252

275. Pelosi L, Berardinelli MG, Forcina L, Ascenzi F, Rizzuto E, Sandri M, et al. Sustained Systemic Levels of IL-6 Impinge Early Muscle Growth and Induce Muscle Atrophy and Wasting in Adulthood. Cells. 2021 Jul 18;10(7):1816. doi:10.3390/cells10071816

276. Park MJ, Choi KM. Interplay of skeletal muscle and adipose tissue: sarcopenic obesity. Metabolism. 2023 Jul;144:155577. doi:10.1016/j.metabol.2023.155577

277. Zammit PS. Function of the myogenic regulatory factors Myf5, MyoD, Myogenin and MRF4 in skeletal muscle, satellite cells and regenerative myogenesis. Semin Cell Dev Biol. 2017 Dec;72:19–32. doi:10.1016/j.semcdb.2017.11.011

278. O'Leary MF, Wallace GR, Davis ET, Murphy DP, Nicholson T, Bennett AJ, et al. Obese subcutaneous adipose tissue impairs human myogenesis, particularly in old skeletal muscle, via resistin-mediated activation of NFκB. Sci Rep. 2018 Oct 18;8(1):15360. doi:10.1038/s41598-018-33840-x

279. Ono Y, Sakamoto K. Lipopolysaccharide inhibits myogenic differentiation of C2C12 myoblasts through the Toll-like receptor 4-nuclear factor-κB signaling pathway and myoblast-derived tumor necrosis factor-α. PLoS One. 2017 Jul 24;12(7):e0182040. doi:10.1371/journal.pone.0182040

280. Yablonka-Reuveni Z, Balestreri TM, Bowen-Pope DF. Regulation of proliferation and differentiation of myoblasts derived from adult mouse skeletal muscle by specific isoforms of PDGF. J Cell Biol. 1990 Oct 1;111(4):1623–9. doi:10.1083/jcb.111.4.1623

281. Lawlor MA, Feng X, Everding DR, Sieger K, Stewart CEH, Rotwein P. Dual Control of Muscle Cell Survival by Distinct Growth Factor-Regulated Signaling Pathways. Mol Cell Biol. 2000 May 1;20(9):3256–65. doi:10.1128/MCB.20.9.3256-3265.2000

282. Gros F, Muller S. The role of lysosomes in metabolic and autoimmune diseases. Nature Reviews Nephrology [Internet]. Nature Research; 2023 Jun 1. p. 366–83. Available from: https://pubmed.ncbi.nlm.nih.gov/36894628/ doi:10.1038/s41581-023-00692-2 PubMed PMID: 36894628.

283. Sandri M. Autophagy in health and disease. 3. Involvement of autophagy in muscle atrophy. American Journal of Physiology-Cell Physiology. 2010 Jun;298(6):C1291–7. doi:10.1152/ajpcell.00531.2009 PubMed PMID: 20089936.

284. Li Z, Hui J, Yang P, Mao H. Microfluidic Organ-on-a-Chip System for Disease Modeling and Drug Development. Biosensors (Basel). 2022 May 27;12(6):370. doi:10.3390/bios12060370

285. Ingber DE. Human organs-on-chips for disease modelling, drug development and personalized medicine. Nature Reviews Genetics 2022. 2022 Mar 25;1–25. doi:10.1038/s41576-022-00466-9 PubMed PMID: 35338360.

286. Li ZA, Tuan RS. Towards establishing human body-on-a-chip systems. Stem Cell Res Ther. 2022 Aug 20;13(1):431. doi:10.1186/s13287-022-03130-5

287. Leung CM, de Haan P, Ronaldson-Bouchard K, Kim GA, Ko J, Rho HS, et al. A guide to the organ-on-a-chip. Nature Reviews Methods Primers 2022 2:1. 2022 May 12;2(1):1–29. doi:10.1038/s43586-022-00118-6

288. Vunjak-Novakovic G, Ronaldson-Bouchard K, Radisic M. Organs-on-a-chip models for biological research. Cell. 2021 Sep;184(18):4597–611. doi:10.1016/j.cell.2021.08.005

289. Juguilon C, Khosravi R, Radisic M, Wu JC. In Vitro Modeling of Interorgan Crosstalk: Multi-Organ-on-a-Chip for Studying Cardiovascular-Kidney-Metabolic Syndrome. Circ Res. 2025 May 23;136(11):1476–93. doi:10.1161/CIRCRESAHA.125.325497

290. Srivastava SK, Foo GW, Aggarwal N, Chang MW. Organ-on-chip technology: Opportunities and challenges. Biotechnology Notes. 2024;5:8–12. doi:10.1016/j.biotno.2024.01.001

291. Obeid PJ, Yammine P, El-Nakat H, Kassab R, Tannous T, Nasr Z, et al. Organ-On-A-Chip Devices: Technology Progress and Challenges. ChemBioChem. 2024 Dec 2;25(23). doi:10.1002/cbic.202400580

292. Zhou L, Huang J, Li C, Gu Q, Li G, Li ZA, et al. Organoids and organs-on-chips: Recent advances, applications in drug development, and regulatory challenges. Med. 2025 Apr;6(4):100667. doi:10.1016/j.medj.2025.100667

293. Caballero D, Reis RL, Kundu SC. Boosting the Clinical Translation of Organ-on-a-Chip Technology. Bioengineering. 2022 Oct 14;9(10):549. doi:10.3390/bioengineering9100549

294. Ismayilzada N, Tarar C, Dabbagh SR, Tokyay BK, Dilmani SA, Sokullu E, et al. Skin-on-a-chip technologies towards clinical translation and commercialization. Biofabrication. 2024 Oct 1;16(4):042001. doi:10.1088/1758-5090/ad5f55

295. Jarvis H, Craig D, Barker R, Spiers G, Stow D, Anstee QM, et al. Metabolic risk factors and incident advanced liver disease in non-alcoholic fatty liver disease (NAFLD): A systematic review and meta-analysis of population-based observational studies. Singal A, editor. PLoS Med. 2020 Apr 30;17(4):e1003100. doi:10.1371/journal.pmed.1003100

296. Fernández-Mincone T, Contreras-Briceño F, Espinosa-Ramírez M, García-Valdés P, López-Fuenzalida A, Riquelme A, et al. Nonalcoholic fatty liver disease and sarcopenia: pathophysiological connections and therapeutic implications. Expert Rev Gastroenterol Hepatol. 2020 Dec 1;14(12):1141–57. doi:10.1080/17474124.2020.1810563

297. Kwon Y, Jeong SJ. Relative Skeletal Muscle Mass Is an Important Factor in Non-Alcoholic Fatty Liver Disease in Non-Obese Children and Adolescents. J Clin Med. 2020 Oct 19;9(10):3355. doi:10.3390/jcm9103355

298. Oh KW, Lee K, Ahn B, Furlani EP. Design of pressure-driven microfluidic networks using electric circuit analogy. Lab Chip. 2012;12(3):515–45. doi:10.1039/C2LC20799K

299. Saravanakumar SM, Cicek PV. Microfluidic Mixing: A Physics-Oriented Review. Micromachines (Basel). 2023 Sep 25;14(10):1827. doi:10.3390/mi14101827

300. Gurkan UA, Wood DK, Carranza D, Herbertson LH, Diamond SL, Du E, et al. Next generation microfluidics: fulfilling the promise of lab-on-a-chip technologies. Lab Chip. 2024;24(7):1867–74. doi:10.1039/D3LC00796K

301. Whitesides GM. The origins and the future of microfluidics. Nature. 2006 Jul 26;442(7101):368–73. doi:10.1038/nature05058

302. Stone HA, Stroock AD, Ajdari A. Engineering Flows in Small Devices: Microfluidics Toward a Lab-on-a-Chip. Annu Rev Fluid Mech. 2004 Jan 21;36(1):381–411. doi:10.1146/annurev.fluid.36.050802.122124

303. Squires TM, Quake SR. Microfluidics: Fluid physics at the nanoliter scale. Rev Mod Phys. 2005 Oct 6;77(3):977–1026. doi:10.1103/RevModPhys.77.977

304. Huh D, Hamilton GA, Ingber DE. From 3D cell culture to organs-on-chips. Trends Cell Biol. 2011 Dec;21(12):745–54. doi:10.1016/j.tcb.2011.09.005

305. Stroock AD, Dertinger SKW, Ajdari A, Mezić I, Stone HA, Whitesides GM. Chaotic Mixer for Microchannels. Science (1979). 2002 Jan 25;295(5555):647–51. doi:10.1126/science.1066238

306. Li L, Chen L, Hu L. Nuclear Factor High-mobility Group Box1 Mediating the Activation of Toll-like Receptor 4 Signaling in Hepatocytes in the Early Stage of Non-alcoholic Fatty Liver Disease in Mice. J Clin Exp Hepatol. 2011 Sep;1(2):123–4. doi:10.1016/S0973-6883(11)60136-9

307. Baffy G. Kupffer cells in non-alcoholic fatty liver disease: The emerging view. J Hepatol. 2009 Jul;51(1):212–23. doi:10.1016/j.jhep.2009.03.008

308. Wree A, Eguchi A, McGeough MD, Pena CA, Johnson CD, Canbay A, et al. NLRP3 inflammasome activation results in hepatocyte pyroptosis, liver inflammation, and fibrosis in mice. Hepatology. 2014 Mar;59(3):898–910. doi:10.1002/hep.26592

309. Koliaki C, Szendroedi J, Kaul K, Jelenik T, Nowotny P, Jankowiak F, et al. Adaptation of Hepatic Mitochondrial Function in Humans with Non-Alcoholic Fatty Liver Is Lost in Steatohepatitis. Cell Metab. 2015 May;21(5):739–46. doi:10.1016/j.cmet.2015.04.004

310. Miura K, Yang L, van Rooijen N, Brenner DA, Ohnishi H, Seki E. Toll-Like Receptor 2 and Palmitic Acid Cooperatively Contribute to the Development of Nonalcoholic Steatohepatitis Through Inflammasome Activation in Mice. Hepatology. 2013 Feb;57(2):577–89. doi:10.1002/hep.26081

311. Lee JY, Ye J, Gao Z, Youn HS, Lee WH, Zhao L, et al. Reciprocal Modulation of Toll-like Receptor-4 Signaling Pathways Involving MyD88 and Phosphatidylinositol 3-Kinase/AKT by Saturated and Polyunsaturated Fatty Acids. Journal of Biological Chemistry. 2003 Sep;278(39):37041–51. doi:10.1074/jbc.M305213200

312. Zhan SS, Jiang JX, Wu J, Halsted C, Friedman SL, Zern MA, et al. Phagocytosis of apoptotic bodies by hepatic stellate cells induces NADPH oxidase and is associated with liver fibrosis in vivo. Hepatology. 2006 Mar;43(3):435–43. doi:10.1002/hep.21093

313. Ibrahim SH, Hirsova P, Tomita K, Bronk SF, Werneburg NW, Harrison SA, et al. Mixed lineage kinase 3 mediates release of C-X-C motif ligand 10–bearing chemotactic extracellular vesicles from lipotoxic hepatocytes. Hepatology. 2016 Mar 11;63(3):731–44. doi:10.1002/hep.28252

314. Seki E, De Minicis S, Österreicher CH, Kluwe J, Osawa Y, Brenner DA, et al. TLR4 enhances TGF-β signaling and hepatic fibrosis. Nature Medicine 2007 13:11. 2007 Oct 21;13(11):1324–32. doi:10.1038/nm1663 PubMed PMID: 17952090.

315. Hritz I, Mandrekar P, Velayudham A, Catalano D, Dolganiuc A, Kodys K, et al. The critical role of toll-like receptor (TLR) 4 in alcoholic liver disease is independent of the common TLR adapter MyD88†. Hepatology. 2008 Oct;48(4):1224–31. doi:10.1002/hep.22470

316. Miura K, Kodama Y, Inokuchi S, Schnabl B, Aoyama T, Ohnishi H, et al. Toll-Like Receptor 9 Promotes Steatohepatitis by Induction of Interleukin-1β in Mice. Gastroenterology. 2010 Jul;139(1):323-334.e7. doi:10.1053/j.gastro.2010.03.052

317. Zhu L, Baker RD, Baker SS. Gut microbiome and nonalcoholic fatty liver diseases. Pediatr Res. 2015 Jan 13;77(1–2):245–51. doi:10.1038/pr.2014.157

318. Mestre R, Patiño T, Barceló X, Anand S, Pérez-Jiménez A, Sánchez S. Force Modulation and Adaptability of 3D-Bioprinted Biological Actuators Based on Skeletal Muscle Tissue. Adv Mater Technol. 2019 Feb 13;4(2). doi:10.1002/admt.201800631

319. García-Lizarribar A, Fernández-Garibay X, Velasco-Mallorquí F, Castaño AG, Samitier J, Ramon-Azcon J. Composite Biomaterials as Long-Lasting Scaffolds for 3D Bioprinting of Highly Aligned Muscle Tissue. Macromol Biosci. 2018 Oct 29;18(10). doi:10.1002/mabi.201800167

320. Grefte S, Vullinghs S, Kuijpers-Jagtman AM, Torensma R, Von den Hoff JW. Matrigel, but not collagen I, maintains the differentiation capacity of muscle derived cells in vitro. Biomedical Materials. 2012 Oct 1;7(5):055004. doi:10.1088/1748-6041/7/5/055004

321. Hinds S, Bian W, Dennis RG, Bursac N. The role of extracellular matrix composition in structure and function of bioengineered skeletal muscle. Biomaterials. 2011 May;32(14):3575–83. doi:10.1016/j.biomaterials.2011.01.062

322. Vandenburgh H, Shansky J, Benesch-Lee F, Skelly K, Spinazzola JM, Saponjian Y, et al. Automated drug screening with contractile muscle tissue engineered from dystrophic myoblasts. The FASEB Journal. 2009 Oct;23(10):3325–34. doi:10.1096/fj.09-134411

323. Fernández-Garibay X, Gómez-Florit M, Domingues RMA, Gomes ME, Fernández-Costa JM, Ramón-Azcón J. Xeno-free bioengineered human skeletal muscle tissue using human platelet lysate-based hydrogels. Biofabrication. 2022 Oct 1;14(4):045015. doi:10.1088/1758-5090/ac8dc8

324. Christensen RK, von Halling Laier C, Kiziltay A, Wilson S, Larsen NB. 3D Printed Hydrogel Multiassay Platforms for Robust Generation of Engineered Contractile Tissues. Biomacromolecules. 2020 Feb 10;21(2):356–65. doi:10.1021/acs.biomac.9b01274

325. Kim JH, Seol YJ, Ko IK, Kang HW, Lee YK, Yoo JJ, et al. 3D Bioprinted Human Skeletal Muscle Constructs for Muscle Function Restoration. Sci Rep. 2018 Aug 17;8(1):12307. doi:10.1038/s41598-018-29968-5

326. Costantini M, Testa S, Mozetic P, Barbetta A, Fuoco C, Fornetti E, et al. Microfluidic-enhanced 3D bioprinting of aligned myoblast-laden hydrogels leads to functionally organized myofibers in vitro and in vivo. Biomaterials. 2017 Jul;131:98–110. doi:10.1016/j.biomaterials.2017.03.026

327. Kim W, Kim G. 3D bioprinting of functional cell-laden bioinks and its application for cell-alignment and maturation. Appl Mater Today. 2020 Jun;19:100588. doi:10.1016/j.apmt.2020.100588

328. Ebrahimi M, Ostrovidov S, Salehi S, Kim SB, Bae H, Khademhosseini A. Enhanced skeletal muscle formation on microfluidic spun gelatin methacryloyl (GelMA) fibres using surface patterning and agrin treatment. J Tissue Eng Regen Med. 2018 Nov;12(11):2151–63. doi:10.1002/term.2738

329. Shi X, Ostrovidov S, Zhao Y, Liang X, Kasuya M, Kurihara K, et al. Microfluidic spinning of cell-responsive grooved microfibers. Adv Funct Mater. 2015;25(15):2250–9. doi:10.1002/adfm.201404531

Appendix A. Signal translation into inflammatory and fibrogenic programs in MASLD.

Appendix A provides a complementary mechanistic overview of the innate immune signals that connect hepatocellular injury, gut-derived microbial products, inflammation, and fibrogenesis during MASLD progression. Specifically, it summarizes selected DAMPs and PAMPs that are relevant to the transition from steatosis to MASH, emphasizing their cellular sources, target pattern-recognition receptors, downstream signaling pathways, and biological outcomes. This appendix is intended to support the mechanistic framework presented in the main text by organizing the molecular cues through which lipotoxic stress, cell death, intestinal dysbiosis, and hepatic immune activation converge on Kupffer cells, recruited macrophages, HSCs, and other liver-resident populations to amplify inflammation and extracellular matrix remodeling.

Table A1. DAMP- and PAMP-mediated signaling pathways involved in inflammatory and fibrogenic programs during MASLD progression.

Ligand (type)	**Main source**	**Target PRRs**	**Downstream effects**	**Biological outcomes**
HMGB1 (DAMP) [112,306,307]	Necrotic or apoptotic hepatocytes under lipotoxicity and oxidative stress	TLR2, TLR4 on KCs, monocyte-derived macrophages and HSCs	MyD88–NF-κB MAPKs (JNK, p38), AP-1 activation ↑TNF, IL-1β, IL-6, CCL2, collagen genes	Amplification of local inflammation, recruitment of inflammatory monocytes, activation and proliferation of HSCs, ECM deposition and fibrosis
Extracellular ATP (DAMP) [111,308]	Injured, necrotic or ballooned hepatocytes and other dying cells	P2X7 and other purinergic receptors on KCs, recruited macrophages and HSCs	P2X7-mediated K^+ efflux NLRP3 inflammasome assembly	IL-1β and IL-18 release, pyroptotic cell death, enhanced chemotaxis and fibrogenic

			Caspase-1 activation Maturation of IL-1β and IL-18	activation of HSCs
Mitochondrial DNA (DAMP) [113,309]	Damaged hepatocytes and extracellular vesicles under lipotoxic and oxidative stress	TLR9 in endosomes of KCs, other myeloid cells and possibly HSCs	MyD88-dependent NF-κB and IRF signaling ↑ Type I interferons and pro-inflammatory cytokines	Transition to MASH, recruitment of inflammatory monocytes, macrophage and HSC activation
Lipotoxic lipids (DAMP) [310,311]	Accumulated within hepatocytes and from dysregulated lipid metabolism	TLR4 on KCs, monocyte-derived macrophages, HSCs and hepatocytes NLRP3 inflammasome	NF-κB, JNK and p38 activation ROS production NLRP3 assembly Caspase-1 activation ↑ TGF-β and PDGF signaling pathways	Hepatocyte death, pro-inflammatory polarization of macrophages, HSC activation, ECM deposition and fibrosis worsening
Hepatocyte apoptotic bodies and EVs (DAMP complexes) [312,313]	Apoptotic hepatocytes and their extracellular vesicles under lipotoxic and ER-stress	Phagocytic receptors and TLRs on KCs and HSCs (cargo-dependent)	NF-κB and MAPKs ↑ TGF-β, PDGF, and fibrogenic transcriptional programs in HSCs	Chemotaxis and activation of macrophages, direct profibrogenic activation of HSCs
LPS (PAMP) [314,315]	Product of dysbiotic gut microbiota reaching the liver via portal blood in “leaky gut”	TLR4 on KCs, monocyte-derived macrophages, HSCs, LSECs and hepatocytes	MyD88- and TRIF-dependent NF-κB and IRF3 activation ↑ TNF, IL-1β, IL-6, CCL2, type I interferons	Recruitment of $CCR2^{+}$ monocytes and neutrophils, chronic HSC activation and fibrogenesis,

			↓ BAMBI in HSCs, sensitizing to TGF-β	increased risk of HCC
Bacterial CpG DNA (PAMP) [107,113,316]	Bacterial DNA from dysbiotic gut	TLR9 in KCs and other hepatic cells	MyD88–NF-κB and IRF7 activation ↑ Pro-inflammatory cytokines and type I interferons	Transition to MASH, reinforcement of macrophage activation, potential contribution to adaptive immune priming and fibrogenesis
Flagellin (PAMP) [112]	Flagellar protein from motile gut bacteria	TLR5 on KCs and other myeloid cells	NF-κB and MAPK activation ↑ Pro-inflammatory cytokines and chemokines	Hepatic inflammation and neutrophil recruitment Cooperation with LPS in driving MASH-associated inflammation
Peptidoglycan (PAMP) [317]	Gram-positive bacterial cell wall components translocating from the gut	TLR2 (in dimers with TLR1/TLR6) on KCs, monocyte-derived macrophages and HSCs	MyD88–NF-κB and MAPK activation ↑ TNF, IL-1β, IL-6 and chemokines	Low-grade chronic inflammation, macrophage activation and HSC priming Synergistic with LPS and DAMPs

Appendix B. Biomaterial requirements and fabrication strategies for *in vitro* skeletal muscle models

Appendix B provides a complementary technical overview of the biomaterial and fabrication strategies used for skeletal muscle bioengineering *in vitro*. It summarizes the main design requirements for muscle-supportive matrices, including biocompatibility, mechanical compliance, degradability, adhesive cues, structural stability, and compatibility with functional maturation. The appendix also discusses the advantages and limitations of commonly used biomaterials, with particular attention to Matrigel-containing systems, and compares fabrication approaches such as hydrogel molding, micromolding, 3D bioprinting, and microfluidic extrusion. This material supports the rationale presented in Chapter 5 by contextualizing the selection of a fibrin/Matrigel-based, post-anchored 3D skeletal muscle platform as an experimentally robust strategy to generate contractile tissues suitable for functional readouts and future organ-on-chip integration.

General requirements for muscle biomaterials

Biomaterials for skeletal muscle engineering must simultaneously support cell viability, alignment, differentiation, force transmission and long-term structural integrity. Key parameters include biocompatibility, degradability, viscoelasticity in the 1–10 kPa range typical of soft muscle tissue, porosity for nutrient diffusion and the presence of adhesion ligands such as laminin-derived peptides or full ECM proteins [185,261]. Electrical and mechanical cues can be further tuned by incorporating conductive fillers like carbon nanotubes, gold nanowires, piezoelectric components or by engineering anisotropic topography via bioprinting, cryogelation or electrospinning [318] .

Natural polymers such as collagen, fibrin, gelatin and tissue-specific dECM provide rich biochemical signaling but can be mechanically weak and subject to rapid cell-mediated degradation, limiting long-term culture unless reinforced. Synthetic or semi-synthetic materials like PEG-fibrinogen, GelMA-CMCMA, PEGDA, and oxidized alginate–gelatin are highly tunable and stable but require biochemical functionalization to support robust myogenesis [142,319].

Advantages and limitations of Matrigel

Matrigel, a basement-membrane extract derived from Engelbreth–Holm–Swarm sarcoma, has been widely used in combination with collagen or fibrin to fabricate skeletal muscle tissues. Its rich composition of laminin, collagen IV, entactin and growth factors provide pro-myogenic cues, enhancing myoblast adhesion, fusion, sarcomeric organization and expression of maturation markers such as myosin heavy chain and α-actinin [320]. In collagen–Matrigel composites, primary dystrophic myoblasts form aligned myotubes that recapitulate disease hallmarks, and collagen–Matrigel micro-bundles [321] have been

used in high-throughput 96-well screening platforms for Duchenne muscular dystrophy therapeutics [142,257,322].

However, Matrigel's tumor-derived and xenogeneic origin, batch-to-batch variability and poorly defined growth factor content pose major limitations for mechanistic studies, regulatory compatibility and clinical translation. Its non-physiological composition and variability can confound interpretation of subtle metabolic phenotypes, which is particularly problematic when modelling MASLD-related sarcopenia where small changes in mitochondrial function or stress responses are important readouts. For these reasons, there is a growing emphasis on replacing Matrigel with more defined, xeno-free matrices, such as human platelet-lysate–based hydrogels or well-characterized dECM formulations, which preserve myogenic potential while improving reproducibility and human relevance [323].

Hydrogel molding and micromolding

Hydrogel molding around posts, frames or Velcro anchors is the most established approach to generate myobundles. It is technically straightforward, compatible with both primary and hiPSC-derived cells, and naturally generates passive tension and uniaxial alignment as the gel compacts between anchor points. Integration with PDMS or 3D-printed PEGDA posts enables direct force measurement via pillar deflection during EPS, supporting quantitative evaluation of pharmacological and cytokine responses. Micromolding using microgrooved PDMS stamps allows fine control over bundle cross-section, confinement and surface patterning, which has been used to identify optimal channel widths and stiffness (for example 0.5 mm channels, 1–3 kPa) for C2C12 maturation and to embed 3D muscles in microfluidic organ-on-chip devices with on-chip biosensing of IL-6 or TNF-α. Limitations include moderate throughput and reliance on soft lithography infrastructure, as well as challenges in scaling to very thick tissues without compromising diffusion [253,256,258,324].

3D bioprinting and microfluidic extrusion

3D bioprinting allows precise spatial patterning of myogenic cells and ECM components into anisotropic architectures, including multi-layered, angle-varying grids that mimic native fascicle arrangements. GelMA-, dECM-, PEG-fibrinogen- and oxidized alginate–gelatin-based bioinks have been printed to produce highly aligned myofibers *in vitro* and to restore 80%+ functional recovery after implantation into rodent muscle-defect models, including pre-vascularized constructs generated by coaxial printing with endothelial cells [325]. Advantages of bioprinting include design flexibility, the ability to co-print support structures like PCL pillars and sacrificial materials for perfusable channels, and a clear path toward automated, standardized manufacturing. Drawbacks are the need to finely balance viscosity, crosslinking, shear stress and oxygenation to preserve cell viability and alignment; natural bioinks alone often degrade or lose mechanical integrity over time, requiring composite formulations with synthetic polymers [319,325–327]. Microfluidic extrusion/spinning of grooved GelMA fibers or aligned hydrogel filaments is a variant that yields long, anisotropic fibers whose surface topography directs myotube

alignment; these fibers can be integrated into larger constructs or chips and have been used to enhance EPS-induced contractility and neuromuscular junction formation [328,329].